

Data-driven Analysis of Heavy Quark Transport in Ultra-relativistic Heavy-ion Collisions

by

Yingru Xu

Department of Physics
Duke University

Date: _____

Approved:

Steffen Bass, Supervisor

Alfred T. Goshaw

Thomas C. Mehen

Stephen W. Teitsworth

Dissertation submitted in partial fulfillment of the
requirements for the degree of Doctor of Philosophy
in the Department of Physics
in the Graduate School of
Duke University

2019

ABSTRACT

Data-driven Analysis of Heavy Quark Transport in
Ultra-relativistic Heavy-ion Collisions

by

Yingru Xu

Department of Physics
Duke University

Date: _____

Approved:

Steffen Bass, Supervisor

Alfred T. Goshaw

Thomas C. Mehen

Stephen W. Teitsworth

An abstract of a dissertation submitted in partial fulfillment of the
requirements for the degree of Doctor of Philosophy
in the Department of Physics
in the Graduate School of
Duke University

2019

Copyright © 2019 by Yingru Xu
All rights reserved

Abstract

Heavy flavor observables provide valuable information on the properties of the hot and dense Quark-Gluon Plasma (QGP) created in ultra-relativistic heavy-ion collisions. Previous study has made significant progress regarding the heavy quark in-medium interaction, energy loss and collective behaviors. Various theoretical models are developed to describe the evolution of heavy quarks in heavy-ion collisions, but also show limited performance as they experience challenges to simultaneously describe all the experimental data.

In this thesis, I present a state-of-the-art Bayesian model-to-data analysis to calibrate a heavy quark evolution model on the experimental data at different collision systems and different energies: the heavy quark evolution model incorporates an improved Langevin dynamics for heavy quarks with an event-by-event viscous hydrodynamical model for the expanding QGP medium, and considers both heavy quark collisional and radiative energy loss. By applying the Bayesian analysis to such modularized framework, the heavy quark evolution model is able to describe the heavy flavor observables in multiple collision system and make prediction of unseen observables. In addition, the estimated heavy quark diffusion coefficient shows a strong positive temperature dependence and strong interaction around the critical temperature.

Finally, by comparing the transport coefficients estimated by various theoretical approaches, I have quantitatively evaluated the contribution from different sources of deviation, which can provide a reference for the theoretical uncertainties regarding the heavy quark transport coefficients.

Acknowledgements

First and foremost, I would like to sincerely thank my advisor, Professor Steffen A. Bass, for his patient guidance, continuous encouragement and generous support during my study at Duke. Working with him is a delightful experience, not only because of his passion and insight into the physics and our research, but also because of his sense of humor that always cheers everyone up. I really appreciate all the opportunities he provided and feel lucky to have him as my advisor.

I would also like to show gratitude to my committee – both from my preliminary exam and defense, including Dr. Chandrasekharan, Dr. Goshaw, Dr. Mehen, Dr. Mueller, Dr. Teitsworth, and the late Dr. Behringer, for their participation in my journey of pursuing my Ph.D, and carefully reading through the annual reports and dissertation.

Next I would like to thank all my groupmates and collaborators, among whom a special thank to Weiyao Ke. He is such a wonderful co-worker as well as a good friend. Every discussion with him is fruitful. Dr. Marlene Nahrgang and Dr. Elena Bratkovskaya are great collaborators and offered me a lot of help, both in my research and my career development. Dr. Shanshan Cao has mentored me selflessly and answered every question I had promptly. Dr. Jussi Auvinen, Dr. Jean-Francois Paquet, Jonah Bernhard and Scott Moreland are reliable seniors that I can knock their doors and get all my questions answered. Also thank Xiaojun Yao, Pierre Moreau, Taesoo Song, Tianyu Dai and the name list can keep going.

Most importantly, none of this could have happened without my family: my parents and my sister as they have been supporting me spiritually throughout my life as always.

This work was supported by the U.S. Department of Energy (DOE) grant number DE-FG02-05ER41367. The computational resources were provided by the Open Science Grid (OSG) funded by DOE and NSF, and by the National Energy Research Scientific Computing Center (NERSC).

Contents

Abstract	iv
Acknowledgements	v
List of Figures	x
List of Tables	xv
1 Introduction	1
1.1 Quantum chromodynamics – QCD	1
1.1.1 QCD Langrangian	2
1.1.2 Two characters of QCD	3
1.1.3 Lattice QCD and the QCD phase diagram	6
1.2 Ultra-relativistic heavy-ion collisions	8
1.2.1 Collective flow	10
1.2.2 Jet quenching	15
1.2.3 Open heavy flavor as hard probes	20
1.2.4 Outline of the dissertation	23
2 Standard model of Heavy-ion Collisions	25
2.1 Initial condition	30
2.1.1 Trento – reduced thickness event-by-event nuclear topology	31
2.1.2 From proton-proton to nucleus-nucleus collision	32
2.1.3 Heavy quark initial condition	34
2.2 Realistic viscous hydrodynamics	37
2.3 Particlization and hadronization	42

2.3.1	Particlization	42
2.3.2	Hadronization	43
2.3.3	Hadronic stage interaction	49
2.4	Experimental observables	51
2.4.1	Multiplicity and centrality	51
2.4.2	Transverse momentum distribution and collective flow	54
2.4.3	Heavy flavor observables: nuclear modification factor and collective flow	57
2.5	Summary	59
3	Transport framework for heavy quark evolution	61
3.1	Summary of various heavy quark in-medium propagation models	61
3.2	Boltzmann Dynamics	67
3.2.1	Boltzmann equation	67
3.2.2	Partonic cross section	69
3.2.3	Monte Carlo implementation	77
3.2.4	Transport coefficients	84
3.3	Langevin Dynamics	88
3.3.1	From Boltzmann to Fokker-Planck	88
3.3.2	Langevin Equation: stochastic realization of the Fokker-Planck equation	90
3.3.3	Einstein relationship and transport coefficients	92
3.3.4	Monte Carlo implementation	94
3.4	Improved Langevin: Langevin with additional radiative energy loss	99
3.4.1	Partonic inelastic scattering	100
3.4.2	Multi-scattering radiative energy loss formalism	104

3.4.3	Recoil force induced by gluon radiation	110
3.5	A full space-time evolution of heavy quarks in heavy-ion collisions	112
3.5.1	Soft medium observables	113
3.5.2	Heavy flavor observables	115
3.6	Summary	124
4	Bayesian methodology	125
4.1	Bayesian inference	126
4.1.1	Bayes' theorem	128
4.1.2	Bayesian calibration	131
4.2	Gaussian Process emulator	137
4.2.1	1-dimensional constrained Gaussian Process	139
4.2.2	Multi-variate predictions: principal component analysis	143
4.2.3	Application and validation of GP emulator	148
4.3	Calibration	150
4.3.1	Likelihood and uncertainties	151
4.4	Summary	152
5	Bayesian model to data comparison	155
5.1	Parameter design	155
5.1.1	Parametrization of the transport coefficients	155
5.2	Preparing the training dataset \mathcal{D}	158
5.2.1	Design points \tilde{X}	158
5.2.2	Model's output \tilde{Y}	160
5.3	Results	162
5.3.1	A closure test: calibration to pseudo-experimental data	162

5.3.2	Calibration to experimental measurements	164
5.4	A more flexible parametrization	171
5.4.1	Pre-equilibrium dynamics	172
5.4.2	More inputs parameters	174
5.4.3	Posterior results	177
5.5	Summary	190
6	Comparison among different models	191
6.1	QGP medium evolution	193
6.1.1	Description of the models	194
6.1.2	Space-time evolution of the QGP medium: PHSD vs. hydrodynamics	197
6.2	Heavy quark evolution in the QGP medium	204
6.2.1	Transport coefficients	206
6.3	Summary	217
7	Conclusions	218
A	Appendix	221
A.0.1	Relativistic kinematics	221
A.0.2	Mandelstam variables	222
A.0.3	Hydrodynamics equations	222
A.0.4	Derive Fokker Planck equation from Langevin equation	223
	Bibliography	226
	Biography	243

List of Figures

1.1	Experimental measurements of QED and QCD coupling constant	3
1.2	Lattice QCD Equation of State	6
1.3	Schematic picture of a heavy-ion collision.	9
1.4	Schematic view of the event-plane in heavy-ion collision	11
1.5	Anisotropic flow of charged hadrons	12
1.6	Nuclear modification factor R_{AA} of charged hadron	16
1.7	R_{AA} and v_2 between pions and electrons from heavy flavor decays at RHIC	19
1.8	R_{AA} and v_2 for D -mesons at the LHC	22
2.1	Space-time picture of a heavy-ion collision event	26
2.2	Heavy quark space-time evolution in heavy-ion collisions	30
2.3	Cross section of the reduced thickness function for a pair of nucleon participant	32
2.4	Examples of initial energy density generated by Trento	34
2.5	Examples of heavy quark position generated by Trento	36
2.6	Initial p_T spectra for charm/bottom production in AA and pp collisions . . .	38
2.7	Temperature dependence of the specific shear and bulk viscosity	40
2.8	Energy density profile for one hydrodynamical evolution in a Pb-Pb collision event	41
2.9	Fragmentation function for quarks into mesons	45
2.10	Recombination probability for heavy quarks	48

2.11	Total cross section for the heavy meson scattering with light hadron	50
2.12	Charged particle pseudo-rapidity distribution	52
2.13	Cartoon example of the centrality with the final observables $\langle N_{\text{part}} \rangle$	53
2.14	Spectra of identified particles pion, kaon, proton	55
2.15	v_2 as a function of p_T in Pb-Pb collision for different $N_{\text{trk}}^{\text{offline}}$ ranges	57
2.16	D -meson reference spectrum in pp collisions at 5.02 TeV	58
2.17	D_0 meson nuclear modification factor R_{AA}	59
3.1	Center of mass frame for a $2 \rightarrow 2$ process.	70
3.2	FEYNMAN diagrams for $Q + g \rightarrow Q + g$	71
3.3	FEYNMAN diagrams for $Q + q \rightarrow Q + q$	72
3.4	Strong coupling constant	75
3.5	Cross section of charm quark scattering with light partons $\sigma_{12 \rightarrow 34}$	77
3.6	Total scattering rate of charm quark scattering with light partons $\Gamma_{12 \rightarrow 34}$	80
3.7	Total scattering rate of charm quark scattering with light partons $\Gamma_{12 \rightarrow 34}$, projected in 3D	81
3.8	Evolution of charm quark energy distribution	84
3.9	Transport coefficients $\eta_D, \kappa_L, \kappa_T$ for heavy quark scattering with light partons	87
3.10	Charm quark distributions in Langevin dynamics and linearized Boltzmann dynamics	96
3.11	Charm quark energy evolution with the different implementation of Ein- stein relationship	97
3.12	Charm quark energy distribution with or without Einstein relationship im- plementation	99

3.13	FEYNMAN diagram for $Q + g \rightarrow Q + g + g$	100
3.14	FEYNMAN diagram for $Q + q \rightarrow Q + q + g$	101
3.15	Heavy quark radiates a gluon $1 \rightarrow 2$ process.	103
3.16	Averaged gluon radiation number for heavy quark propagating in a static medium	109
3.17	Event-by-event viscous hydrodynamical model calculation of soft observables	114
3.18	Charm quark/ D -meson R_{AA} and v_2 in Pb-Pb collisions	116
3.19	Charm quark/ D -meson R_{AA} in Pb-Pb collisions	118
3.20	Charm quark transport coefficients	121
3.21	D -meson R_{AA} and v_2 in Pb-Pb collisions	122
4.1	Workflow for the Bayesian model-to-data comparison framework.	127
4.2	A sketch of the Bayes' theorem.	127
4.3	Example of 50 events with $\mathcal{D} = \{(p_i, y_i)\}$	135
4.4	Posterior distribution of parameters estimated by the MCMC method	136
4.5	Implementation of Gaussian Process emulator with different covariance function	142
4.6	SVD transformation of the physical observable space to principal component space	146
4.7	Application of the PCA in heavy quark observables	147
4.8	Comparison between GP emulators' prediction against model calculation	149
4.9	Correlation matrices for the uncertainties	152
5.1	Spatial diffusion coefficient parametrization with respect to γ	156

5.2	Prior distribution of input parameters	158
5.3	Improved Langevin model calculation of D -meson observables with prior parameters	161
5.4	Improved Langevin model calculation of D -meson observables in Pb-Pb collisionsV	163
5.5	Posterior distribution of the diffusion coefficient parameters	165
5.6	Gaussian Process Emulator prediction for 50 random parameter sets	167
5.7	Posterior distribution of the transport coefficients parameters (α, β, γ)	168
5.8	Posterior range of the spatial diffusion coefficient $D_s 2\pi T$	170
5.9	A septic to demonstrate the pre-equilibrium interaction	174
5.10	Heavy quark special diffusion coefficient	175
5.11	Prior range of the charm quark diffusion coefficient	176
5.12	Improved Langevin model calculation of D -meson observables with prior parameters	176
5.13	Posterior distribution of the heavy quark evolution model parameters	178
5.14	Posterior range of the spatial diffusion coefficients $D_s 2\pi T$	182
5.15	Charm quark diffusion coefficient evaluated dynamically	184
5.16	Improved Langevin calculation of the D -meson R_{AA} and v_2 after calibration	185
5.17	Improved Langevin calculation of D -meson v_3 after calibration	187
5.18	Improved Langevin calculation of D -meson Event Shape Engineering observables	187
5.19	Improved Langevin calculation of D -meson Event Shape Engineering observables	189

6.1	Heavy quark diffusion coefficient	192
6.2	Shear and bulk viscosity $\eta/s, \zeta/s$	196
6.3	Initial condition for hydrodynamics	197
6.4	Contour plots of the local energy density e in the transverse plane	198
6.5	Components of the 3-velocity $(\beta_x, \beta_y, \beta_z)$	199
6.6	Radial distribution of the Fourier modes	201
6.7	Event-by-event averaged spatial eccentricity ε_2	203
6.8	Event-by-event averaged total momentum anisotropy	204
6.9	Heavy quark evolution implementation	205
6.10	Total charm quark transport coefficients with radiative process	207
6.11	Initial conditions at $\tau_0 = 0.6$ fm/c for Au-Au collisions at 200 GeV	210
6.12	Time evolution of the spatial and momentum anisotropy of the QGP medium	211
6.13	Charm quark elliptic flow development inside a hydrodynamical medium .	212
6.14	Charm quark R_{AA} as function of rapidity	213
6.15	Charm quark R_{AA} as function of rapidity	215

List of Tables

3.1	Open heavy flavor models	66
3.2	Value of \hat{q} at $\tau_0 = 0.6$ fm/c in the 0-5% centrality hydro events	108
5.1	Prior range and description for the parameters that determines the diffusion coefficient	159
5.2	D -meson variables to be compared between model calculation and experimental measurements	160
5.3	Prior range and description for the parameters that determines the diffusion coefficient	177

Chapter 1

Introduction

The first few microseconds after the Big Bang, the temperature and energy density of our Universe was so high that hadrons — bound states of quarks and anti-quarks — could not form. Instead deconfined quarks, anti-quarks, and gluons existed in a thermalized state known as Quark-Gluon Plasma (QGP). Only when the critical temperature of the Universe dropped below a critical value $T_c \simeq 154 \pm 9$ MeV, colored degrees of freedom confined into color singlet objects and the first hadron formed. The QGP medium, which is perhaps the simplest system of strongly interacting particles that exists in the context of Quantum Chromodynamics (QCD), provides us a unique opportunity to study the theory of the strong force and the phase diagrams of the QCD.

1.1 Quantum chromodynamics – QCD

Quantum Chromodynamics (QCD), being the theory of the strong force, is one important piece of the Standard Model. The fundamental degrees of freedom in theory are quarks and gluons, often referred to as partons, which carry color charge and cannot be directly seen in nature due to color confinement. Elementary quarks and gluons form composites, hadrons, which are particles that can be detected in nature. Mesons are bound states made of one quark and one anti-quark ¹, while baryons are made of three quarks.

¹valence quark, different from sea quarks which come virtual quark-antiquark pair

1.1.1 QCD Langrangian

Many similarities exist between QCD and quantum electrodynamics (QED), which is the theory to describe the electromagnetic force. QED has two degrees of freedom (positive and negative electric charges) while QCD has three degrees of freedom (red, blue, and green color charges). In both QCD and QED, the forces between the like charges are repulsive while the forces between different charges are attractive. The interaction between electrons is transmitted by photons in QED, analogous to the gluons transmitting force between quarks in QCD.

We refer QED belonging to the $U(1)$ group due to one type of photon forming the generator of the group. QCD belongs to the $SU(3)$ group with eight types of gluons being the generators. In a simplified representation, we can write the QCD Lagrangian in a similar way as QED one:[1]:

$$\mathcal{L}_{QCD} = \bar{\Psi}(i\gamma_{\mu}D^{\mu} - m)\Psi - \frac{1}{4}F_{\mu\nu}^a F_a^{\mu\nu}. \quad (1.1)$$

Ψ is the $4N_c N_f$ -dimensional spinor of the quark field with $N_c = 3$ colors and N_f flavor system, γ^{μ} are the Dirac matrices and m is the quark mass matrix. The covariant derivative is defined as:

$$D_{\mu} \equiv \partial_{\mu} - igT_a A_{\mu}^a, \quad (1.2)$$

where $g = \sqrt{4\pi\alpha_s}$ characterizes the strong coupling strength, A_{μ}^a is the gluon field and T_a is the generator of the local $SU(N_c)$ symmetry². The gluon field strength tensor is defined as

$$F_{\mu\nu}^a = (\partial_{\mu}A_{\nu}^a - \partial_{\nu}A_{\mu}^a + gf_{bc}^a A_{\mu}^b A_{\nu}^c). \quad (1.3)$$

The first term on the right hand side Eqn. 1.1 describes the dynamics of quarks and their

²In this case, $N_c = 3$ is the number of color charges.

interaction with gluons, and the second term describes the dynamics of gluons. Different from QED where photons do not interact with each other, the gluons carry color charges and therefore can couple to themselves. This non-Abelian feature of QCD renders itself to be much more complicated than QED, as in an Abelian theory the elements commute with each other and it is not the case in QCD.

In principle, every phenomenon in QCD is describable by the Lagrangian. However, in practice, only the perturbative regime with small coupling strength is theoretically accessible. In the study of the strong force, we must rely on lattice calculation or phenomenological modeling to understand the non-perturbative effects and explore the properties of the QCD matter. Before we move on to the phenomenological model related to the strongly interacting QCD matter, let us review two critical features of the QCD.

1.1.2 Two characters of QCD

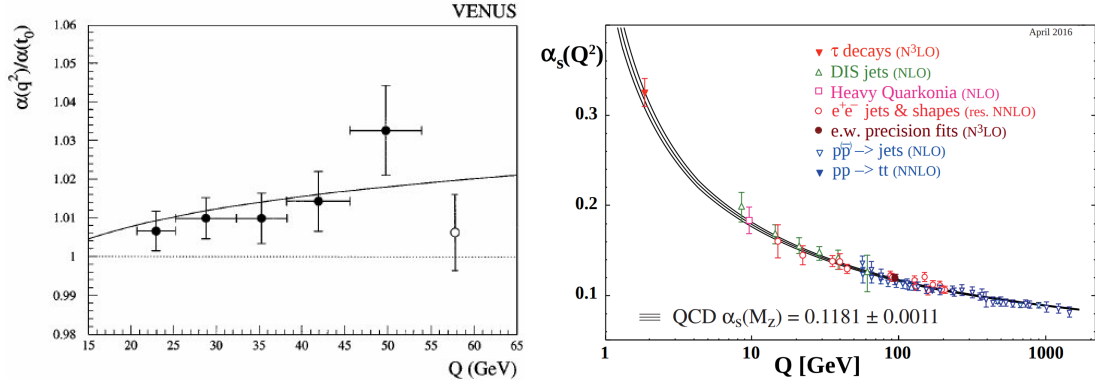


Figure 1.1: [Left]: experimental results of the effective QED coupling from e^+e^- collision, measured by VENUS collaboration. Here t_0 represent a typical momentum transfer scale and choose as $|t_0| = (10\text{GeV})^2$. [Right]: summary of measurements of α_s as a function of energy scale Q . The respective degree of QCD perturbation theory used in the extraction of α_s is indicated in the brackets as next-to-leading order and next-to-next-to-leading order approximation [2].

- Asymptotic freedom[3, 4]

One of the most remarkable properties of the QCD is the fact that the strong coupling constant becomes small for processes involving large momentum transfer Q^2 – “hard processes”. To better demonstrate its consequence, recall what happens in QED. In QED, the electron-positron pairs polarize the surrounding vacuum, resulting in a stronger electric interaction at shorter distance/larger energy. In the momentum space, the dependence of the effective coupling α_{em} with respect to the momentum transfer carried by photon is given by:

$$\alpha_{\text{em}} = \frac{\alpha_{\text{em}}(0)}{1 - \frac{\alpha_{\text{em}}(0)}{3\pi} \log\left(\frac{Q^2}{m_e^2}\right)}, \quad (1.4)$$

where $\alpha_{\text{em}}(0) = 1/137$ and the expression diverges when $Q_{\text{max}} \sim 10^{280}$ MeV (Laudau pole), far beyond any particle accelerator energies we can achieve so far.

In QCD the situation is different. The self-interaction of gluons adds an additional contribution to the one-loop correction, resulting in a change of sign for the β function. The coupling constant becomes small at shorter distance and large at large distance. It is referred to as the anti-screening. The formula for the one-loop running coupling constant in QCD is:

$$\alpha_s(Q^2) = \frac{\alpha_s(Q_0^2)}{1 + \frac{\alpha_s(Q_0^2)}{12\pi} (11N_c - 2N_f) \log\left(\frac{Q^2}{Q_0^2}\right)}. \quad (1.5)$$

Figure. 1.1 confirms the experimental verification of this prediction. The left panel shows the results for QED coupling while the right panel shows the running coupling for the strong interaction. Note that α_s is large compared to the electromagnetic coupling $\alpha_{\text{em}} \sim 1/137$; the running of the strong coupling is also strong, comparing to a few percents of increase for a large momentum transfer in QED.

The equation 1.5 can be further simplified when we define a QCD scale parameter

Λ_{QCD} as $\frac{1}{\alpha_s(Q^2)} \equiv \frac{11N_c - 2N_f}{12\pi} \log(Q^2/\Lambda^2)$, now we have:

$$\alpha_s(Q^2) = \frac{12\pi}{(11N_c - 2N_f) \log\left(\frac{Q^2}{\Lambda_{\text{QCD}}^2}\right)}. \quad (1.6)$$

The QCD scale Λ_{QCD} is approximately 0.2 GeV. When the momentum transfer Q^2 falls below Λ_{QCD}^2 , the coupling constant becomes large and perturbative QCD, which relies on the small number expansion, breaks down.

- Color confinement

The asymptotic freedom allows us to probe the interaction among quarks and gluons at a short distance where the coupling is small. To the contrary, the growth of the coupling at large distance leading to the binding of quarks and gluons into confined colorless hadrons of size $\sim 1\text{fm}$. Confinement is also the consequence of gluon carrying color charge and coupling to each other. To model the confinement in a phenomenological way, we can express the quark-antiquark potential in terms of a Cornell potential:

$$V(r) = -\frac{4}{3} \frac{\alpha_s(r)}{r} + \sigma r, \quad (1.7)$$

where α_s is the strong coupling constant, σ is the tension coefficient, and r is the distance between quark pairs. The first term on the right hand side of Eqn. 1.7 is analogous to the Coulomb potential, but with the strong coupling constant. The second term is unique to QCD and increases with increasing distance. When the quark separation is small, the Coulomb part dominates, and the theory almost becomes identical to QED but with a larger coupling. However, for a large separation distance, the linear part dominates, preventing two quarks from becoming completely free.

At finite temperature, various properties of QCD become sensitive to confinement.

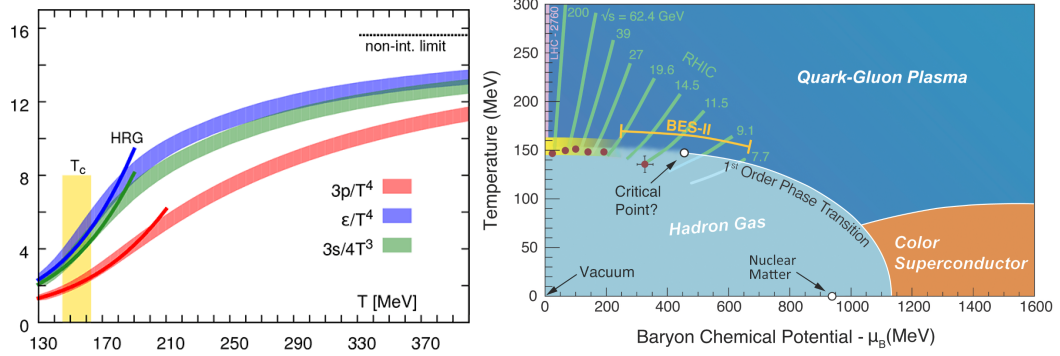


Figure 1.2: [Left]: lattice QCD calculation of the pressure, energy density and entropy density as a function of temperature, calculated by Hot QCD collaboration in a (2+1)-flavor QCD [7]. The dark lines show the prediction for the (Hadron Resonance Gas) HRG model. The horizontal lines in the upper right corresponds to the idea gas limit for the energy density e/T^4 , and the yellow vertical band marks the crossover region $T_c = (154 \pm 9)$ MeV. [Right]: Semi-quantitative sketch of the phase diagram in the plane of temperature T and baryon chemical potential μ_B .

In particular, QCD predicts a phase transition from ordinary confined nuclear matter to a deconfined new state of quarks and gluons at extremely high temperature and/or density[5]. Understanding the structure of the QCD phase diagram is one of the keys to our fundamental description of nature [6].

1.1.3 Lattice QCD and the QCD phase diagram

Lattice QCD is an exact method to solve the QCD Lagrangian and compute the thermodynamic properties of QCD matter and its Equation of State (EoS). In lattice QCD calculations, one directly computes the grand partition function \mathcal{Z} by discretizing the space-time on a lattice ($V \times 1/T$) and extrapolating to the continuum limit:

$$\mathcal{Z}(T, V, \mu) = \int \mathcal{D}\bar{\Psi} \mathcal{D}\Psi A_a^\nu \exp \left[\int (\mathcal{L}_{QCD} + \mu \mathcal{N}) \right]. \quad (1.8)$$

where μ is the quark chemical potential associated with quark number conservation. From the grand partition function, one can derive other thermodynamic quantities, such as pres-

sure (p), entropy (s), number density (n) and so on:

$$p(T, \mu) = T \frac{\partial \ln \mathcal{Z}}{\partial V}, s = \frac{\partial p}{\partial T} \Big|_{\mu}, n = \frac{\partial p}{\partial \mu} \Big|_T. \quad (1.9)$$

The left panel of Fig. 1.2 shows the lattice QCD calculation of the normalized pressure p , energy density ε and entropy density s as a function of temperature T . The solid lines are a hadron resonance gas (HRG) estimation, which shows a reasonable agreement with the lattice QCD calculation at lower temperature $T < 150$ MeV. The vertical yellow band marks the cross-over region, where the QCD matter experiences the transition from ordinary nuclear matter (a hadronic gas) to a deconfined state of quarks and gluons – Quark-Gluon Plasma (QGP). The increase of normalized energy density ε/T^4 and entropy density $3s/4T^3$ with respect to temperature is a direct manifestation of the cross-over, as the QGP matter has more thermodynamic degrees of freedom due to the color deconfinement.

The lattice calculation shown in the EoS is done with $\mu_B = 0$, corresponding to the vertical y-axis region on the right panel of Fig. 1.2, which illustrates a sketch of our current understanding of the QCD phase diagram in a plane of temperature T and baryon chemical potential μ_B . The phase space is separated into three regions, where at the low temperature and low chemical potential region, the QCD matter is in the hadronic phase. The nuclear matter can experience the transition into a slow compression resulting in the cold matter at very high baryon density; and a rapid compression leading to strong heating at high temperature [8]. The former compression is not achievable yet in a laboratory but is believed to exist in the interior of a neutron star. Under such condition, one would expect that the neutrons undergo the first order phase transition, which dissolve and condensate into a color superconductor at low temperature. More reviews on this phase can be found on [8–10].

The second type of compression has been achieved in a heavy-ion collision. During the

collision, two nuclei collide with each other with speed close to the speed of light, and melt the overlap region, resulting in a phase transition from hadronic state to the deconfined QGP. Such an extra-ordinary state is also believed to be the state of our early Universe right after the Big Bang. The phase transition at zero or low baryon chemical potential has been studied by lattice QCD calculation, which shows not a first order phase transition but a smooth cross-over at the temperature around $T_c = (154 \pm 9)\text{MeV}$. At larger baryon chemical potential, due to the sign problem [11] one has to rely on phenomenological models and comparison with experiment to explore this region.

The first order phase transition at low temperature, large baryon chemical potential and a cross-over at high temperature, low baryon chemical potential imply that there might be a critical point somewhere in between. In the laboratory, the only experiments which can help us to find the critical points and explore the phase transition to QGP matter are ultra-relativistic heavy-ion collisions. The two heavy-ion colliders currently operating are the Large Hadron Collider (LHC) at CERN (Conseil Europeen pour la Recherche Nucleaire, Geneva, Switzerland) and the Relativistic Heavy-ion Collider (RHIC) at BNL (Brookhaven National Laboratory, New York, USA). In the next section, we will review a few key experimental discoveries in heavy-ion collisions.

1.2 Ultra-relativistic heavy-ion collisions

The search for the QGP medium under laboratory condition started in the late 1980s[12]. In 2000, CERN announced circumstantial evidence for the creation of the new state of matter in Pb-Pb collisions at the SPS (Super Proton Synchrotron) accelerator. It is not until 2005, when BNL presented the results of their first five years of measurements of Au-Au collisions at $\sqrt{s_{NN}} = 200 \text{ GeV}$ at RHIC, that the QGP matter revealed its creation in a laboratory. Since then, experiments at different collision systems and collision energies

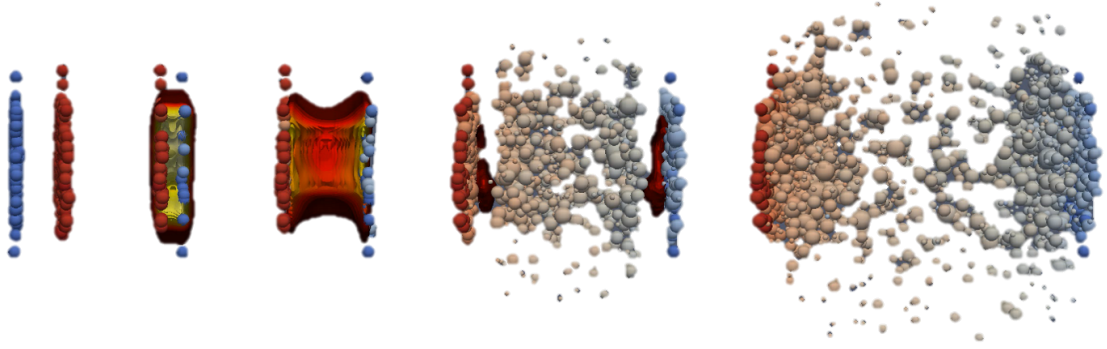


Figure 1.3: Schematic picture of a heavy-ion collision.

have been conducted and the heavy-ion community has been exploring the QCD phase diagram and studying the properties of the QGP medium.

In ultra-relativistic heavy-ion collisions, two nuclei are accelerated to nearly the speed of light. The two Lorentz-contracted pancakes of nuclei then collide with each other and deposit energy in a compact overlap region. The energy density of the overlap region is so high that the nuclear matter “melts” into a deconfined state of quarks and gluons. After a short time, the system reaches a thermal equilibrium state known as Quark-Gluon Plasma (QGP). The QGP medium then expands, cools down and hadronizes into final state hadrons, which will be detected and relevant observables are measured.

Figure. 1.3 depicts a schematic picture of the different stages in heavy-ion collisions. The timescale for the QGP phase evolution is in the order of $< 20 \text{ fm}/c$ (in a Pb-Pb collision). After the system cools down below a critical temperature T_c , the system undergoes “hadronization” to colorless hadrons, “chemical freezeout”³, “thermal freezeout”⁴. Exper-

³Here the chemical freezeout is referred to as when inelastic processes that change the hadronic species and abundance stop. However, I should mention the separation of hadronization and chemical freezeout, the concept of chemical freezeout, as well as the phase transition temperature and chemical freezeout temperature are still under debate. In this thesis, we follow the philosophy of Ref. [13, 14] where chemical freezeout is a process within the hadronic phase. For an alternative philosophy, where chemical freezeout is interpreted as a statistical process associated with a phase transition, please refer to Ref. [15].

⁴Thermal freezeout is referred to when elastic and inelastic processes cease and the momentum of hadrons stop changing.

imentally, only the time-integrated quantities, such as the momentum spectra of the final state hadrons (d^3N/d^3p), the particle multiplicity and yields (N) etc. can be measured.

Two of the most profound discoveries in heavy-ion collisions are: the QGP matter is a hot and dense plasma which behaves like a near perfect liquid with small viscosity and exhibits a collective flow; high energetic partons interact strongly with the medium, resulting in a significant energy loss and strong suppression of the particle spectra comparing with proton-proton collisions, also is referred to as jet-quenching.

1.2.1 Collective flow

Prior to the discoveries of RHIC and the LHC, the QGP was expected to be a gas-like state due to the asymptotic freedom and color Debye screening. However, the collective behavior, especially elliptic flow seen in RHIC Au-Au collision data, showed the quantitative agreement with the prediction from a ideal fluid dynamics for the first time[21, 22]. This led to the assumption that the quark-gluon plasma behaves like a “perfect fluid”, with a small viscosity over entropy density ratio (η/s).

Collective behavior means that the emitted particles exhibit some common pattern, such as a collective motion in the beam direction (longitudinal flow), a common motion of particles with respect to the spherical symmetry (radial flow), and azimuthal angle (transverse/azimuthal flow). It is one of the most compelling evidence for whether or not a QGP is created and whether the thermal equilibrium is achieved during ultra-relativistic heavy-ion collisions. Investigation of such behavior provides us with insight into the fundamental properties of the QCD system, such as details of the Equation of state, initial state fluctuations, and the viscosity of the QGP medium.

We will focus on azimuthal anisotropic flow, which corresponds to particle emission with respect to the azimuthal angle in the transverse plane. The origin of the anisotropic

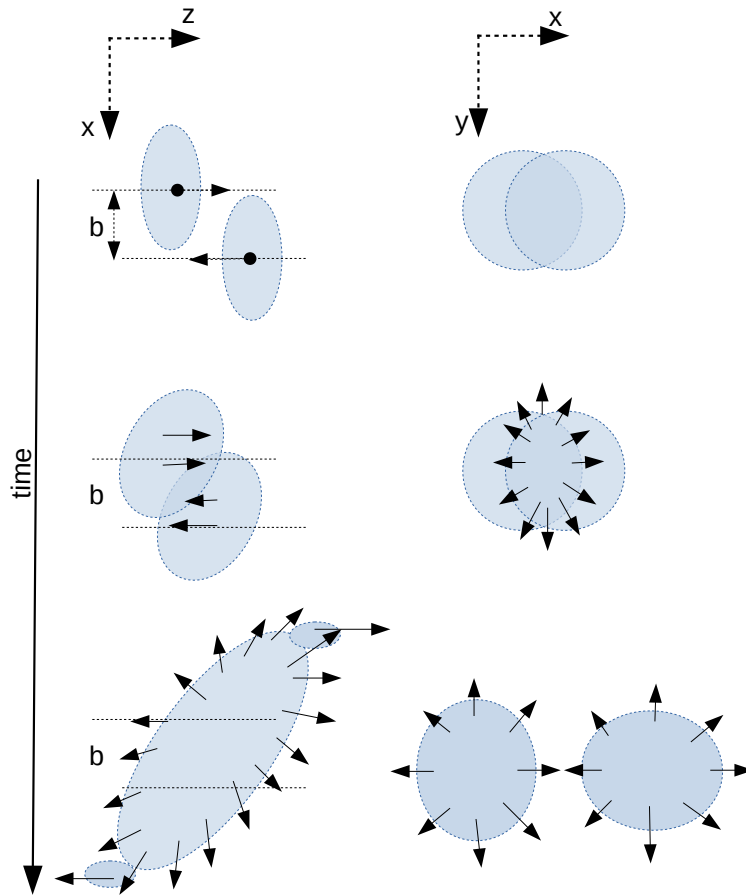


Figure 1.4: Schematic view of the time evolution in heavy-ion collision and the development of the collective flow. Left, the time evolution of the collision reaction in the reaction plane, Right: a sketch of the transverse plane at mid-rapidity, several phases of a typical reaction can be identified.

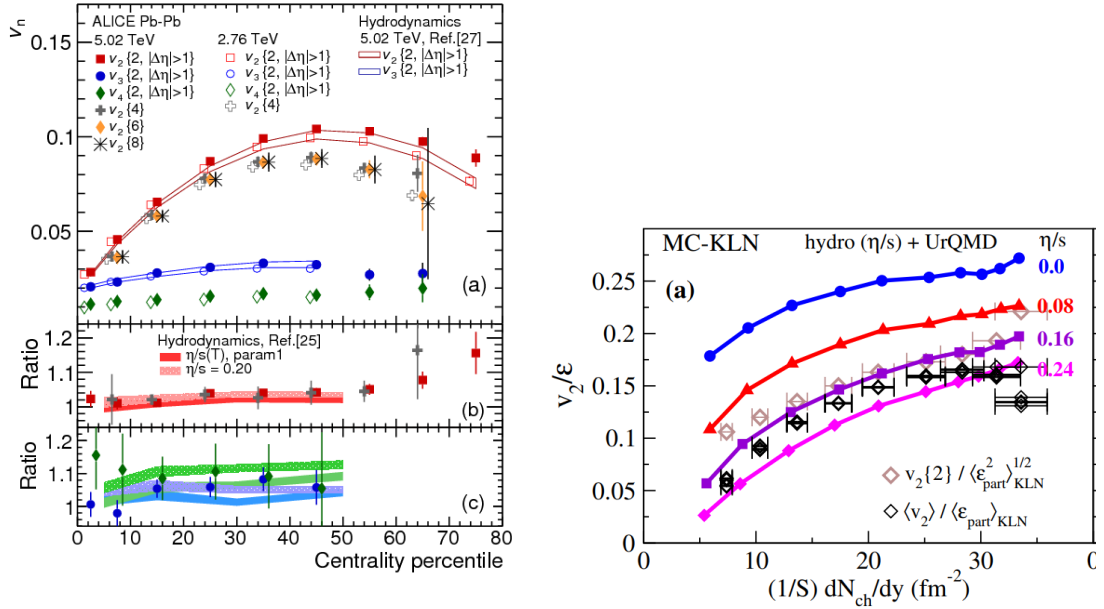


Figure 1.5: [Left]: Anisotropic flow integrated over $0.2 < p_T < 5$ GeV for two-particle and multi-particle correlation as a function of centrality for Pb-Pb collisions at 2.76 and 5.02 TeV. Comparing the hydrodynamical model prediction [16, 17] (lines and bands) with ALICE measurements [18] (error bars and dots). The two lower panels show the ratio between beam energies and the corresponding model predictions. Figure from [19] [Right]: eccentricity-scaled elliptic flow v_2/ϵ_2 with respect to charge particle density per unit overlap area $1/S dN_{ch}/dy$. The markers are constructed using the experimental measured elliptic flow $\langle v_2 \rangle$ and two-particle cumulant $v_2\{2\}$, along with the charged-particle density dN_{ch}/dy . The colored lines are the results calculated by hydrodynamical models with several specific shear viscosity $\eta/s = ., 0.08, 0.16, 0.24$. The eccentricity ϵ_2 is obtained from the MC-KLN initial condition model [20].

flow generally is believed to be the anisotropy of the initial geometry. Figure 1.4 depicts a simplified sketch of a heavy-ion collision event. When initially two nuclei approach each other in the beam direction (z -direction), their orientation in space and the initial beam direction defines the reaction plane xy . The distance between two centers of the nuclei is referred to as impact parameter b . After they overlap, the energy of the original longitudinal motion is converted into the internal degrees of freedom in the reaction, new particles are created and thermalization occurs. After a short time, the energy density starts to relax, the system undergoes expansion, the temperature and density reduces along with the expansion till the hadronization.

In a non-central collision where the impact parameter $b > 0$, the overlapping region has an elliptical almond shape which results in a steeper pressure gradient along the x -axis compared to the y -axis. The difference of the pressure gradient drives the medium expansion preferably in the x -direction. After the medium hadronizes into hadrons, the azimuthal distribution of the final state particles shows the anisotropy, where the averaged p_x component is larger than p_y component. Thus the initial spatial anisotropy is converted to a momentum anisotropy.

To express the momentum anisotropy mathematically, we can expand the final-state particle azimuthal distribution as a Fourier series:

$$E \frac{d^3 N}{d^3 p} = \frac{d^3 N}{p_T dp_T dy d\phi}(p_T, y, \phi) = \frac{1}{2\pi} \frac{d^2 N}{p_T dp_T dy} \left[1 + \sum_{n=1}^{\infty} 2v_n(p_T, y) \cos[n(\phi - \Psi_n^{\text{RP}})] \right], \quad (1.10)$$

where E, p_T, y, ϕ are the energy, transverse momentum, rapidity, and azimuthal angle of the particle, Ψ^{RP} is the reaction plane angle associated with the initial density distribution. The Fourier coefficients $v_n(p_T, y)$, among which the first three are named as direct(v_1), elliptic(v_2) and triangular(v_3) flow according to their geometric origin, characterize the

anisotropy of the system, they are given by:

$$v_n e^{in\Psi_n^{\text{EP}}} = \frac{\int p_T dp_T dy d\phi e^{in\phi} \frac{dN}{dy p_T dp_T d\phi}}{\int p_T dp_T dy d\phi \frac{dN}{dy p_T dp_T d\phi}} = \langle e^{in\phi} \rangle, \quad (1.11)$$

the angular bracket denote the average over particles of interest in all selected events, Ψ_n^{EP} is the event-plane angle that points to the direction where the n^{th} harmonic coefficient is the largest⁵.

The initial spatial anisotropy, although is not accessible in experimental measurements, is of great interest from the theoretical point of view. It can be characterized by the initial harmonic eccentricity coefficients:

$$\varepsilon_n e^{in\Psi_n^{\text{RP}}} \equiv \frac{\int r dr d\phi r^n e^{in\phi} e(r, \phi)}{\int r dr d\phi r^n e(r, \phi)} = \frac{\{r^n e^{in\phi}\}}{\{r^n\}}, \quad (1.12)$$

where $e(r, \phi)$ is the initial energy density distribution in the transverse plane, and the curly bracket denotes average over the initial energy density.

Without considering the initial state fluctuation, we expect a near-linear dependence of the flow coefficients v_n on the spatial eccentricity coefficient ε_n , at least for lower order harmonics v_2, v_3 . The conversion efficiency from ε_n to v_n depends on the details of the EoS, the properties of the system such as the shear and bulk viscosity (η, ζ) and other unknown factors. By measuring the flow anisotropies, we can, in principle, determine the properties of the medium experimentally. Figure. 1.5 shows the centrality dependence of the integrated flow v_2 in Pb-Pb collisions at 2.76 and 5.02 TeV, and compares the calculation from a hydrodynamical model with experimental measurements by ALICE collaboration. The elliptic flow v_2 shows a strong dependence on centrality up to 50% due to the correlation of the increasing impact parameter with the initial-state anisotropy. For higher centrality,

⁵The reaction plane angle related to the initial condition, which is un-measurable. In experiment, we use the event-plane angle to approximate the reaction-plane angle. Without the interference between different orders, we expect Ψ^{RP} and Ψ^{EP} point to the same direction on average and up to event-by-event-fluctuations.

the QGP medium does not survive long enough for the flow to fully develop even though the anisotropy is large in those collisions. Meanwhile, the triangular and quadrangular flow v_3, v_4 have weaker dependence in centrality since they are mostly driven by the initial-state fluctuation.

The right panel of Fig. 1.5 shows the eccentricity-scaled elliptic flow v_2/ε_2 with respect to the charged particle density per unit overlap area $1/SdN_{\text{ch}}/dy$ for Au-Au collisions at $\sqrt{s_{NN}} = 200$ GeV. The symbols are calculations using the experimental measurements of elliptic flow v_2 and charged particle density dN_{ch}/dy , while the colored lines are the hydro calculation with different shear viscosity values. The ratio between v_2/ε_2 is strongly dependent on the specific shear viscosity η/s , which can be used as the criterion to calibrate the hydrodynamical model. In the case of the initial condition being generated from an MC-KLN model, the optimal value for η/s is around 0.2⁶.

1.2.2 Jet quenching

“A jet is a narrow cone of hadrons and other particles produced by the hadronization of a quark or gluon with large transverse momentum in a particle physics or heavy-ion experiment” [24]. “Jet-quenching” is one of the “smoking guns” for the creation of the QGP medium, described as the suppression of the high p_T ($p_T \gg \Lambda_{\text{QCD}}$) hadron spectra in heavy-ion collisions compared to the corresponding observables in proton-proton collisions.

One important assumption in QCD is that we can separate the short and long distance processes and thus the production of a hadron h with large transverse momentum p_T can

⁶I should remind that the extraction of the shear viscosity is a complex process and requires systematic investigation. The extraction is highly correlated with different components such as the initial conditions, the bulk viscosity implementation, the hadronic state interaction and so on.

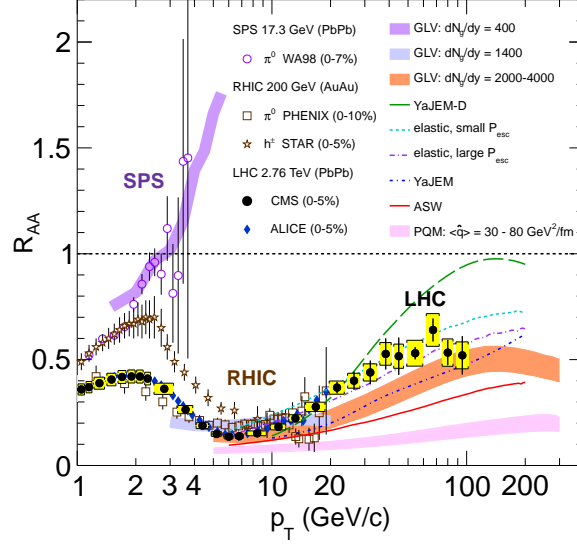


Figure 1.6: Experimental measurements of nuclear modification factor R_{AA} of neutral pions π^0 , charged hadrons h^\pm and charged particle at Pb-Pb collisions at 17.3 GeV, Pb-Pb collisions at 2.76 TeV and Au-Au collisions at 200 GeV, as a function of transverse momentum p_T , compared with several theoretical models. The error bars on the points are statistical uncertainties, and the yellow boxes around the CMS points are the systematic uncertainties. Figure is taken from [23].

be factorized as:

$$\sigma^{A+B \rightarrow h} \sim f_a^A(x_q, Q^2) \otimes f_b^B(x_2, Q^2) \otimes \sigma^{a+b \rightarrow c+x}(x_1, x_2, zp_T, Q^2) \otimes D_{k \rightarrow h}(z, Q^2). \quad (1.13)$$

$\sigma^{a+b \rightarrow c+x}$ is the cross section of short-distance process of parton a, b scatter and produce final state parton c , which can be computed perturbatively up to some order of α_s above a lower p_T limit. The two terms $f_a^A(x, Q^2), f_b^B(x, Q^2)$ describe the parton distribution function (PDF) of a parton (a/b) inside the collision object (protons, nuclei) A/B . The fragmentation function $D_{k \rightarrow h}(z, Q^2)$ describes the process of a parton c propagating and hadronizing into a hadron h . The long-distance processes, in this case, the parton distribution functions and hadronization processes are non-perturbative yet assumed to be universal, therefore we can rely on experimental measurements to determine the fragmentation

function.

In ultra-relativistic heavy-ion collisions, due to the existence of the QGP medium, the high p_T parton interacts with the medium and its propagation is modified:

$$D_{k \rightarrow h}(z, Q^2) \rightarrow D'_{k \rightarrow h}(z, Q^2). \quad (1.14)$$

We can quantitatively measure the modification by comparing the cross section/spectra of the hadron h in a nucleus-nucleus collision with that in a proton-proton collision:

$$R_{AA}^h(p_T) = \frac{dN_{AA}^h/dp_T}{\langle N_{coll} \rangle d\sigma_{pp}^h/dp_T}, \quad (1.15)$$

where $\langle N_{coll} \rangle$ is the average number of binary nucleon-nucleon collisions in AA collisions. This is called the nuclear modification factor and is one of the most important observables in heavy-ion collisions. For a nucleus-nucleus collision that is assumed to be a superposition of $\langle N_{coll} \rangle$ independent nucleon-nucleon collisions, the nuclear modification factor approximately equals to unity if there is no medium modification, which is indeed the case for gauge bosons such as photons, W and Z bosons that do not strongly interact with the medium [25, 26]. However, the experimental data of the light particles reveals a very different behavior. Figure 1.6 shows the R_{AA} of charged hadrons and identified particles (h^\pm, π) in the central collisions from three different collision systems: Pb-Pb collisions at $\sqrt{s_{NN}} = 17.3$ GeV, Pb-Pb collisions at 2.76 TeV and Au-Au collisions at 200 GeV, and compares the experimental measurements with a few theoretical model calculations. It is seen that the high-momentum particles are strongly suppressed at RHIC and LHC. Moreover, for collisions with higher center-of-mass energy (2.76 TeV vs. 200 GeV), the medium created in the collision has a higher temperature and this leads to more energy loss for the parton, results in the slightly larger suppression in the LHC energies. Finally, the rise of R_{AA} at LHC energies for very high momentum p_T suggests that the energy loss of the

high momentum jet decrease with their energy, as one would expect from the asymptotic freedom.

In addition to the in-medium interaction - which is called the hot nuclear matter effect or final state effect, the value of R_{AA} also depends on cold nuclear matter effects, i.e. the parton distribution function of a parton a inside a nucleus A - nPDF $f_a^A(x_q, Q^2)$ - can be different from a parton distribution function in proton - PDF $f_a^p(x_q, Q^2)$. The former can be factorized as parametrization of the latter one - $f_a^A(x_q, Q^2) = R_a^A(x_q, Q^2)f_a^p(x_q, Q^2)$. An up-to-date parametrization of this effect, including the nuclear shadowing effect and the Cronin effect [27, 28] is essential for properly separating the contributions of different aspects of the collision dynamics in order to describe the experimental results.

One of the theoretical tools to understand parton energy loss in the QGP medium, is the introduction of a set of transport coefficients $\hat{q}, \hat{e}, \eta_D, \kappa_L, \kappa_T, D_s 2\pi T$ as quantitative variables relevant to the parton energy loss and in-medium interactions. These transport coefficients - among which $\hat{q} = 2\kappa_T$ is defined as the parton transverse momentum broadening, κ_L is defined as the parton longitudinal momentum variance, \hat{e} is defined as the parton energy loss, η_D is defined as the drag coefficients, $D_s 2\pi T$ is defined as the spatial diffusion coefficient - are properties of the medium, but also depend on the momentum of the parton. The estimation of those transport coefficients provides us insights into the quasi-particle nature of the QGP medium, as well as the interaction mechanisms in the QCD system. The typical estimates for those coefficients show sizable uncertainties and vary significantly among different models. How to systematically estimate these coefficients and evaluate them among different models will be the main focus of this thesis work.

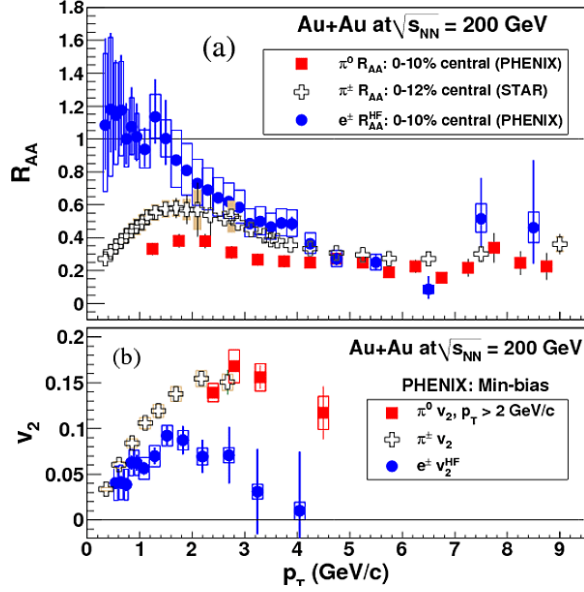


Figure 1.7: Comparison of R_{AA} and v_2 between pions and electrons from heavy flavor decays in Au-Au collisions at $\sqrt{s_{NN}} = 200$ GeV [29, 14, 30–32]. The errorbars corresponds to statistical uncertainty while the vertical boxes and bands correspond to systematic errors. **[Upper]:** at low p_T , the R_{AA} of electrons is consistent with unity, in agreement with the observed scaling of the total charm yield with the number of binary collisions. For higher p_T a strong suppression of heavy flavor decayed electrons is observed and comparable with light hadrons. Figure from [33]. **[Lower]:** Considerable anisotropic flow of heavy-flavor electrons v_2^{HF} with πv_2 in minimum-bias Au-Au collisions.

1.2.3 Open heavy flavor as hard probes

Heavy quarks – charm and bottom – like jets, are considered as one of the important hard probes of the QGP medium. Their masses ($m_c \sim 1.3 - 1.5$ GeV, $m_b \sim 4.2 - 4.5$ GeV), as implied by the name, are much larger than the typical temperature of the QGP medium and the QCD scale ($\Lambda_{\text{QCD}} = 0.2$ GeV). This has several implications:

- Heavy quarks are produced via partonic hard scatterings at the beginning of the collision. Their large masses act as a long-distance cutoff and therefore the partonic hard scattering can be calculated in the perturbative approach, even for the production of low momentum heavy quarks.
- Heavy quarks are produced during a very short times before the QGP thermalization. They propagate through the medium and experience the whole evolution of the system. During the propagation, heavy quarks interact with the medium and their spectra are modified and therefore sensitive to the interactions between heavy quarks and the medium, which provide valuable information on the QGP properties.
- Low p_T heavy quarks participate in the collective expansion of the system through the interaction with the medium. The thermalization time of heavy quarks is much longer than the light quarks by a factor of $M_Q/T \sim 5 - 15$. It is possible that heavy quarks are not fully thermalized in the medium and their spectra can be significantly modified but still retain memories of their interaction history.
- Furthermore, heavy flavor hadrons can be easily tagged due to flavor conservation. Experimentally, the D -mesons ($D^+(c\bar{d})$, $D^-(\bar{c}d)$, $D^0(c\bar{u})$, $\bar{D}^0(\bar{c}u)$, $D_s^+(c\bar{s})$, $D_s^-(\bar{c}s)$) can be reconstructed through their decay products — the hadronic decay channel to pions(π) and kaons(κ), or semi-leptonic decay channel to electrons(e) and muons(μ).

Before the measurements of heavy flavor observables, it was expected that the dominant

energy loss mechanism of heavy quarks would be gluon radiation, just like for jets. Since the gluon bremsstrahlung radiation of an accelerated heavy quark is suppressed within an angular cone of size $\theta < M_Q/E$ (dead cone effect), one would expect that the heavy quarks will lose less energy in the medium compared to light quarks and gluons. The nuclear modification factor would show a pattern of a gradually increasing with the increase of mass $R_{AA}^h < R_{AA}^c < R_{AA}^b$.

However, the experimental measurements of electrons from semi-leptonic decay of open heavy flavor hadrons have shown two striking results: 1) a small R_{AA} of e^{HF} comparable with that of light hadrons at high p_T ; 2) large v_2^{HF} at low p_T comparable with that of light hadrons, as shown in fig. 1.7. Both the strong suppression and the simultaneous participation in the collective expansion indicate that heavy flavor quarks interact strongly with the QGP medium and lose a large amount of energy.

The left panel of Fig. 1.8 compares R_{AA} and v_2 of D -meson, B -meson and charged hadron in Pb-Pb collisions at 5.02 TeV in minimum-bias events. The D -meson R_{AA} shows a maximum suppression at a p_T range of 6-10 GeV/c, and a significant smaller suppression for high p_T . Additionally, the D -meson v_2 is consistent with the charged particles v_2 . For non-central collisions, large and positive values of D -meson v_2 are observed at both RHIC and the LHC, as shown in the right panel of Fig. 1.8 where the ALICE measurements of the D -meson v_2 and pion v_2 are compared, indicating a strong collective flow. At high p_T (>10 GeV/c), the non-zero v_2 of heavy mesons is also measured. It should be noted that in this kinetic region, v_2 is no longer sensitive to collective phenomena but is most sensitive to the in-medium energy loss.

One possible explanation for the strong suppression of heavy flavor observables is the collisional energy loss mechanism, which has been pointed out to be comparable with radiative energy loss over a wide range of momenta, and is important for heavy quark interactions in the medium. The contribution from collisional energy loss mechanisms has

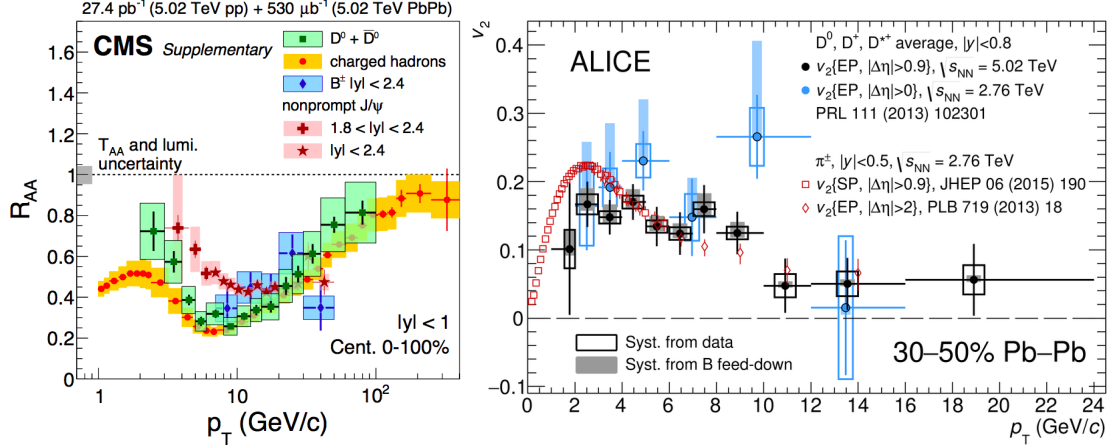


Figure 1.8: [Left]: Nuclear modification factor of charged particles, D^0 meson, non-prompt J/ψ and B^* mesons performed by CMS at Pb-Pb collisions at 5.02 TeV. Experiment data are taken from [34–36]. [Right]: Average of D^0, D^+, D^{*+} v_2 as a function of p_T at Pb-Pb collisions at $\sqrt{s_{NN}} = 5.02$ TeV (black errorbars), compared with the same measurement at $\sqrt{s_{NN}} = 2.76$ TeV (blue errorbars) and to the π^\pm v_2 measurements (red errorbars).

been included in many theoretical frameworks that describe the heavy flavor evolution in the QGP medium, and has shown its ability to describe part of the observations.

The relevant question to be addressed are:

- What is the variance of energy loss mechanisms and the kinematic range to separate between collisional and radiative energy loss mechanisms?
- What are the heavy quark transport coefficients, and how to interpret those coefficients?
- What are the properties of the QGP medium, and how would the interaction between heavy quarks and the medium reflect the nature of this QCD system?

To answer those questions, a variety of theoretical models are developed, and through a comparison of the theoretical calculation with the experimental measurements, one could in principle, differentiate the different interaction mechanisms, constrain the transport coefficients and understand the underlying nature of the QGP system.

1.2.4 Outline of the dissertation

The thesis is organized as follows:

In chapter 2 I will briefly introduce the “standard model” of heavy-ion collisions, which is a phenomenological model of the QGP medium based on a relativistic viscous hydrodynamical framework. The standard model incorporates with a heavy quark evolution model, which together describe a consistent full space-time evolution of the heavy quarks inside a heavy-ion collision from the initial production to the final measurements.

In chapter 3 I will focus on heavy quark in-medium propagation, where the partonic scattering cross section of heavy quarks with light partons are calculated, and the transport coefficients of heavy quarks are evaluated via a leading-order perturbative QCD approach. Then I will implement a linearized Boltzmann approach, reduce it to a Langevin dynamics and improve the Langevin dynamics with an additional contribution for radiative processes. The results of heavy meson observables are calculated using the default set-up, without further tuning of the parameters and calibration to experimental measurements.

Chapter 4 will be devoted to introducing a Bayesian model-to-data analysis framework. The Bayesian framework is a state-of-the-art statistical analysis which is applied in our analysis to calibrate the heavy quark transport model to experimental measurements of D -meson observables. The advantages of such a framework are that it provides us with an opportunity to conduct a systematic and rigorous evaluation of the theoretical model, which optimizes the model to its best performance and takes into consideration of the theoretical and experimental uncertainties.

In chapter 5 I will apply the Bayesian analysis framework to the heavy quark transport model in heavy-ion collisions, and present the results of such an analysis: an optimized transport model that is able to describe the heavy flavor experimental observables; a systematic estimation of the charm quark transport coefficients. Such application demon-

strates that such Bayesian optimization and parameter estimation can succeed in heavy-ion physics, even for rare probes.

In chapter 6 I will compare the heavy flavor transport coefficients estimated by different theoretical models. It shows that the part of the current theoretical uncertainties regarding the heavy flavor transport coefficients come from the details of framework implementation. In order to make a precise estimation of the heavy flavor transport coefficients and to understand the properties of the QGP system, one should look towards a universal framework that could eliminate the implementation difference.

Finally, a summary of the thesis will be given at Chapter 7.

Chapter 2

Standard model of Heavy-ion Collisions

Over the past two decades, significant progress has been made regarding the study of hot and dense nuclear matter – the Quark-Gluon Plasma (QGP) – that is created in ultra-relativistic heavy-ion collisions. It is now widely accepted that the QGP is a strongly-correlated fluid, rather than a weakly-coupled gas. Extensive and precise experimental measurements coupled with theoretical developments have revealed a multi-stage dynamical picture of heavy-ion collisions events, as visualized in Fig. 2.1.

This picture has been called “standard model of heavy-ion collisions”. It contains the key elements of the underlying physics for heavy-ion collisions at different stages. In subsequent chapters, I will incorporate the evolution of open heavy flavors into this framework in order to describe the evolution of heavy quarks in heavy-ion collisions, and estimate properties of the QGP medium – mainly the heavy quark transport properties.

The “standard model of heavy-ion collisions” can be separated into sequential stages:

- **Initial conditions:** the initial conditions describe the energy/entropy density distribution of the system right after the collision. It fluctuates event-by-event, and such fluctuations contribute to the final state anisotropy. Different models have been developed in order to generate the initial condition for heavy-ion collisions: the geometric initial condition Glauber model [37, 20], a color glass condensate (CGC) inspired Monte Carlo KLN model [38, 39], and classical Yang-Mills dynamics of gluon fields combined with CGC-based saturation scale model IP-Glasma [40, 41]. In this work, we use T_{RENTO} [42], a parameteric initial condition generator which maps the nuclear overlap density into an initial entropy density distribution.

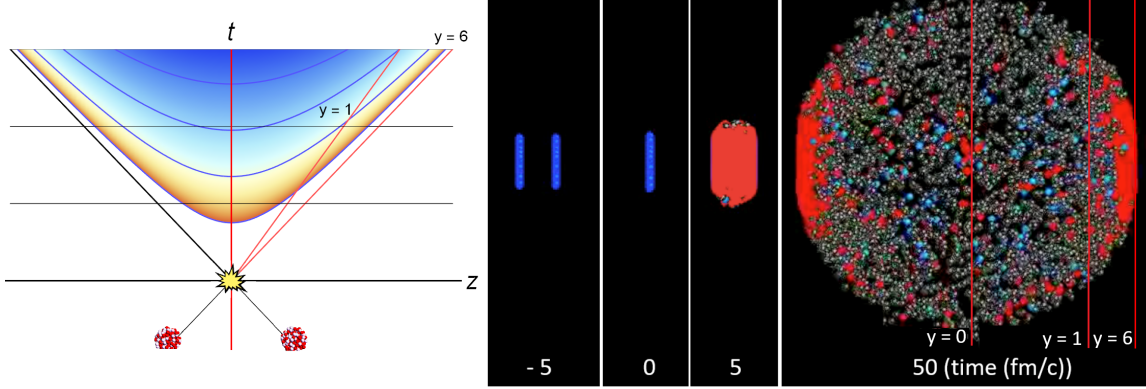


Figure 2.1: **Left:** space-time picture of a heavy-ion collision event, where the color indicates the temperature of the system. **Right:** snapshots of a central Pb-Pb collision at $\sqrt{s_{NN}} = 2.76$ TeV at different timesteps.

- QGP phase evolution – relativistic viscous hydrodynamics: one of the key components of the “standard model of heavy-ion collision” is that the evolution of the QGP medium can be simulated by an effective field theory model – relativistic viscous hydrodynamics model. In this work we use an event-by-event (2+1)-dimensional viscous hydrodynamical model – VISHNU [43, 44] – to describe the evolution of the QGP medium in this stage.
- Particlization and hadronization: the hydrodynamical model describes the long-wavelength evolution where the system is dense and strongly coupled. As the QGP medium expands and cools down, the macroscopic description breaks down and we should (smoothly) switch to a microscopic model that is based on kinetic theory and better suited to describe the system. Such a change of the system’s degrees of freedom is referred to as “particlization”. Furthermore, the switching of the description is related to (but not equal to) a more fundamental physical phase transition process – “hadronization”, during which the deconfined quarks and gluons hadronize into confined hadrons. One would expect that the switching temperature T_{switch} should be close to the critical temperature T_c of the QCD Equation of State. In this work,

we are using particle samplers `iSS` and `frzout` to sample hadron species from the momentum distribution of the soft medium.

- Hadronic stage: after the system hadronizes into a hadron resonance gas, the hadrons keep interaction with each other (scattering and decaying) until reaching the kinetic freeze-out. The particles then fly into detectors and experimental measurements are made. The dynamics of the hadronic system from the switching temperature T_{switch} to kinetic freeze-out can be described by a microscopic transport model based on a Boltzmann equation - UrQMD [45, 46].

The framework listed above provides a reliable description of the QGP medium evolution in heavy-ion collisions, from which we can calculate observables of the soft sector which are comparable to experimental measurements such as charged particle/identified particle spectra, multiplicity, mean transverse momentum, mean energy, momentum anisotropy etc., and estimate the intrinsic properties of the system, such as the shear and bulk viscosity, as well as the correlation between initial fluctuation and system anisotropy.

To gain more insight into the system, especially the behavior of particles at high momentum region (where the perturbation QCD is applicable), one has to look at other probes – hard probes, including but not limited to heavy quarks, jets, photons etc. This thesis work focuses on the evolution of heavy quarks in heavy-ion collisions. In order to integrate heavy quark dynamics into the “standard model of heavy-ion collisions”, we exploit a transport framework, where the dynamics of heavy quarks are described by transport equations – either a Boltzmann equation or a Langevin equation. The interaction between heavy quarks and the medium is described correspondingly as scattering between partons (Boltzmann) or random kicks from the medium constituents (Langevin). In addition to the in-medium dynamics, one has to generate an initial condition for heavy quarks that is consistent with the soft medium, adapt the hadronization process as well as the later stage interactions among

hadrons.

- Initial conditions: the initial conditions for heavy quarks contain two parts: 1) An initial momentum distribution of heavy quarks that are produced via hard scattering. It is calculated using a pQCD calculation of the fixed-order plus next-to-leading log formula (FONLL) [47, 48]. In addition, we adopt to EPS09 next-to-leading-order parametrization to describe the nuclear PDF [28, 49]. 2) The other part of the initial condition is the initial position distribution for heavy quarks. It is generated consistently with the initial energy/entropy density distribution for the event-by-event hydrodynamical evolution by the parametric initial condition model T_{RENTO}. The heavy quark production vertices are based on the binary collision distribution as determined by the thickness function \hat{T}_{AB} .
- In-medium evolution: After their production, the heavy quarks propagate through the QGP medium. During their propagation through the QGP medium, they interact with the medium and lose energy. In a quasi-particle picture of the QGP medium, the space-time evolution of the heavy quarks can be described by the Boltzmann transport equation. With a small momentum transfer assumption, it can also be described by the Langevin equation.
- Hadronization – a hybrid model of fragmentation and recombination: When the temperature of the QGP medium drops below the critical temperature $T_c = 154$ MeV, the medium undergoes a transition from a deconfined QGP to a confined hadron gas. Meanwhile, the heavy quarks hadronize into heavy flavor hadrons (meson and baryon). The hadronization of heavy quarks is described by a hybrid model of fragmentation and recombination, where the former one is simulated by PYTHIA[50] and the latter is described by the Wigner function with the harmonic oscillators overlapping.

- Hadronic stage: hadronic interactions are simulated in the same UrQMD framework as all other hadron-hadron interactions. Elastic scattering between D -meson and π, ρ, K are considered. The rescattering and decay of heavy mesons in this stage has been found to further contribute to the suppression of its p_T spectra and momentum anisotropy.

The full space-time evolution model for heavy quarks in heavy-ion collisions is sketched in Fig. 2.2, where the workflow of the computational modeling maps to the evolution of the system at each stage. I should mention that there are other frameworks to model the evolution of the QGP medium instead of an effective hydrodynamical model. For instance, a kinetic-based partonic transport model – BAMPS (Boltzmann Approach for Multi-parton scattering)[51, 52], with the medium consisting of partons and the interactions within medium being described by collisional and radiative scatterings; or a quasi-particle transport model – PHSD[53, 54] (parton hadron string dynamics), which describes the QGP evolution as an interplay between partons, strings and hadrons. Those model explore different assumption of the QGP medium and are able to describe a variety of observables, as well as estimate the properties of the system. We do not intend to compare the alternatives here but utilize the hydrodynamical-based framework, which is the most natural choice for the integration with the heavy quark evolution framework.

The heavy quark in-medium transport model will be explained in great detail in the next chapter 3. For this chapter, we will briefly introduce the medium evolution framework as a background for heavy quark evolution, as well as other components regarding the heavy quark production, hadronization and hadronic stage scattering in the framework.

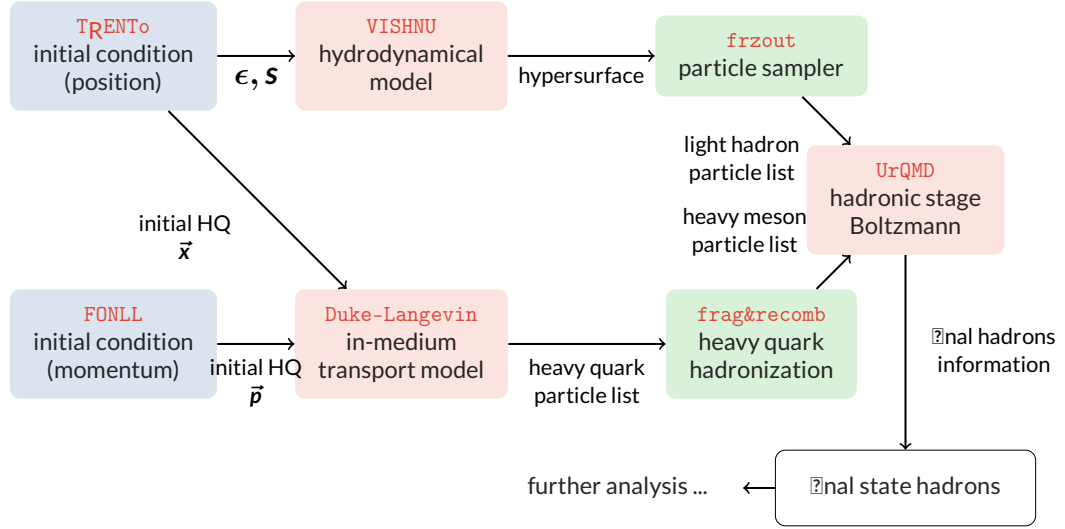


Figure 2.2: A summary of the modularized description of heavy quark space-time evolution in heavy-ion collisions.

2.1 Initial condition

In heavy-ion collisions, initial partons production occurs via the initial soft and hard processes. Hard processes, which involve large momentum transfer, can be calculated by perturbative QCD. Unfortunately, soft processes involving non-perturbative physics are rather difficult to calculate. If one only requires an initial input for the hydrodynamical models, it is reasonable to choose a top-down phenomenological model, which generates the initial condition and later can be compared with experimental data rather than studying the underlying physics of parton production or the initial entropy deposition mechanism.

2.1.1 Trento – reduced thickness event-by-event nuclear topology

In our framework, I use T_{RENTO} , a parametric initial condition model developed at Duke, to generate a realistic initial entropy/energy profile from proton-proton, proton-nucleus, nucleus-nucleus collisions. T_{RENTO} does not assume a particular physical mechanism for the energy deposition in heavy-ion collisions, but constructs a static initial profile in the transverse plane by mapping the nuclear density overlap function to the initial density via an effective function at a proper time τ :

$$\left. \frac{ds}{dy} \right|_{\tau} = f(T_A(x, y), T_B(x, y)), \quad (2.1)$$

where ds/dy is the entropy density s with respect to the rapidity y at mid-rapidity (a boost-invariance simplification). $T_A(x, y)$ is the nuclear thickness function as an integration of participant nuclear matter density ρ_A^{part} along with the beam direction z :

$$T_{A/B}(x, y) \propto \int dz \rho_{A/B}^{\text{part}}(x, y, z). \quad (2.2)$$

The effective function f , does not arise from first principle calculation, but is proposed in the form of a general mean with the dimensionless free parameter p :

$$f(T_A, T_B) \equiv \left(\frac{T_A^p + T_B^p}{2} \right)^{1/p}. \quad (2.3)$$

By varying p , one can change the mapping of the entropy/energy density distribution from the initial nuclear thickness function, as shown in Fig. 2.3. With $p = 1$ the general mean $f = (T_A + T_B)/2$ is equivalent to a Monte Carlo wounded nucleon model that deposits the entropy blob for each nucleon, while with $p = 0$, the model deposit a single blob at the midpoint of the collision. The value of p is constraint by a data-driven comparison over

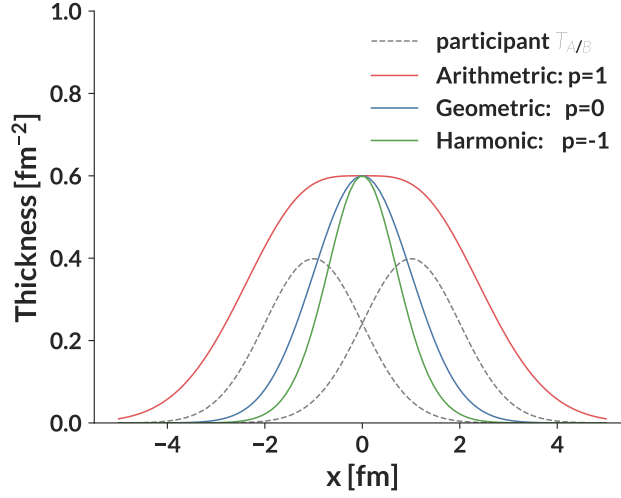


Figure 2.3: Cross section of the reduced thickness function for a pair of nucleon participant. The black dashed lines are one-dimensional participant nucleon thickness function T_A, T_B , where colored line are the general mean f taking the value of $p = -1, 0, 1$.

experimental measurements of soft observables. It was found that taking $p = 0$, when the effective function reduce to a geometric mean of the two nucleus thickness function $f \propto \sqrt{T_A T_B}$, the model is optimized to describe the soft observables in p-Pb, Pb-Pb collisions at different collision energies [44, 55].

2.1.2 From proton-proton to nucleus-nucleus collision

Starting with a proton-proton collision, the collision probability between two protons i, j with impact parameter b along with z direction follows:

$$P_{\text{coll}}^{\text{coll}}(b) = 1 - \exp \left[-\sigma_{gg} \int dx dy \int dz \rho_i(x + b/2, y, z) \int dz \rho_j(x - b/2, y, z) \right], \quad (2.4)$$

where σ_{gg} is an effective parton-parton cross section, which is tuned so that the nucleon-nucleon cross section is same as the total inelastic cross section measured by experiments:

$$\sigma_{\text{NN}}^{\text{inel}} = \int 2\pi b db P_{\text{coll}}(b). \quad (2.5)$$

$dz\rho_{i/j}(x, y, z)$ corresponds to the nuclear density integrated along the beam direction z , and is chosen to be a Gaussian distribution with an effective nucleon width ω .

$$T_{i/j}(x, y) = \int dz\rho(x, y, z) = \frac{1}{2\pi\omega^2} \exp\left(-\frac{x^2 + y^2}{2\omega^2}\right). \quad (2.6)$$

Therefore the thickness function for a nucleus A can be read as the sum of all participant nucleons i :

$$T_{A/B} = \sum_{i=0}^{N_{\text{part}}} \gamma_i \frac{1}{2\pi\omega^2} \exp\left(-\frac{x^2 + y^2}{2\omega^2}\right), \quad (2.7)$$

The ‘‘participants’’ indicates that the nucleons collide at least once. The proton-nucleus(p-A) and nucleus-nucleus(A-B) collision can be read as the superposition of nucleon-nucleon(p-p) collisions.

With the definition of the ‘‘thickness function’’, Eqn. 3.23, which asserts the probability of two nucleon i, j (inside nucleus A, B) colliding inelastically equals:

$$P_{ij}^{\text{coll}}(b) = \frac{\sigma_{\text{NN}}^{\text{inel}}}{AB} \int d^2x T_A(\mathbf{x}_{\perp}) T_B(\mathbf{x}_{\perp} - b) = \frac{\sigma_{\text{NN}}^{\text{inel}} T_{AB}(b)}{AB}, \quad (2.8)$$

where $T_{AB}(b) = \int d^2x T_A(\mathbf{x}_{\perp}) T_B(\mathbf{x}_{\perp} - b)$ is known as the nuclear thickness function.

The initial transverse entropy/energy density is then calculated by the effective function which takes the inputs of nucleon thickness function:

$$\frac{ds}{dy}\Big|_{\tau} = \text{norm} \times f(T_A(x, y), T_B(x, y)) \propto T_{AB} \propto \left(\frac{T_A^{\text{p}} + T_B^{\text{p}}}{2}\right)^{1/p}. \quad (2.9)$$

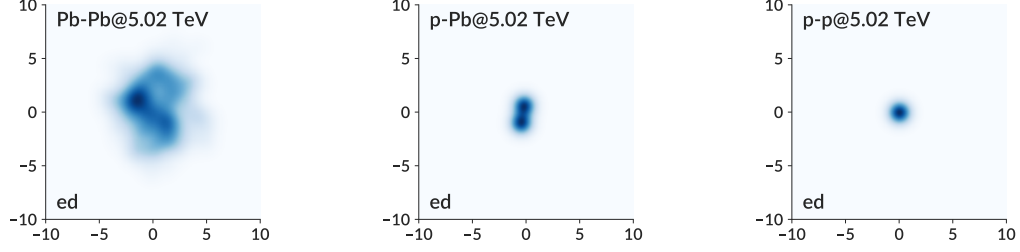


Figure 2.4: Examples of initial energy density generated by `Trento` for a single collision in: Pb-Pb, p-Pb, p-p at $\sqrt{s_{NN}} = 5.02$ TeV. The energy density profile is projected in the transverse plane.

In Fig. 2.4 I present the initial energy density in the transverse plane that are generated by `TRENTO` for three different collision systems at the same collision energy (per nucleon): Pb-Pb, p-Pb, pp at $\sqrt{s_{NN}} = 5.02$ TeV. One can clearly see the initial geometric anisotropy in a non-central Pb-Pb collision. However, for the initial anisotropy in p-Pb and even p-p collisions, one has to include more details in the initial condition model, such as sub-nucleon structure. An updated version of `TRENTO` has incorporated such features, see [55] for more details.

2.1.3 Heavy quark initial condition

Due to their large masses, the heavy quarks are produced prominently at the early stage of heavy-ion collisions via hard scatterings. In this work, the initial position distribution of heavy quarks is generated consistently with the initial energy density for the event-by-event hydrodynamical evolution.

Initial condition in position space

In previous section, we calculated the probability of nucleon-nucleon collisions within a nucleus-nucleus collision:

$$P_{ij}^{\text{coll}}(b) = \frac{\sigma_{NN}^{\text{inel}} T_{AB}(b)}{AB}, \quad (2.10)$$

The probability of observing n such pairwise collisions can be described by a binomial distribution:

$$P(n, b) = \binom{AB}{b} \left[\frac{\sigma_{\text{NN}}^{\text{inel}T_{AB}(b)}}{AB} \right]^n \left[1 - \frac{\sigma_{\text{NN}}^{\text{inel}T_{AB}(b)}}{AB} \right]^{AB-n}. \quad (2.11)$$

The average number of collisions is then given by:

$$\langle N_{\text{coll}}(b) \rangle = \sum_{n=1}^{AB} n P(n, b) = \sigma_{\text{NN}}^{\text{inel}T_{AB}(b)}. \quad (2.12)$$

This is called the binary collision number. The number of heavy quarks produced in the initial hard scattering of each nucleus nucleus collision then can be evaluated as:

$$N_Q = N_{\text{coll}} \frac{\sigma^{NN \rightarrow Q}}{\sigma_{\text{NN}}^{\text{inel}}}. \quad (2.13)$$

In this work, the nuclear thickness function related to the binary collisions is generated by the `TRENTO` model. Heavy quarks are then oversampled (in order to achieve statistical significance in the calculation of observables), but each event is reweighted with the binary collision number. Figure. 2.5 present three random initial conditions for heavy quark production in Pb-Pb collisions at 5.02 TeV but with different impact parameters. The black dots are the sampled¹ heavy quark initial position while the colormap corresponds to the initial energy density profile.

Initial condition in momentum space

The initial momentum distribution of heavy quarks, on the other hand, can be calculated using the perturbative QCD. The leading order process to produce the heavy quark-anti-

¹In the actual running of the model, heavy quarks are oversampled and then re-weighted in order to achieve the statistical significance.

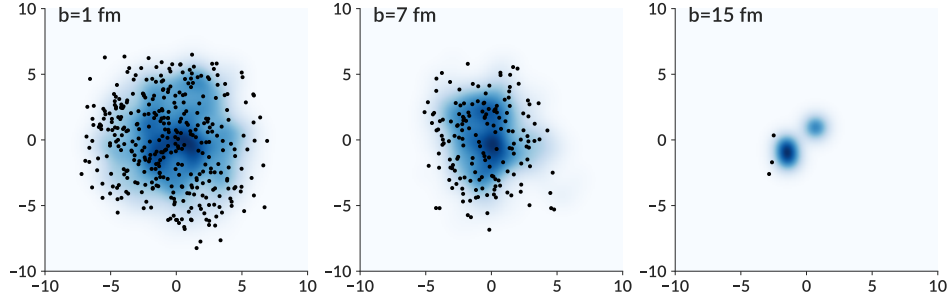


Figure 2.5: Examples of initial energy density and heavy quark position generated by `trento`. Corresponding to three different impact parameters b in Pb-Pb collisions at 5.02 TeV.

quark pairs are the gluon fusion and quark-anti-quark annihilation. The related matrix elements for those processes are:

$$\sum |\mathcal{M}_{q\bar{q} \rightarrow Q\bar{Q}}|^2 = \frac{64}{9} \pi^2 \alpha_s^2 (M_T) \frac{(M^2 - t)^2 + (M^2 - u)^2 + sM^2 s}{s^2}, \quad (2.14)$$

$$\begin{aligned} \sum |\mathcal{M}_{gg \rightarrow Q\bar{Q}}|^2 = & \pi^2 \alpha_s^2 (M_T) \left[\frac{12}{s^2} (M^2 - t)(M^2 - u) \right. \\ & + \frac{8}{3} \frac{(M^2 - t)(M^2 - u) - 2M^2(M^2 + t)}{(M^2 - t)^2} \\ & + \frac{8}{3} \frac{(M^2 - t)(M^2 - u) - 2M^2(M^2 + u)}{(M^2 - u)^2} \\ & - \frac{2}{3} \frac{M^2(s - 4M^2)}{(M^2 - t)(M^2 - u)} \\ & - 6 \frac{(M^2 - t)(M^2 - u) + M^2(u - t)}{s(M^2 - t)} \\ & \left. - 6 \frac{(M^2 - t)(M^2 - u) + M^2(t - u)}{s(M^2 - u)} \right] \end{aligned} \quad (2.15)$$

where α_s is the strong coupling constant, M is the mass of heavy quarks, $M_T = \sqrt{M^2 + p_T^2}$ is the transverse mass and s, u, t are the Mandelstam variables whose defi-

inition can refer to Appendix A.0.2. In this work, we adopt the fixed-order plus next-to-leading log formula (FONLL) to calculate the heavy quark initial momentum distribution, which conveniently allows one to switch between different parton distribution function parametrization. We employ the CTEC6 parametrization for the PDF.

While the CTEC6 PDF parametrizes the parton distribution function inside a nucleon $f_{a/A}(Q^2)$, one has to modify those nucleon PDFs when applied in the parton distribution function inside a nucleus. Such modification is often referred to as the “nuclear shadowing effect” or “cold nuclear matter effect”. We use the EPS09 NLO parametrization for the nuclear shadowing effect in this work. Figure. 2.6 displays the initial heavy quark transverse momentum distribution in both proton-proton(without shadowing) and nucleus-nucleus (including shadowing, and rescaled by the binary collision number) for Au-Au collisions at 200 GeV and Pb-Pb collisions at 2.76 and 5.02 TeV. The ratio between those two – R_{AA}^{IS} ² – is the nuclear modification due to the cold nuclear matter effect. One can see that the influence of cold nuclear matter effect, which reduced the production rate of charm quarks in low p_T , and such suppression is more profound at the LHC than RHIC. On the contrary, for the production of bottom quarks at low p_T , the shadowing effect reduces the yields at the LHC energies but slightly enhances at RHIC.

2.2 Realistic viscous hydrodynamics

The realistic viscous hydrodynamics is one of the most successful models to simulate the evolution of the strongly-coupled QGP medium in heavy-ion collisions, and is also one of the key components of the “standard model of heavy-ion collisions”. It is a macroscopic

²Here I use a subscript as IS to show that this is the ratio of the heavy flavor momentum spectra between a nucleus-nucleus collision and a normalized proton-proton collision. The deviation from unity is due to the initial state effects.

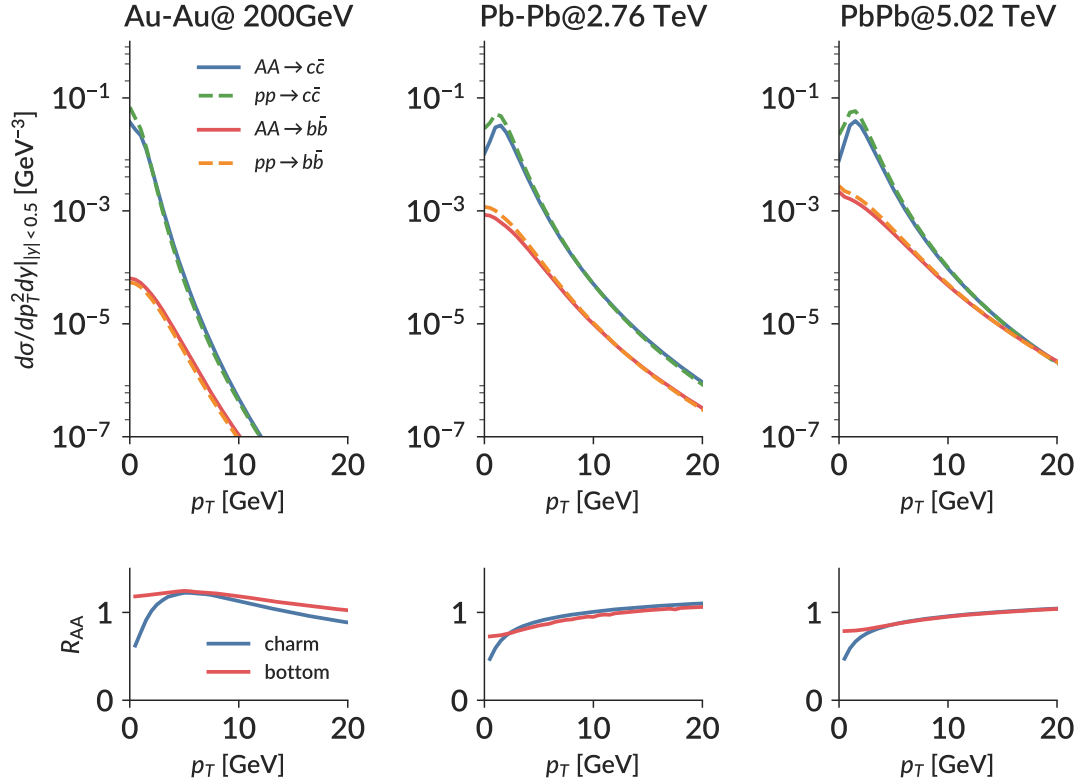


Figure 2.6: [Upper]: Initial p_T spectra for charm/bottom production in AA and pp collisions. The momentum distribution is calculated with FONLL and include nuclear PDF and EPS09 parametrization for shadowing effect. [Lower]: R_{AA} resulting from the cold nuclear matter effect.

model based on the conservation of energy, momentum, and charge current:

$$\partial_\mu T^{\mu\nu} = 0, \partial_\mu N^\mu = 0, \quad (2.16)$$

where $T^{\mu\nu} = (e + p)u^\mu u^\nu - pg^{\mu\nu} + \pi^{\mu\nu} - (g^{\mu\nu} - u^\mu u^\nu)\Pi$ is the energy momentum tensor, $N^\mu = nu^\mu + V^\mu$ is the net baryon charge current in the Landau frame, e and p are the energy density and pressure in the local fluid rest frame, u^ν is the local fluid velocity, and V^μ is the baryon flow. The higher order term $\pi^{\mu\nu}$ and Π are the first order shear and bulk viscous corrections. In relativistic Navier-Stokes theory, the viscous terms can be further decomposed as[]

$$\pi^{\mu\nu} = 2\eta\Delta^{\mu\nu\alpha\beta}\partial_\alpha u_\beta, \Pi = -\zeta\partial_\mu u^\mu, \quad (2.17)$$

where

$$\Delta^{\mu\nu\alpha\beta} = \frac{1}{2}(\Delta^{\mu\alpha}\Delta^{\nu\beta} + \Delta_{\nu\alpha}\Delta_{\mu\beta}) - \frac{1}{3}\Delta^{\mu\nu}\Delta^{\alpha\beta}, \Delta^{\mu\nu} = g^{\mu\nu} - u^\mu u^\nu \quad (2.18)$$

is the projection operator orthogonal to u^μ . η, ζ are the shear and bulk viscosities which describes the fluid dissipative corrections at the leading order. They are the key properties of the QGP medium and determining their values with high precision is one of the primary goals for heavy-ion physics.

To model the dynamics of the QGP fluid, one solves the above 5 equation for 6 unknown variables (energy density e , pressure p , net baryon density n , and three independent components in the fluid four-velocity u^μ). With an additional relation, the Equation of State (EoS) $p = p(n, e)$, the equations are closed and can be solved numerically given proper initial conditions. We use a modern QCD EoS based on continuum extrapolated lattice calculations at zero baryon density calculated by the HotQCD collaboration [7] and blended into a hadron resonance gas EoS in the interval temperature $110 \leq T \leq 130$ MeV

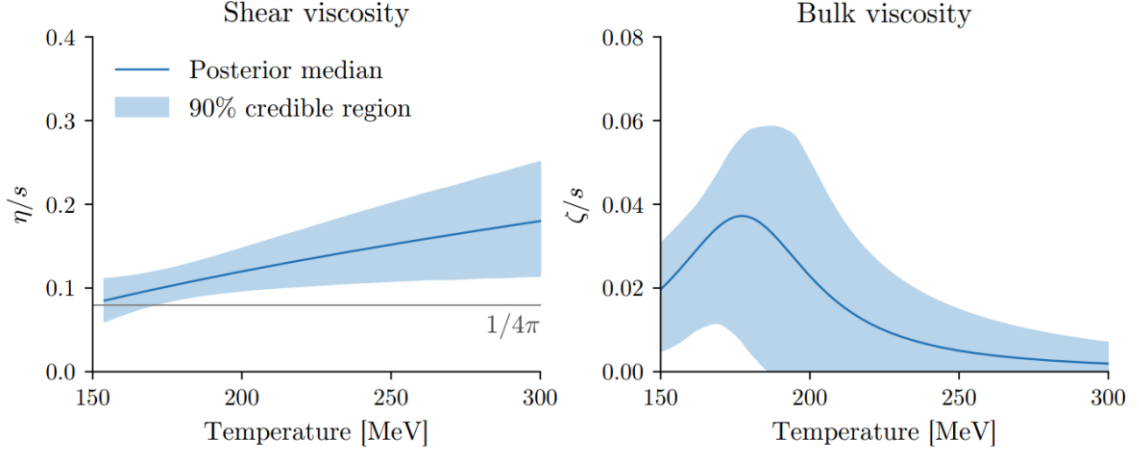


Figure 2.7: Temperature dependence of the specific shear and bulk viscosity $\eta/s(T) = a + b \cdot (T - T_c) \cdot (T/T_c)^\gamma$ [left] and $\zeta/s(T) = c / (1 + (T-w)^2)$ [right]. Lines are the posterior median value results from the Bayesian model-to-data analysis; colored area are the 90% credible region. The horizontal line in the shear viscosity plot indicates the conjectured lower bound $1/(4\pi)$. Figure from [57].

using a smooth step interpolation function [56].

For our framework, we use VISHNU (2+1) [43], which is an extensively tested implementation of the boost variant (2+1)-dimensional viscous hydrodynamics that has been updated to handle fluctuating event-by-event initial conditions [58]. It also includes both the shear and bulk viscosity corrections through the second-order Israel-Stewart equation in the 14-momentum approximation [59]. Refer Appendix A.0.3 for more details. The values of the shear and bulk viscosities are ad hoc parameters of hydrodynamics and they have been determined through a state-of-the-art model-to-data Bayesian comparison [44]. In Fig. 2.7 we plot the ratio of shear and bulk viscosities to entropy that is estimated by such a Bayesian analysis. For our calculation, the maximum likelihood value from Tab.III of Ref.[44]³ and Tab.5.9 of Ref. [57]⁴ are used.

In order to start the hydrodynamical evolution, an initial condition is required. The

³In the scenario of without pre-equilibrium dynamics.

⁴In the scenario of pre-equilibrium dynamics is modeled as free-streaming process.

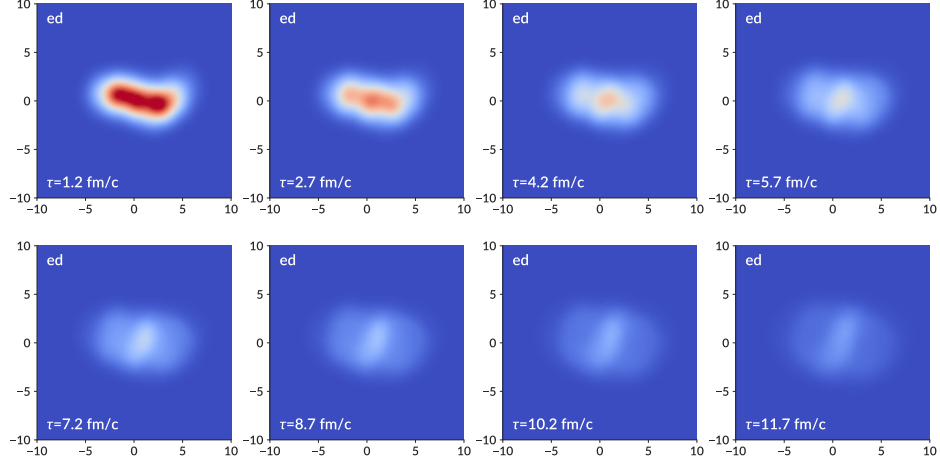


Figure 2.8: The energy density profile for one hydrodynamical evolution of a Pb-Pb collision at 5.02 TeV with impact parameter $b = 13$ fm.

initial condition model provides the state of the heavy-ion collisions at the hydrodynamical thermalization time τ_0 , approximately $\tau_0 < 1$ fm/c. The pre-equilibrium stage is the least understood phase of the heavy-ion collisions. As mentioned before, although one can explicitly augment pre-equilibrium dynamics into the hydrodynamical model, starting from the collision time 0^+ and conduct a full initial state calculation, one can also initialize the medium at τ_0 . In our studies, I explore both scenarios, and compare the effect of pre-equilibrium stage evolution to our estimation of the heavy quark transport coefficients. Figure 2.8 visualizes the evolution of the medium energy density (multiplied by τ) in a Pb-Pb collision at 5.02 TeV (with impact parameter $b = 13$ fm), starting from $\tau_0 = 0.6$ fm/c. The matter distribution features hot spots in the transverse plane, reflecting the fluctuating initial energy density. As the time increase, the bumps in the energy density spread and gradually dissolve as the medium expands.

2.3 Particlization and hadronization

The hydrodynamical model used in heavy-ion collisions is based on two assumptions: local equilibrium and long-range interaction. Once the system expands and cools down, the long-range interaction assumption breaks down, and the hydrodynamical model would fail to describe the dynamics of the system. In principle, there is a temperature window near the cross-over region, where both macroscopic and microscopic models are applicable, while at a lower-temperature region, a microscopic approach is superior. Hence, it is reasonable to switch from a macroscopic model that describes a continuous fluid to a microscopic model that is consistent with discrete particles. This switch in the modeling, referred to as particlization, is a modeling artifact and should be distinct from physical process such as hadronization, as the latter one refers to the phase transition process when the degrees of freedom of the system change from quarks and gluons to hadrons. Nevertheless, the switching temperature T_{switch} is very close to the QCD critical temperature T_c .

2.3.1 Particlization

The particlization is performed on a space-time hypersurface with a constant temperature T_{switch} . A common approach is applying the Cooper-Frye formula on the particlization hypersurface Σ :

$$E \frac{dN_i}{d^3p}(x^\mu, p^\mu) = \frac{g_i}{(2\pi)^3} \int_{\Sigma} f_i(x^\mu, p) p^\mu d^3\sigma_\mu, \quad (2.19)$$

in which g_i is the spin degeneracy of species i , $d\sigma_\mu = (\cosh \eta_s, -\frac{\partial\tau}{\partial x}, \frac{\partial\tau}{\partial y}, -\sinh \eta_s) \tau dx dy d\eta_s$ is the infinitesimal surface element on the hypersurface with longitudinal boost-invariance. $f_i(x^\mu, p)$, which represents the phase space distribution of the species i , consists of two parts: a local thermal equilibrium distribution part $f_0(x^\mu, p)$ (Bose-Einstein distribution for bosons, and Fermi-Dirac distribution for fermions), and the deviation from local thermal distribution due to viscous effects $\delta f(x^\mu, p^\mu) = \delta f_{\text{shear}} + \delta f_{\text{bulk}}$.

In this thesis work, we use `frzout` sampler⁵ which takes a simple form for the viscous correction of the particle distribution as an expansion over the thermal distribution :

$$\delta f(x^\mu, p^\mu) = f_0(1 \pm f_0) \frac{\tau}{ET} \left[\frac{1}{2\eta} p^i p^j \pi_{ij} + \frac{1}{\xi} \left(\frac{p^2}{3} - c_s^2 E^2 \right) \Pi \right], \quad (2.20)$$

where π_{ij} is the shear tensor, τ is the shear and bulk relaxation time. It has several advantages compared with our previous implementation (using the `iSS` sampler):

- For formed hadrons, the resonance widths are included rather than assigning a constant pole mass to every resonance;
- The bulk viscosity correction component f_{bulk} is taken into consideration, which has an effect on the final state particle multiplicity.

2.3.2 Hadronization

On the one hand, the particlization describes the artificial conversion process when a description of a hadronic system changes from a macroscopic model whose constituents are fluid cells, to a microscopic model whose constituents are hadrons. On the other hand, hadronization is a physical process, which describes a phase transition from the QGP phase to a hadronic resonance gas (HRG) phase. For the soft medium described by a hydrodynamical model, although the hadronization isn't described explicitly, it occurs as the system's Equation of State changes from the QGP EoS to HRG EoS around the critical temperature $T_c = 154 \text{ MeV}$, (as shown in Fig. 1.2), which happens prior to particlization at $T_{\text{switch}} = 144 \text{ MeV}$.

For the partons at higher transverse momentum (larger than a few GeV/c), the modeling of their hadronization process is more complicated. In proton-proton collisions where

⁵The computational particlization model is available at <https://github.com/Duke-QCD/frzout>

no QGP medium is created, hadrons are created by the fragmentation of the energetic partons. This parton-hadron transition process is non-perturbative but assumed to be universal. Therefore we can rely on experimental measurements, such as $e^+e^- \rightarrow hX$ to parametrize a fragmentation function for different hadronization processes. If this were still the case in heavy-ion collisions, the probability for an energetic parton to fragment into mesons should be much larger than to fragment into baryons, as a larger mass and a non-zero baryon number are required to form the baryon. However, in Au-Au collisions at 200 GeV at RHIC, it is found that baryons and mesons are created in nearly equal proportions — the so-called “baryon puzzle”. In addition, in the same p_T region, the elliptic anisotropy v_2 of the baryons is nearly 50% larger than that of the mesons. Those observations support the recombination model, i.e., in an environment of high density of partons, two/three partons recombine with each other to form a hadron.

Therefore the hadronization of the heavy quarks in this work is described by a hybrid model of fragmentation and recombination at the critical temperature $T_c = 154$ MeV. Lower p_T heavy quarks tend to recombine with light partons to form a hadron, while the higher p_T heavy quarks fragment into hadronic bound states.

Heavy quark fragmentation

In the fragmentation picture, a single parton i 's spectrum is convoluted into a hadron h which carries a fraction $z = p_h/p_i < 1$ of the parton momentum with the probability $D_i^h(z, \mu^2)$. This is the parton fragmentation function whose actual form is parametrized and later tuned globally by calibrating on the experimental data in e^+e^- collisions.

Heavy flavor hadrons retain a large fraction of the heavy quark momentum, therefore the fragmentation function is much harder than that of a light hadrons, i.e., peaks at a larger value of z . Some of the popular parametrization of the heavy flavor fragmentation functions are [2]:

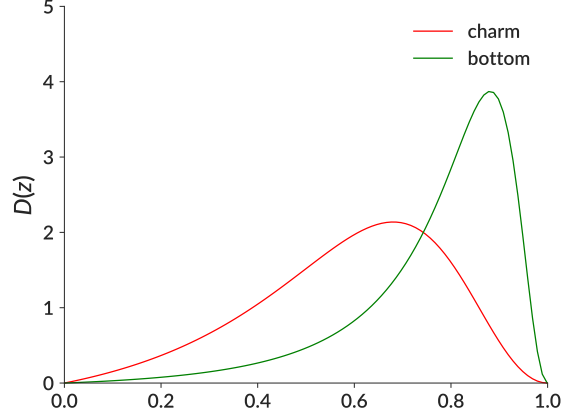


Figure 2.9: The fragmentation functions (Peterson parametrization) for charm/bottom fragment into D/B -mesons.

- Lund symmetric (default in PYTHIA): $D_{np}(z) \propto \frac{1}{z} z^{a\alpha} \left(\frac{1-z}{z}\right)^{a\beta} \exp\left(-\frac{bm_{\perp}^2}{z}\right)$
- Peterson: $D_{np}(z) \propto \frac{1}{z} \left(1 - \frac{1}{z} - \frac{\epsilon}{1-z}\right)^{-2}$
- Kartvelishvili: $D_{np}(z) \propto z^{\alpha}(1-z)$
- Bowler: $D_{np}(z) \propto z^{-(1+bm_{h,\perp}^2)}(1-z)^a \exp\left(-\frac{bm_{h,\perp}^2}{z}\right)$
- Collins&Spiller: $D_{np}(z) \propto \left(\frac{1-z}{z} + \frac{(2-z)\epsilon}{1-z}\right) \times (1+z^2) \left(1 - \frac{1}{z} - \frac{\epsilon}{1-z}\right)^{-2}$
- Bowler: $D_{np}(z) \propto z^{-(1+bm_{h,\perp}^2)}(1-z)^a \exp\left(-\frac{bm_{h,\perp}^2}{z}\right)$.

In this framework, we use PYTHIA6 to implement the fragmentation of the heavy quarks into heavy flavor hadrons. The Peterson parametrization [60] is chosen, whose dependence on the fraction z is shown in Fig 2.9 for both charm and bottom quarks, with the nominal values of the fragmentation parameter $\epsilon = 0.06$ for charm quarks and $\epsilon = 0.006$ for bottom quarks.

Recombination

In the recombination picture, a quark-antiquark pair or three quarks populated from a dense medium can form a meson or baryon correspondingly. The probability of recombination is determined by the overlapping between the initial and final state wavefunctions.

In the case of two quarks (one heavy quark and one light quark forming a meson M), the recombination probability is the integration over the Wigner function $f_M^W(\vec{Q}, \vec{k})$:

$$\begin{aligned}
| \langle M | \vec{p}_1, \vec{x}_1; \vec{p}_2, \vec{x}_2 \rangle | &= \int d^3r_1 \int d^3r_2 \frac{1}{\sqrt{V}} e^{-i\vec{k}_1 \times \vec{r}_1} \frac{1}{\sqrt{V}} e^{-i\vec{k}_2 \times \vec{r}_2} \frac{1}{\sqrt{V}} \phi_M^* e^{i\vec{K} \times \vec{R}} \\
&= \int d^3r \frac{1}{\sqrt{V}} e^{-i\vec{k} \times \vec{r}} \phi_M^*(\vec{r}), | \langle M | \vec{p}_1, \vec{x}_1; \vec{p}_2, \vec{x}_2 \rangle |^2 \\
&= \int d^3r \int d^3r' \frac{1}{V} \phi_M^*(\vec{r}) \phi_M(\vec{r}') e^{-i\vec{k} \times \vec{r}} e^{-i\vec{k} \times \vec{r}'} \\
&\stackrel{Q=\frac{r+r'}{2}, s=r-r'}{\rightarrow} \int dQ \int d^3s \frac{1}{V} \phi_M^*(\vec{Q} + \vec{s}/2) \phi_M(\vec{Q} - \vec{s}/2) e^{-i\vec{k} \times \vec{s}} \\
&= \int dQ \int \frac{1}{V} f_M^w(\vec{Q}, \vec{k}).
\end{aligned}$$

In addition, we use a simple harmonic oscillator function to approximate the meson wave function at its rest frame $\phi_M(\vec{r})$:

$$\phi_M(\vec{r}) = \left(\frac{\mu\omega}{\pi} \right)^{3/4} e^{-\frac{1}{2}\mu\omega^2 r^2}, \quad (2.21)$$

where $\mu = \frac{m_1 m_2}{m_1 + m_2}$ is the reduced mass, and ω is a pre-defined angular frequency of the

harmonic oscillator. Substitute Eqn. 2.21 into Eqn. 2.21, one get the Wigner function as:

$$\begin{aligned}
f_M^W(\vec{r}, \vec{k}) &= g_M \int d^3s e^{-i\vec{k}\cdot\vec{s}} \left(\frac{\mu\omega}{\pi}\right)^{3/2} e^{-\frac{1}{2}\mu\omega(\vec{r}+\vec{s}/2)^2 - \frac{1}{2}\mu\omega(\vec{r}-\vec{s}/2)^2} \\
&= 2\pi g_M \int_{-1}^1 d(\cos\theta) \int_0^\infty s^2 ds \left(\frac{\mu\omega}{\pi}\right)^{3/2} e^{-\mu\omega r^2} e^{-\mu\omega s^2/4} e^{-ks\cos\theta} \\
&= 2\pi g_M \left(\frac{\mu\omega}{\pi}\right)^{3/2} e^{-\mu\omega r^2} \int_0^\infty s^2 ds e^{-\mu\omega s^2/4} \frac{1}{-iks} (e^{-iks} - e^{iks}) \\
&= 2\pi g_M \left(\frac{\mu\omega}{\pi}\right)^{3/2} e^{-\mu\omega r^2} \frac{1}{ik} e^{-\frac{1}{\mu\omega}k^2} \int_0^\infty ds s \left[e^{-\frac{1}{4}\mu\omega(s-\frac{2i}{\mu\omega}k)^2} - e^{-\frac{1}{4}\mu\omega(s+\frac{2i}{\mu\omega}k)^2} \right] \\
&= 8g_M e^{-\mu\omega r^2} e^{-\frac{k^2}{\mu\omega}}.
\end{aligned}$$

g_M is the degeneracy factor which takes into consideration of the spin-color degrees of freedom – $g_M = 1/(2 \times 3 \times 2 \times 3)$ for D -meson ground state, and $g_M = 3/(2 \times 3 \times 2 \times 3)$ for the first excited state of D -meson. For three quarks recombining into a baryon, the Wigner function can be extended as two particles first recombine with each other and then the two particle system recombines with a third quark to form a baryon.

We can use the Wigner function 2.22 to calculate the probability of a heavy quark recombining with a light quark from QGP medium to form a heavy meson at T_c . The overall normalization factor is determined by the assumption that the recombination probability equals to 1 for zero-momentum heavy quarks⁶.

Figure. 2.10 shows the recombination probability with respect to the heavy quark momentum at critical temperature $T_c = 154$ MeV, where the solid lines correspond to the probability to recombine into all the heavy flavor hadrons and the dashed lines correspond to recombine into heavy mesons. The probability for a heavy quark to recombine with another quark decreases with its increasing momentum. In addition, comparing between the charm and bottom quark, with the same momentum p_T , bottom quarks have a larger recombination probability due to their larger mass.

⁶The recombination probability sums over all the possible heavy flavor meson and baryon channels, in our study, including both the ground state and first excite state of D -meson, $\Lambda_D, \Sigma_D, \Xi_D$ and Ω_D .

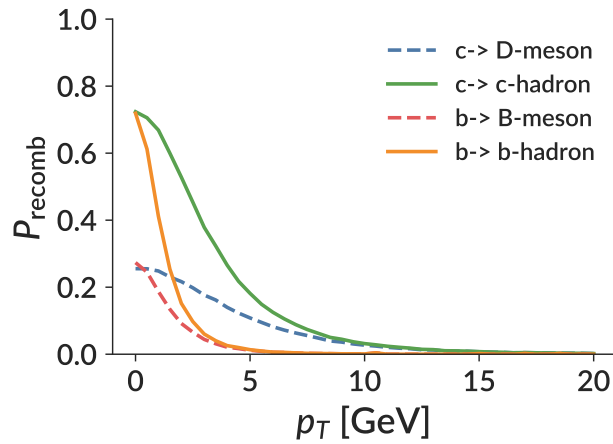


Figure 2.10: Recombination probability for charm and bottom quarks as a function of heavy quark momentum.

Hybrid model of fragmentation plus recombination

With the recombination probability calculated as a function of heavy quark momentum \vec{p} shown in Fig. 2.10, and the fragmentation function implemented with `PYTHIA`, one can simulate the process of heavy flavor hadronizing into heavy flavor hadrons. The algorithm

for the implementation in the hybrid model is summarized as follows:

Algorithm 1: Heavy flavor hadronization

Input: Heavy quark energy momentum (E, p) after propagating through the QGP medium

Output: Heavy flavor hadron

First, generate a random number ξ between 0 and 1 to determine if a heavy quark hadronizes into hadrons via mechanism;

if $\xi > \text{the probability } P_{HQ \rightarrow \text{hadron}}$ **then**

 Heavy quark hadronizes via fragmentation through PYTHIA;

else

 Heavy quark hadronizes via recombination;

while *No meson.baryon is formed or max tries has reached* **do**

 A u or d quark is sampled from a thermal distribution in the local rest frame of the cell;

 Boost back to the lab frame to combine with the given quarks according to Eqn 2.22;

end

end

2.3.3 Hadronic stage interaction

After the QGP medium undergoes the phase transition and hadronizes into a hadron resonance gas, the hadrons will keep decaying and scattering with each other until kinetic freezeout. The dynamics of the hadronic system during this stage can be simulated by a microscopic transport model by solving the Boltzmann equation:

$$\frac{df_i(x, p)}{dt} = C_i(x, p), \quad (2.22)$$

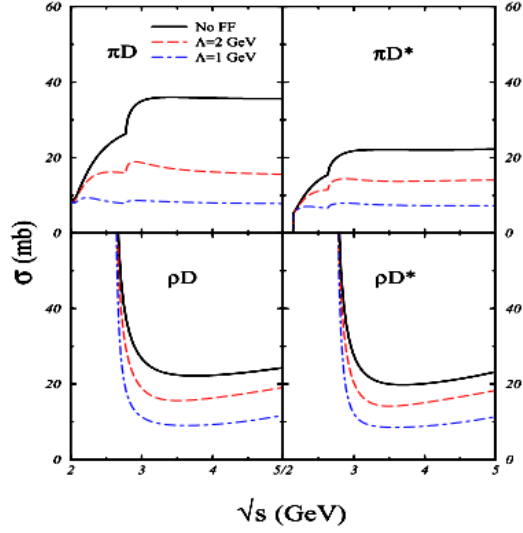


Figure 2.11: Total cross section for the heavy meson scattering with light hadron π, ρ as a function of energy. Due to the finite size effect of hadrons, form factors are needed at interaction vertices. The solid black lines are the cross section without form factor, where the cutoff parameter $\Lambda = \infty$. Taking into consideration of the form factor, which suppresses modestly (by a factor of two) of the total cross section, the magnitude of the cross section decreases with decreasing cutoff parameter.

which states that the time evolution of phase space distribution $f_i(x, p)$ of species i is determined by the collision terms (\mathcal{C}), including binary collisions, $2 \rightarrow n$ inelastic process, annihilation, resonance formation and decays.

The Ultra-relativistic Quantum Molecule Dynamics model (URQMD) is one of the most widely used models to simulate such processes in the hadronic stage. It solves the Boltzmann equation by sampling the collision term stochastically and propagating the particles along a straight-line trajectory. The inputs for the URQMD model are the cross section σ_{tot} between different species, which depend on the particle species and collision energies, and are tabulated from experimental data or parametrized according to the analytic calculations. In the semi-classical criterion, the cross section between a pair of particles is approximated as $\sigma_{\text{tot}}(\sqrt{s}) = \pi d_0^2$, which means that if the relative distance between the two particles $d_{\text{trans}} < d_0$, the collision would happen.

For the heavy flavor hadrons scattering with light hadrons, we implement the interaction of the D -meson with pions and rho mesons (π, ρ) whose cross section is calculated in [61]. 8 different processes are included in the calculation $\pi D \leftrightarrow \rho D^*, \pi D^* \leftrightarrow \rho D, \pi D \rightarrow \pi D, \pi D^* \rightarrow \pi D^*, \rho D \rightarrow \rho D, \rho D^* \rightarrow \rho D^*$, and the total cross sections as function of the scattering energy are plotted in Fig. 2.11. After hadrons cease interacting and reach kinetic freeze-out, the energy and momentum of light and heavy hadrons are collected to construct the final observables.

2.4 Experimental observables

Two particle accelerators are currently performing ultra-relativistic heavy-ion collisions: the Relativistic Heavy-ion Collider (RHIC) at Brookhaven National Lab, NY, and the Large Hadron Collider (LHC) in Geneva Switzerland. RHIC has been conducting the heavy-ion collision experiments since 2000, colliding nucleus including gold (Au), uranium (U), copper (Cu), proton (p), deuteron (d) and helium-3 (He) at center-of-mass energies $\sqrt{s_{NN}}$ range from 7.7 to 200 GeV per nucleon-nucleon pair. The LHC turned on in 2009, colliding proton-proton (p-p), proton-lead (p-Pb), lead-lead(Pb-Pb) and Xe-Xe at a much higher center-of-mass energy (with the p-p collisions at 14 TeV, while for Pb-Pb collisions at 2.76 and 5.02 TeV). Although the LHC reaches higher collision energy, RHIC experiments can cover more collision systems over a wider energy range, which is crucial for exploring the QCD critical point.

2.4.1 Multiplicity and centrality

The most straightforward observables in heavy-ion collision experiments are the multiplicity – number of produced particles, and produced energy. The particle multiplicity per unit

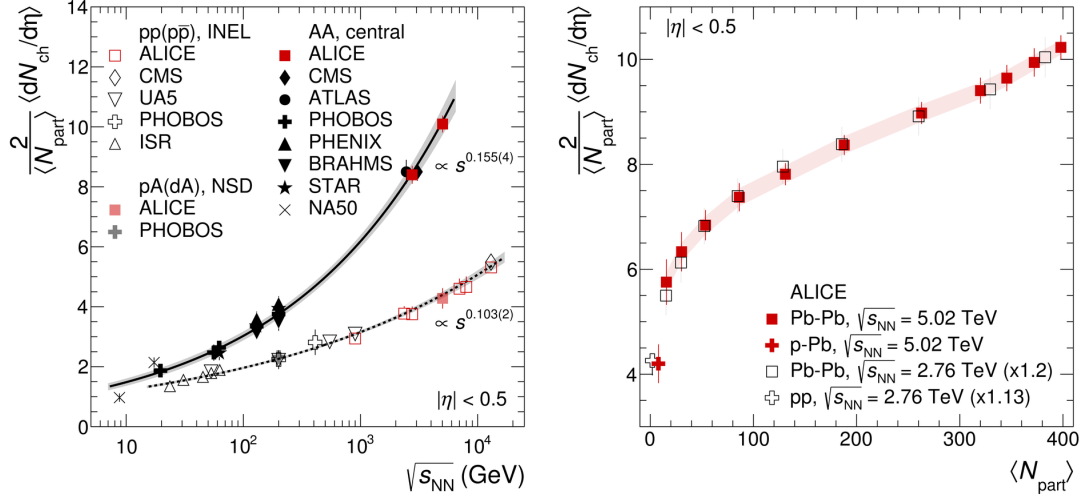


Figure 2.12: [Left]: values of $\frac{2}{\langle N_{\text{part}} \rangle} \langle dN_{\text{ch}}/d\eta \rangle$ for central Pb-Pb, Au-Au, and p-p collisions as a function of $\sqrt{s_{\text{NN}}}$. lines represent a fit with $s_{\text{NN}}^{0.155}$ and $s_{\text{NN}}^{0.103}$, both describes the scaling for AA and pp collisions very well. [Right]: $\frac{2}{\langle N_{\text{part}} \rangle} \langle dN_{\text{ch}}/d\eta \rangle$ for Pb-Pb collisions at $\sqrt{s_{\text{NN}}} = 5.02 \text{ TeV}$ in centrality range 0-80% as a function of $\langle N_{\text{part}} \rangle$. Data from lower energy (2.76 TeV) Pb-Pb and p-p collisions scaled by a factor of 1.2 and 1.13 respectively for comparison. Figure from [62].

pseudo-rapidity⁷ in the central rapidity region $dN_{\text{ch}}/d\eta|_{|\eta|<0.5}$ is directly related to the collision energy and the number of participant nucleons N_{part} ⁸.

The left panel of Fig. 2.12 plots the charged particle multiplicity at midrapidity per participant pair $\frac{2}{\langle N_{\text{part}} \rangle} \langle dN_{\text{ch}}/d\eta \rangle$ as a function of collision energy in different collision systems. It has shown a fairly good fit with an energy scaled as $s_{\text{NN}}^{0.155}$ and $s_{\text{NN}}^{0.103}$ for AA and pp collisions respectively, with little dependence on the species of the nucleus.

The right panel shows the charged particle multiplicity at midrapidity per participant pair as a function of number of participants. More central collisions – those with small impact parameter and more overlap – have more participants, and therefore produce more

⁷For the definition of all the kinetic quantities that are commonly used in high energy particle and heavy-ion physics, please refers to the Appendix A.0.1.

⁸A “participant” is the nucleon who has undergone at least one inelastic collision in nucleus-nucleus collisions. It is generally smaller than the number of binary collisions N_{coll} as one “participant” can participate in multiple binary collisions.

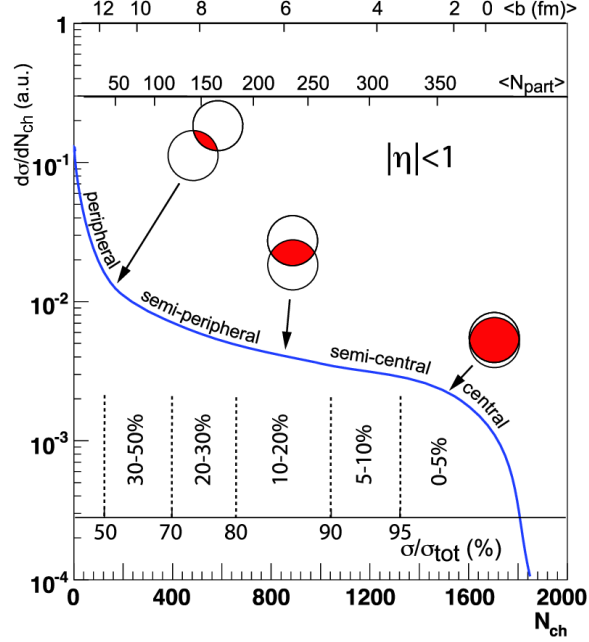


Figure 2.13: Cartoon example of the correlation of the centrality with final observables N_{ch} and other quantities such as $\langle N_{part} \rangle$ impact parameter b . Figure from [20].

particles. In the most central collisions, $N_{part} \sim 400$, around 10 charged particles are produced per participant pair in the mid-rapidity region of $\sqrt{s_{NN}} = 5.02$ TeV. In addition, the shape of the multiplicity- N_{part} is almost identical at both 2.76 and 5.02 TeV collisions.

In heavy-ion collisions, the collision events are categorized into different centrality classes, which is based on the final-state observables that quantify the matter produced in the collision, such as the charged particle multiplicity N_{ch} , production energy E_T . For example, the 0-5% centrality corresponds to the most central collisions that produce the most particles. One can relate the final state observables to initial condition quantities such as the number participants $\langle N_{part} \rangle$ or impact parameter b , as shown in Fig. 2.13. However, those are often theoretical treatment. In our calculation, we follow the same procedure like experimental measurements to bin minimum bias events into different centralities according to the final state charged particle multiplicity at mid-rapidity. By doing so, we try to be consistent with experimental measurements and eliminate any unwanted deviation due to

the choice of computing method.

In addition to the multiplicity, the identified particle yields (such as the pion, kaon, proton multiplicity per unit rapidity) are also often reported as important observables. Such identified particle yields give us some insight on the chemical freeze-out of the system, as if one assumes that if the QGP medium is thermalized during the QGP phase, the identified particle yields will be controlled by their Boltzmann factor $e^{-m/T}$ and spin degeneracy. A simple statistical hadronization model based on such assumptions has been very successful in the description of the identified particle yields in heavy-ion collisions [63].

2.4.2 Transverse momentum distribution and collective flow

Another standard measurement in heavy-ion collisions is the p_T spectra – distributions of the particle yield as a function of the transverse momentum. As shown in Fig. 2.14, the p_T distributions of the identified particles are almost thermal in the hydrodynamically applicable region ($p_T \leq 3$ GeV), with a peak at low p_T and an exponential tail. In heavy-ion collisions, a majority of particles are produced in the low momentum region. The slope of each curve corresponds to the kinetic freeze-out temperature T_{kin} , which decreases with centrality. While the height of the curve corresponds to the particle yield, while follows the mass hierarchy.

event-plane

Multiple particle correlations, especially the collective flow are among the most compelling evidence that a strongly-interacting quark-gluon plasma has been created in heavy-ion collisions.

In Section 1.2.1 I have introduced the collective flow coefficients as the quantity to characterize the momentum anisotropy for final state particles. Mathematically, it is the

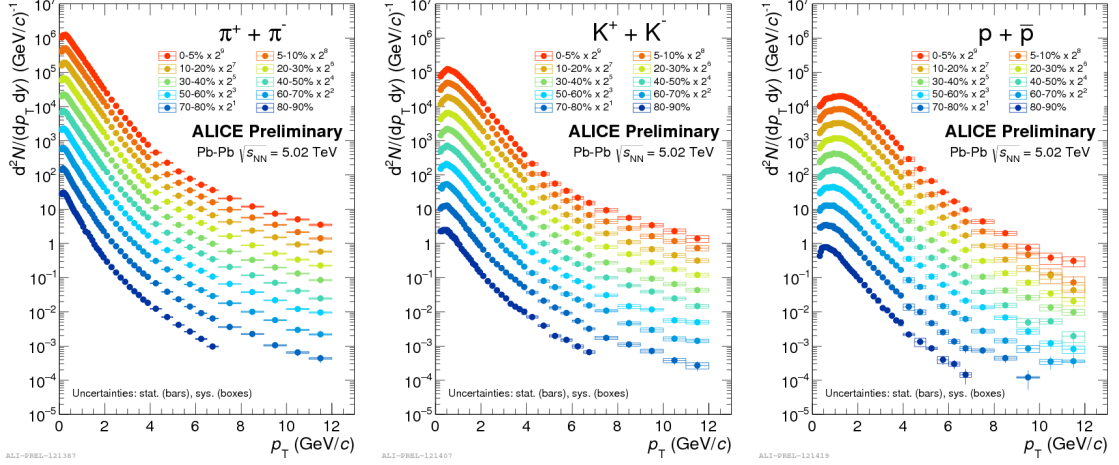


Figure 2.14: Spectra of identified particles (pion [left], kaon [middle], proton [right]) as function of p_T for different centrality classes in Pb-Pb collisions at $\sqrt{s_{NN}} = 5.02$ TeV. Figure from [64].

n -th harmonics in the Fourier expansion of the final state particle azimuthal distribution:

$$\frac{dN}{d\phi} \propto 1 + \sum_{n=1}^{\infty} 2v_n \cos [n(\phi - \Psi_n^{\text{RP}})], \quad (2.23)$$

Ψ^{RP} is the reaction plane angle that is associated with the initial density distribution. In experiment, the initial condition is un-measurable therefore the reaction plane angle is approximated by the event-plane angle Ψ^{EP} , which is defined according to the final state particle azimuthal distribution in which direction the n -th harmonic is the largest. The event-plane method to calculate the flow coefficients is then:

$$v_n = \left\langle \cos [n(\phi - \Psi_n^{\text{EP}})] \right\rangle. \quad (2.24)$$

cumulants

Other than the event-plane method, the flow coefficients v_n can also be estimated via multi-particle azimuthal correlations – cumulants [65–67]. One can construct the Q-vectors,

defined as:

$$Q_n = \sum_{i=1}^M e^{in\phi_i}, \quad (2.25)$$

which sum over all the particle of interest i . M is the total number of particle of interest.

The squares of Q_n is equivalent to the sum over pairs:

$$|Q_n|^2 = \sum_{i,j=1}^M \exp^{in(\phi_i-\phi_j)} = M + \sum_{i \neq j}^M e^{in(\phi_i-\phi_j)}. \quad (2.26)$$

On the other hand, the two particle correlation in a single events is:

$$\langle 2 \rangle = \left\langle \exp^{in(\phi_i-\phi_j)} \right\rangle = \frac{1}{M(M-1)} \sum_{i \neq j}^M e^{in(\phi_i-\phi_j)}, \quad (2.27)$$

comparing with Eqn. 2.26 one get:

$$\langle 2 \rangle = \frac{|Q_n|^2 - M}{M(M-1)}. \quad (2.28)$$

For multiple collisions in a single centrality bins, one could average over the single events two particle correlation, and the n -order cumulant from two particle correlation can be specified:

$$c_n\{2\} = \langle \langle 2 \rangle \rangle = \left\langle \left\langle \exp^{in(\phi_i-\phi_j)} \right\rangle \right\rangle = \frac{\sum_i^{nevents} M_i(M_i-1) \langle 2 \rangle}{\sum_i^{nevents} M_i(M_i-1)}. \quad (2.29)$$

The flow coefficients v_n estimated from the cumulant equals to:

$$v_n\{2\} = \sqrt{c_n\{2\}}. \quad (2.30)$$

I should emphasize though, the difference between $v_2(\text{EP})$ and $v_2\{2\}$ is very subtle. Figure. 2.15 compares the v_2 calculated with different methods in Pb-Pb collisions at 2.76

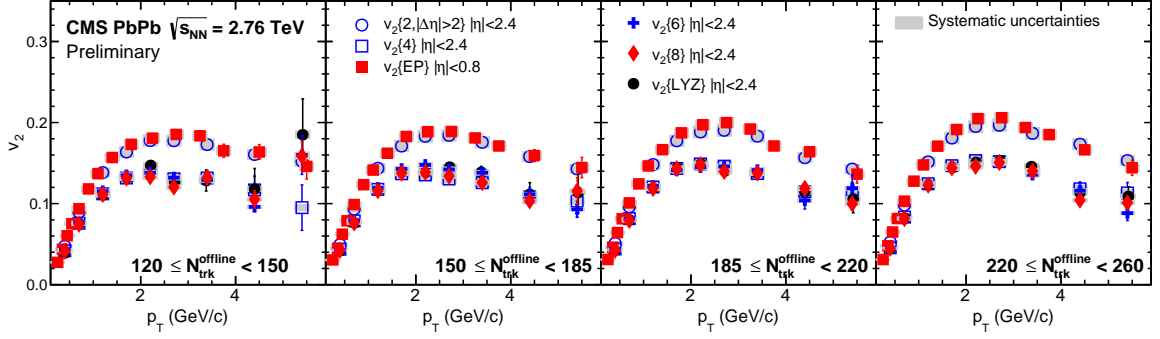


Figure 2.15: v_2 as a function of p_T in Pb-Pb collision for different $N_{\text{trk}}^{\text{offline}}$ ranges. Comparison among different method to v_2 calculation method. Figure from [68]

TeV. The red squares are the result from event-plane method while the empty circles are the cumulant flow v_2 . One can see little difference between those two.

2.4.3 Heavy flavor observables: nuclear modification factor and collective flow

When it comes to the heavy flavor observables, the two most important observables are the nuclear modification factor R_{AA} and elliptic flow v_2 .

The nuclear modification factor R_{AA} is defined as the particle yield in nucleus-nucleus (AA) collisions divided by the scaled yield in the proton-proton (pp) collisions:

$$R_{AA}(p_T) = \frac{d^2 N_{AA}/dp_T dy}{\langle N_{\text{coll}} d^2 N_{pp}/dp_T dy \rangle}. \quad (2.31)$$

When one simulates the heavy quark evolution in heavy-ion collisions and calculates the heavy meson R_{AA} , it is generally useful to calculate the heavy meson spectra $dN/dp_T dy$ in pp collisions in the same framework – with the initial momentum spectra calculated using a nucleon parton distribution function and without medium modification. In addition, heavy quarks hadronize into heavy flavor hadrons via fragmentation using PYHTIA. This could eliminate some degree of theoretical uncertainty. In Fig. 2.16 the D -meson spectrum calculated from our framework is compared with the experimental measurements of the p-p

collisions at 2.76 TeV, which shows a consistency within the experimental uncertainties.

In Fig. 2.17 we present the experimental measurements of D -meson R_{AA} as function of p_T or $\langle N_{\text{part}} \rangle$ at RHIC and the LHC. At both energies, heavy meson production at high p_T has experienced significant suppression compared to that in pp collisions.

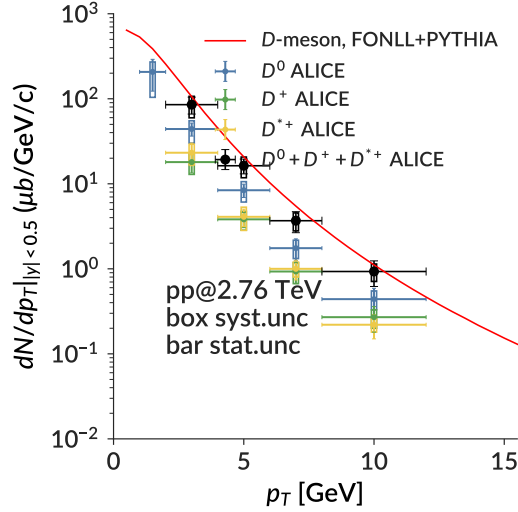


Figure 2.16: D -meson reference spectrum in pp collisions at 5.02 TeV. The errorbars are experimental measurements by ALICE for different D -meson species, while the red line is the calculation by FONLL + PYTHIA.

Regarding the calculation of the heavy meson elliptic flow, various approaches are developed. One can use the event-plane method:

$$v_n = \left\langle \cos \left[2(\phi - \Psi_n^{\text{EP}}) \right] \right\rangle = \left\langle \frac{p_y^2 - p_x^2}{p_x^2 - p_y^2} \right\rangle, \quad (2.32)$$

where $\langle \rangle$ indicates an average over all the selected D -meson in all selected events. The two particle cumulant method can also be used to calculate the D -meson elliptic flow, which

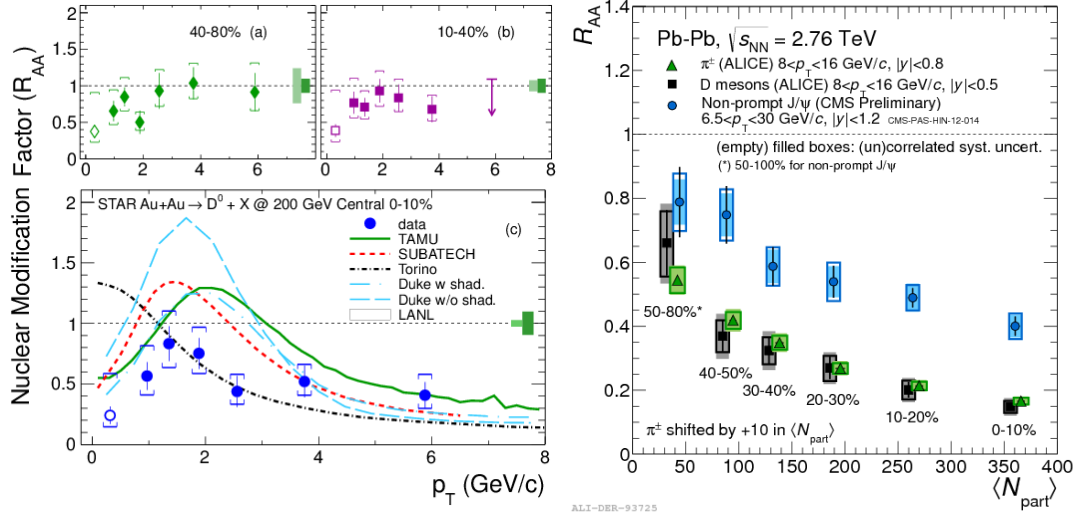


Figure 2.17: [Left]: D_0 meson nuclear modification factor R_{AA} as a function of p_T in Au-Au collisions at $\sqrt{s_{NN}} = 200$ GeV for different centralities measured by STAR collaboration [69]. Note that in the most bottom panel, the experimental measurements are compared with theoretical calculation. [Right]: D -meson p_T integrated R_{AA} as a function of number of participant $\langle N_{part} \rangle$ in Pb-Pb collisions at 2.76 TeV measured by ALICE collaboration [70]. Comparing between open heavy flavor meson and the light hadron π , both experience similar expression in the collisions.

correlates the D -mesons with the light hadrons via:

$$v_2\{2\} = \frac{\langle \vec{u} \cdot \vec{Q} \rangle}{\sqrt{\frac{Q_a Q_b}{N_a N_b}}}. \quad (2.33)$$

The vector $\vec{u} = \sum_{i=1}^{M_Q} \exp^{i\phi_i}$ is the Q-vector for D -mesons, \vec{Q} , \vec{Q}_a , \vec{Q}_b are the Q-vectors for charged particles correspondingly⁹.

2.5 Summary

In this chapter, I have summarized the “standard model of heavy-ion collisions”, which describes the evolution of the QGP medium as multi-stage evolving processes based on

⁹ \vec{Q} includes all the selected charged particles as reference particle, \vec{Q}_a refers to the sum of charged particles whose rapidity $y < 0$ while \vec{Q}_b refers to sum of charged particles with $y > 0$.

the relativistic viscous hydrodynamical framework. In addition, I introduced the heavy quark evolution framework that coupled with the “standard model”, which modularizes the heavy quark evolution as: a) initial condition generation; b) in-medium propagation; c) hadronization; d) hadronic stage rescattering. The experimental observables regarding the soft matter and the heavy flavor are reviewed.

Next chapter, I will describe the heavy quark in-medium propagation, where I would like to investigate the energy loss mechanism of heavy quarks and estimate the transport properties of heavy quark inside the QGP medium.

Chapter 3

Transport framework for heavy quark evolution

In the last chapter, we established a consistent space-time evolution picture for both heavy quarks and the QGP medium in heavy-ion collisions. This chapter will be dedicated to studying the key ingredient of this framework: the heavy quark in-medium propagation.

3.1 Summary of various heavy quark in-medium propagation models

During their propagation through the QGP medium, heavy quarks interact with the medium constituents and lose energy. The interaction between heavy quarks and the medium depends on the medium temperature T , local flow $\vec{\beta}$, and the assumption of the medium degrees of freedom. Therefore the dynamics of the heavy quarks are sensitive to the medium properties and heavy quarks can be considered as valuable probes of the medium.

Various approaches have been developed to describe the propagation of heavy quarks through the QGP medium. Table 3.1 briefly summarizes some of the heavy quark evolution models on the market. Those models are separated into three different categories according to the different assumptions made regarding the medium and the different interaction mechanisms. The transport coefficient based model employs Langevin dynamics, which ignores the medium constituents but focuses on macroscopic properties of the medium, such as the temperature evolution and transport coefficients. The cross-section based model assumes a quasi-particle picture of the QGP medium and describes the heavy quark dynamics with a Boltzmann equation. Heavy quarks typically interact with the medium by scattering. Further separation of different models can be made, for example, based on the energy loss mechanisms: collisional vs. radiative vs. both.

A more comprehensive overview of the heavy flavor evolution models can be found in [71], here I will only highlight a few typical models:

- `Duke Langevin` [72, 73]: The `Duke Langevin` model describes the propagation of the heavy quarks in the QGP medium following an improved Langevin model. The advantages of the Langevin approach is that it makes no assumption on the medium degrees of freedom, but characterizes the medium evolution by its local temperature and flow velocity, which can be obtained from a hydrodynamical model. The Langevin model is improved by including a recoil force which accounts for radiative energy loss of heavy quarks in the medium. In addition, it takes advantage of modern Bayesian model-to-data comparison analysis technique, and estimates the transport coefficients by calibrating on experimental data of D -meson R_{AA}, v_2 in different collision systems.
- `Duke Lido` [74]: The `Duke Lido` model studies the heavy quark in-medium propagation by solving a linearized Boltzmann equation, where heavy quarks lose and gain energy by scattering with the medium constituents (massless light quarks and gluons). The interaction strength between heavy quarks and the light partons are encoded as scattering rates, and the light partons are sampled from a thermal distribution with a temperature given by a viscous hydrodynamical model. The elastic scattering rates are calculated with a running coupling constant and regulated by a Debye screening mass, while the inelastic scattering rates are calculated using the Gunion-Bertsche approximation and also include the LPM effects. Moreover, this framework includes a diffusion component, which models non-perturbative small momentum transfer processes.
- PHSD transport approach [75, 76]: The Parton-Hadron-String dynamics (PHSD) transport approach is a microscopic covariant dynamical model which simulates the strongly interacting QGP medium based on Kadanoff-Baym equations. Therefore, PHSD employs a non-equilibrium dynamics of the QGP evolution instead of a local thermal equi-

librium evolution like hydro. The QGP medium consists of light partons whose mass and width are determined by fitting the lattice Equation of State (EoS). Heavy quarks interact with the off-shell quasi-particle elastically, with the running coupling that is scaled by the local temperature.

- AMPT [77]: A multi-phase transport model (AMPT) is a microscopic parton cascade model. It starts from an initial condition generated from a multiple mini-jets model (HIJING[78]), and describes the dynamics of the QGP medium as a parton cascade with only two-body scatterings. The partonic cross sections are obtained from pQCD with screening masses. The heavy quark interaction with the medium is modeled as elastic partonic scatterings with the medium constituents.
- MC@sHQ [79–81]: A pQCD inspired “Monte Carlo at heavy quark approach” MC@sHQ describes the heavy quark interacting with the medium by solving the linearized Boltzmann equation. Being a cross-section based transport model, it shares the same assumption with the Duke Lido model but differs at: a) the matrix elements (instead of the Debye screening propagator, it adopts an effective scalar propagator with a self-consistent Debye screening mass); 2) both collisional and radiative energy losses are considered but the MC@sHQ does not consider the gluon absorption $3 \rightarrow 2$ process to maintain the detailed balance. With an overall K -factor (which is induced in order to account for any contributions from higher order processes or non-perturbative effects), the model is able to describe the heavy meson R_{AA} and v_2 with both the collisional energy loss only and collisional + radiative energy loss processes.
- AdS/CFT [82, 83] in a static fireball: The anti-de-Sitter/conformal field theory (AdS/CFT) connects a field theory in n -dimensions and string theory in $n + 1$ dimensions, which is most well understood between $\mathcal{N} = 4$ super Yang-Mills (SYM) field theory and Type IIB string theory, as those two theories are considered as duals to each other. Although

no one has yet found an exact dual string theory close to QCD, the AdS/CFT model connects the parameters of the QCD to those of SYM, and therefore can estimate the properties of a QCD medium with string theory. In AdS/CFT, the heavy quarks are modeled as strings who lose energy to the thermal plasma via the momentum flowing down. The main assumption for applying AdS/CFT correspondence is the strong coupling, which therefore provides us an upper limit for the heavy quarks suppression in the heavy-ion collisions (strong coupling limit).

- Catania-QPM [84, 85]: Catania-QPM is a full space-time microscopic transport model that describes both heavy quark and the massless light quark and gluon evolution by solving a full relativistic Boltzmann equation. The Boltzmann equation is solved numerically with a test-particle method. Heavy quarks interact with the bulk constituents elastically, whose scattering cross section is calculated via a leading-order pQCD approach. The matrix element employs a temperature dependent running coupling $\alpha_s(T)$ and a leading order Debye screening mass.
- BAMPS [86–89]: Similar to Catania-QPM, BAMPS is also a full space-time transport models that solves the full Boltzmann equations for both heavy quarks and massless light partons. Different from the Catania-QPM model, BAMPS also includes the radiative process and the reverse $3 \rightarrow 2$ process. The inelastic scattering between heavy quarks and the light partons are described by the scattering rate, which is calculated by integrating over the Gunion-Bertsche matrix elements. The LPM effects are taken into consideration as is a temperature dependent running coupling $\alpha_s(T)$ and a leading order Debye screening mass.
- WHDG [90, 91]: WHDG calculates heavy quark radiative processes within the DGLV opacity expansion from pQCD based matrix elements. The radiative energy loss of heavy quarks includes all orders in opacity, finite gluon mass effect, and the Landau-

Pomeranchuk-Migdal (LPM) effect by the coherent re-summation of multiple gluon emission. Rather than utilizing a dynamically evolved QGP medium, the medium is supplied by a geometric picture, whose initial condition are constraint through fitting to the pion R_{AA}^π at RHIC energies, however, the same parametrization slightly underestimates the charged hadrons R_{AA} at the LHC energies. This model can describe the D -meson R_{AA} at both RHIC and the LHC energies fairly well. Due to the lack of flow in the medium implementation, the elliptic flow of heavy flavor hadrons is negligible.

- `T-matrix` [92–94]: The `T-matrix` model describes the heavy quark dynamics in the QGP medium following a traditional Langevin equation. Being a transport coefficient based model, it shares a common spirit with the `Duke Langevin` model as making no assumption on the medium constituents but focuses on heavy quark transport coefficients. However, it differs from the `Duke Langevin` model in: 1) The `T-matrix` does not consider the radiative energy loss of heavy quark; 2) The transport coefficients are calculated with a `T-matrix` approach, where the heavy quarks interact with the medium through a potential, which is obtained from Lattice QCD calculation. Due to the lack of radiative energy loss, the model underestimates the suppression of heavy quarks in the high p_T region, where the energy loss of the heavy quarks is dominated by radiative energy loss.

model	HQ production	medium modeling	HQ-medium interaction	HQ hadronization
transport coefficient based (Langevin)				
Duke improved Langevin	FONLL + EPS09 NLO	EbE (2+1)D viscous hydro	Langevin: col+rad	frag + recomb
TAMU T-matrix	FONLL + EPS09 NLO	(2+1)D ideal expansion	Langevin: col	frag + recomb
Catania-pQCD	pQCD at NLO	microscopic Boltzmann	Langevin: col	recomb
cross-section based (Boltzmann)				
Duke Lido	FONLL + EPS09 NLO	EbE (2+1)D viscous hydro	Boltzmann: col+rad	frag+recomb
AMPT	HIJING	parton cascade	col	
MC@sHQ	FONLL + EPS09 NLO	(3+1)D expansion (EPOS)	Boltzmann: col+rad	frag+recomb
Catania-QPM		(3+1)D parton cascade	Boltzmann: col	coalescence
WHDG	FONLL	no fluid dynamical evolution	rad	frag
BAMPS	MC@NLO	(3+1)D parton cascade	Boltzmann: col+rad	frag+recomb
LBL-CCNU	MC@NLO	(2+1)D viscous hydro	Boltzmann: col+rad	frag+recomb
PHSD	PYTHIA	parton-hadron-string dynamics	Boltzmann: col	frag
other				
AdS/CFT	FONLL	no fluid dynamical evolution	AdS/CFT drag	frag

Table 3.1: Open heavy flavor models

3.2 Boltzmann Dynamics

Two of the most popular transport models to describe the heavy quark in-medium propagation are: transport coefficient based Langevin model, and the cross-section based Boltzmann equation model. Comparing these two approaches, the Langevin model can be viewed as an approximation of the Boltzmann transport equation with multiple small momentum transfer assumption. It results in a significant simplification of the heavy quark in-medium dynamics. Another advantage for the Langevin approach is that it makes no assumption on the microscopic interaction mechanism, therefore it is more suitable for a data-driven study that focuses on the macroscopic properties of the QGP medium — the transport coefficients. On the other hand, the Boltzmann dynamics make an assumption on the underlying interaction mechanism (for example, a pQCD $2 \rightarrow n$ scattering), and the distribution of the medium constituents, which provides us insight into the quasi-particle nature of the QGP medium and the applicability of perturbative QCD. Although it has been discussed recently that the relaxation from Boltzmann dynamics to Langevin dynamics may not be valid for charm quarks [95], here I shall compare the two approaches and show that both are phenomenologically applicable to heavy-ion collisions so far, and that there is currently insufficient evidence to rule either one out.

3.2.1 Boltzmann equation

The evolution of the heavy quark phase-space distribution can be described by the Boltzmann equation:

$$\left(\frac{\partial}{\partial t} + \frac{\vec{p}}{E} \frac{\partial}{\partial \vec{x}} \right) f_Q(t, \vec{x}, \vec{p}) = \mathcal{C}[f_Q], \quad (3.1)$$

where $f_Q(t, \vec{x}, \vec{p})$ is the heavy quark distribution in the full space-time. $\mathcal{C}[f_Q]$ represents the collision integral, which can be written as the difference between the gain and loss terms:

$$\mathcal{C}[f_Q(\vec{p})] = \int d^3k [\omega(p \vec{+} k, \vec{k}) f_Q(\vec{p} + \vec{k}) - \omega(\vec{p}, \vec{k}) f_Q(\vec{p})]. \quad (3.2)$$

In Eqn. 3.2, $\omega(\vec{p}, \vec{k})$ denotes the collision rate per unit momentum phase space for a heavy quark changing momentum from \vec{p} to $\vec{p} - \vec{k}$. Therefore the first term on the right hand side represents the gain term while the second term represents the loss term. In a microscopic picture where the QGP medium consists of light quarks and gluons, heavy quarks interact with the medium and change momentum by scattering with the light partons. For example, in an elastic two body scattering process $1(Q) + 2(q/g) \rightarrow 3(Q') + 4(q'/g')$, where we have:

$$\begin{aligned} p_1 &= (E_1, \vec{p}), \\ p_3 &= (E_3, \vec{p}_3) = (E_3, \vec{p} + \vec{k}), \\ p_2 &= (E_2, \vec{p}_2), \\ p_4 &= (E_4, \vec{p}_4) = (E_4, \vec{p}_2 - \vec{k}), \end{aligned}$$

the collision rate can be written in terms of the cross section $\sigma_{12 \rightarrow 34}$:

$$\begin{aligned} \omega(\vec{p}, \vec{k}) &= d_{q/g} \int \frac{d^3p_2}{(2\pi)^3} f_2(p_2) v_{\text{rel}} \frac{d\sigma_{12 \rightarrow 34}}{d\Omega} \\ &= \frac{1}{d_Q} \frac{1}{2E_1} \int \frac{d^3p_2}{(2\pi)^3 2E_2} \frac{d^3p_3}{(2\pi)^3 2E_3} \frac{d^3p_4}{(2\pi)^3 2E_4} f_2(\vec{p}_2) \sum |\mathcal{M}|_{12 \rightarrow 34}^2 (2\pi)^4 \delta^{(4)}(p_1 + p_2 - p_3 - p_4), \end{aligned}$$

d_i is the spin-color degeneracy factor ($d_q = 2 \times 3$ for quarks, $d_g = 2 \times 8$ for gluons.) \sum indicates the summation over all the different scattering channels, and $\mathcal{M}_{12 \rightarrow 34}$ represents the matrix element for the scattering process $12 \rightarrow 34$. By substituting Eqn. 3.3 into

Eqn. 3.2, we get:

$$\mathcal{C}^{12 \rightarrow 34}(\vec{p}) = \frac{1}{d_Q} \frac{1}{2E_1} \int \frac{d^3 p_2}{(2\pi)^3 2E_2} \frac{d^3 p_3}{(2\pi)^3 2E_3} \frac{d^3 p_4}{(2\pi)^3 2E_4} \sum |\mathcal{M}_{12 \rightarrow 34}|^2 [f_3 f_4 - f_1 f_2] \\ \times (2\pi)^4 \delta^{(4)}(p_1 + p_2 - p_3 - p_4).$$

Therefore, in order to determine the time evolution of the heavy quarks, one would require two additional pieces of information:

- Momentum distribution $f_i(p_i)$ for parton i . We make the assumption that the scattering partner q/g — which is part of the QGP medium — follows a thermal distribution. The distribution depends the local temperature T and the local flow velocity u and can be denoted as $f_i(p_i \cdot u, T)$. For the light quarks, it follows the Fermi-Dirac distribution $f_{\text{FD}} = d_q (1 - e^{-p_2 \cdot u/T})^{-1}$, and for the gluons, it follows the Bose-Einstein distribution $F_{\text{BE}} = d_g (1 + e^{-p_2 \cdot u/T})^{-1}$. To be more precise, one should include the Bose enhancement and Pauli blocking factors $1 \pm f(p, T)$ for the final state thermal particles, but those are ignored in this study due to the small correction compared to other uncertainties in the model. The medium temperature and flow information T, u are obtained from a hydrodynamical evolution model.
- Matrix element $\mathcal{M}_{12 \rightarrow 34}$, which is calculated by using the perturbative QCD and counting all the possible Feynman diagrams. In the following, I will summarize the leading order Feynman diagrams for heavy quarks scattering with the light partons.

3.2.2 Partonic cross section

The partonic cross sections for heavy quark scattering with light partons are calculated in perturbative QCD approach with matrix elements regulated by a Debye screening mass.

In the pQCD expansion of the cross section, in orders of the coupling constant α_s , the

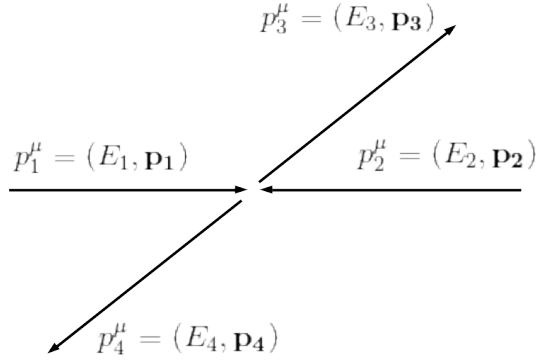


Figure 3.1: Center of mass frame for a $2 \rightarrow 2$ process.

elastic $2 \rightarrow 2$ scatterings are the lowest order contribution. They play an important role in heavy quark propagation in the QGP medium, especially at small momentum transfers. It should be noted that the lowest order contribution in terms of the cross section does not necessarily imply the leading order in terms of energy loss. It is generally believed that the radiative processes contribute significantly in the high momentum region.

in vacuum

In a microscopic description, heavy quarks interact with the QGP medium via elastic scattering with light partons:

$$Q + g \rightarrow Q + g, \quad (3.3)$$

$$Q + q \rightarrow Q + q. \quad (3.4)$$

In the center-of-mass frame, illustrated schematically in Fig. 3.1, the differential cross section is given by:

$$\frac{d\sigma}{dt} = \frac{1}{16\pi\sqrt{s}|\mathbf{p}_1|} \frac{1}{2E_1 2E_2 v_{\text{rel}}} |\mathcal{M}_{12 \rightarrow 34}|^2, \quad (3.5)$$

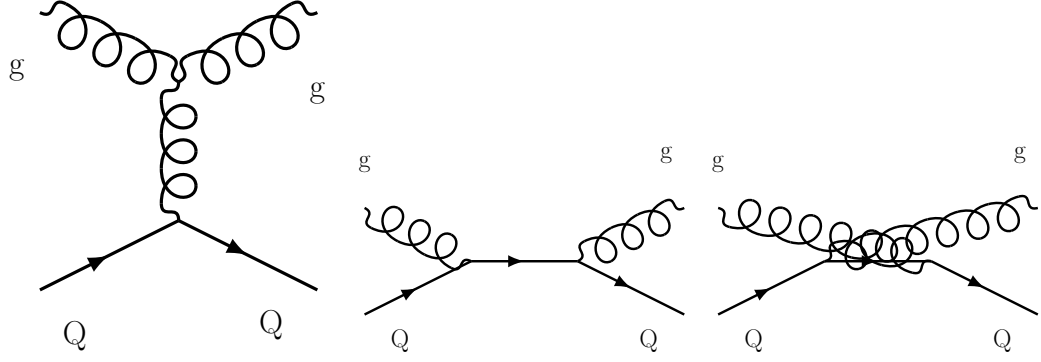


Figure 3.2: Leading order pQCD Feynman diagrams for heavy quark elastic scattering with gluons $Q + g \rightarrow Q + g$ — represents t, s, u channels from left to right. Time line goes from left to right.

where we introduce the Mandelstam variables as:

$$\begin{aligned}
 s &= (p_1 + p_2)^2 = (p_3 + p_4)^2, \\
 t &= (p_1 - p_3)^2 = (p_2 - p_4)^2, \\
 u &= (p_1 - p_4)^2 = (p_2 - p_3)^2.
 \end{aligned}$$

v_{rel} is the relative velocity of the two incoming particles and is given by:

$$v_{\text{rel}} = \frac{\sqrt{(p_1^\mu p_{2\mu})^2 - m_1^2 m_2^2}}{E_1 E_2}. \quad (3.6)$$

$\mathcal{M}_{12 \rightarrow 34}$ is the matrix elements for $2 \rightarrow 2$ scattering processes. As shown in the Feynman diagrams which are plotted in Fig. 3.2 and 3.3, one can construct the matrix elements following Feynmann rules.

In the case of one heavy quark scattering with one massless light parton ($m_1 = M, m_2 = 0$), the differential cross section is explicitly given by:

$$\frac{d\sigma}{dt} = \frac{|\mathcal{M}_{12 \rightarrow 34}|^2}{16\pi(s - M^2)^2}. \quad (3.7)$$

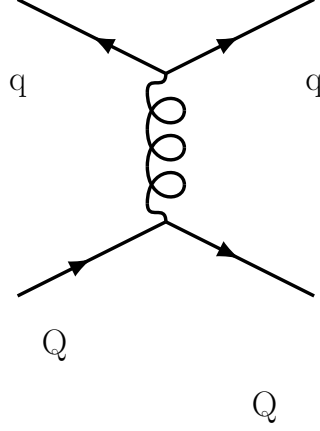


Figure 3.3: Leading order pQCD Feynman diagrams for heavy quark elastic scattering with light quarks $Q + q \rightarrow Q + q$ — only t channel survives. Time line goes from left to right.

For the $Q + g \rightarrow Q + g$ processes, the matrix element expressed in terms of Madelstrem variables reads:

$$\begin{aligned}
 |\mathcal{M}_{Qg \rightarrow Qg}|^2 = & \pi^2 \alpha_s^2 \left[\frac{32(s - M^2)(M^2 - u)}{t^2} + \frac{64(s - M^2)(M^2 - u) + 2M^2(s + M^2)}{9(s - M^2)^2} \right. \\
 & + \frac{64(s - M^2)(M^2 - u) + 2M^2(u + M^2)}{9(M^2 - u)^2} + \frac{16}{9} \frac{M^2(4M^2 - t)}{(s - M^2)(M^2 - u)} \\
 & \left. + 16 \frac{(s - M^2)(M^2 - u) + M^2(s - u)}{t(s - M^2)} - 16 \frac{(s - M^2)(M^2 - u) - M^2(s - u)}{t(M^2 - u)} \right],
 \end{aligned}$$

where the first term on the right hand side of the equation corresponds to the t channel (the most left diagram on Fig. 3.2). This is the dominant contribution. For a heavy quark scattering with a light quark $Q + q \rightarrow Q + q$, its matrix element reads:

$$|\mathcal{M}_{Qq \rightarrow Qq}|^2 = \frac{64}{9} \pi^2 \alpha_s^2 \frac{(M^2 - u)^2 + (s - M^2)^2 + 2M^2 t}{t^2}. \quad (3.8)$$

The total cross section can be obtained by integrating the differential cross section of

Eqn. 3.5 over the variable t ,

$$\sigma_{12 \rightarrow 34}(s) = \int_{t_{\min}}^{t_{\max}} \frac{d\sigma}{dt} dt, \quad (3.9)$$

where the integration boundary for the variable t goes from $t_{\max} = 0$ (forward scattering) and $t_{\min} = -\frac{(s-M^2)^2}{s}$ (backward scattering). It is clear that the upper boundary — $t_{\max} = 0$ — leads to a (infrared) divergence in the cross section due to the singularity in the t scattering channel. To regularize this infrared divergence, one can introduce a cut-off scale to exclude the small momentum transfer processes. In a medium, however, the gluon propagator acquires an effective mass (Debye screening mass), which can cure the divergence.

in medium

Before discussing the matrix element for the $2 \rightarrow 2$ process in a QGP medium, I should briefly review the concept of a screening mass. In a thermodynamic description of a charged system, the charges are distributed in a continuous medium. Beyond the Debye length scale (the inverse of Debye mass), the equilibrium plasma is undisturbed by a static source. The net effect of being undisturbed is that the propagator is modified by adding a screening mass $\mu_t = \kappa_t m_D^2$ that is proportional to the Debye mass, and all the small momentum transfer processes with $t < \mu_t$ are limited,

$$\frac{1}{t} \rightarrow \frac{1}{t - \mu_t}. \quad (3.10)$$

The Debye mass for the gluon can be calculated as [51]:

$$m_D^2 = \pi \alpha_s d_g \int \frac{d^3 p}{(2\pi)^3} \frac{\partial}{\partial p} (N_c f_g + n_f f_q), \quad (3.11)$$

and for light quarks

$$m_q^2 = 4\pi\alpha_s \left(\frac{N_c^2 - 1}{2N_c} \right) \int \frac{d^3p}{(2\pi)^3} \frac{1}{|p|} (f_g + f_q), \quad (3.12)$$

where $N_c = 3$ is the number of color charges, $d_g = 2 \cdot 8 = 16$ is the degeneracy factor for gluons, n_f is the number of flavors, and f_i represents the distribution for gluons and quarks. Assuming the local equilibrium and a classical Boltzmann statistics for gluons and quarks — $f_i = \exp[-E/T]$ — the Debye mass for quarks and gluons can be integrated as:

$$m_D^2 = \frac{8\alpha_s}{\pi} (N_c + n_f) T^2. \quad (3.13)$$

coupling constant

The strong coupling constant α_s is dependent on the re-normalization scale Q^2 , which is determined by the virtuality of each channels, i.e. $Q^2 = t, Q^2 = s - M^2, Q^2 = u - M^2$ correspondingly for t, s, u channels. Taking the form Eqn. 1.6, the strong coupling constant is defined as:

$$\alpha_s(Q^2) = \frac{\alpha_0}{\log(Q^2/\Lambda^2)}, \quad (3.14)$$

where the $\Lambda = 0.2$ GeV is the QCD scale. Taking $Q^2 \rightarrow 0$, the matrix element will be divergent, and the coupling constant $\alpha_s(Q^2)$ will diverge as well. Therefore in this study, I have regulated the coupling constant with an additional screening scale, which depends on the medium temperature and is defined as $\mu\pi T$ ¹ The regulated running coupling constant is plotted in Fig. 3.4, where on the left it shows the dependence of the running coupling with respect to different temperatures while on the right it shows the dependence with respect to the ad hoc parameter μ .

¹One should distinguish between the screening scale and minimum momentum transfer. The screening scale sets the maximum value for the coupling constant, but it does not imply that the minimum momentum transfer equals $\mu\pi T$, although those two may result in the same value for the coupling constant.

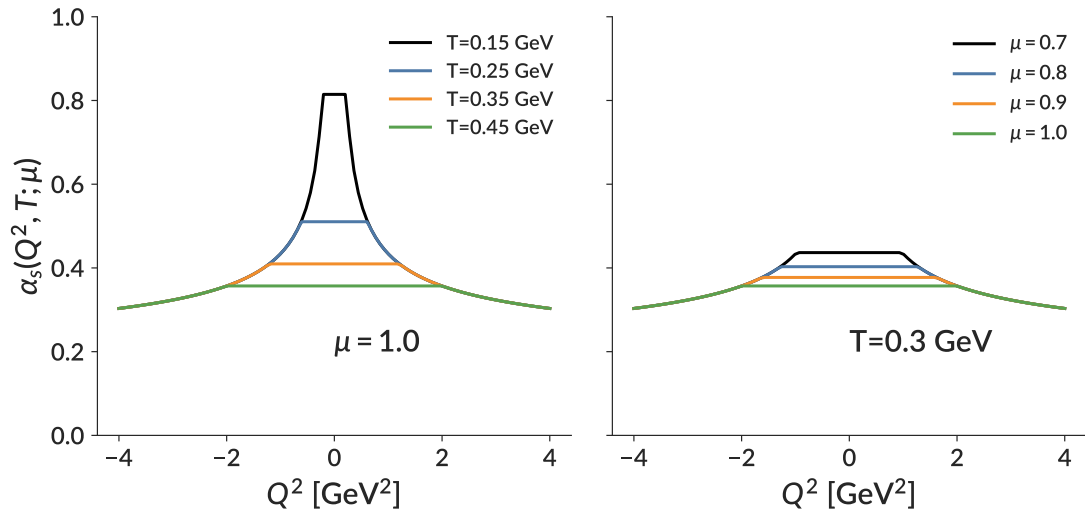


Figure 3.4: [Left]: strong coupling constant as a function of the momentum scale for different temperature, with an fixed renormalization scale $\mu = 1$; [Right]: strong coupling constant for different renormalization scale μ at fixed temperature.

Moreover, one can also use a fixed strong coupling constant α_s , denoted as an effective coupling constant in the medium. It is particularly useful when there is no dynamical process involved.

Combining the Debye screening with the coupling constant, the matrix elements for

heavy quark scattering with the light partons in the medium is updated as:

$$\begin{aligned}
|\mathcal{M}_{Qg \rightarrow Qg}|^2 = \pi^2 & \left[32\alpha_s^2(t) \frac{(s - M^2)(M^2 - u)}{(t - m_D^2)(t - \Lambda^2)} \right. \\
& + \frac{64}{9}\alpha_s^2(s - M^2) \frac{(s - M^2)(M^2 - u) + 2M^2(s + M^2)}{(s - M^2 + m_D^2)^2} \\
& + \frac{64}{9}\alpha_s^2(u - M^2) \frac{(s - M^2)(M^2 - u) + 2M^2(u + M^2)}{(M^2 - u + m_D^2)^2} \\
& + \frac{16}{9}\alpha_s(s - M^2)\alpha_s(u - M^2) \frac{M^2(4M^2 - t)}{(s - M^2 + m_D^2)(M^2 - u + m_D^2)} \\
& + 16\alpha_s(t)\alpha_s(u - M^2) \frac{(s - M^2)(M^2 - u) + M^2(s - u)}{(t - m_D^2)(s - M^2 + m_D^2)} \\
& \left. - 16\alpha_s(t)\alpha_s(u - M^2) \frac{(s - M^2)(M^2 - u) - M^2(s - u)}{(t - m_D^2)(M^2 - u + m_D^2)} \right], \tag{3.15}
\end{aligned}$$

$$|\mathcal{M}_{Qq \rightarrow Qq}|^2 = \frac{64}{9}\pi^2\alpha_s^2(t) \frac{(M^2 - u)^2 + (s - M^2)^2 + 2M^2t}{(t - m_D^2)(t - \Lambda)}. \tag{3.16}$$

We can, therefore, integrate the cross section for the heavy quark elastic scattering processes. Figure. 3.5 shows the cross section of a charm quark ($M = 1.3 \text{ GeV}$) scattering with the light partons in a QGP medium and compared between a running coupling constant — whose value is defined by Eqn. 3.14 — and a fixed coupling constant — ($\alpha_s = 0.45$). One can see that those two calculation deviate from each other significantly in low temperature region. $\sigma^{Qg \rightarrow Qg}$ is approximately twice as large as $\sigma^{Qq \rightarrow Qq}$. It is due to the ratio between the different color prefactors which yields $|\mathcal{M}_{Qg \rightarrow Qg}|^2 \simeq \frac{9}{4}|\mathcal{M}_{Qq \rightarrow Qq}|^2$.

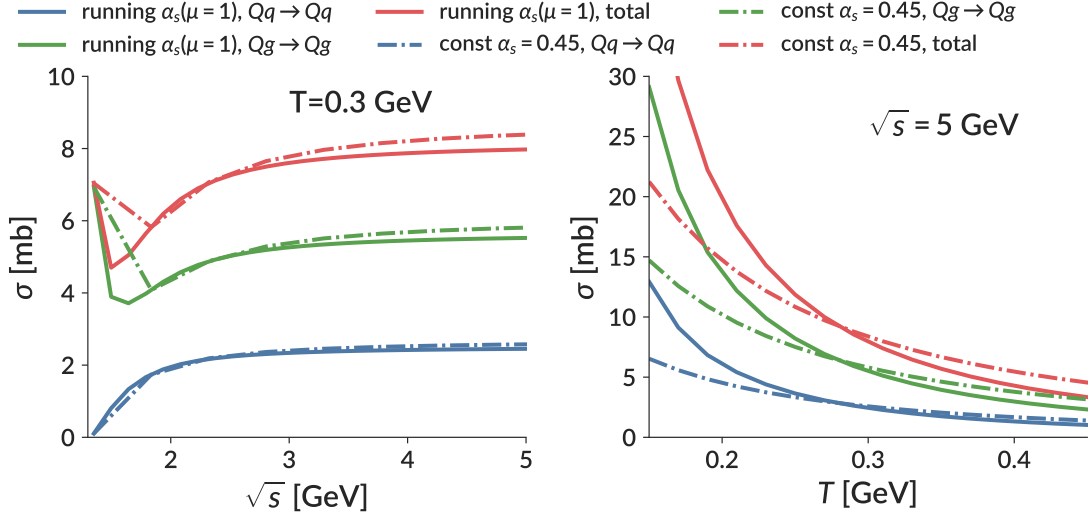


Figure 3.5: Charm quark ($M = 1.3$ GeV) cross section of $12 \rightarrow 34$ elastic scatterings with respect to center of mass energy \sqrt{s} [left] and temperature [right]. Compared between a running coupling constant result — where the coupling constant is defined by Eqn. 3.14, and a fixed coupling constant.

3.2.3 Monte Carlo implementation

Scattering rate

The linearized Boltzmann equation 3.2, which describes the evolution of the heavy quark phase-space distribution due to the collisional integral reads:

$$\left(\frac{\partial}{\partial t} + \frac{\vec{p}}{E} \frac{\partial}{\partial \vec{x}} \right) f_Q(t, \vec{x}, \vec{p}) = \mathcal{C}_Q^{2 \rightarrow 2} + \mathcal{C}_Q^{2 \rightarrow 3} + \mathcal{C}_Q^{3 \rightarrow 2} + \dots \quad (3.17)$$

where the leading order collisional integral $\mathcal{C}^{2 \rightarrow 2}(\vec{p})$ can be expressed with matrix elements as:

$$\begin{aligned} \mathcal{C}^{2 \rightarrow 2}(\vec{p}) = & \frac{1}{d_Q} \frac{1}{2E_1} \int \frac{d^3 p_2}{(2\pi)^3 2E_2} \frac{d^3 p_3}{(2\pi)^3 2E_3} \frac{d^3 p_4}{(2\pi)^3 2E_4} \sum |\mathcal{M}|_{12 \rightarrow 34}^2 [f_3 f_4 - f_1 f_2] \\ & \times (2\pi)^4 \delta^{(4)}(p_1 + p_2 - p_3 - p_4). \end{aligned} \quad (3.18)$$

For a Monte Carlo implementation to solve the linearized Boltzmann equation, the distribution of heavy quarks $f_Q(\vec{p})$ is represented as an ensemble of independent particles that scatter with the medium constituents (light quarks and gluons). When a heavy quark with energy-momentum $p_1 = (E_1, \vec{p}_1)$ propagates in a thermal medium with temperature T , it scatters multiple times with thermal particles — whose energy momentum $p_2 = (E_2, \vec{p}_2)$ follows the momentum distribution of an equilibrium medium $f_2(p_2 \cdot u, T)$.² In a time interval Δt , the average number of scattering for a $12 \rightarrow 34$ process is $\Gamma(E_1, T)\Delta t$, where $\Gamma(E_1, T)$ is the scattering rate and reads³:

$$\begin{aligned} \Gamma_{12 \rightarrow 34}(E_1, T) &= \frac{1}{2E_1} \int \frac{d^3 p_2}{(2\pi)^3 2E_2} \frac{d^3 p_3}{(2\pi)^3 2E_3} \frac{d^3 p_4}{(2\pi)^3 2E_4} f_1(E_2, T) \sum |\mathcal{M}|_{12 \rightarrow 34}^2 \\ &\quad \times (2\pi)^4 \delta^{(4)}(p_1 + p_2 - p_3 - p_4) \quad (3.19) \\ &= \int \frac{d^3 p_2}{(2\pi)^3} f_2(E_2, T) \Theta(s \geq 2m^2) \frac{2s}{2E_1 2E_2} \sigma_{12 \rightarrow 34}(s, T). \end{aligned}$$

The total scattering rate $\Gamma(E_1, T)$ then sums over all the possible channels with all types of collision partners (for a particular heavy quark $p_1 = (E_1, \vec{p}_1)$):

$$\Gamma_1(E_1, T) = \sum_{2,3,4} \Gamma_{12 \rightarrow 34}(E_1, T). \quad (3.20)$$

The energy and temperature dependence of the scattering rate is plotted in Fig. 3.6, where I have compared different scattering channels: solid blue line represent the scattering rate with light quarks while green dashed line represents the scattering rate with gluons.

²In the local rest frame of the cell, the momentum distribution $f(E_2, T)$ follows a Fermi-Dirac distribution $f_{FD} = d_q(1 - e^{-E_2/T})^{-1}$ for light quarks and an Einstein-Bose distribution $f_{BE} = d_g(1 + e^{-E_2/T})^{-1}$ for gluons. In addition, one should also take into account of the Bose enhancement and Pauli blocking factors $1 \pm f(E, T)$ for the final state thermal particles. However, those are small corrections compared to other uncertainties in this study. Instead, we use the classical Boltzmann distribution for both quarks and gluons.

³The scattering rate depends on the frame. In our implementation, the scattering rate is always calculated in the local rest frame of the cell. To calculate the scattering rate in the lab frame, one should use the flow velocity information to determine the light parton momentum distribution.

Although the cross section for heavy quark scattering with a gluon is larger than that with light quark — $\sigma_{Qg \rightarrow Qg} \simeq \frac{9}{4} \sigma_{Qq \rightarrow Qq}$ — after summing over all the degeneracy, that is $d_g = 2 \cdot 8$ (spin-color) for gluons, and $d_{q+\bar{q}} = 2 \cdot 3 \cdot 3 \cdot 2$ (spin, color, flavor, particle-anti-particle), the total scattering rates of those two are comparable to each other.

In addition, I compared the scattering rate calculated from a running coupling constant (solid red line) with a fixed one (red dashed line), where the latter shows a stronger positive temperature dependence for the total scattering rate. Considering only the t channel scattering we can understand this behavior in the following way, in the high energy limit where $E_1, s \gg m^2, T^2$,

$$\begin{aligned} \frac{d\sigma}{dt} &\propto \frac{\alpha_s^2}{t^2} \Rightarrow \sigma \propto \alpha_s^2 \left(\frac{1}{m_D^2} - \frac{1}{s - m^2} \right) \propto \alpha_s^2 \frac{1}{m_D^2}, \\ \Gamma &\propto \int p_2^2 dp_2 e^{-p_2/T} \frac{s}{E_1 E_2} \sigma \propto \frac{\alpha_s^2 T^3}{m_D^2}, \\ m_D^2 &\propto \alpha_s T^2 \Rightarrow \Gamma \propto \alpha_s T. \end{aligned} \tag{3.21}$$

Although the scattering rate $\alpha_s T$ shows a positive temperature dependence, the running coupling constant however, as shown in Fig. 3.4, has a negative temperature dependence. Therefore the overall effect leads to a stronger temperature dependence for a fixed coupling constant. A 3D projection of the scattering rate is also presented in Fig. 3.7.

Numerical implementation for a Boltzmann dynamics

When heavy quark propagates in the medium, the average number of scatterings it experiences in a time interval Δt equals to $\langle n_s \rangle = \Gamma \Delta t$. The scattering process is a rare event which follows a Poisson distribution, therefore the probability of n_s collisions in Δt follows:

$$P(n_s \geq 1) = e^{-\Gamma \Delta t} \frac{(\Gamma \Delta t)^{n_s}}{n_s!}, \tag{3.22}$$

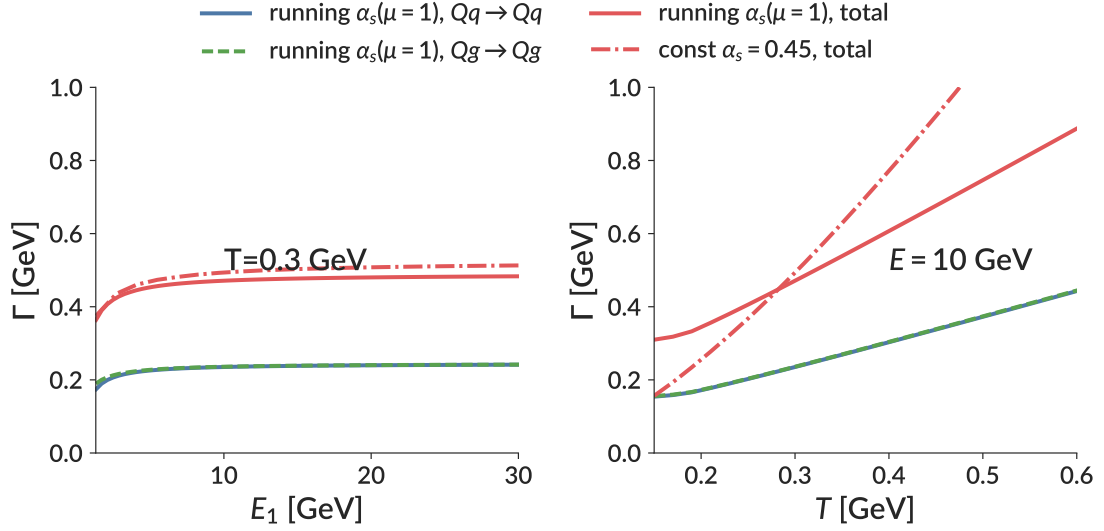


Figure 3.6: Total scattering rate $\Gamma_{12 \rightarrow 34}$ with respect to heavy quark energy [**left**], and medium temperature [**right**]. Running and fixed coupling constant are varied.

and the probability for no collisions in the time interval Δt is:

$$P(n_s = 0) = 1 - \sum_{n_s=1}^{\infty} P(n_s) = e^{-\Gamma \Delta t}. \quad (3.23)$$

To determine whether a scattering process happens in a time period $t_i \sim t_i + \Delta t$, a random number between 0 and 1 is generated and compared with the probability $P(\Gamma(E_1, T))$. If the random number is smaller than the probability, a specific scattering channel is chosen according to their individual scattering probability, and the final state particle momenta are sampled according to the differential cross section, e.g., $d\sigma/dt$ for the $12 \rightarrow 34$ processes. The outgoing heavy quark (E_3, \vec{p}_3) then propagates to the next time step $t_i + \Delta t$ with the new energy and momentum $\vec{p}_{\text{new}} = \vec{p}_3$. If no scattering happens, the heavy quark keeps the original energy and momentum p_1 and propagates to the next time step.

I should mention a few more details regarding the numerical implement action of the scattering process: first, while heavy quark propagates in the QGP medium, a few different reference frame transformation needs to be taken care of between: lab frame, local rest

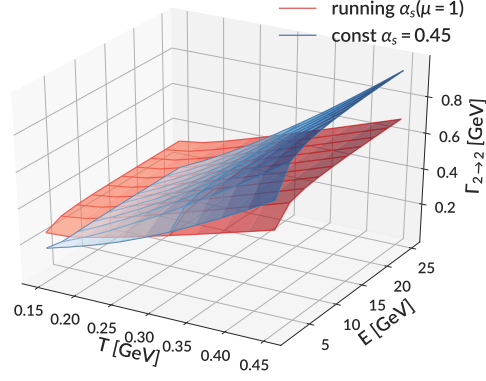


Figure 3.7: 3D projection of the total scattering rate $\Gamma_{12\rightarrow 34}$ with respect to heavy quark energy [left], and medium temperature [right].

frame of the cell, and the center of mass frame (CMS) of the scattering partners. While heavy quarks propagate in the QGP medium with respect to the lab frame, the scattering rate $\Gamma(E_1, T)$, however, is calculated in the local rest frame of the fluid cell, where the light parton distribution can be written as a simple Fermi-Direc/Bose-Einstein/Boltzmann distribution. Therefore at each time step one should boost the time step difference Δt (lab frame) into the local rest frame of the cell — $\Delta t_{\text{lab}} \rightarrow \Delta t = \frac{\Delta t_{\text{lab}}}{\gamma}$, where $\gamma = \frac{1}{1-|\beta|^2}$, and the heavy quarks energy momentum should be boosted from the lab frame to the local rest frame $(E_{1,\text{lab}}, \vec{p}_{1,\text{lab}}) \rightarrow (E_1, \vec{p}_1)$. The light quark (E_2, \vec{p}_2) is then sampled from a thermal medium T following a classical Boltzmann distribution $f_2(p_2) = \exp[-p_2/T]$.

Secondly, in practice the cross section σ is calculated in the CMS frame of the two scattering partners, and it is most convenient to sample the final state outgoing particle (E_3, \vec{p}_3) in the CMS frame. In the local rest frame, the CMS has velocity $\vec{v}_{\text{CMS}} = \frac{\vec{p}_1 + \vec{p}_2}{E_1 + E_2}$, the energy momentum of two initial particles in the CMS frame then yields:

$$\begin{aligned}
 E' &= \gamma(E - \vec{v}_{\text{CMS}} \cdot \vec{p}), \\
 \vec{p}' &= p + \gamma_{\text{CMS}} \vec{v}_{\text{CMS}} \left(\frac{\gamma_{\text{CMS}}}{\gamma_{\text{CMS}} + 1} \vec{p} \cdot \vec{v}_{\text{CMS}} - E \right).
 \end{aligned}
 \tag{3.24}$$

where $\gamma_{\text{CMS}} = \frac{1}{\sqrt{1-v_{\text{CMS}}^2}}$ is the Lorentz factor for transforming from the local rest frame of the fluid to the CMS frame. To further simplify the calculation, we can rotate the system by $(p_1^*)^\mu = \mathcal{R}^{\mu\nu}(p'_1)_\nu$ so that $\vec{p}_1^* = (0, 0, p_1^*)$ lies in the z-axis. The required rotation matrix $\mathcal{R}^{\mu\nu}$ is:

$$\mathcal{R}^{\mu\nu} = \begin{pmatrix} 1 & 0 & 0 & 0 \\ 0 & \cos \psi \cos \phi & \cos \psi \sin \phi & -\sin \psi \\ 0 & -\sin \phi & \cos \phi & 0 \\ 0 & \sin \psi \cos \phi & \sin \psi \sin \phi & \cos \psi \end{pmatrix}. \quad (3.25)$$

To sample the final state particles, the Mandelstam variable $t = (p_1^* - p_3^*)^2$ is sampled according to the differential cross section $d\sigma/dt$, from which we can calculate the final state particle energy momentum in the CMS frame. The rotation-boost to the lab frame is performed by an inversion rotation \mathcal{R}^{-1} followed by two reverse boosts (CMS frame to local rest frame of the cell, and the local rest frame to lab frame).

$$\mathcal{R}^{-1} = \begin{pmatrix} 1 & 0 & 0 & 0 \\ 0 & \cos \psi \cos \phi & -\sin \phi & \sin \psi \cos \phi \\ 0 & \cos \psi \sin \phi & \cos \phi & \sin \psi \sin \phi \\ 0 & -\sin \psi & 0 & \cos \psi \end{pmatrix}. \quad (3.26)$$

$$\begin{aligned} E &= \gamma(E' + \vec{v}_{\text{CMS}} \cdot \vec{p}'), \\ \vec{p} &= \vec{p}' + \gamma \vec{v}_{\text{CMS}} \left(\frac{\gamma}{\gamma + 1} \vec{p}' \cdot \vec{v}_{\text{CMS}} + E' \right). \end{aligned} \quad (3.27)$$

To summarize, Algorithm 2 illustrates the propagation of heavy quarks in the medium

following linearized Boltzmann dynamics:

Algorithm 2: Boltzmann dynamics

Input: 1. An ensemble of heavy quarks (\vec{x}, \vec{p}) ; 2. the medium evolution profile

$$(T, \vec{\beta})$$

Output: An ensemble of final state heavy quarks (\vec{x}, \vec{p}) propagate through the medium, where the surrounding temperature $T > T_c$.

$$t = t_0;$$

foreach heavy quark (\vec{x}, \vec{p}) **do**

while $T(t, \vec{x}) > T_c$ **do**

 Interpolate temperature T and flow velocity $u^\mu = (\gamma, \gamma \cdot \vec{\beta})$ of the local cell at position $(t, \vec{x}) = (\tau, x, y, \eta)$;

 Boost heavy quark p to the local rest frame of the cell p_1 ;

 Compute the collision probability P for time period Δt according to Eqn. 3.23 ;

 Generate random number $x \in [0, 1)$;

if $x < P$ **then**

 Choose a scattering channel and sample the scattering partner p_2 ;

 Boost and rotate heavy quark and light parton to the center of mass frame of the scattering ;

 Sample new final state outgoing particles with momentum p_3 ;

 Reverse rotation and boost from local rest frame to lab frame $p_3 \rightarrow p'$;

 Update the heavy quark momentum with p' ;

end

$$t = t + \Delta t ;$$

 Propagate heavy quark to time t , update position \vec{x} .

end

end

Static medium evolution

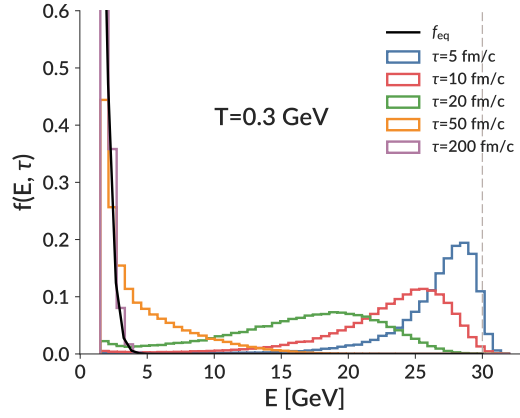


Figure 3.8: Evolution of energy distribution for charm quarks evolve in a static medium (constant temperature $T = 0.3$ GeV). Starting from initial energy as $E_0 = 30$ GeV, charm quarks lose energy and reach thermal equilibrium (black line) at sufficient time.

Figure 3.8 shows the evolution of the charm quark ($M = 1.3$ GeV) distribution starting from an initial energy of $E_0 = 30$ GeV while propagating in an infinite static medium with a constant temperature $T = 0.3$ GeV. With sufficient time (e.g $\tau = 200$ fm/c), the distribution of charm quarks reaches equilibrium (plotted in black solid line).

3.2.4 Transport coefficients

One of the goals of the relativistic heavy-ion program in the next 5-10 years is: “the quantitative determination of the transport coefficients in the Quark Gluon Plasma, such as the temperature-dependent shear-viscosity to entropy-density ratio $\eta/s(T)$, and the energy loss transport coefficients \hat{e} and \hat{q} ” [96]. The reduction of the interaction within the QGP medium to a few transport coefficients has multiple advantages. On one side, for different approaches that model the interaction between quarks, gluons and the medium, the transport coefficients provide an opportunity for comparison among various approaches which take different assumptions to describe the in-medium interactions. On the other

side, it allows for a constraint of the value and functional form of the interaction strength by comparing the theoretical calculation with the experimental data.

In a scattering picture, the average of a quantity X in a medium at temperature T can be computed using the scattering cross sections:

$$\langle X \rangle \equiv \int \frac{d^3 p_2}{(2\pi)^3} f_2(E_2, T) \Theta(s \geq 2m^2) \frac{2s}{2E_1 2E_2} \sigma(s, T)_{12 \rightarrow 34} \cdot X. \quad (3.28)$$

In particular, we have the scattering rate $\Gamma \equiv \langle 1 \rangle$.

The energy loss rate \hat{e} is defined as the average of energy loss per unit time $\hat{e} = \frac{d}{dt} \langle E - E_3 \rangle$. Similarly, the momentum broadening rate (momentum transport coefficient) \hat{q} is defined as:

$$\hat{q} = \langle \vec{p}_3 - \vec{p}_1 \cdot \vec{p}_3 / |p_1| \rangle. \quad (3.29)$$

For a heavy quark moving in z direction, the momentum transport coefficient \hat{q} can be decomposed into the transverse and longitudinal components⁴:

$$\begin{aligned} \kappa_T &= \frac{1}{2} \frac{d}{dt} \langle (\Delta p_x)^2 + (\Delta p_y)^2 \rangle, \\ \kappa_L &= \frac{d}{dt} \langle (\Delta p_z)^2 \rangle. \end{aligned}$$

In addition, the drag coefficient, which is related to the momentum change in z direction can be defined as:

$$\eta_D = -\frac{1}{p} \frac{d}{dt} \langle p_z \rangle. \quad (3.30)$$

Figure 3.9 shows the heavy quark transport coefficients ($\eta_D, \kappa_L, \kappa_T$) with respect to heavy quark energy at different temperature [left] and with respect to temperature [right] at different energies. The coupling constant is chosen as the running one with $\alpha_s(\mu = 1)$.

⁴It is common to express the momentum transport coefficients as κ_t, κ_L , where $\kappa_T = \frac{1}{2} \hat{q}_\perp$ as the momentum variance in the transverse direction, and $\kappa_L = \hat{q}_\parallel$ as the momentum variance in longitudinal direction.

As shown in the figure, the drag coefficient η_D has a positive temperature dependence while negative momentum dependence. The longitudinal momentum transport coefficient κ_L increases almost linearly with increasing momentum, while the transverse momentum transport coefficients κ_T saturates at higher momenta.

Large-angle scattering

For heavy quark scattering with light quarks, only t channel survives. The differential cross section Eqn. 3.16 can be rewritten as:

$$\frac{d\sigma}{dt} = \frac{128}{9} \frac{\pi\alpha_s^2}{16(s-M^2)^2} \left(\frac{(s-M^2)^2}{t^2} + \frac{s}{t} + \frac{1}{2} \right). \quad (3.31)$$

In the large-angle scattering limit, where the momentum transfer $t \Rightarrow (gT)^2$, one could estimate the transport coefficients as:

$$\begin{aligned} \frac{d\sigma}{dt} &\propto \frac{\alpha_s^2}{t^2}, \\ \kappa_T &\propto \int p_2^2 dp_2 e^{-p_2/T} \frac{s}{E_1 E_2} dt \frac{\alpha_s^2}{t^2} \cdot t \\ &\propto T^3 \alpha_s^2 \log t|_{m_D^2}^s, \end{aligned} \quad (3.32)$$

With $s = 2E_1 E_2 (1 + \cos_{12}) \sim 6E_1 T$, we can obtain the momentum diffusion coefficient as:

$$\kappa_T \propto T^3 \alpha_s^2 \log \left(\frac{E_1 T}{m_D^2} \right). \quad (3.33)$$

Soft diffusion

Consider a heavy quark with $M \gg T$ propagates in the QGP medium and interacts with a thermal parton $E_2 \sim T$, the typical momentum transfer is $q \sim T$ and it takes a large number of collisions $n > M/q$ to significantly change the heavy quark momentum. It is

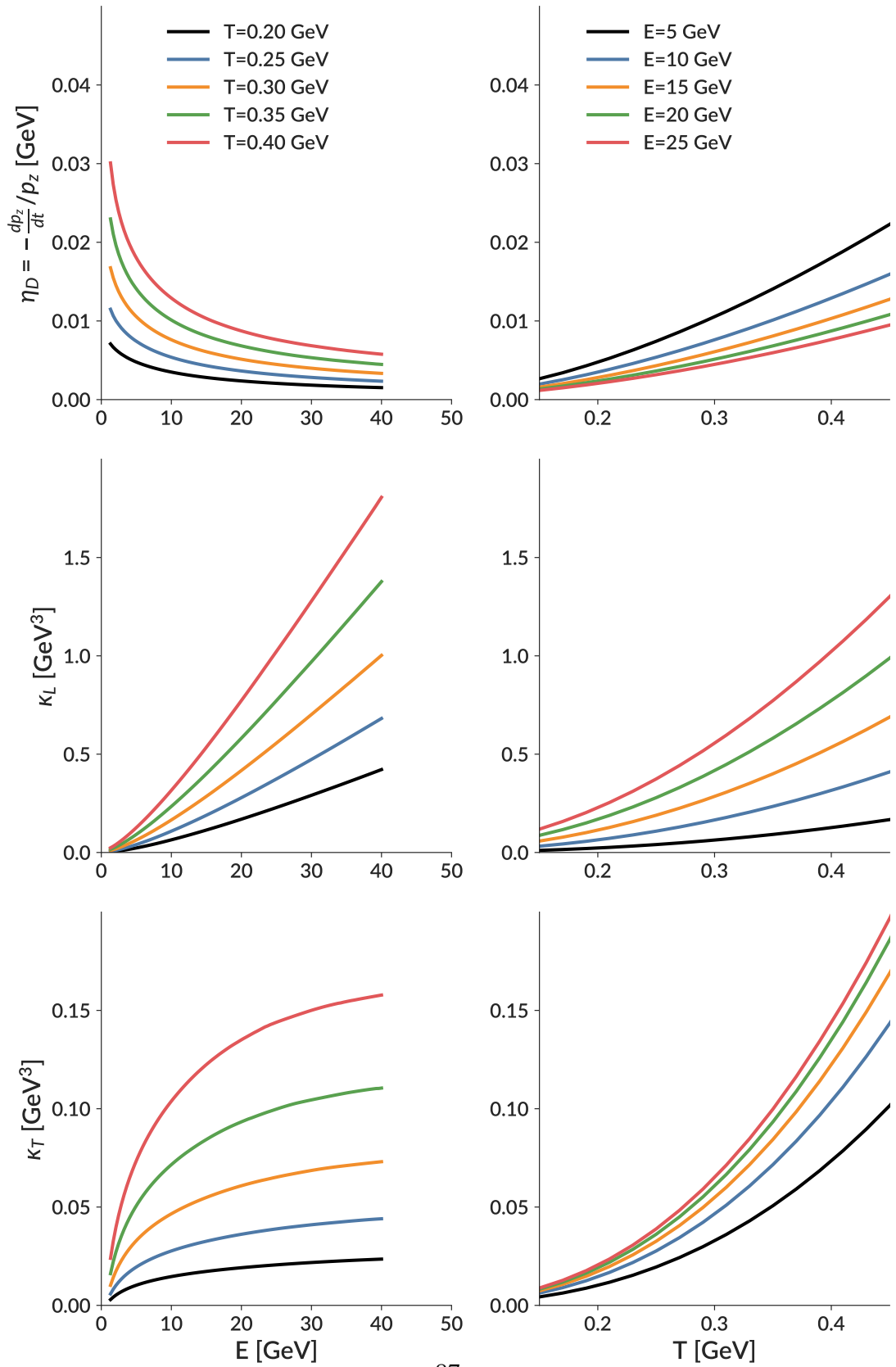


Figure 3.9: Transport coefficients $\eta_D, \kappa_L, \kappa_T$ calculated from elastic $2 \rightarrow 2$ scatterings, with fixed coupling constant $\alpha_s(\mu = 1)$. **[Left]** energy dependence; **[Right]** temperature dependence.

reasonable to assume that heavy quarks interact with the medium by experiencing multiple uncorrelated momentum kicks, i.e. diffusion process. To calculate these small momentum transfer processes, one can use a re-summation scheme known as the Hard Thermal Loop (HTL) effective theory [97, 98], where the momentum exchange between heavy quarks and the medium happens through a soft gauge-boson — gluon. It has shown that [99] at leading order, the HTL corrections can be reduced to a simple Debye screening $1/Q^2 = 1/q^2 \rightarrow 1/(q^2 + m_D^2)$. Summing over color, spin of the incoming thermal partons, and all the quantum numbers of the final state particles, the matrix element squared can be written as [100]:

$$\begin{aligned} |\mathcal{M}_{Qq \rightarrow Qq}|^2 &= \frac{C_Q \alpha_s^2}{4\pi} 16M^2 E_2^2 (1 + \cos \theta_{24}) \left(\frac{1}{q^2 + m_D^2} \right)^2, \\ |\mathcal{M}_{Qq \rightarrow Qq}|^2 &= \frac{N_c C_Q \alpha_s^2}{4\pi} 16M^2 E_2^2 (1 + \cos \theta_{24}) \left(\frac{1}{q^2 + m_D^2} \right)^2, \end{aligned} \quad (3.34)$$

C_Q denotes the color Casimir of heavy quark and an extra factor of 2 for quark to account for the anti-quarks.

The total momentum diffusion coefficient then equals to [100]:

$$3\kappa = \frac{C_H g^4 T^3}{6\pi} \left[N_c \left(\log \frac{2T}{m_D} + \frac{1}{2} - \gamma_E + \frac{\xi'(2)}{\xi(2)} \right) + \frac{N_f}{2} \left(\log \frac{4T}{m_D} + \frac{1}{2} - \gamma_E + \frac{\xi'(2)}{\xi} \right) \right]. \quad (3.35)$$

3.3 Langevin Dynamics

3.3.1 From Boltzmann to Fokker-Planck

With the assumption that the momentum transfer during heavy quark - light parton interaction is small ($\mathbf{k} \ll \mathbf{p}$), one can Taylor expand the right hand side of Eqn. 3.2 with respect

to \mathbf{k} :

$$\omega(\mathbf{p} + \mathbf{k})f_Q(\mathbf{p} + \mathbf{k}) \approx \omega(\mathbf{p})f_Q(\mathbf{p}) + k_i \frac{\partial}{\partial p_i} [\omega(\mathbf{p})f_Q(\mathbf{p})] + \frac{1}{2} k_i k_j \frac{\partial^2}{\partial p_i \partial p_j} [\omega(\mathbf{p}, \mathbf{k})f_Q(\mathbf{p})]. \quad (3.36)$$

The Boltzmann equation 3.1 can then reduced to the Fokker-Planck equation:

$$\frac{\partial}{\partial t} f_Q(t, \mathbf{p}) = \frac{\partial}{\partial p_i} \{A_i(\mathbf{p})f_Q(t, \mathbf{p}) + \frac{\partial}{\partial p_j} [B_{ij}(\mathbf{p})f_Q(t, \mathbf{p})]\}, \quad (3.37)$$

where we define the drag and diffusion terms as:

$$A_i(\mathbf{p}) = \int d^3 k \omega(\mathbf{p}, \mathbf{k}) k_i = \langle p - p' \rangle_i \quad (3.38)$$

$$B_{ij}(\mathbf{p}) = \frac{1}{2} \int d^3 k \omega(\mathbf{p}, \mathbf{k}) k_i k_j = \frac{1}{2} \langle (p - p')_i (p - p')_j \rangle \quad (3.39)$$

$\langle X \rangle$ stands for integration of X in phase space, whose functional form is defined in Eqn. 3.28.

We can further simplify the equation considering the rotational symmetry in the local rest frame of the cell, in which case the direction of A_i and B_{ij} only depends on \mathbf{p} :

$$A_i(\mathbf{p}) = A(\mathbf{p})p_i, \\ B_{ij}(\mathbf{p}) = B_0(\mathbf{p})P_{ij}^{\parallel}(\mathbf{p}) + B_1(\mathbf{p})P_{ij}^{\perp}(\mathbf{p}),$$

where the projection operators in the transverse and longitudinal directions are defined as:

$$P_{ij}^{\parallel}(\mathbf{p}) \equiv \frac{p_j p_j}{p^2}, \\ P_{ij}^{\perp}(\mathbf{p}) \equiv \delta_{ij} - \frac{p_i p_j}{p^2}.$$

and satisfy the relations:

$$P_{ij}^\perp \equiv \delta_{ij} - \frac{p_i p_j}{p^2}, P_{ij}^{\parallel} \equiv \frac{p_i p_j}{p^2},$$

$$P_{ij}^{\parallel} P_{ij}^{\parallel} = 1, P_{ij}^\perp P_{ij}^\perp = 2, P_{ij}^{\parallel} P_{ij}^\perp = 0.$$

3.3.2 Langevin Equation: stochastic realization of the Fokker-Planck equation

The Fokker-Planck equation describes the time evolution of the phase space distribution $f_Q(t, \mathbf{p})$ with interactions encoded as drag and diffusion coefficients. It is the exact equivalent of the Langevin equation when the noise term in the latter is Gaussian white noise. The Langevin equation describes the motion of a Brownian particle that experiences consecutive kicks while propagating in a medium and reads:

$$\begin{aligned} \frac{dx_i}{dt} &= \frac{p_i}{E}, \\ \frac{dp_i}{dt} &= -\eta_D p_i + \xi_i(t). \end{aligned} \tag{3.40}$$

Here η_D is the momentum drag coefficient, and $\xi_i(t)$ describes the uncorrelated random momentum kicks (Gaussian white noise) which satisfies:

$$\begin{aligned} \langle \xi_i(t) \rangle &= 0, \\ \langle \xi_i(t) \xi_j(t') \rangle &= \left(\kappa_L \frac{p_i p_j}{p^2} + \kappa_T \left(\delta_{ij} - \frac{p_i p_j}{p^2} \right) \right) \delta(t - t'), \end{aligned}$$

Therefore $\eta_D p$ is the momentum loss per unit time, κ_L, κ_T are the variance of the longitudinal and transverse momentum transfer per unit time.

One way to show the equivalence between the Fokker-Planck and the Langevin equa-

tion is to covert the Langevin equation to a path integral expression and recognize the Fokker-Planck equation as an Euclidean Schrodinger equation, which also has a path integral representation. Another way is first to derive the equation of motion for the probability distribution $\rho(\mathbf{x}, \mathbf{p}, t)$ and find the Brownian particles in the interval $(x, x + dx), (p, p + dp)$ at time t for one realization of the random kick $\xi(t)$, then average $\rho(\mathbf{x}, \mathbf{p}, t)$ over many realization of the random force. A detailed deviation can be found in Appendix A.0.4.

While discretizing the time step and realizing the Langevin equation, it remains ambiguous at which momentum the drag and random noise η_D, ξ_i are evaluated. Therefore we can define a general momentum evaluation form:

$$\xi_{ij} = \xi(\mathbf{p} + Cd\mathbf{p}), \quad (3.41)$$

with $C \in [0, 1]$. For The pre-point/Ito updating scenario, $C = 0, \xi_i = \xi(\mathbf{p})$, and the momentum update is evaluated as:

$$p_i^{t+\Delta t} - p_i^t = A_i^{\text{ito}}(p_i^t)\Delta t + \xi_i(p_i^t)\Delta t, \quad (3.42)$$

with the coefficients:

$$\begin{aligned} A_i^{\text{ito}}(\mathbf{p}) &\equiv -\eta_D(p)p^i, \\ B^{ij}(\mathbf{p}) &\equiv \kappa_L(p)\frac{p_i p_j}{p^2} + \kappa_T(p)(\delta_{ij} - \frac{p_i p_j}{p^2}). \end{aligned}$$

The realization of the Fokker-Planck equation in the pre-point scenario takes the form:

$$\frac{\partial f_Q(t, \mathbf{p})}{\partial t} + \frac{\partial}{\partial p_i} \left(A_i^{\text{ito}}(\mathbf{p}) f_Q(t, \mathbf{p}) \right) - \frac{1}{2} \frac{\partial^2}{\partial p_i \partial p_j} (B_{ij}(\mathbf{p}) f_Q(t, \mathbf{p})) = 0 \quad (3.43)$$

The other choice of the discretization which has $C > 0$, ($C = 1/2$ refers to the mid-

point/Stratonovich discretization, $C = 1$ refers to the post-point/Hanggi-Klimontovich), the momentum update is evaluated as:

$$p_i^{t+\Delta t} - p_i^t = A_i^{\text{other}}(\bar{p}_i)\Delta t + \xi_i(\bar{p}_i)\Delta t, \quad (3.44)$$

where $\bar{\mathbf{p}} = (1 - C)\mathbf{p}^{t+\Delta t} + C\mathbf{p}^t$, with the coefficients:

$$\begin{aligned} A_i^{\text{other}}(\mathbf{p}) &\equiv -\eta_D(p)p^i - C\frac{\partial B_{ij}(\mathbf{p})}{\partial p_j}, \\ B^{ij}(\mathbf{p}) &\equiv \kappa_L(p)\frac{p_i p_j}{p^2} + \kappa_T(p)(\delta_{ij} - \frac{p_i p_j}{p^2}). \end{aligned} \quad (3.45)$$

The corresponding Fokker-Planck equation takes the form:

$$\frac{\partial f_Q(t, \mathbf{p})}{\partial t} + \frac{\partial}{\partial p_i} \left(A_i^{\text{other}}(\mathbf{p}) f_Q(t, \mathbf{p}) \right) - \frac{1}{2} \frac{\partial}{\partial p_i} \left(B_{ij}(\mathbf{p}) \frac{\partial}{\partial p_j} f_Q(t, \mathbf{p}) \right) = 0. \quad (3.46)$$

3.3.3 Einstein relationship and transport coefficients

In an infinite medium in thermal equilibrium, the particle distribution after evolving for a sufficient amount of time should reach thermal equilibrium — $f(\mathbf{p}, t \rightarrow \infty) \sim e^{-E/T}$, where T is the temperature of the medium. Applying this equilibrium distribution to the Fokker-Planck equation, and with the relation:

$$\begin{aligned} \frac{\partial B_{ij}}{\partial p_j} &= \frac{\partial}{\partial p_j} [B^{//} \hat{p}_i \hat{p}_j + B^\perp (\delta_{ij} - \hat{p}_i \hat{p}_j)] = \frac{\partial}{\partial p^2} B^{//} \cdot 2p_i + \frac{B^{//} - B^\perp}{dp^2} \cdot 2p_i, \\ \frac{\partial}{\partial p_j} (B_{ij} \cdot f) &= \left(\frac{\partial B^{//}}{\partial p^2} \cdot 2p_i + \frac{B^{//} - B^\perp}{p^2} \cdot 2p_i - B^{//} \frac{p_i}{ET} \right) f, \end{aligned} \quad (3.47)$$

we obtain the following relationship between the drag and diffusion coefficients:

$$A - \frac{B^{//}}{2ET} + \frac{\partial B^{//}}{\partial p^2} + \frac{B^{//} - B^\perp}{p^2} = 0. \quad (3.48)$$

It is referred to as the Einstein relationship, also known as fluctuation dissipation relation. It is the criterion for particles that experience interaction with the medium to reach thermal equilibrium in the infinite time. This relation, in terms of η , κ_L , κ_T can be expressed as

$$\begin{aligned} C = 0 : \eta_D &= \frac{\kappa_L}{2ET} - \frac{\kappa_L - \kappa_T}{p^2} - \frac{\partial \kappa_L}{\partial p^2}, \\ C = 1 : \eta_D &= \frac{\kappa_L}{2ET} - \frac{(\sqrt{\kappa_L} - \sqrt{\kappa_T})^2}{p^2}. \end{aligned} \quad (3.49)$$

In addition to the drag coefficient η_D and momentum transfer coefficient κ_L, κ_T , the spatial diffusion coefficient is also commonly used to characterize the interaction strength between the heavy quarks and the medium. The spatial diffusion coefficient D_s , can be calculated by initializing a particle at $\mathbf{x}(t = 0)$ and evaluating the variance of its position at a later time $\mathbf{x}(t)$:

$$\langle x_i(t)x_j(t) \rangle = 2D_s t \delta_{ij}, \quad (3.50)$$

Given

$$\begin{aligned} x_i(t) &= \int_0^t dt' \frac{p_i(t')}{M}, \\ p_i(t) &= \int_{-\infty}^t dt' e^{\eta_D(t'-t)} \xi_i(t'), \end{aligned} \quad (3.51)$$

where the first equation is the update for heavy quark position, and the second equation is solution for the differential equation 3.40, we have

$$\begin{aligned} \langle x_i(t)x_j(t) \rangle &= \int_0^t dt_1 \int_0^t dt_2 \frac{1}{M^2} \langle p_i(t_1)p_j(t_2) \rangle \\ &= \frac{\kappa_{ii}}{M^2 \eta_D^2} \left[t - \frac{1}{\eta_D} (1 - e^{-\eta_D t}) \right]. \end{aligned} \quad (3.52)$$

Taking the large t limit, we obtain the spatial diffusion coefficient:

$$D_s = \frac{\kappa_T}{2M^2 \eta_D^2}, \quad (3.53)$$

for a particle with momentum $\mathbf{p} = 0$, $\eta_D(\mathbf{p} = 0) = \frac{\kappa_T}{2MT}$, therefore the spatial diffusion coefficient is related to the momentum transfer coefficient as:

$$D_s(\mathbf{p} = 0) = \frac{T^2}{\kappa_T}. \quad (3.54)$$

3.3.4 Monte Carlo implementation

In the Monte Carlo implementation of the transport coefficient based Langevin framework, the inputs are the initial ensemble of heavy quarks, the medium information, as well as the external values for the transport coefficients. During the propagation of the heavy quarks

through the medium, they constantly experience drag and thermal forces.

Algorithm 3: Langevin dynamics realized with two-step post-point update

Input: 1. An ensemble of heavy quarks (\vec{x}, \vec{p}) ; 2. the medium evolution profile $(T, \vec{\beta})$; 3. the interaction strength between heavy quarks and the medium $\eta_D, \kappa_L, \kappa_T$

Output: An ensemble of final state heavy quarks (\vec{x}, \vec{p}) that propagated through the medium, where the surrounding temperature $T < T_c$.

$t = t_0$;

foreach heavy quark (\vec{x}, \vec{p}) **do**

while $T(t, \vec{x}) > T_c$ **do**

 Interpolate temperature T and flow velocity $\vec{\beta}$ of the local cell at position $(t, \vec{x}) = (\tau, x, y, \eta)$;

 Boost heavy quark p to the local rest frame of the cell p_1 ;

 Rotate the heavy quarks to align the momentum in z direction

$\mathbf{p} = (0, 0, p_z)$;

repeat

 Interpolate/compute the drag and momentum transfer coefficient

$\eta_D(\mathbf{p}, T), \kappa_L(\mathbf{p}, T), \kappa_T(\mathbf{p}, T)$;

 Generate the thermal force with an Gaussain white noise distribution ρ ;

 Update the momentum $\mathbf{p} = (0, 0, p_z)$ with the drag and thermal random forces to a temporal momentum as

$\mathbf{p} = (\sqrt{\kappa_T \Delta t} \rho_x, \sqrt{\kappa_T \Delta t} \rho_y, p_z \cdot (1 - \eta_D \Delta t) + \sqrt{\kappa_L \Delta t} \rho_z)$

until 2 iterations;

$t = t + \Delta t$;

 Propagate heavy quark to time t , update position \vec{x} .

end

end

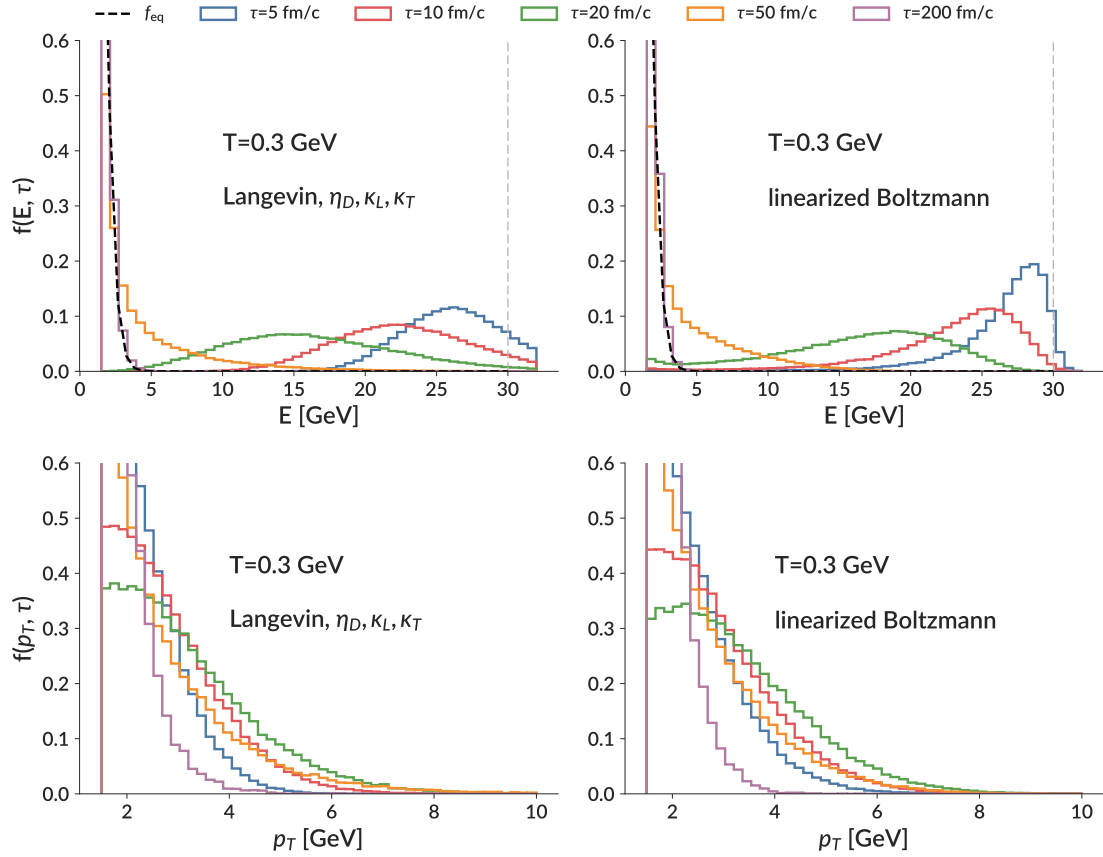


Figure 3.10: Comparison between the charm quark distributions following the Langevin dynamics [left] and the linearized Boltzmann dynamics [right]. The upper panels are the energy distribution while the lower panel are the transverse momentum distribution.

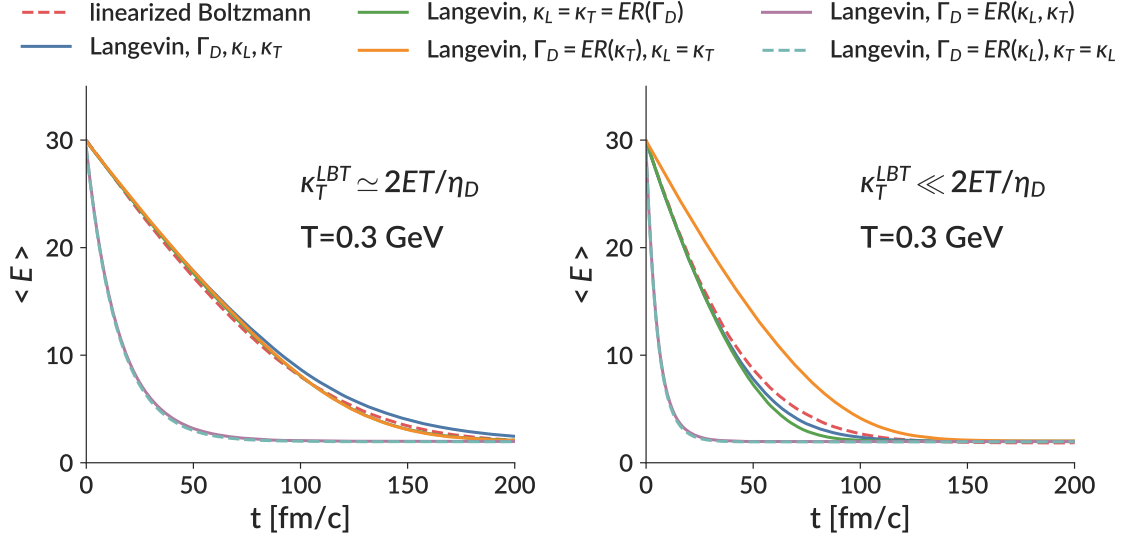


Figure 3.11: Comparison between different implementation of Einstein relationship in an infinite static medium with temperature $T = 0.3$ GeV. The charm quarks are initialized with the same momentum as $\vec{p} = (0, 0, 30)$ GeV and propagate in the medium for 200 fm/c.

We can use the drag and momentum transport coefficients calculated from perturbative QCD in Section. 3.2.4 to characterize the interaction strength between heavy quarks and the medium. Starting from the same initial energy $E_0 = 30$ GeV, an ensemble of charm quarks propagates in an infinite QGP medium (constant temperature $T = 0.3$ GeV) and gradually loses energy. Figure. 3.10 shows the evolution of the energy distribution for heavy quarks following a Langevin dynamics on the left panel and the evolution of energy distribution following a linearized Boltzmann dynamics on the right panel. One can see that: following the Langevin dynamics, charm quark distribution is driven to the final state more rapidly than the one following the linearized Boltzmann dynamics. For the transverse momentum distribution on the lower panel, the two are comparable with each other though small differences can be found.

When heavy quarks propagate in the medium following Boltzmann dynamics, the H-theorem guarantees that the system approaches equilibrium after sufficient enough time. However, directly feeding the drag and momentum transport coefficients from a pQCD

calculation to a Langevin calculation does not fulfill the equilibrium requirements. One has to apply the Einstein relationship between the transport coefficients $\eta_D, \kappa_L, \kappa_T$ to ensure the proper equilibrium state. We are therefore facing an ambiguity when imposing the Einstein relationship, as only two(one) variables out of three are required by Eqn. 3.49. Figure 3.11 compares the results from different implementation of the Einstein relationship in a static medium. The charm quarks, the same as before, are initialized with an identical initial energy $E_0 = 30$ GeV and then propagate in an infinite static medium for 200 fm/c. As shown in the left panel of Fig. 3.11, which compares the evolution of the averaged energy for different implementations of the Einstein relationship. Without using the longitudinal momentum transport coefficient κ_L in the relationship (namely the purple and cyan dashed lines), the heavy quarks lose energy in a similar fashion following either Boltzmann and Langevin dynamics.

We should note that the coincidence that the implementation of $\eta_D = ER(\kappa_T), \kappa_T = \kappa_L = ER(\eta_D)$ is similar to the linearized Boltzmann result is, as a matter of fact, model-dependent. In the leading-order pQCD calculation, where the t -channel is the main contribution to the cross section, the relationship between the drag η_D and the transverse momentum coefficients κ_T is approximately close to the Einstein relationship $\kappa_T \approx 2ET\eta_D$, which results in the overlap between the red dashed curve (linearized Boltzmann evolution) and the green curve (Langevin evolution). However, considering higher-order contributions and different regulators, such a relationship is not guaranteed. The right panel of Fig. 3.11 shows an extreme scenario, where I only include the s -channel elastic scattering — just for the purpose of demonstration — the average energy approach to equilibrium shows significant deviation between the $\eta_D = ER(\kappa_T)$ and $\kappa_T = ER(\eta_D)$ implementations.

Figure 3.12 compares the evolution of the energy distribution for charm quarks with or without the implementation of the Einstein relationship propagating in a static medium (constant temperature $T = 0.3$ GeV) for 200 fm/c. One can see that even though the evo-

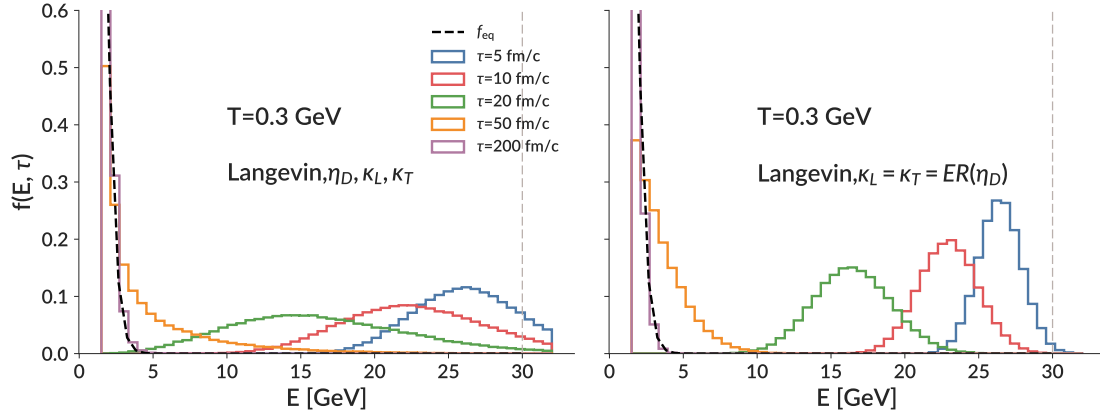


Figure 3.12: Comparison between the charm quark energy distribution without [left] or with [right] the implementation of the Einstein relationship propagating in a static medium with constant temperature $T = 0.3$ GeV. Heavy quarks are initialized with an identical initial energy $\vec{p} = (0, 0, 30)$ GeV and propagate in the medium for 200 fm/c.

lution of the average energy is similar to each other (blue line and green line in Fig. 3.11), the one without the Einstein relationship has a broader distribution than the one with the Einstein relationship. Both show a Gaussian shape but with different width. It implies that a comparison with experimental data, using a differential observable could provide some insight into the intrinsic dynamics of thermalization inside the plasma.

3.4 Improved Langevin: Langevin with additional radiative energy loss

In the previous two sections, I have shown the dynamics of heavy quarks inside a QGP medium while considering only collisional energy loss: elastic scattering with the medium partons in the linearized Boltzmann picture, and diffusion in the Langevin picture. However, for a heavy quark with sufficiently large momentum, a different kind of energy loss — medium-induced gluon radiation — also plays a significant role during its propagation in the medium.

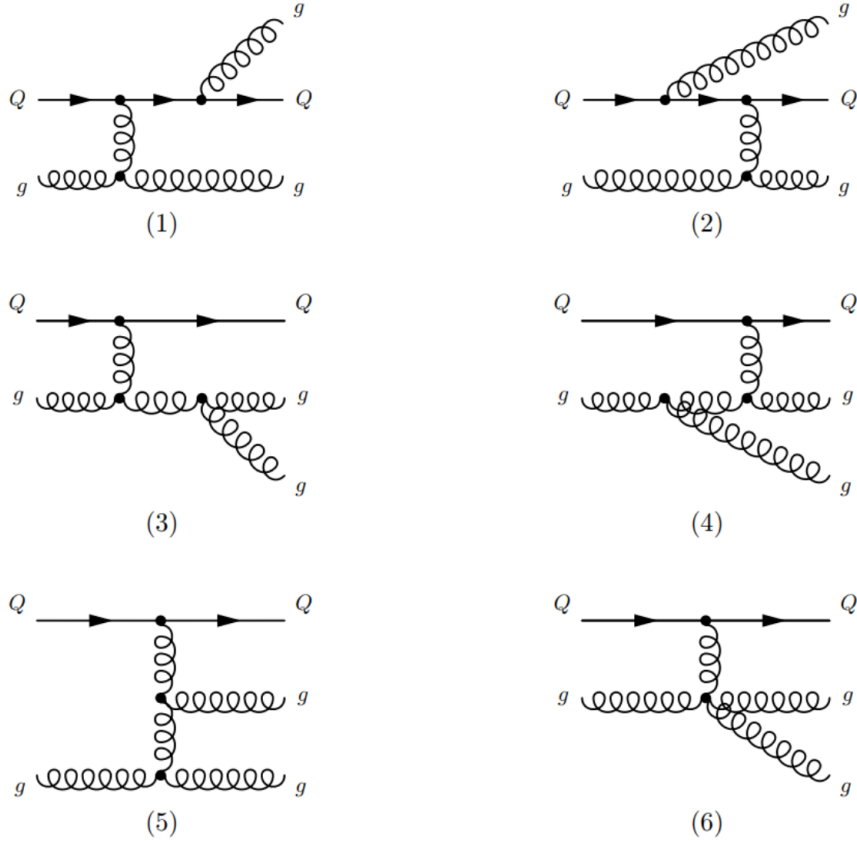


Figure 3.13: Next to leading order pQCD Feynman diagram (t channel) for heavy quark inelastic scattering with gluons $Q + g \rightarrow Q + g + g$ and radiation of a gluon. Time line goes from left to right.

3.4.1 Partonic inelastic scattering

The next order correction for heavy quark radiative energy loss is the $2 \rightarrow 3$ scattering with an additional gluon in the final state:

$$\begin{aligned}
 Q + q &\rightarrow Q + q + g, \\
 Q + g &\rightarrow Q + g + g.
 \end{aligned}
 \tag{3.55}$$

For the process $Q + g \rightarrow Q + g + g$ there are 16 Feynman diagrams due to the self coupling of the gluon. However, the t -channel dominates the total cross section in the approximation of small momentum transfer — where t is small. Therefore while studying the radiative

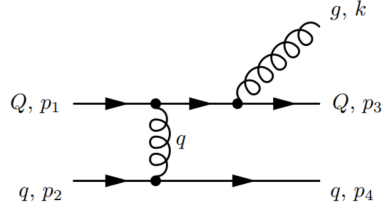


Figure 3.14: Next to leading order pQCD Feynman diagrams for heavy quark inelastically scattering with light quarks $Q + q \rightarrow Q + q + g$. Time line goes from left to right.

energy loss from partonic scattering point of view, I will focus on t channel scattering, whose Feynman diagrams are shown in Fig. 3.13. The process $Qq \rightarrow Qq$ is similar to that of $Qg \rightarrow Qg$ but without the diagram 6 in Fig. 3.13.

We inherit the notation from elastic scattering, where the initial heavy quark and its scattering partner are denoted as (p_1, p_2) , and the final state heavy quark and light parton are denoted as (p_3, p_4) . In addition, the radiated gluon is denoted as k (with gluon energy as ω) while the momentum transfer (i.e. the internal gluon propagator) is denoted as q . A commonly used approximation for the $2 \rightarrow 3$ scattering is the Gunion-Bertsch matrix element derived in 1981 [101] for light quark scattering $qq' \rightarrow qq'g$ and later re-derived for heavy quarks in [102–104]. Here I will only list the matrix element for the gluon radiation process $Qq \rightarrow Qqg$ in the light-cone gauge⁵:

$$|\mathcal{M}_{Qq \rightarrow Qqg}|^2 \simeq \frac{\alpha^2}{4\pi} |\mathcal{M}_{Qq \rightarrow Qq}|^2 (1 - \bar{x})^2 \left[\frac{\mathbf{k}_\perp}{k_\perp^2 + x^2 M^2} + \frac{\mathbf{q}_\perp - \mathbf{k}_\perp}{(\mathbf{q}_\perp - \mathbf{k}_\perp)^2 + x^2 M^2} \right]^2, \quad (3.56)$$

where $\bar{x} = \frac{k_\perp}{\sqrt{s}} e^{|y|}$ is the fraction of the momentum carried away by the radiated gluon. The simplification from the full matrix element to the Gunion-Bertsch matrix element requires two assumptions: high-energy limit; the radiated gluon and momentum transfer are soft:

$$k_\perp \ll \sqrt{s}, q_\perp \ll \sqrt{s}, xq_\perp \ll k_\perp. \quad (3.57)$$

⁵A more detailed derivation can be found in the corresponding reference

If one further assumes that the radiated gluon k is much softer than the transferred momentum ($k_{\perp} \ll q_{\perp}$, which implies $\bar{x} \rightarrow 0$), the Gunion-Bertsch matrix element can be reduced to a gauge invariant form⁶:

$$|\mathcal{M}_{Qq \rightarrow Qqg}|^2 \simeq \frac{12\alpha_s^2}{4\pi} |\mathcal{M}_{Qq \rightarrow Qq}|^2 \left[\frac{\mathbf{k}_{\perp}}{k_{\perp}^2 + x^2 M^2} \right]^2, \quad (3.58)$$

Two effects need extra attention while we investigate the heavy quark radiative energy loss in the QGP medium:

dead cone effect

The dead cone effect [105] refers to the fact that the gluon bremsstrahlung off a heavy quark is suppressed at the angle smaller than the dead cone angle $\theta_D = M/E$. Therefore for heavy quarks with low energy, the collisional energy loss is considered to be the dominant mechanism as the radiative process is suppressed.

The dead cone effect is also present in the Gunion-Bertsch matrix element shown in Eqn. 3.58, as for small angle θ radiation, the momentum of the emitted gluon can be approximated as $k_{\perp} = \omega \sin \theta \simeq \omega \theta$ and $x = \frac{k_{\perp} e^{|y|}}{\sqrt{s}} \simeq \frac{2\omega}{\sqrt{s}} \simeq \frac{2\omega}{2E} \simeq \frac{k_{\perp}}{\theta E}$, Eqn. 3.58 is then simplified as:

$$\begin{aligned} |\mathcal{M}_{Qq \rightarrow Qqg}|^2 &\simeq 12 \frac{\alpha_s^2}{4\pi} |\mathcal{M}_{Qq \rightarrow Qq}|^2 \frac{k_{\perp}^2}{(k_{\perp}^2 + x^2 M^2)^2} \\ &\simeq 12 \frac{\alpha_s^2}{4\pi} |\mathcal{M}_{Qq \rightarrow Qq}|^2 \frac{1}{|k_{\perp}^2|} \frac{1}{(1 + \frac{\theta_D^2}{\theta^2})^2}, \end{aligned} \quad (3.59)$$

where $\theta_D = M/E$ is the dead cone angle, and $\mathcal{D} = (1 + \frac{\theta_D^2}{\theta^2})^{-2} < 1$ is referred as the dead

⁶A matrix element should be gauge invariant if there is no assumption being made. However, using approximation as in Gunion-Bertsch matrix element breaks the gauge invariant, or at least restricts the region of validity. It is shown in Ref. [89] that both the calculation of the matrix elements in Feynman gauge and light cone gauge agree within their approximation, and by comparing with the exact matrix element, the employed approximation are reasonable.

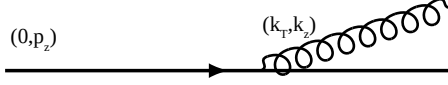


Figure 3.15: Heavy quark radiates a gluon $1 \rightarrow 2$ process.

cone factor, which results in the reduction of the total gluon radiation emitted by the heavy quark.

Laudau-Pomeranchuk-Migdal effect

The Laudau-Pomeranchuk-Migdal (LPM) effect describes another type of suppression of the gluon radiation process. The gluon radiated from a heavy quark scattering with the medium is a quantum process which does not happen instantaneously. According to the principle of uncertainty, the gluon formation time τ_f and its virtual energy ΔE of the radiation process satisfy:

$$\tau_f \Delta E \simeq 1. \quad (3.60)$$

A fast-moving heavy quark in the lab frame emits gluon at small angle when boosted to the lab frame even though the radiation angle is large in the CMS frame. Considering a heavy quark with energy-momentum $p_{\text{init}} = (\sqrt{M^2 + p_z^2}, 0, p_z)$ emits a gluon that has the energy momentum of $(\sqrt{z^2 p_z^2 + k_\perp^2}, k_\perp, z p_z)$, where $z = k_z/p_z$ is the longitudinal fraction of the emitted gluon. The virtuality of this process is:

$$\begin{aligned} \Delta E &= E_{HQ}^{\text{final}} + \omega - E_{HQ}^{\text{initial}} \\ &= \sqrt{(1-x)^2 p_z^2 + k_\perp^2} + M^2 + \sqrt{x^2 p_z^2 + k_\perp^2} - \sqrt{p_\perp^2 + M^2}. \end{aligned}$$

In a soft gluon radiation process $z \ll 1$, for a fast moving heavy quark $p_z \gg M$, the gluon formation time in the lab frame can then be approximated as:

$$\tau_f \simeq \frac{1}{\Delta E} \simeq \frac{2\omega}{k_{\perp}^2 + z^2 M^2}. \quad (3.61)$$

When a heavy quark propagates in the medium, the radiation processes are induced by the medium. If the formation time of the radiated gluon is large compared to the time interval between heavy quark interaction with the medium (a.k.a heavy quark mean free path $\tau_f < \lambda$), an interference effect takes place and suppresses the radiation process.

However, the implementation of the LPM effect in a Monte Carlo scattering picture such as the linearized Boltzmann framework is rather difficult, as in such a scattering picture, all the interactions are point-like, requiring an iterative evaluation of the mean free path λ in space-time. One solution for mimic the LPM effect is to restrict the phase space interval of the radiation process with a coherence factor:

$$\frac{d^3 k}{(2\pi)^2 2k} \rightarrow \frac{d^3 k}{(2\pi)^2 2k} 4 \sin^2 \left(\frac{t - t_0}{2\tau_f} \right), \quad (3.62)$$

where $(t - t_0)$ is time interval since the last gluon emission at time t_0 . With such a coherence factor, the emission of gluon at time $(t - t_0) < \tau_f$ are suppressed.

3.4.2 Multi-scattering radiative energy loss formalism

High energy jet in-medium radiation is one of the most important topics in heavy-ion physics and more sophisticated treatments have been considered in great detail. Four major phenomenological schemes that have been developed and widely used are:

- Higher Twist [106–110]: Higher Twist describes the multiple scattering of a parton as power corrections to the leading twist cross section, where the correc-

tions are enhanced by the medium length L and suppressed by the power of hard scale Q^2 . The underlying concept applies the factorization theorem, which states the hadron production in nuclear collision process is divided into: the non-perturbative parton distribution function, the perturbative partonic scattering cross sections and the non-perturbative fragmentation function. We can therefore formulate the final cross section for producing a hadron h as a convolution of initial nuclear distribution $f_{A/i}(x, Q^2)$, the hard partonic cross section to produce a parton $\sigma^{ij/c}$ and a medium modified fragmentation function for the final hadron $D^{c \rightarrow h}(x, \mu_F^2)$:

$$d\sigma^{A+B \rightarrow h+X} = \sum_{ij} f_{A/i}(x_i, Q^2) f_{B/j}(x_j, Q^2) \otimes d\sigma^{ij \rightarrow c}(x_1, x_2, \alpha_s(\mu^2)) \otimes D^{c \rightarrow h}(x, \mu_F^2), \quad (3.63)$$

The medium modification is encoded into the fragmentation function, which is separated as a medium-dependent additive contribution added to the leading-order vacuum contribution: $D_{\text{med}}^{i \rightarrow h} = D_{\text{vac}}^{i \rightarrow h} + \Delta D_{\text{med}}^{i \rightarrow h}$. The medium-dependent contribution $\Delta D_{\text{med}}^{i \rightarrow h}$ contains twist-4 parton matrix elements and describes the additional scattering of the hard parton with another nucleon inside the nucleus.⁷ The Higher Twist formalism involves one free parameter — the jet transport coefficient \hat{q} — and needs to be fixed by a fitting to experimental measurements.

- Path integral formalism of re-scattering summation on multiple static centers (BDMP5-Z/ASW) [111, 113]: The BDMP5-Z/ASW formalism computes the radiated gluon energy distribution $\omega dI/d\omega$ as a function of the transport coefficient \hat{q} by taking into account of the n static rescattering centers and modifies the gluon radiation energy k_{\perp} . In a study of a finite size medium with length L , the radiative energy loss shows a quadratic path length dependence: $\Delta E_{\text{rad}} \propto L^2$, which is different from collisional energy

⁷In the deep inelastic scattering, the photon-photon scattering can be expanded as a product of particle current operations, which is ordered by the difference of the dimension and the spin, or twist, of the operators.

loss as the latter shows a linear dependence: $\Delta E_{\text{col}} \propto L$. The BDMPS-Z/ASW approach assumes a static medium, which weakens its predictive power in a dynamically evolved QGP medium that is created in heavy-ion collisions. In a Bjorken expansion of the QGP medium [114], where the system is expanding into the longitudinal z -direction and cools down as a function of proper time τ according to the scaling law $\tau^\alpha T^3 = \tau_0^\alpha T_0^3$, the energy loss is found to be six times larger than the one in a static medium.

- Opacity expansion (GLV) [115–119]: The GLV formalism calculates the parton energy loss in a dense deconfined medium consisting of almost static scattering centers which produce a screened Yukawa potential. Different from the BDMPS formalism, which assumes multiple soft scatterings for the hard parton ($N_{sc} \gg 1$), the GLV formalism starts from a single hard radiation off the hard parton ($N_{sc} \sim 1$), and then expands to multiple scatterings via a recursive diagrammatic procedure — “opacity expansion”. By construction, given the single and double scattering combination at order n , one can build the gluon distribution at order $n + 1$ in opacity. It is found that the first-order of opacity is dominating therefore it is enough to assume only a few scatterings. The radiative heavy quark energy loss approaches the incoherent(linear) limit in path length dependence.
- Finite temperature field theory approach (AMY) [120–123]: the AMY formulates a leading-order perturbative QCD hard thermal loop effective field theory to treat the energy loss of a hard parton in a weakly coupled medium. The main difference between AMY and BDMPS-Z/ASW/GLV approaches is that the latter assume the medium as a collections of static scattering centers, while the former one assume the medium consists of light quarks and gluons, forming an equilibrium QCD medium at temperature T . The weak coupling assumption implies the hierarchy $T \gg gT \gg$

g^2T , and the hard parton scattering off other medium constituents experiences a momentum transfer of order $\mathcal{O}(gT)$. These scatterings are split into two parts: a $2 \rightarrow 2$ scattering which is calculated in leading order pQCD and with the HTL self-energy contribution; a medium-induced $1 \rightarrow 2$ ($a \rightarrow bc$) splitting, whose splitting rates $\frac{dP_a(p)}{dt} = \int dk \sum_{b,c} \left[P_b(p+k) \frac{d\Gamma_{ac}^b(p+k,p)}{dkdt} - P_a(p) \frac{d\Gamma_{bc}^a(p,k)}{dkdt} \right]$ are calculated and used to evolve the hard parton distribution.

The four energy loss schemes can be roughly divided into two groups — those that determine the radiative gluon spectrum by the initial parton (GLV/BMSPS-Z/ASW), and those that calculate the change of the final distribution of the hard parton (AMY/HT) energy directly. The differences among those schemes lie in the different assumptions of: the nature of the medium, the virtuality of the energetic parton, and the kinetic approximations of the parton-medium interactions. Further detailed comparisons among those approaches can be found in Ref. [124, 125]. In [124] those schemes are implemented in a uniform medium with fixed length and fixed temperature where the quantitative differences are found due to specific approximations. In addition, all those approaches can be reduced to a version which contains only one free tunable parameter \hat{q}_g , which is the momentum transport coefficient of gluons and can be extracted from a comparison with experimental measurements. In [125] those schemes are implemented with a 3-dimensional hydrodynamic approach, where the hard parton nuclear modification factor R_{AA} is compared with experimental data. Although a quantitative consistency of the momentum transport coefficients \hat{q} is observed, it still differs by a factor of 3, as listed in Tab 3.2. Additional constraints on \hat{q} , such as the reproduction of the azimuthal anisotropy, are required in order to reduce the uncertainty.

Comparison between HT and GB matrix elements

In this thesis work, we adopted the Higher Twist formalism for heavy quark radiative energy loss in the QGP medium. Under the assumption of collinear ($\omega \gg k_T$) and soft

$\hat{q}(\vec{r}, \tau)$ scaled as	ASW \hat{q}_0	HT \hat{q}_0	AMY \hat{q}_0
$T(\vec{r}, \tau)$	10 GeV ² /fm	2.3 GeV ² /fm	4.1 GeV ² /fm
$\epsilon^{3/4}(\vec{r}, \tau)$	18.5 GeV ² /fm	4.5 GeV ² /fm	—
$s(\vec{r}, \tau)$	—	4.3 GeV ² /fm	—

Table 3.2: Value of \hat{q} at $\tau_0 = 0.6$ fm/c in the cell at $\vec{r}=0$ of the 0-5% centrality hydro events, in different energy loss schemes. Also presented is the variation of \hat{q} with different choices of scaling of $\hat{q}(\vec{r}, \tau)$ with different local intensive properties of the medium. $T(\vec{r}, \tau)$ is the temperature, $\epsilon(\vec{r}, \tau)$ is the energy density and $s(\vec{r}, \tau)$ is the entropy density at location (\vec{r}, τ)

($\omega \ll E$) radiation , the medium-induced gluon spectrum can be expressed as:

$$\frac{dN}{dxdk_{\perp}dt} = \frac{2\alpha_s P(x)\hat{q}_g}{\pi k_{\perp}^4} \sin^2\left(\frac{t-t_i}{2\tau_f}\right) \left(\frac{k_{\perp}^2}{k_{\perp}^2 + x^2 M^2}\right)^4, \quad (3.64)$$

where k_{\perp} is the transverse momentum of the emitted gluon. $P(x)$ represents the medium-modified splitting function for a parton radiating a gluon which carries a momentum fraction of x ,

$$P(x) = \frac{(1-x)(2-2x+x^2)}{x}. \quad (3.65)$$

τ_f is the formation time of the radiated gluon and is defined as:

$$\tau_f = \frac{2Ex(1-x)}{(k_{\perp}^2 + x^2 M^2)}. \quad (3.66)$$

The gluon emission spectrum depends on the gluon momentum transport coefficient \hat{q}_g . In our implementation, it is connected to the quark transport coefficient by the color factors as $\hat{q}_g = C_A/C_F \hat{q}$, the later is obtained from elastic scattering. In addition, it also has a time dependence, where $(t-t_i)$ represents the time interval since the last gluon emission. Therefore under this construction, the radiative energy loss of heavy quarks depends only on the momentum transport coefficient \hat{q} .

When integrating for the averaged emitted gluon number, a lower bound $xE \geq \pi T$ is

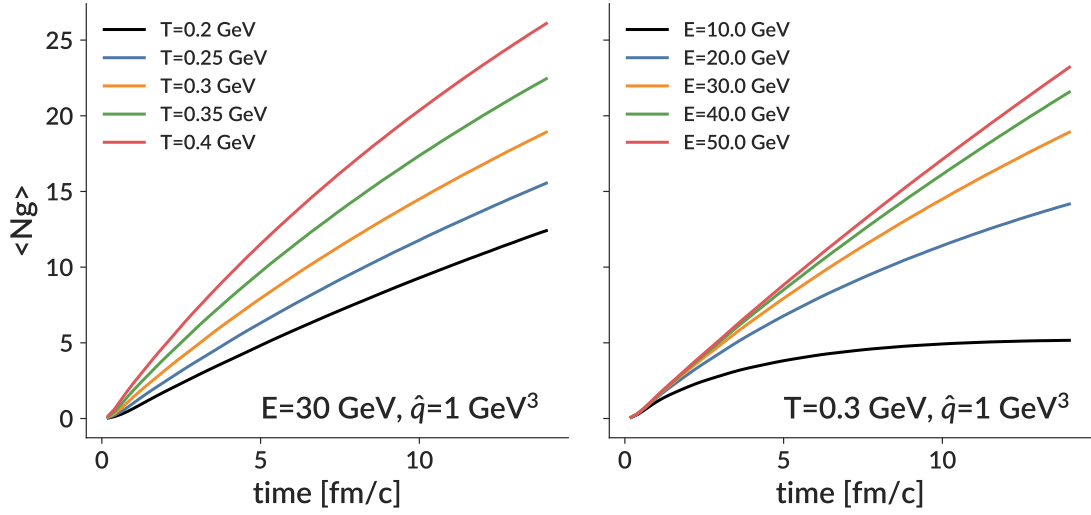


Figure 3.16: Averaged gluon radiation number as a function of time for heavy quark propagating in a static medium. **[Left]:** varying the temperature of the medium; **[Right]:** varying the energy of the heavy quark.

imposed for two reasons: firstly, it avoids the infrared divergence at $x \rightarrow 0$ limit; secondly without the proper reverse process (gluon absorption), heavy quarks will continue to lose energy if no lower limit cut-off is applied. With such a cut-off, the heavy quark distribution in a thermal medium reaches a near-thermal equilibrium distribution, with an effective temperature slightly shifted to a lower value (about 5% in a static medium with a constant temperature of 0.3 GeV) [72].

Figure 3.16 shows the integrated emitted gluon number $\langle N_g \rangle$ as a function of time for different medium temperatures and heavy quark energies. As shown in the figure, the average gluon radiation increases with increasing temperature and momentum, it also shows a positive time dependence with a saturation trend for lower energy heavy quarks.

The Higher Twist formalism shares some similarity with the Gunion-Bertsche formalism when specific assumptions are made. The Gunion-Bertsche assumes that $k \gg q \rightarrow$

$x \simeq 0$ in addition to the soft and collinear approximation, therefore the matrix element is:

$$\begin{aligned}
|\mathcal{M}_{Qq \rightarrow Qqg}|^2 &\simeq \frac{\alpha^2}{4\pi} |\mathcal{M}_{Qq \rightarrow Qq}|^2 (1 - \bar{x})^2 \left[\frac{\mathbf{k}_\perp}{k_\perp^2 + x^2 M^2} + \frac{\mathbf{q}_\perp - \mathbf{k}_\perp}{(\mathbf{q}_\perp - \mathbf{k}_\perp)^2 + x^2 M^2} \right]^2 \\
&\simeq_{x \rightarrow 0} \frac{\alpha^2}{4\pi} |\mathcal{M}_{Qq \rightarrow Qq}|^2 \left[\frac{\mathbf{k}_\perp}{k_\perp^2 + x^2 M^2} + \frac{(\mathbf{q}_\perp - \mathbf{k}_\perp)}{(\mathbf{q}_\perp - \mathbf{k}_\perp)^2} \right]^2 \\
&\simeq_{x \rightarrow 0} \frac{\alpha^2}{4\pi} |\mathcal{M}_{Qq \rightarrow Qq}|^2 \frac{1}{k_\perp^4}.
\end{aligned} \tag{3.67}$$

Note that the dependence on $\frac{1}{k_\perp^4}$, and compare with what is shown in Higher Twist formalism.

3.4.3 Recoil force induced by gluon radiation

In order to incorporate the heavy quark radiative energy loss to a Langevin framework, we introduce a recoil force that results from the heavy quark radiating a gluon and formulate it as the momentum change of the emitted gluon [72]:

$$f_i^{\text{gluon}} = -\frac{dp_i^{\text{gluon}}}{dt}, \tag{3.68}$$

The improved Langevin equation is then updated as:

$$\frac{dp_i}{dt} = -\eta_D p_i + \xi_i(t) + f_i^{\text{gluon}}, \tag{3.69}$$

The number of emitted gluon in a time interval $\langle N_g \rangle$ may not be always smaller than 1, therefore it cannot be treated as the gluon emission probability. We therefore allow multiple gluon emissions to happen in a time interval Δt . It follows a Poisson distribution:

$$P(n) = \frac{\langle N_g \rangle^n}{n!} e^{-\langle N_g \rangle}, \tag{3.70}$$

We can obtain the total probability for the gluon radiation process ($n > 0$) as:

$$P_{\text{rad}} = 1 - e^{-\langle N_g \rangle}. \quad (3.71)$$

The average number of emitted gluons $\langle N_g \rangle$ is first calculated by integration of the spectrum and then tabulated. The probability of gluon emission process is determined by Eqn. 3.71. If the radiation process happens, the number of emitted gluon is sampled according to the Poisson distribution and the momentum of the emitted gluon is sampled according to the gluon spectrum. Algorithm 4 summarizes the gluon emission process for heavy quarks propagating in the medium.

Algorithm 4: Gluon radiation process

Input: Heavy quark energy E , medium temperature T , time interval since last gluon emission $t - t_i$

Output: Emitted gluon momentum if the radiation process happens; otherwise return 0

Interpolate/Calculate the momentum transport coefficient \hat{q} , the average number of emitted gluon $\langle N_g \rangle$;

Calculate the probability for the radiative process P_{rad} according to Eqn. 3.71 ;

Generate a random number $x \in [0, 1)$;

if ($x < P_{\text{rad}}$) **then**

Sample the number of emitted gluons according to the poison distribution Eqn. 3.70 ;

Sample the gluon momentum (ω, k_{\perp}) according to the gluon emission spectrum Eqn. 3.64 using multi-variate rejection sampling.

end

3.5 A full space-time evolution of heavy quarks in heavy-ion collisions

So far I have explained the full space-time evolution heavy quarks in heavy-ion collisions, which is based on a transport model — that describes the heavy quark in-medium propagation, incorporating a relativistic viscous hydrodynamical model — that simulates the evolution of the QGP medium until a switching temperature $T_{\text{switch}} < T_c$. After the QGP system hadronizes into a hadron resonance gas, the hadron-hadron interactions are simulated by UrQMD model.

Three different collision systems at RHIC and the LHC are explored — Au-Au collisions at 200 GeV, Pb-Pb collisions at 2.76 TeV and at 5.02 TeV. In each calculation, 5000 minimum bias events⁸ are generated and run through the event-by-event viscous hydrodynamical model. Each hydro event simulates the soft medium evolution from the formation of the medium until the QGP medium hadronizes into a hadron resonance gas, and the UrQMD model takes over to allow for hadron rescattering until kinetic freezeout. The QGP medium evolution profile (the medium temperature and flow $T(\tau, x, y, \eta), \vec{u}(\tau, x, y, \eta)$) are stored as the background for heavy quark propagation in the QGP phase. For each hydro events, heavy quarks are oversampled — 600,000 heavy quarks are initialized with the position distribution consistent with the corresponding initial entropy density — and evolve until heavy mesons are formed and undergo hadronic rescattering and decaying. The energy and momentum of heavy mesons and light hadrons are collected to calculate the final state observables using the following scheme:

- Minimum bias events are first binned into different centrality classes according to the final state charged hadron multiplicity N_{ch} at mid-rapidity;
- Heavy meson selection is based on the corresponding experimental kinematic cut for

⁸Minimum bias events refer to the unbiased subsample events drawn from the whole population of the collision events from the most central to the most peripheral with equal probabilities.

specific ranges in rapidity, centrality and transverse momentum;

- The nuclear modification factor R_{AA} is calculated by comparing the ratio between the heavy meson spectrum in heavy-ion collisions with the reference heavy meson spectrum in the proton-proton collisions. The reference spectrum is calculated using a heavy quark FONLL distribution followed by a fragmentation process that is performed by PYTHIA. The D -meson yields are compared to experimental measurements in Fig. 2.16;
- The heavy meson elliptic flow is calculated consistent with the experimental method. For example, in Au-Au collisions and Pb-Pb collisions at 2.76 TeV, an event-plane method is used, while for the Pb-Pb collisions at 5.02 TeV, the two-particle cumulant method is used, although little difference has been noticed for the two different methods.

3.5.1 Soft medium observables

The soft matter evolution depends on the free-streaming time, initial renormalization scale, the mapping function from the nuclear parton distribution function to initial entropy density, the shear and bulk viscosity to entropy density ratio in the QGP phase, and the switching temperature from a hydrodynamical description to a microscopic Boltzmann description. All the parameters, either ad hoc artificial parameters that are model-dependent, or physical properties of the QGP medium, are calibrated on experimental measurements of the soft medium observables by an independent Bayesian model-to-data analysis [44].

For the soft matter observables, the charged-particle yield $dN_{ch}/d\eta$, identified-particle yields dN/dy for pion, kaon and proton (π, K, p), identified particle mean p_T and two-particle flow cumulants $v_n\{2\}$ are calculated for different centrality bins. Fig. 3.17 shows the calculated soft medium observables compared to data to demonstrate the ability of the

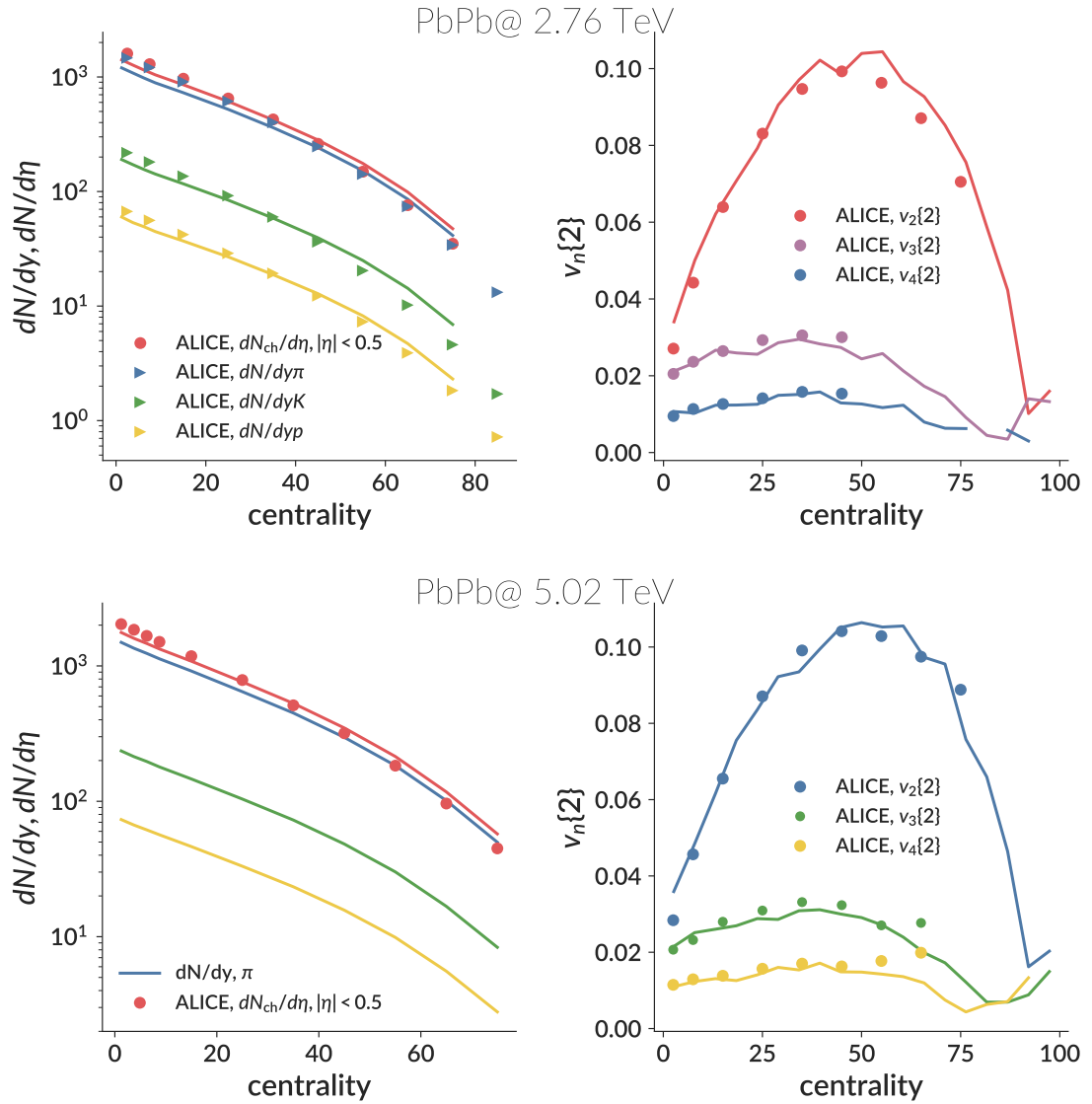


Figure 3.17: Event-by-event viscous hydrodynamical model calculation (color lines) of the soft medium observables for Pb-Pb collisions at 2.76 TeV [**upper**] and 5.02 TeV [**lower**]. All the parameters regarding the soft medium evolution are calibrated to experimental measurements and this results is calculated taking the MAP parameters from Table 5.5 of [57].

model to describe the evolution of the QGP medium.

3.5.2 Heavy flavor observables

Nuclear modification factor R_{AA} and v_2

The two main heavy quark observables are the nuclear modification factor R_{AA} for heavy mesons, which is defined as the particle yield in nucleus-nucleus (AA) collisions divided by the scaled yield in proton-proton (pp) collisions, and the heavy meson elliptic flow, which is defined as the second order harmonics of the momentum azimuthal distribution.

From charm quark to D -meson

In an improved Langevin framework, the interaction between heavy quarks and the medium is implemented as a diffusion process, which is determined by the transport coefficients $\eta_D(E, T)$, $\kappa_L(E, T)$, $\kappa_\perp(E, T)$, $D_s 2\pi T$ etc. They serve as the input for the improved Langevin model, whose values are estimated either from the first principle, or parametrized and later determined from a comparison between the model's calculation and experimental measurements.

For now in this section, I will focus on the former scenario: that is the transport coefficients fed into the improved Langevin framework are calculated via a leading-order pQCD approach, which is explained in Sec. 3.2.4. The temperature and momentum dependence is plotted in Fig. 3.6 and 3.7.

The upper panel of Fig. 3.19 presents a calculation of the mid-rapidity nuclear modification factor R_{AA} as a function of transverse momentum p_T for different centralities for charm quarks (green dashed line), D -meson before the hadronic stage rescattering (solid green line) and D -meson after the hadronic stage rescattering (solid blue line) in Pb-Pb collisions at 5.02 TeV. The lower panel shows the charm quark and D -meson elliptic flow as a

Pb-Pb 5.02 TeV, improved Langevin, $\alpha_s(\mu = 1)$

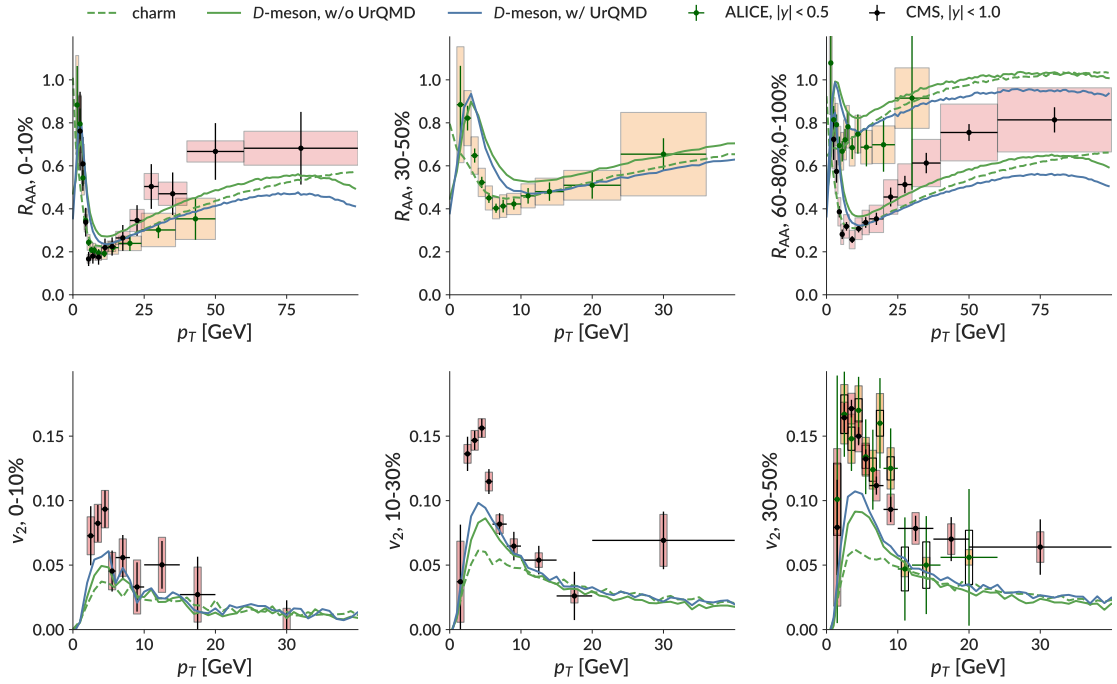


Figure 3.18: [**Upper**]: Charm quark/ D -meson R_{AA} as a function of p_T for different centralities in Pb-Pb collision at $\sqrt{s_{NN}} = 5.02$ TeV; [**Lower**]: Charm quark/ D -meson elliptic flow as a function of p_T for different centralities. The experimental measurements are taken from ALICE [126] and CMS [127].

function of p_T . The renormalization factor μ which determines the running coupling constant scale is chosen as $\mu = 1$. Comparing with experimental measurements (errorbars and boxes), without further tuning for the transport coefficients, the improved Langevin framework is able to quantitatively describe the experimental observables, especially the energy loss related nuclear modification factor R_{AA} . For central collisions (0 – 10%) heavy quarks experience a hotter medium, lose more energy and exhibit a larger suppression. For the elliptic flow v_2 , the calculations from the improved Langevin model also show a general trend of small anisotropy in the most central collisions, and larger anisotropy in mid-central collisions. However, this calculation significantly underestimates the elliptic flow in mid-central collisions.

The comparison between charm quarks (green dashed lines) and the D -meson right after the hadronization (solid green lines) implies that:

- A heavy quark with a light anti-quark, D -meson gains significant anisotropy from the light quark at lower momentum region. It is not achievable from a pure fragmentation hadronization mechanism;
- D -mesons at higher momentum hadronizes from heavy quark fragmentation as no significant increase of the anisotropy;
- Recombination with a light quark results in a peak for the R_{AA} around $p_T \in [2, 5]$ GeV.

Furthermore, comparing the calculation for D -mesons right after hadronization (green solid lines) with D -meson after hadronic interaction (solid blue lines), one can see that:

- The hadronic interaction further increases the anisotropy of D -mesons in the lower momentum region of v_2 ;
- Rescattering with light hadrons only marginally changes the energy of the D -mesons;

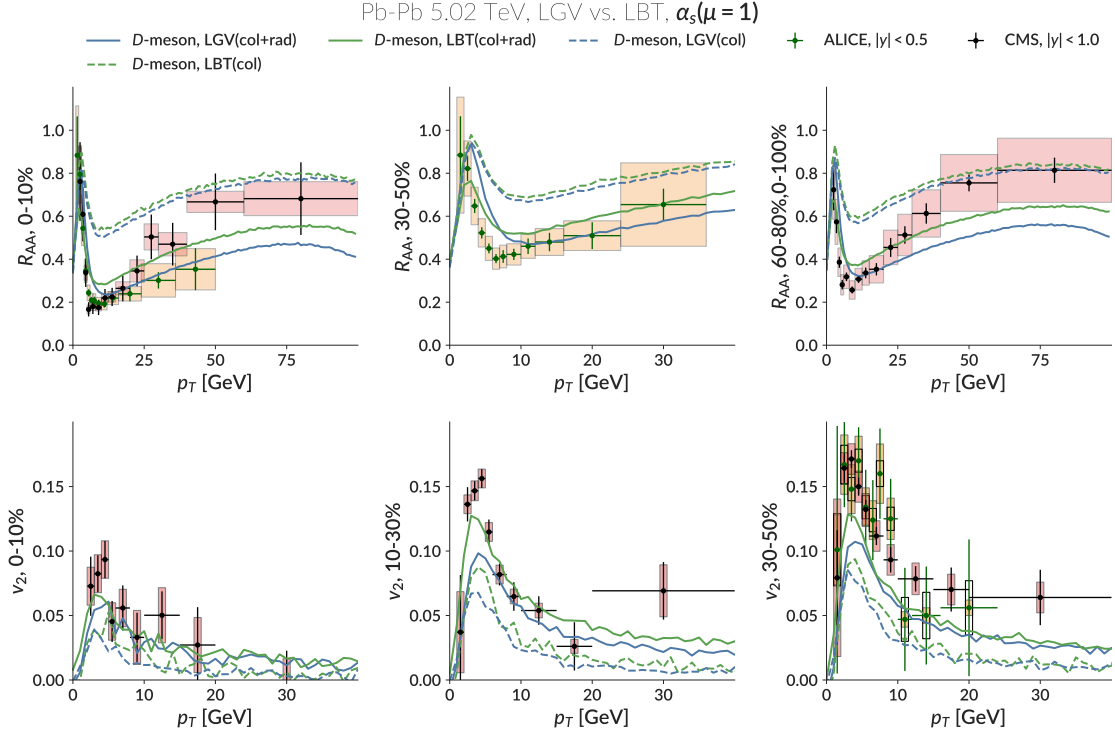


Figure 3.19: [Upper]: D -meson R_{AA} as a function of p_T in different centralities in Pb-Pb collision at $\sqrt{s_{NN}} = 5.02$ TeV; [Lower]: D -meson elliptic flow as a function of p_T in different centralities. Comparison between the calculation from different transport model (Langevin vs. improved Langevin vs. linearized Boltzmann(col) vs. linearized Boltzmann(col+rad)). The experimental measurements are taken from ALICE [126] and CMS collaboration [127].

- The consistently smaller value for R_{AA} at higher momentum results from the decay of D -meson in the hadronic stage.

From linearized Boltzmann to improved Langevin dynamics

With a Langevin approach, one can ignore the microscopic details of the interactions but instead focus on the macroscopic transport coefficients, while with a linearized Boltzmann, one can obtain more insights of the intrinsic quasi-particle nature of the QGP medium and the detailed interaction mechanisms.

The idea of viewing the Langevin evolution as a small momentum transfer approxima-

tion has been widely used while studying the heavy quark evolution in QGP medium, since the typical momentum transfer from the thermal medium is at the scale of temperature T , which is much smaller than the energy of heavy quarks — with a heavy mass $M > T$. However, such an assumption has been questioned recently, especially for charm quarks. In Ref. [95], the authors argue that when modeling the charm quark propagation in a static QGP medium, the suppression seen in the intermediate momentum region as calculated by the Langevin approach can deviate from the full Boltzmann transport from 10-15% to 40-50%, depending on the choice of the Debye screening mass.

A direct comparison between those two models can help us understand the underlying model uncertainty when one estimates the global coefficients from a model-to-data comparison⁹ In Fig. 3.12 and 3.11 I compare the evolution of the heavy quark distribution following either a Langevin or a linearized Boltzmann evolution in a static medium, with only the collisional energy loss is enabled. The comparison shows that while following a Langevin dynamics, the heavy quarks tend to lose energy faster than when they follow a linearized Boltzmann dynamics.

While propagating in a QGP medium, however, the differences between the Langevin dynamics and the linearized Boltzmann dynamics needs to be investigated with caution. In Fig. 3.19 I plot the results of heavy flavor observables in Pb-Pb collisions at 5.02 TeV, with different in-medium interactions:

- Langevin dynamics (collisional energy loss only): blue dashed lines
- improved Langevin dynamics (collisional + radiative energy loss): blue solid lines
- linearized Boltzmann dynamics (collisional energy loss only): green dashed lines
- linearized Boltzmann dynamics (collisional + radiative energy loss): green dashed

⁹I should remind that I do not intend to rule one model out, as the current experimental data does not enable us to draw a definitive conclusion.

lines

One finds that:

- Comparing between the collisional only and collisional + radiative energy loss cases, the radiative processes contribute significantly to heavy quark energy loss at high momenta as well as to the development of momentum anisotropy in the intermediate p_T range.
- Comparing the two collisional only evolution calculations, both linearized Boltzmann and Langevin dynamics achieve similar suppression (similar R_{AA} values), while heavy quarks evolving with linearized Boltzmann dynamics typically generate more anisotropic flow.
- For the energy loss involving both collisional and radiative processes, the current setup results in a stronger suppression for the improved Langevin equation, and contrarily, a smaller anisotropic flow. The difference between the suppression can be explained by the different radiative energy loss scheme that two models implement — as the improved Langevin model utilizes a `Higher Twist` formalism while the linearized Boltzmann dynamics explores the `Gunion-Bertsche` matrix elements. A more interesting observation is the smaller value of v_2 showing in the calculation with the improved Langevin models, which implies a more efficient anisotropy development in a matrix-element based linearized Boltzmann dynamics, mainly due to the anisotropic cross section for the radiative process.

Varying parameters

Finally, I would like to talk about the limitations of transport coefficients calculated in pQCD and the possibility of tuning the model parameters. In a Langevin approach, the

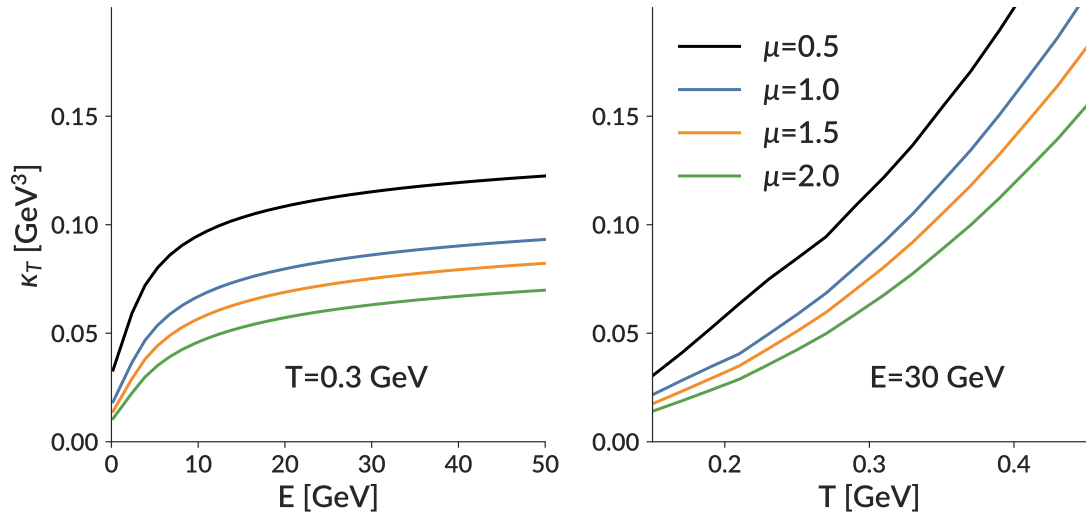


Figure 3.20: Charm quark transport coefficients κ_T as a function of momentum [**left**] and as a function of temperature [**right**]. Varying with different renormalization scale μ .

interaction strength between heavy quarks and the medium depends on the transport coefficients that are determined externally. One can compute the transport coefficients from the first principles, for example, via a lattice QCD approach. However, such an approach currently suffers from enormous computational requirements and currently only the diffusion coefficients at zero momentum are evaluated. Even with a leading order pQCD calculation, one would expect that the transport coefficients depend on the choice of the strong coupling constant α_s . This actually provides us with an opportunity to adjust the coupling constant such that the model's calculation fulfills the experimental observations.

A general procedure for such a model-to-data calibration can be set up as follows: we have a system with some final state observables that can be measured by experiment, and some properties of the system that characterize the behaviors of the system need to be estimated. One can use a computational/theoretical model to describe the evolution of the system, encode the properties of the system with some ad hoc parameters, and calculate the final observables. By varying the ad hoc parameters such that the computational/theoretical

model is able to describe the experimental measurements, one can estimate the intrinsic properties of the system.

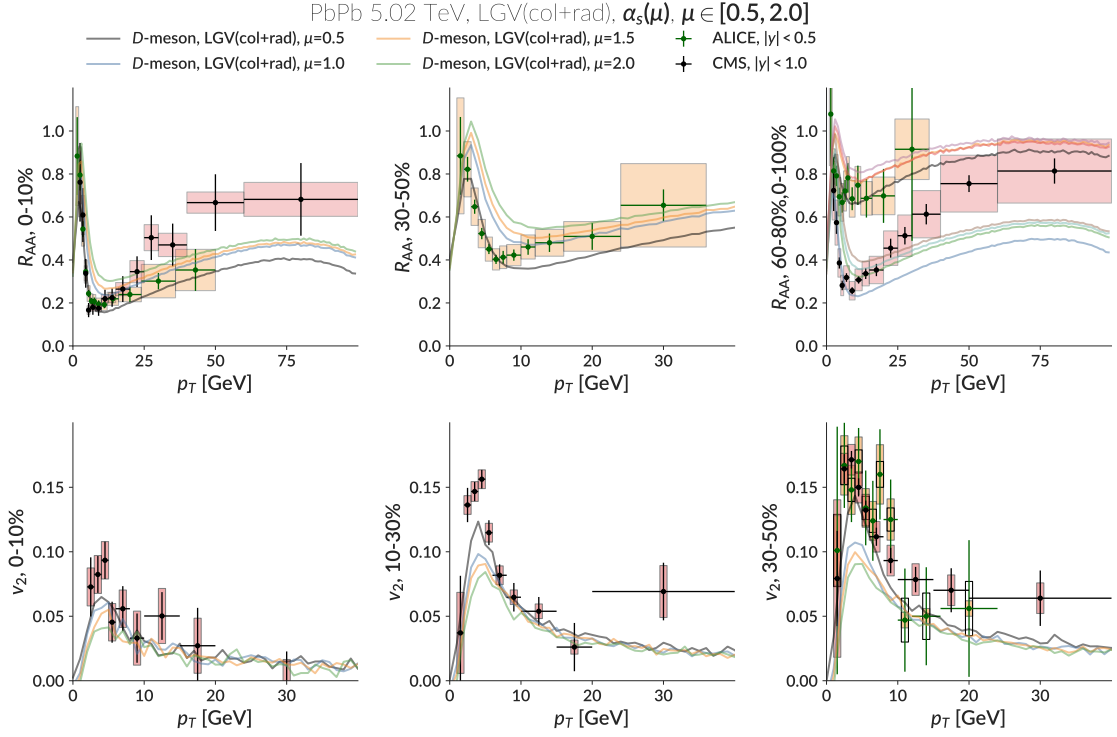


Figure 3.21: [Upper]: D -meson R_{AA} as a function of p_T in different centralities in Pb-Pb collision at $\sqrt{s_{NN}} = 5.02$ TeV; [Lower]: D -meson elliptic flow as a function of p_T in different centralities. Comparison between different values of the renormalization value μ . The experimental measurements are taken from ALICE [126] and CMS collaboration [127].

In the case of calculating the transport coefficients with a leading order pQCD approach and a running coupling constant, the ad hoc parameter of the model is the renormalization scale μ . As shown in Fig. 3.20 by varying the value μ from 0.5 to 2.0, the transverse transport coefficients differ by a factor of 2. The corresponding output for the heavy flavor observables are present in Fig. 3.21, where each color corresponds to one full run of the heavy quark evolution in heavy-ion collisions taking different renormalization scale value μ . One can see that, with the decreasing value of renormalization scale, which results in a higher value for the transport coefficients, the interaction between heavy quarks and the

medium gets stronger, leading to a stronger suppression and a larger elliptic flow.

Of course, one can also directly use a fixed coupling constant α_s and change its value, as the medium modified coupling constant at leading-order pQCD is quite ambiguous and one may use the effective averaged coupling constant to characterize the interaction strength between heavy quarks and the medium. Another common practice is to go beyond the leading-order assumption and multiply with a global scaling factor K , in order to account for higher order and non-perturbative contributions.

With only one or two parameters, one may be able to adjust the parameters by a traditional tuning procedure: by comparing the heavy flavor observables (such as the nuclear modification factor R_{AA} and the elliptic flow v_2) between theoretical calculation and the experimental data, those values can be tuned by eye or by “ χ -square” fitting — i.e. minimizing the standard error scaled by the experimental uncertainties $\chi^2 = \sum_{i=1}^N \frac{(y_{\text{model}} - y_{\text{exp}})^2}{2\sigma_{\text{exp}}^2}$. However, such a procedure becomes exceedingly difficult if multiple parameters need to be varied simultaneously or one has to compare a large selection of experimental measurements, as all the parameters are interdependent and affect multiple observables at once. Furthermore, it is not easy to take all the uncertainties consistently into consideration. A more sophisticated and systematic model-to-data comparison is required. The Bayesian model-to-data comparison framework fits perfectly in such a task. First of all, it rigorously treats experimental and theoretical uncertainties, which can be formulated as the covariance matrices. Secondly, the Markov chain Monte Carlo random walk is able to perform a thorough exploration of the parameter space completely within a proper prior range. Last but not least, the result of a Bayesian comparison is the posterior distribution of the parameters, which not only provides the “best-fit” values, but also provides the uncertainties (credibility region) of the estimation.

3.6 Summary

In this section, I reviewed in detail the two heavy quark in-medium models: the Langevin approach and the linearized Boltzmann approach. Utilizing perturbative QCD approach, I first calculated the partonic cross sections between heavy quarks and the light partons, and evaluated the scattering rate as well as macroscopic properties of the QGP medium: the heavy quark transport coefficients.

In addition to incorporate the radiative energy loss for heavy quarks with higher momentum, the Higher Twist formalism is adopted and a recoil force from the emitted gluon is induced in the Langevin framework. Both the collisional and radiative energy losses depend on the transport coefficients (or the coupling constant). Therefore one may estimate the transport coefficients through a comparison between the model's calculation and experimental measurements of the final state observables.

Finally, I pointed out the limitation of optimizing the transport model via a traditional “ χ -square” fitting procedure. In the next chapter, I will review a modern Bayesian model-to-data framework, which is a more rigorous and complete framework that is suitable for our task.

Chapter 4

Bayesian methodology

So far I have introduced a full space-time heavy quark evolution model for heavy-ion collisions, which incorporates a heavy quark transport model to describe its in-medium propagation, with a relativistic viscous hydrodynamic model to simulate the QGP medium evolution. The calculation of heavy flavor observables depends on the properties of the QGP medium and the interaction strength between heavy quarks and the medium. In contrast to the soft medium properties, the transport coefficients related to the medium interaction with the hard probes (jets and heavy quarks), such as \hat{q} , \hat{e} , D_s , κ_T , κ_L , η_D are not yet understood in a similarly quantitative level. This is in part due to the experimental difficulty in measuring “rare process”, but also due to the complexity of modeling the dynamics of these hard probes interacting with the QGP medium, Nevertheless, significant progress has been made in recent years: a number of transport models on the market are now able to describe a selection of heavy quark observables and perform qualitative estimates of the diffusion coefficients [91, 128, 81, 86, 93, 72, 129–131, 92, 85, 132, 79, 133, 134].

In this chapter, I will introduce a rigorous and complete approach to optimize the transport model and determine the parameters using a Bayesian model-to-data comparison framework, which determines the desired distribution of parameters by performing a random walk in parameter space and calibrating on the experimental data. This type of model-to-data comparison using Bayesian statistics has been applied with great success in the soft sector of heavy-ion physics: for example to constrain the Equation of the State in QCD matter purely from the experimental measurements [135, 136], and for the extraction of the temperature dependence of the specific shear and bulk viscosities of the QGP [44, 137, 55]. Beyond heavy-ion physics, this type of analysis has been widely used in

nuclear and astrophysics, as well as other fundamental research: for example an estimation of the photometric redshift[138], a global fit of the CKM matrix [139], and an estimation of the properties of the Binary Black Hole Merger[140]. In this thesis work, this framework is applied in estimation the heavy flavor transport coefficients in the QGP medium.

However, before the applying of the Bayesian analysis to our heavy quark transport model, I will review some of the basis for the Bayesian methodology in this chapter. The workflow for the Bayesian analysis is laid out in Fig. 4.1. In such an analysis, the computationally expensive physical model is first evaluated at a small number of points in parameter space. The Gaussian Process emulators are then trained and utilized as fast surrogates to the model to interpolate the parameter space and provide model prediction for arbitrary values of the input parameters. Thus one can perform a Markov chain Monte Carlo exploration of the complete parameter space and obtain the results of such analysis — the posterior distribution of the varying parameters that optimally describe the experimental data. This chapter is not intended to be a thorough explanation of the whole framework, for which purpose I refer the reader to [141–143].

4.1 Bayesian inference

“Bayesian inference is a method of statistical inference in which Bayes’ theorem is used to update the probability of the hypothesis as more evidence and information becomes available. [144]”. It is usually carried out in the following way:

- 1 Choose a probability distribution $p(\mathbf{x})$ — as the prior distribution, which expresses our belief about the parameter \mathbf{x} before any observation;
- 2 Choose a statistical model $\mathcal{L}(\mathcal{D}|\mathbf{x})$ — as the likelihood function, which reflects our belief about the output y given a specific parameter \mathbf{x} ;

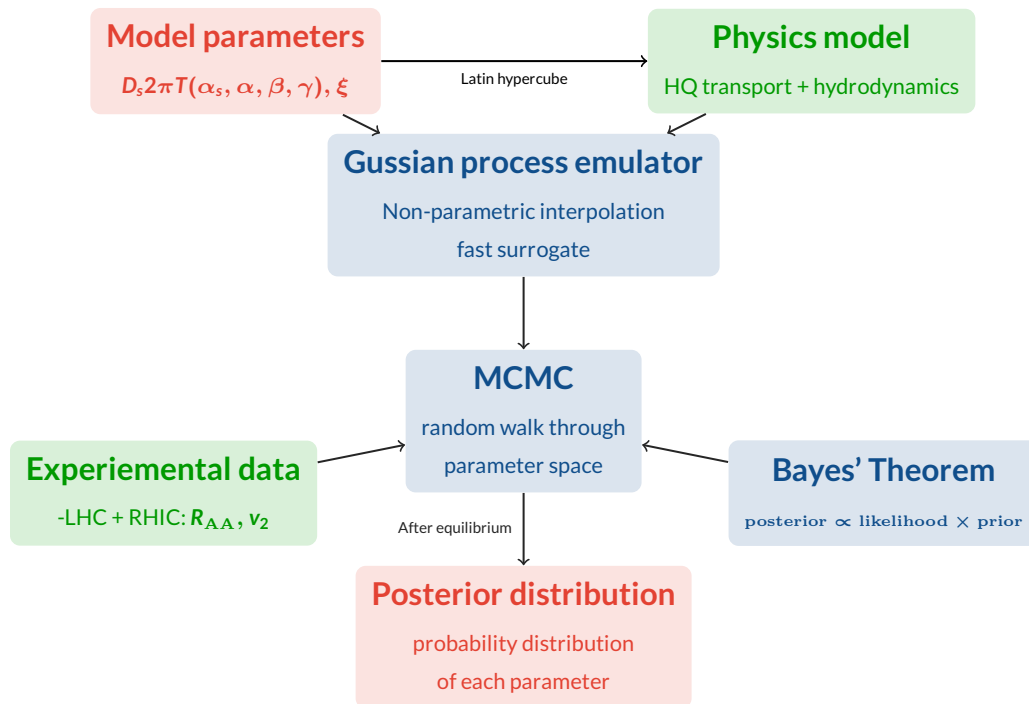


Figure 4.1: Workflow for the Bayesian model-to-data comparison framework.

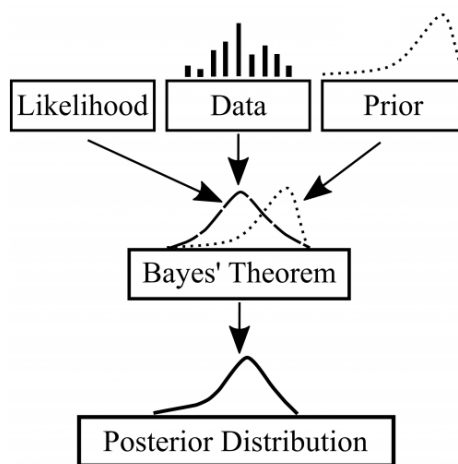


Figure 4.2: A sketch of the Bayes' theorem.

- 3 After observation $\mathcal{D} = \{y_1, \dots, y_n\}$, we update our beliefs and calculate the posterior distribution $p(\mathbf{x}|\mathcal{D})$.

4.1.1 Bayes' theorem

According to the Bayes' theorem, given the observation $\mathcal{D} = \{y_1, y_2, \dots, y_n\}$, the posterior distribution of the parameter \mathbf{x} is proportional to the multiplication of the likelihood $\mathcal{L}(y|\mathbf{x})$ and the prior distribution $p(\mathbf{x})$, as shown in Fig. 4.2:

$$P(\mathbf{x}|\mathcal{D}) = \frac{\mathcal{L}(\mathcal{D}|\mathbf{x})p(\mathbf{x})}{\int \mathcal{L}(\mathcal{D}|\mathbf{x})d\mathbf{x}} \propto \mathcal{L}(\mathcal{D}|\mathbf{x})P(\mathbf{x}), \quad (4.1)$$

where $\int \mathcal{L}(\mathcal{D}|\mathbf{x})d\mathbf{x}$ is the normalization constant, which is also called the evidence.

Prior distribution $p(\mathbf{x})$

The prior distribution $p(\mathbf{x})$ contains our belief for the parameters \mathbf{x} based on our current experience. A good choice of the prior distribution can generally accelerate the calculation of the posterior distribution. For example, one can construct a conjugate prior distribution, in which case the prior and posterior distribution are in the same distribution family¹. The advantage of a conjugate prior is that it can give a closed-form expression for the posterior, otherwise numerical integration is necessary for solving the posterior distribution.

In this thesis work, we choose an uniform distribution for the prior by assigning a finite range for each parameter. This prior distribution is then a constrained hyper-cube in a

¹For example, Gaussian family is conjugate to itself while considering a Gaussian likelihood; the beta distribution is conjugate to itself while considering a Bernoulli likelihood function

multi-dimensional space:

$$p(\mathbf{x}) = \begin{cases} 1 & \min(x_i) \leq x_i \leq \max(x_i) \\ 0 & \text{else} \end{cases}. \quad (4.2)$$

Likelihood $\mathcal{L}(\mathcal{D}|\mathbf{x})$

The likelihood function $\mathcal{L}(\mathcal{D}|\mathbf{x})$ is the probability of having an observation as \mathcal{D} given a specific parameter \mathbf{x} . For a physical process with the observation $\mathcal{D} = \{y_{\text{obs}}(p_T)\}$ — where p_T is used as a representation of different observation conditions in a heavy-ion collision experiment, such as the collision energy $\sqrt{s_{\text{NN}}}$, momentum range p_T , collision system, rapidity etc.— we can use a computational model to simulate this physical process, whose output y is dependent on some ad hoc parameters (input) \mathbf{x} as well as the experimental condition p_T :

$$y = f(\mathbf{x}; p_T) + \epsilon_M, \quad (4.3)$$

where ϵ_M is the model's uncertainty. Here we can assume a normal distribution for the models' statistical uncertainty $\epsilon_M \sim \mathcal{N}(0, \sigma_M^2)$. Then the likelihood that the model's calculation matches the experimental measurements — which is expressed as the sum of true events added by the measurement error $y_{\text{obs}} = \eta(p_T) + \sigma_{\text{exp}}$, follows a Gaussian distribution:

$$\mathcal{L}(y_{\text{exp}}|\mathbf{x}) = \frac{1}{\sqrt{2\pi\sigma^2}} \exp\left[-\frac{1}{2} \frac{(f(x) - y_{\text{exp}})^2}{\sigma_M^2 + \sigma_{\text{exp}}^2}\right]. \quad (4.4)$$

Now assuming there exists a true value of the parameter $\mathbf{x} = \boldsymbol{\mu}$, with which the computational model is able to describe the experimental observables $y_{\text{obs}} = f(\boldsymbol{\mu}; p_T) + \epsilon_M + \sigma_{\text{exp}}$, then the values of $\boldsymbol{\mu}$ from a frequentist point of view, can be obtained by optimiz-

ing(maximizing) the likelihood function, which is also referred as the maximum likelihood estimation (ML

$$\max_{\mathbf{x}=\mu} \mathcal{L}(y_{\text{exp}}|\mathbf{x}). \quad (4.5)$$

In the case of multi-variate output \mathbf{y} , the likelihood function for the multi-variate output is expressed as:

$$\mathcal{L}(\mathbf{y}_{\text{obs}}|\mathbf{x}) = \frac{1}{\sqrt{(2\pi)^m \det \Sigma}} \exp \left[-\frac{1}{2} [\mathbf{f}(\mathbf{x}) - \mathbf{y}_{\text{obs}}]^T \Sigma^{-1} [\mathbf{f}(\mathbf{x}) - \mathbf{y}_{\text{obs}}] \right], \quad (4.6)$$

where m is the dimension of the output y , $\Sigma = \Sigma_M + \Sigma_{\text{exp}}$ are the uncertainty covariance matrices, which contains both statistical and systematic uncertainties:

$$\Sigma_{\text{stats}} = \begin{pmatrix} \sigma_{11}^2 & \cdots & 0 \\ \vdots & \sigma_{ii}^2 & \vdots \\ 0 & \cdots & \sigma_{mm}^2 \end{pmatrix}, \Sigma_{\text{sys}} = \begin{pmatrix} \sigma_{11}^2 & \cdots & \sigma_{1m}^2 \\ \vdots & \ddots & \vdots \\ \sigma_{m1}^2 & \cdots & \sigma_{mm}^2 \end{pmatrix} \quad (4.7)$$

Posterior distribution $p(\mathbf{x}|\mathcal{D})$

The posterior distribution $P(\mathbf{x}|\mathcal{D})$ can be evaluated following Bayes' theorem. It contains information from both prior knowledge and experimental observation. The optimal values for the true parameter μ in this case are obtained by maximizing the posterior distribution (Bayesian point of view), which is also referred to as Maximum A Posteriori (MAP)²:

$$\max_{\mathbf{x}=\mu} P(\mathbf{x}|\mathcal{D}). \quad (4.8)$$

²Generally the MAP estimation result is different from the maximum likelihood estimation (MLE), the latter one is, based on its name, optimized from maximize the likelihood and often compared with the “ χ -squared fit”, if no model's uncertainties are considered. However, in this work, since the prior distribution is uniform, the MAP estimation is the same as MLE values.

4.1.2 Bayesian calibration

Analytic solution

There are various ways to evaluate Eqn. 4.1 and calculate the posterior distribution of the parameters. In some cases, one can directly perform the multiplication and obtain an analytic form. For example, considering a set of observation over events $\mathcal{D} = \{(p_1, y_1), (p_2, y_2), \dots, (p_N, p_N)\}$, each (p_i, y_i) represents an observation y_i at the different experimental condition p_i . For every observation y_i , the measurements uncertainties follow a Gaussian distribution: $y_i(p_i) = \eta(p_i) + \sigma_i$, i.e. a white noise with respect to the true reality $\eta(x_i)$. Now considering a computational model to describe the physical process, which has a linear relationship as mathematical form:

$$f(p) = mp + b. \quad (4.9)$$

In this case the input parameter $\mathbf{x} = (m, b)$ are the slope and intercept of the linear function. Give the parameter (m, b) , the likelihood that the computational model describes the observation y_i at each condition p_i is:

$$L(y_i|x_i, \sigma_i, m, b) = \frac{1}{\sqrt{2\pi\sigma_{yi}^2}} \exp \left[-\frac{(y_i - mp_i - b)^2}{2\sigma_i^2} \right], \quad (4.10)$$

the total likelihood is the product of the conditional probabilities $\mathcal{L} = \prod_{i=1}^N L(y_i|x_i, \sigma_{yi}, m, b)$, taking the logarithmic form:

$$\ln \mathcal{L} = \text{const} - \sum_{i=1}^N \frac{(y_i - mx_i - b)^2}{2\sigma_{yi}^2}. \quad (4.11)$$

We assign a uniformly distributed prior distribution:

$$P(\mathbf{x}) = U(a, b), \quad (4.12)$$

The log-posterior distribution shares the same form as the log-likelihood:

$$P(\mathbf{x}|y_i) = \text{const} - \sum_{i=1}^N \frac{(y_i - m x_i - b)^2}{2\sigma_{y_i}^2}. \quad (4.13)$$

We construct the matrices:

$$\mathbf{Y} = \begin{pmatrix} y_1 \\ y_2 \\ \vdots \\ y_N \end{pmatrix}, \mathbf{P} = \begin{pmatrix} 1 & p_1 \\ 1 & p_2 \\ \dots & \dots \\ 1 & p_N \end{pmatrix}, \Sigma = \begin{pmatrix} \sigma_1^2 & 0 & \dots & 0 \\ 0 & \sigma_2^2 & \dots & 0 \\ \vdots & \dots & \sigma_i^2 & \dots \\ 0 & 0 & \dots & \sigma_N^2 \end{pmatrix}, \quad (4.14)$$

The best-fit values for the parameter m and b are the components of a column vector \mathbf{X} which is solved by:

$$\mathbf{X} = \begin{pmatrix} b \\ m \end{pmatrix} = [\mathbf{P}^T \Sigma^{-1} \mathbf{P}]^{-1} [\mathbf{P}^T \Sigma^{-1} \mathbf{Y}]. \quad (4.15)$$

This is actually equivalent to the solution of minimizing the χ -squared value, which is the total squared error scaled by the uncertainties.

However, in practice, the analytic solution is often intractable. One challenge is to specify a suitable mathematical form that can properly map from the parameter space \mathbf{x} to the output space \mathbf{y} . When modeling a complex physical process, one often has to make use of a computational model which can not be reduced into a closed-form. The second challenge comes from a suitable prior distribution, which should spread out the probability over the parameter space and avoid zero or small probabilities for possible events. Moreover, one has to handle carefully the model's uncertainties as well as the experimental uncertainties. All these challenges have motivated us to utilize a more sophisticated and robust method.

Markov Chain Monte Carlo method

One alternative choice is the Markov chain Monte Carlo (MCMC) method to estimate the posterior distribution of the parameters. It utilizes Markov chains to approximate the posterior distribution via randomly drawing samples from the posterior probability distribution.

There are several variants of the MCMC method — Metropolis-Hasting, Gibbs, Hamiltonian, etc. [145]. A general iterative algorithm is constructed as the following:

- 1 Given the current state as \mathbf{x}_t , propose a new position as \mathbf{x}' . The new position can be sampled randomly from a distribution $q(\mathbf{x})$
- 2 Accept or reject the new position \mathbf{x}' with the probabilities based on the ratio between the two posterior probability, which is also called acceptance rate:

$$a(\mathbf{x}_t, \mathbf{x}') = \min \left(1, \frac{\mathcal{L}(\mathbf{x}'|y)q(\mathbf{x}')}{\mathcal{L}(\mathbf{x}_t|y)q(\mathbf{x}_t)} \right) \quad (4.16)$$

- 3 Update the state to position $\mathbf{x}_{t+1} = \mathbf{x}'$ if accepted, otherwise $\mathbf{x}_{t+1} = \mathbf{x}_t$. Repeat this process for many steps, the resulting samples $\{\mathbf{x}_1, \mathbf{x}_2, \dots, \mathbf{x}_N\}$ approximate the posterior distribution of $\mathcal{L}(\mathbf{x}|y)$. Generally it is helpful to discard the early samples, and only keep the samples after equilibrium is revealed (which means the sample distribution has converged to the posterior distribution).

In this thesis work, I use `emcee`, an affine invariant MCMC ensemble sampler to perform the random walk in the parameter space. A more detailed explanation of the mathematical derivation and implementation can be found in [146, 147]. Here I will only summarize a few practical considerations.

- The walkers are the sampler to the Markov chain which will update their states based on the proposed positions. In `emcee`, the next position of the walkers are not only

dependent on the current state, but that also dependent on other walkers. Regarding the number of walkers, the more the better, but also takes more time. Typically $O(10^3)$ walkers are constructed.

- **Burn-in:** it is generally a good idea to run a few “burn-in” steps (typically 1000 steps) to let the walkers explore the parameter space and finally converge into the maximum posterior probability density region. In this work, a two-stages burn-in method is used: randomly generate the walkers and run n_1 burn-in steps, then resample the walkers according to the distribution from the first half random walkers, and performs the rest $n - n_1$ burn-in steps.
- **Acceptance rate:** One way to test if the random walk performs well is to plot the histogram of the walkers’ positions that have generated so far. Another way is to check the mean acceptance rate $\langle a(\mathbf{x}_t, \mathbf{x}') \rangle$. If the acceptance rate is very low, it means that the walkers are stuck; and if the acceptance rate is very large, it means that the sampling is performed completely randomly. Typically the acceptance rate should range between $0.2 \sim 0.5$ if everything works as planned.

A one-dimensional example

Now I have explained the procedure to estimate the posterior distribution of the parameter \mathbf{x} , in the following, I will apply the procedure on an example using a 1-dimensional dataset.

For a set of observation under different conditions — $\mathcal{D} = \{(p_1, y_1), (p_2, y_2), \dots, (p_n, y_n)\}$, whose relation are plotted in Fig. 4.3 as the black errorbars. For every observation y_i , the measurements uncertainties follow a Gaussian distribution: $y_i(p_i) = \eta(p_i) + \sigma_i$. The true process — plotted as the black solid line — follows a linear relationship:

$$\eta(p) = mp + b, \tag{4.17}$$

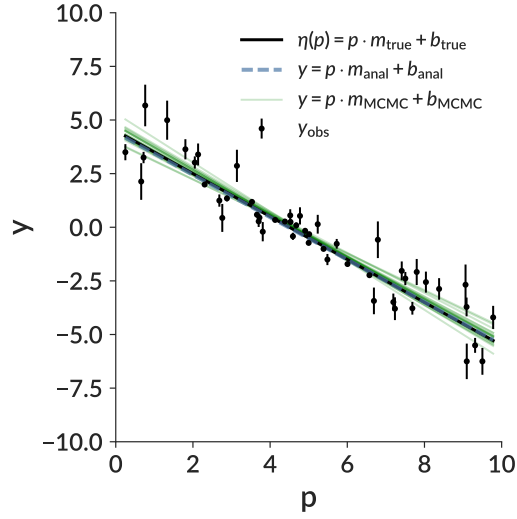


Figure 4.3: The observation of 50 events of $\mathcal{D} = \{(p_i, y_i)\}$ with the underlying truth as a linear relation and plotted as the black solid line. The observation uncertainties follows a Gaussian distribution with the variance $\sigma_i \sim \mathcal{N}(0, \kappa y_i + \varepsilon)$.

with

$$m_{\text{true}} = -1, b_{\text{true}} = 4.5, \quad (4.18)$$

and the observation uncertainties follow a distribution as:

$$\sigma_i \sim \mathcal{N}(0, 0.5y_i + \varepsilon), \varepsilon \sim \mathcal{N}(0.1, 0.5). \quad (4.19)$$

According to Eqn. 4.15, one can calculate one set of “best-fit” parameters, that minimize the “ χ -squared”. The result is $(m, b) = (-0.989, 4.422)$, which is plotted as the blue dashed line.

One can also use the MCMC method to calculate the posterior distribution of the parameters. Following the process mentioned above, we have:

- 1 A prior distribution for parameters to be estimated: $m \in [-5, 5]$, $b \in [0, 10]$, and a computational model with $f(p) = mp + b$. Initially we sample N random walkers in

the parameter space.

- 2 At each parameter point, we evaluate the likelihood $\mathcal{L}(\mathcal{D}|m, b; p)$. In practice we use the log likelihood as: $\ln \mathcal{L}(\mathcal{D}|m, b, \sigma_i; p) = -\frac{1}{2} \sum_N \left[-\frac{(y_i - mp_i - b)^2}{\sigma_i^2} + \ln(2\pi\sigma_i^2) \right]$, where the uncertainty $\sigma_i^2 = \varepsilon_i^2 + \kappa^2 y_i^2$ is the Gaussian variance underestimated by some fraction κ . The parameters are updated to the next states based on the affine invariant method which is performed by the sampler `emcee`.
- 3 After sufficient time, the distribution of the samples will be approximately equal to the posterior distribution, which is shown in Fig. 4.4. We can now choose parameter values sampled from the posterior distribution, and the estimated model using 20 random samples drawn from the posterior distribution is plotted as the green curves in Fig. 4.3.

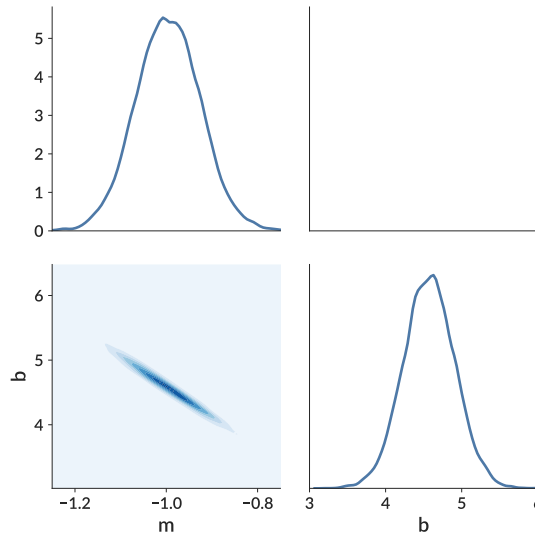


Figure 4.4: The posterior distribution of the parameters estimated by the MCMC method.

The result of the Bayesian analysis is the posterior distribution of the parameters given the information of the experimental observation and our prior assumptions. The marginal distribution, which is the distribution that integrates all the other parameters out are shown

in the diagonal of Fig. 4.4. One can estimate the mean and the median of individual parameters. In this case, we can evaluate the values for the parameters as:

$$\begin{aligned} m_{\text{mean}} &= -1.004, b_{\text{mean}} = 4.610; \\ m_{\text{median}} &= -1.002, b_{\text{median}} = 4.598. \end{aligned} \tag{4.20}$$

Moreover, the more profound benefit of the Bayesian approach goes beyond the estimation the “best-fit” parameters, is that it properly facilitates the uncertainties and estimates the credible region (CR) as the degree of uncertainty about the estimated values. Typically we can use 95% of the CR, which corresponds to 2σ deviation from the median value³.

Regarding our examples, the 95% CR estimation for the parameter is:

$$m = -1.002_{-0.138}^{+0.131}, b = 4.498_{-0.639}^{+0.657}, \tag{4.21}$$

which isn’t bad given the true values as: $m = -1.0, b = 4.5$.

4.2 Gaussian Process emulator

So far we have discussed the general steps to perform a Bayesian analysis to estimate the posterior distribution of the parameters. In order to calibrate the computational model to the experimental observation, the walkers randomly explore the parameter space, where each step is accepted or rejected according to the acceptance rate. Therefore the likelihood at each parameter point is evaluated, which leads to the evaluation of the model’s calculation. Taking a random walk throughout a 3-dimensional space often requires $\mathcal{O}(1000 \times 100)$ steps and the number increase exponentially if we try to include more parameters.

³The concept of credible region to a Bayesianist is very similar to the concept fo confidence interval to a frequentist, even though these two are numerically equivalent in a lot of cases, their interpretation is very different

For the event-by-event heavy quark evolution model in heavy-ion collisions, $\mathcal{O}(10^4)$ minimum bias events are often generated in order to get sufficient statistics and compare with experimental measurements. Given the amount of CPU hours required, it is unfeasible to utilize the complex computational model to calculate the output y while performing the random walk. A Gaussian Process emulator is therefore used as a fast surrogate model that predicts the computational model's output $f(\mathbf{x}; p)$ at any arbitrary point \mathbf{x} in parameter space. From the parameter-space point of view, the Gaussian Process can be thought as a projection from the parameter space \mathbf{x} to the output space y with a mapping function $\phi(\mathbf{x})$. Another interpretation of the Gaussian Process comes from the output space point of view, where "A Gaussian Process is a collection of random variables, as any finite number of which have a joint Gaussian distribution." [143]. A Gaussian Process emulator has several advantages:

- It is a non-parametric regression model: the Gaussian Process emulator does not assume a specific form for the mapping from \mathbf{x} to y , therefore it is flexible enough to fit the complex mapping functions;
- A Gaussian Process emulator predicts the distribution of the output y : that is to say, not only the mean of the prediction is provided, but also uncertainty associated with the prediction. This is important in our quantitative estimation in the high precision era.

4.2.1 1-dimensional constrained Gaussian Process

A Gaussian Process is completely determined by its mean and covariance function, for any function $f(\mathbf{x})$ it can be decomposed as:

$$f(\mathbf{x}) \sim \mathcal{GP}(\mu(\mathbf{x}), \sigma(\mathbf{x}, \mathbf{x}')), \quad (4.22)$$

where $\mu(\mathbf{x}) = \mathbb{E}[f(\mathbf{x})]$ is the mean function and $\sigma(\mathbf{x}, \mathbf{x}') = \mathbb{E}[(f(\mathbf{x}) - \mu(\mathbf{x}))(f(\mathbf{x}') - \mu(\mathbf{x}'))]$ is the covariance. The assumption $(y_1, y_2) \sim \mathcal{N}(\boldsymbol{\mu}, \Sigma)$ directly leads to the requirement that $y_1 \sim \mathcal{N}(\mu_{11}, \Sigma_{11})$, where Σ_{11} is the submatrix of the covariance matrix Σ .

Now consider a training dataset with n observations⁴. A computational model simulates a physical process (e.g. our heavy quark transport model that simulates the evolution of the heavy quarks in heavy-ion collisions). The model's output y is dependent on the input parameter \mathbf{x} and it has been evaluated at n different input points $\tilde{X} = (\mathbf{x}_1, \mathbf{x}_2, \dots, \mathbf{x}_n)^T$. The corresponding model's output $y_i = f(\mathbf{x}_i)$ yields a n -dimensional output vector⁵:

$$\tilde{X} = \begin{pmatrix} x_{11} & \cdots & x_{1p} \\ \vdots & \ddots & \vdots \\ x_{n1} & \cdots & x_{np} \end{pmatrix} \Rightarrow \tilde{Y} = \begin{pmatrix} y_1 \\ \vdots \\ y_n \end{pmatrix}. \quad (4.23)$$

Then by definition, the output \tilde{Y} can be re-formulated as a conditional Gaussian Process which is a collection of normal distribution:

$$\tilde{Y} = \mathcal{GP}(\tilde{X}) \sim \mathcal{N}(\mu(\tilde{X}), K_{\tilde{X}, \tilde{X}}), \quad (4.24)$$

where $\mu(\tilde{X})$ is the mean vector of each input \mathbf{x} and it is often assumed to be normal (or you can standardize the training data by subtracting the mean) , and

$$K_{\tilde{X}, \tilde{X}} = \begin{pmatrix} \sigma(\mathbf{x}_1, \mathbf{x}_2) & \cdots & \sigma(\mathbf{x}_1, \mathbf{x}_n) \\ \vdots & \ddots & \vdots \\ \sigma(\mathbf{x}_n, \mathbf{x}_1) & \cdots & \sigma(\mathbf{x}_n, \mathbf{x}_n) \end{pmatrix} \quad (4.25)$$

⁴Please note here the different meaning of observations. In previous session, we have one set of fixed parameter set and make N observation at different experimental conditions p_T . Here we have n different sets of parameters, and at each set of the parameter, we make an observation.

⁵Gaussian process is essentially a mapping from p -dimensional parameter space to 1-dimensional output space. For now let us consider there is only one output for each input.

is the covariance matrix that is constructed by the the covariance function $\sigma(\mathbf{x}, \mathbf{x}')$ and characterizes the correlation between inputs.

Noise free prediction

In the simple case where the observations are without noise, at any arbitrary input \mathbf{x}_* ⁶, the model output $y_* = f(\mathbf{x}_*)$ has the joint multivariate normal distribution with the training dataset $\mathcal{D} = \sum_{i=1}^N \{\mathbf{x}_i, y_i\} = (\tilde{X}, \tilde{Y})$:

$$\begin{pmatrix} y_* \\ \tilde{Y} \end{pmatrix} \sim \mathcal{N} \left(\begin{pmatrix} \mu(x_*) \\ \mu(\tilde{Y}) \end{pmatrix}, \begin{pmatrix} K_{*,*} & K_{*,\tilde{X}} \\ K_{\tilde{X},*} & K_{\tilde{X},\tilde{X}} \end{pmatrix} \right), \quad (4.26)$$

where $K_{*,*}, K_{\tilde{X},*}$ have the same form as Eqn. 4.25 but with respect to different \mathbf{x} . Therefore we can estimate the distribution of a predicted output y_* as:

$$y_* | x_*, \tilde{X}, \tilde{Y} \sim \mathcal{N}(\mu, K), \quad (4.27)$$

where

$$\begin{aligned} \mu &= \mu(\mathbf{x}_*) + K_{*,\tilde{X}} K_{\tilde{X},\tilde{X}}^{-1} (\tilde{Y} - \mu(\tilde{X})), \\ K &= K_{*,*} - K_{*,\tilde{X}} K_{\tilde{X},\tilde{X}}^{-1} K_{\tilde{X},*}. \end{aligned} \quad (4.28)$$

The inference of the Gaussian Process is determined by the covariance function $\sigma(\mathbf{x}, \mathbf{x}')$. Various choice can be made for the covariance function based on our knowledge and assumptions of the inputs. Typically it has some free parameters, for example, a commonly used squared-exponential covariance function in the m -dimensional parameter space has

⁶The star symbol here are used to represent the output predicted from the GP emulators.

the form:

$$\sigma(\mathbf{x}, \mathbf{x}') = \sigma_{\mathcal{GP}}^2 \exp \left[- \sum_{k=1}^m \frac{(x_k - x'_k)^2}{2l_k^2} \right]. \quad (4.29)$$

has (hyper-)parameters $(l_k, \sigma_{\mathcal{GP}})$.

This covariance function is infinitely differentiable, therefore the Gaussian Process emulator is very smooth. In addition, inputs that are close to each other in the parameter space are highly correlated, whilst those far away are uncorrelated. The correlation strength between pairs of inputs is controlled by the hyperparameters $(\kappa_l, \sigma_{\mathcal{GP}})$. Varying the hyperparameters, one could in principle obtain different correlations between observables. There are various ways to optimize the hyperparameters. In this study, we optimize the hyperparameters during the fitting process by maximizing the log-marginal likelihood (LML):

$$\log p(\tilde{Y}|\tilde{X}) = -\frac{1}{2} \tilde{Y}^T K^{-1} \tilde{Y} - \frac{1}{2} \log |K| - \frac{n}{2} \log 2\pi, \quad (4.30)$$

in which we define $K \equiv K_{\tilde{X}, \tilde{X}}$.

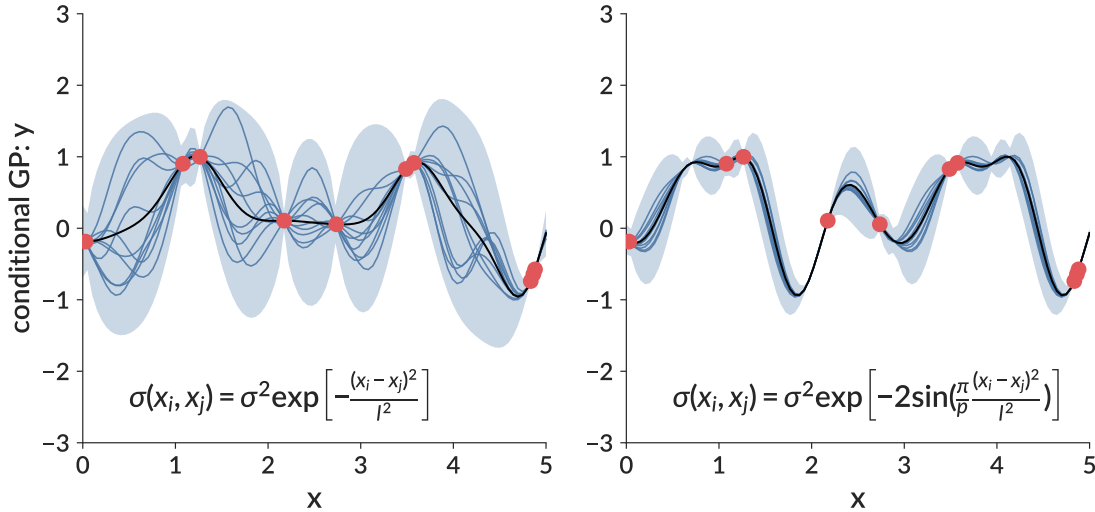


Figure 4.5: Implementation of Gaussian Process emulator with different covariance function: **[Left]**: exponential squared kernel ; **[Right]**: exponential sin kernel.

A practical implementation of the Gaussian Process emulator is shown in Fig. 4.5, where the 10 red points are the observations $\mathcal{D} = \{(x_i, y_i)\}$. A Gaussian Process emulator is trained to fit the observation points. One can choose different covariance functions to represent the correlation between different inputs c_i . In Fig. 4.5, I plot the predicted y distribution with the Gaussian Process emulator taking different forms of the covariance function. One can clearly see its effect on the final estimation. In both panels, the black lines are the mean for the prediction, while the blue lines are a few random samples generated from the estimated distribution (according to Eqn. 4.27). The shadow area represents the 95% confidence intervals.

Predictions with noise

In a more realistic scenario that the model's calculation has uncertainties associated with it. While evaluating the input parameter this can now be written as $y = f(\mathbf{x}) + \epsilon$. Assuming the additional uncertainties ϵ follow independent Gaussian noise with variance σ_{model}^2 , the covariance function then becomes:

$$\begin{aligned} \text{cov}(y_i, y_j) &= \sigma(\mathbf{x}_i, \mathbf{x}_j) + \sigma_n^2 \delta_{ij}, \\ K_{X,X} &\Rightarrow K_{X,X} + \sigma_{\text{model}}^2 \mathbb{I}, \end{aligned} \tag{4.31}$$

The joint multi-variant normal distribution Eqn. 4.26 becomes:

$$\begin{pmatrix} y_* \\ \tilde{Y} \end{pmatrix} \sim \mathcal{N} \left(\begin{pmatrix} \mu(x_*) \\ \mu(\tilde{Y}) \end{pmatrix}, \begin{pmatrix} K_{*,*} + \sigma_n^2 \mathbb{I} & K_{*,\tilde{X}} \\ K_{\tilde{X},*} & K_{\tilde{X},\tilde{X}} \end{pmatrix} \right), \tag{4.32}$$

The conditional GP distribution corresponding to Eqn. 4.27 is then updated as:

$$\begin{aligned}
y_* | x_*, \tilde{X}, \tilde{Y} &\sim \mathcal{N}(\mu, K), \\
\mu &= \mu(\mathbf{x}_*) + K_{*,\tilde{X}} \left[K_{\tilde{X},\tilde{X}} + \sigma_n^2 \mathbb{I} \right]^{-1} (\tilde{Y} - \mu(\tilde{X})), \\
K &= K_{*,*} - K_{*,\tilde{X}} \left[K_{\tilde{X},\tilde{X}} + \sigma_n^2 \mathbb{I} \right]^{-1} K_{\tilde{X},*}.
\end{aligned}$$

4.2.2 Multi-variate predictions: principal component analysis

A Gaussian Process is as a matter of fact, a mapping from the p -dimensional input parameter space \mathbf{x} to a scalar output space y . In the case of multi-variate output $y \Rightarrow \mathbf{y}$, where \mathbf{y} is a m -dimensional vector:

$$\tilde{X} = \begin{pmatrix} x_{11} & \cdots & x_{1p} \\ \vdots & \ddots & \vdots \\ x_{n1} & \cdots & x_{np} \end{pmatrix} \Rightarrow \tilde{Y} = \begin{pmatrix} y_{11} & \cdots & y_{1m} \\ \vdots & \ddots & \vdots \\ y_{n1} & \cdots & y_{nm} \end{pmatrix}. \quad (4.33)$$

One can, of course, construct a Gaussian Process emulator for each of the observables. However, as the variables in the output are highly correlated, it is often suffering from a “multi-collinear” problem, as a few variables are collinearly related to each other, and without proper treatment, we get redundant information from the output and end up with the wrong interpretation of the final estimation. It is therefore useful to reduce a high dimensional and correlated output to a lower dimensional and orthogonal output of principal components (PCs), which are linear combinations of the original output observables, and preserve the important information of the training dataset.

In practice, the outputs from the training datasets \tilde{Y} are standardized (by subtracting the mean and dividing by the standard deviation of each observables), and decomposed via

the singular value decomposition (SVD) method:

$$Y_{m \times n} = U_{m \times n} S_{n \times n} V_{n \times n}^T. \quad (4.34)$$

The columns of $U(V^T)$ are the left(right)-singular vector of Y , which are sets of orthogonal eigen-vectors of $YY^T(Y^TY)$. The output matrix Y can then be transformed into principal component space:

$$Z = \sqrt{n}YV. \quad (4.35)$$

And S is the diagonal matrix whose elements $\lambda_{i(i=1,\dots,n)}$ are the squared root of the eigenvalues of $Y^TY = (USV^T)^TUSV^T = VS^2V^T$. The eigenvalues λ_i are proportional to the variance that contributes the i -th PC, and are sorted into descending order. The cumulative variance explained by the first m' -PCs ($m' \leq m$) then equals to:

$$CV(m') = \frac{\sum_{i=1}^{m'} \lambda_i}{\sum_{i=1}^m \lambda_i}. \quad (4.36)$$

This can be used as the criterion to measure how much information (mainly variance) has been preserved in the principal component space.

If the variables in the physical observable space are highly linearly/collinearly correlated with each other — which is often the case for the multi-variate output in a physical system, by decomposition, the first few principal components in the PC space are not only orthogonal with each other, but also are able to explain most of the variance in the training dataset. We can therefore only select the first m' elements in the principal component space, and use the new training dataset $\mathcal{D}' = \{(\mathbf{x}_i, \mathbf{z}_i)\}$ to train m' Gaussian Process emulators, and make predictions of \mathbf{z}_* at each arbitrary parameter \mathbf{x} . For each element in the principal component space \mathbf{z}_i , a Gaussian process emulator is constructed and makes prediction for any arbitrary input parameter \mathbf{x}_* independently. Once the output \mathbf{z}_* are predicted by the

GP emulators, one would perform a transformation to predict the output \mathbf{y}_* .

$$\mathbf{y}_* = \frac{1}{\sqrt{n}} \mathbf{z}_* V. \quad (4.37)$$

In our later Bayesian analysis with the heavy quark evolution model, one can evaluate the model's performance — $\mathbf{y} = (R_{AA}, v_2)$ at different values of transport coefficients — $\mathbf{x} = D_s$. Figure. 4.6 shows a typical principal component analysis (PCA) using our training dataset: PCA transformation from the physical observable space into the principal space, where the former one shows a strong linear/collinear relation between variables. After PCA, the principal components are rotated and orthogonal to each other.

Figure. 4.7 shows the linear combination coefficients in front of the principal components with regard to the original physical space observables, i.e., the columns of V . Each point is an evaluation of D -meson R_{AA} or v_2 at different p_T and centrality bins. The first PC, which explains about 80% of the training dataset variance, accounts for a negative correlation with all R_{AA} s (negative value) and positive correlation with elliptic flow v_2 s (positive value). In addition, all the physical observables have a similar value of the coefficients, implied that they contribute nearly equally in terms of the variance (as we have standardized the training dataset).

The right panel of Fig. 4.7 plots the cumulative variance explained by the first m' -th principal component. As shown in the figure, the first few PCs can explain most of the variance from the model's outputs. In this study, I choose 8 PCs in the analysis, which are sufficient to explain more than 99% of the model's variance. It is a significant reduction from the original physical space, the latter typically has a dimension in the order of tens. It will help with the acceleration of calibration via MCMC method as well.

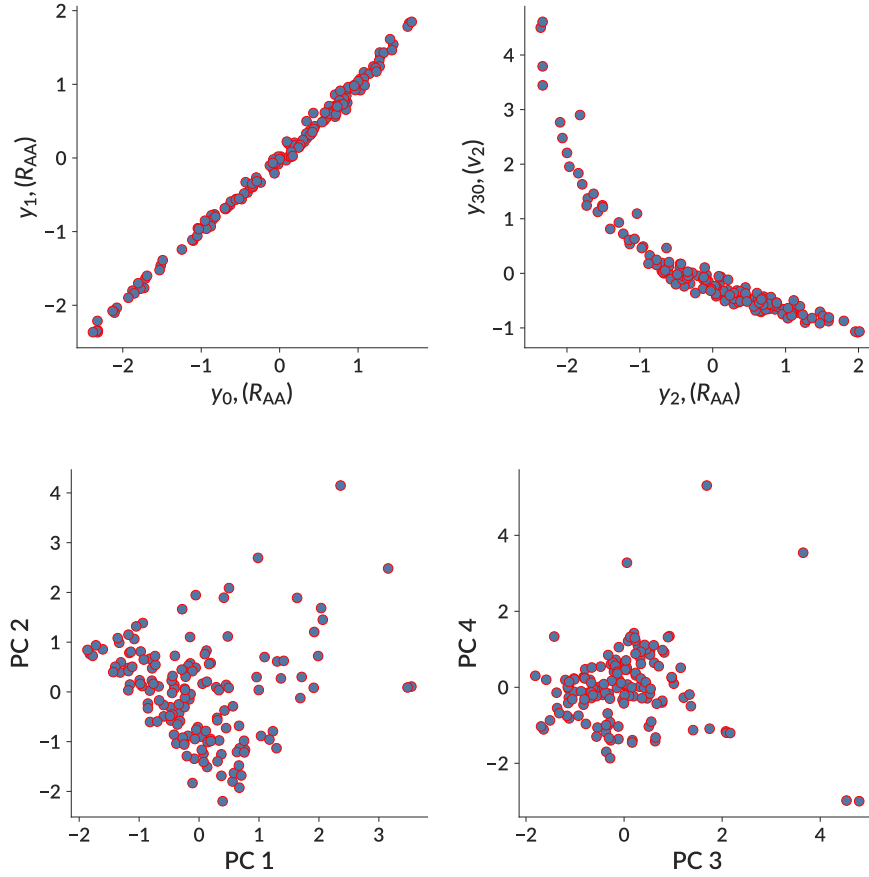


Figure 4.6: SVD transformation of the physical observable space to principal component space. The original physical space observables show a strong negative linear (between two R_{AA} evaluated at different p_T) and collinear (between R_{AA} and v_2) relation. The R_{AA} and v_2 are evaluated as D -meson observables in Pb-Pb collisions at 5.02 TeV with different choice of transport coefficients. After transformation, the PCs are uncorrelated with each other.

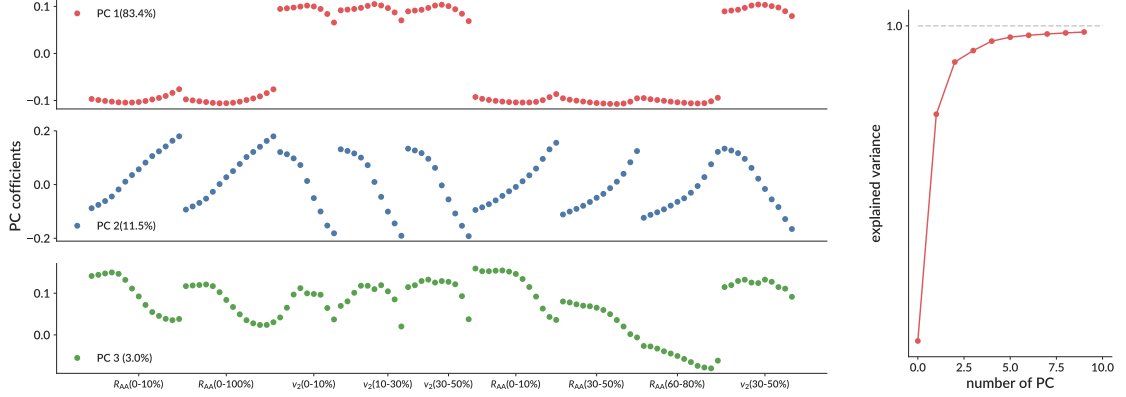


Figure 4.7: Application of the PCA to heavy quark evolution model’s calculation of D -meson observables — R_{AA}, v_2 . **[Left]:** linear combination coefficients in front of the top 3 principal components with concerning of different physical observables. Each point represent an evaluation at different p_T and centrality bins. **[Right]:** cumulative explained variance fraction for the top 10 principal components.

transformation of the uncertainty

While the Gaussian Process emulators make prediction of the m' principal components, in addition to the mean value \bar{z} , it also provides the uncertainties associated with the predictions. Since all the principal components are orthogonal to each other, the uncertainty matrix Σ^{PC} is a diagonal matrix whose elements are the standard deviation for each principal component:

$$\Sigma^{\text{PC}} = \begin{pmatrix} \sigma_1^2 & \cdots & 0 \\ \vdots & \sigma_i^2 & \vdots \\ 0 & \cdots & \sigma_{m'}^2 \end{pmatrix}. \quad (4.38)$$

The uncertainty in the PC space also needs to be transformed into the original physical space in order to account for the uncertainties coming from the (emulator) model’s uncertainty, In addition, one should also consider the uncertainties coming from the remaining neglected PCs.

For the case of linear combinations, where the output y in the physical space is a linear combination of z in the PC space — $y = \frac{1}{\sqrt{n}}zV$, the transformation/propagation of the

variables uncertainties is given by:

$$\Sigma_{ij}^{\text{physical}} = \frac{1}{n} \sum_k^{m'} \sum_k^{m'} V_{ik} \Sigma_{kl}^{\text{PC}} V_{jl}, \quad (4.39)$$

or in matrix notation:

$$\Sigma^{\text{physical}} = \frac{1}{n} V \Sigma^{\text{PC}} V^T. \quad (4.40)$$

For the uncertainties coming from the remaining neglected PCs, I used a truncated covariance matrix to take the last $m - m'$ elements to represents the remaining uncertainties:

$$\Sigma^{\text{trunc}} = \frac{1}{n} (V^T V)[m' : m, m' : m]. \quad (4.41)$$

The overall uncertainties coming from the Gaussian Process emulator then can be expressed as:

$$\Sigma_{GP} = \Sigma^{\text{physical}} + \Sigma^{\text{trunc}}. \quad (4.42)$$

4.2.3 Application and validation of GP emulator

Gaussian Process kernel

As shown in Fig. 4.5, while utilizing the Gaussian Process emulator to interpolate and predict the results from arbitrary inputs \mathbf{x} , one needs to specify the covariance function, which demonstrates the correlation between the input parameters. Different covariance functions, or kernels, impose different strength of the correlation, which can lead to different prediction of the mean values as well as uncertainty estimations. In this work, I choose a commonly used squared exponential kernel, as one would expect that inputs in the input in the parameter space that are closer to each other have higher correlation, in addition to a

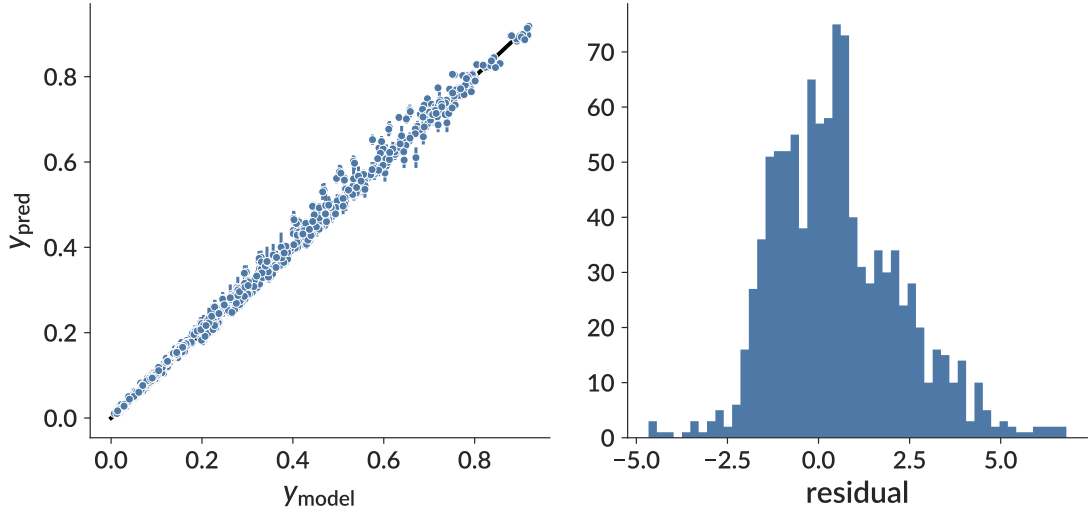


Figure 4.8: [Left]: Comparison between GP emulators’ prediction of output y_{pred} against the heavy quark evolution model calculation y_{model} ; [Right]: histogram of the predicted residual.

noise kernel. The overall covariance function for the output z taking different \mathbf{x} is:

$$\text{cov}(\mathbf{z}_1, \mathbf{z}_2) = \sigma(\mathbf{x}_1, \mathbf{x}_2) = - \sum_{k=1}^m \sigma_k^2 \exp \left[\frac{|\mathbf{x}_1 - \mathbf{x}_2|^2}{2l_k^2} \right] + \sigma_n^2 \delta(\mathbf{x}_1 - \mathbf{x}_2). \quad (4.43)$$

The correlation strength between pairs of inputs is controlled by the hyperparameters $(\sigma_k, l_k, \sigma_n)$, the last one allows for some small deviation between the GP emulator prediction and the training points. The GP emulators are trained in a manner of “maximum likelihood estimation” using the `scikit-learn` — a python library specializing in statistics and machine learning. For more information regarding the hyperparameter tuning please refer to the `scikit-learn` user manual.

validation of the GP emulators

The performance of GP emulators directly affects the prediction result, and therefore affects our estimation of the posterior distribution of the parameters. In order to test the emula-

tors' ability to predict the physical model's output faithfully, I generate another 15 sets of validation inputs and evaluate the corresponding outputs using the full heavy quark evolution model. The validation dataset is independent of the training dataset and (in principle) should have a similar distribution of the population of prior design points. By comparing the physical model's outputs with the GP emulators' prediction, as shown in Fig. 4.8, where we have plotted the model's calculation of observables against its corresponding predictions, the GP emulators perform reasonably well, with the $y = x$ black line indicating that the GP emulators' prediction is equal to the model's calculation.

To quantify the emulators' performance, one could also plot the distribution of the residual. The GP emulators do not predict the models' output exactly, but give the prediction \mathbf{y}_{pred} , and the uncertainty σ_{pred} . One would expect that the normalized residual follows the normal distribution:

$$\text{residual} \equiv \frac{\mathbf{y}_{\text{pred}} - \mathbf{y}_{\text{target}}}{\sigma_{\text{pred}}} \sim \mathcal{N}(0, 1), \quad (4.44)$$

The right panel of Fig. 4.8 reveals the distribution of the residual, thus we have shown that our GP emulators indeed are able to make valid predictions.

4.3 Calibration

With the trained GP emulators, the experimental observation of the physical observables \mathbf{y}_{exp} , along with the experimental uncertainties Σ_{exp} , we are now able to apply Bayes' theorem and estimate the posterior distribution of the model parameters:

$$P(\mathbf{x}|\mathcal{D}, \mathbf{y}_{\text{exp}}) \propto P(\mathcal{D}, \mathbf{y}_{\text{exp}}|\mathbf{x})P(\mathbf{x}). \quad (4.45)$$

4.3.1 Likelihood and uncertainties

While one uses the MCMC method to explore the parameter space and estimate the posterior distribution of the parameters, at each step the proposed state \mathbf{x}' is accepted or rejected according to the relative likelihood, or acceptance rate, which is a function that depends on the output \mathbf{y} and its deviation from the experimental observations — \mathbf{y}_{exp}

$$P(\mathcal{D}, \mathbf{y}_{\text{exp}} | \mathbf{x}) = \frac{1}{(2\pi)^m |\Sigma|} \exp \left[-\frac{1}{2} (\mathbf{y}_{\text{exp}} - \mathbf{y}) \Sigma^{-1} (\mathbf{y}_{\text{exp}} - \mathbf{y})^{-1} \right], \quad (4.46)$$

where $\Sigma = \Sigma_{\text{model}}(\mathbf{x}) + \Sigma_{\text{exp}}$ is the total covariance matrix that accounts for all the known uncertainties during the GP emulator prediction, physical model prediction, and the experimental measurements.

The model uncertainty includes only the uncertainty results from the Gaussian Process emulator prediction:

$$\Sigma_{\text{model}} = \Sigma_{\text{GP}}, \quad (4.47)$$

the experimental covariance matrix Σ_{exp} can be separated into a statistical contribution and a systematic contribution:

$$\Sigma_{\text{exp}} = \Sigma_{\text{exp}}^{\text{stat}} + \Sigma_{\text{exp}}^{\text{sys}}, \quad (4.48)$$

where the statistical uncertainties in Σ^{stat} are uncorrelated and has the form:

$$\Sigma_{\text{exp}}^{\text{stat}} = \text{diag} \left[(\sigma_{y_1}^{\text{stat}})^2, (\sigma_{y_2}^{\text{stat}})^2, \dots, (\sigma_{y_m}^{\text{stat}})^2 \right], \quad (4.49)$$

The systematic uncertainties $\Sigma_{\text{exp}}^{\text{sys}}$, however, are correlated among different observables and non-diagonal. Without detailed information on the experimental measurements, one might find it difficult to construct the systematic covariance function. Therefore I propose to use

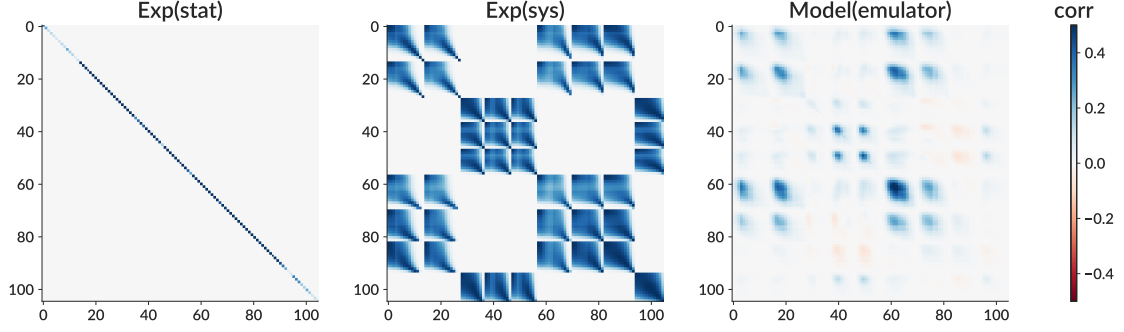


Figure 4.9: Correlation matrices for the experimental statistical uncertainties [**left**], experimental systematic uncertainties [**middle**] and the model uncertainties, in current setup only uncertainties from GP emulators prediction are considered $\Sigma_{\text{model}} = \Sigma_{\text{GP}}$.

a Pearson correlation form only among observables in the same classes⁷:

$$\Sigma_{\text{exp}}^{\text{sys}} = \frac{1}{\sigma_i \sigma_j} \exp \left[-\frac{1}{2} \left(\frac{p_{T_i} - p_{T_j}}{l} \right)^2 \right], \quad (4.50)$$

where σ_i, σ_j is the standard deviation of observable y_i, y_j correspondingly. The hyperparameter l are chosen as the p_T range of the measurements, it is set as $l = 10$ currently⁸. Figure 4.9 visualizes the correlation matrices⁹, and from left to right displays: experimental statistical uncertainties, experimental systematic uncertainties, model uncertainties.

4.4 Summary

So far I have talked about Bayes' Theorem, the choice of the prior distribution, the Bayesian calibration process, the Gaussian Process emulators which deal with the challenge of the

⁷What do we mean by observables in the same class: for example, the D -meson $R_{AA}(p_T)$ as a function of p_T in the same centrality bins are referred as the observables in the same classes. Those observables are correlated with each other but not necessary for the R_{AA} in other centralities or $v_2(p_T)$ results in any centrality.

⁸It should also be remembered that the strength of the correlation are controlled by the value of l . In principle, the larger l , the more correlation between different p_T bins, the less information that are provided by the measurements, results in a weaker constraint.

⁹The correlation matrix is the normalized covariance matrix: $\text{corr}(y_i, y_j) = \text{cov}(y_i, y_j) / \sigma_i \sigma_j$. It is plotted here for better visualization.

computational expensive model, and principal components analysis that deals with the high-dimensional output issue. Figure 4.1 summaries the practical workflow for the state-of-the-art Bayesian model-to-data comparison framework that is utilized in this thesis work:

Algorithm 5: Bayesian calibration

Input: Prior distribution of parameters $P(\mathbf{x})$, training datasets $\mathcal{D} = \{(\mathbf{x}_i, \mathbf{y}_i)\}$, experimental observation and experimental uncertainties $\mathbf{y}_{\text{exp}}, \Sigma_{\text{exp}}$

Output: posterior distribution of parameters $p(\mathbf{x}|\mathcal{D})$

Standardize output matrix \tilde{Y} and decompose it into principal space \tilde{Z} ;

Train Gaussian Process emulator on training dataset $\mathcal{D}' = \{\tilde{X}, \tilde{Z}\}$, such that the emulator can function as a fast surrogate model of the heavy quark evolution model, and make prediction of the output \mathbf{z} at every arbitrary input parameter \mathbf{x} ;

transform the output \mathbf{z} from the principal component space to physical process \mathbf{y} ;

Initialize the input parameter \mathbf{x} ;

while *Walkers not in equilibrium* **do**

 perform the MCMC random walk in the parameter space;

 generate candidates for new state;

if *accept (as a function of loglikelihood)* **then**

 update the walker to the new state;

else

 stay in current state;

end

 record the position of the parameter;

end

The final distribution of the random walkers approximates the posterior distribution of the parameters $P(\mathbf{x}|\mathcal{D})$.

In the next chapter, I will apply this framework to heavy quark transport models in heavy-ion collisions. By calibrating the model's parameters on the experimental measure-

ments, one can optimize the model's performance, and more important, obtain the posterior distribution of the parameters and estimate the desired properties of the system — in this case, the heavy quark transport coefficients.

Chapter 5

Bayesian model to data comparison

In this chapter, I will apply the state-of-the-art Bayesian model-to-data comparison framework to the heavy quark evolution model and estimate the heavy quark transport coefficients. Starting from an improved Langevin model, we will discuss with the parametrization of the diffusion coefficient, followed by the prior distribution of the parameters, construction of the training dataset, Gaussian Process Emulators training, and finally the Markov chain Monte Carlo random walk to estimate the posterior distribution of the parameters, from which we can reconstruct and estimate the transport coefficients. In the end, we will use the estimated transport coefficients to calculate the observables that are not in the training dataset, to verify the applicability of the improved Langevin model in describing the heavy quark evolution in heavy-ion collisions.

5.1 Parameter design

5.1.1 Parametrization of the transport coefficients

When constructing the heavy flavor transport coefficients, one has to keep in mind that, at sufficiently high temperature and high momenta, the interaction between heavy quarks and the medium in the strongly interacting QGP medium can be described via the perturbative QCD. On the other hand, in the low momentum and low temperature region, where the convergence of the perturbative term is rather poor [131, 148], significant contributions come from non-perturbative effects.

Therefore in this study, I used a generalized parametrization for the spatial diffusion coefficient D_s – the diffusion coefficient is the only transport coefficient we will parametrize

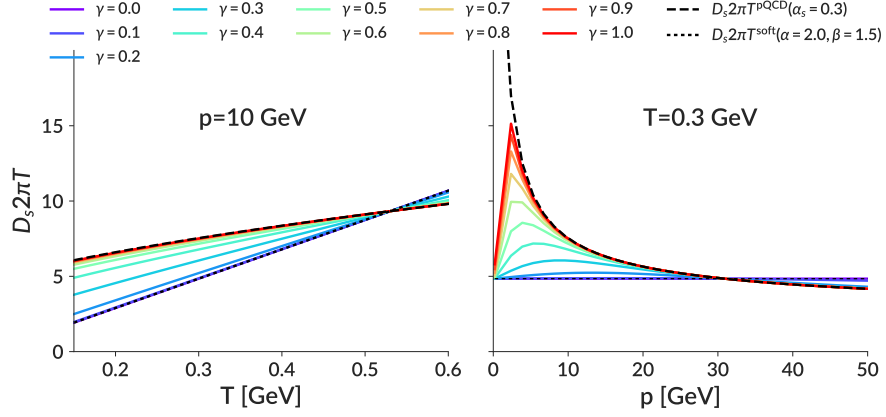


Figure 5.1: An example of the spatial diffusion coefficient parametrization with respect to γ . The soft component takes the form as $(D_s 2\pi T)^{\text{soft}} = \alpha \cdot (1 + \beta(T/T_c - 1))$, with $(\alpha, \beta) = (2.0, 1.5)$ here and is plotted as short dashed black line. The pQCD component $D_s 2\pi T^{\text{pQCD}}$ is calculated by summing the leading order $2 \rightarrow 2$ elastic scattering channels and taking a constant strong coupling as $\alpha_s = 0.3$. It is plotted as black dashed line.

in this study, whilst the others can be determined with the Einstein relationship. It is parametrized as a combination of a soft component and a pQCD component:

$$D_s 2\pi T(\alpha, \beta, \gamma; T, p) = \frac{1}{1 + (\gamma^2 p)^2} (D_s 2\pi T)^{\text{soft}} + \frac{(\gamma^2 p)^2}{1 + (\gamma^2 p)^2} (D_s 2\pi T)^{\text{pQCD}}, \quad (5.1)$$

in which the soft component $(D_s 2\pi T)^{\text{soft}}$ is parametrized as being linearly dependent on temperature:

$$(D_s 2\pi T)^{\text{soft}} = \alpha \cdot (1 + \beta(T/T_c - 1)). \quad (5.2)$$

The parametrization accounts for non-perturbative effects, and is also the diffusion coefficient in the $p = 0$ GeV/c limit. One can compare its value with the lattice QCD calculation of the spatial diffusion coefficient at zero momentum. The parameter α represents the spatial diffusion coefficient at zero momentum near T_c , and the parameter β is the slope of $D_s 2\pi T(p = 0)$ above T_c . The linear temperature-dependent relation is inspired by the approximate linear temperature dependence of the shear viscosity to entropy density

ratio[44].

The pQCD component $(D_s 2\pi T)^{\text{pQCD}}$ is the contribution from the perturbative processes, and is related to \hat{q}^{pQCD} via $(D_s 2\pi T)^{\text{pQCD}} = 8\pi/(\hat{q}^{\text{pQCD}}/T^3)$. The value of the pQCD component is dependent on the coupling constant, where I choose a fixed coupling constant $\alpha_s = 0.3$. It is calculated by summing over all the leading order $2 \rightarrow 2$ scatterings between heavy quarks and thermal partons (light quarks and gluons) as stated in Sec. 4 and the temperature and momentum dependence is shown in Fig. 3.9.

The parameter γ controls the ratio between the soft component and the pQCD component. For $p < 1/\gamma^2$, the soft component dominates while for $p > 1/\gamma^2$ pQCD component dominates. The momentum dependence of the diffusion coefficient varies through different values of γ . Figure. 5.1 shows the combined diffusion coefficient for different values of γ as a function of temperature at fixed momentum [left] and as a function of momentum at fixed temperature [right]. The short dashed line is the soft component $D_s 2\pi T^{\text{soft}}$ taking $(\alpha, \beta) = (2.0, 1.5)$, while the long dashed black line is the pQCD component $D_s 2\pi T^{\text{pQCD}}$ taking the coupling constant $\alpha_s = 0.3$. The value of γ changes from 0 to 1 while the line color changes from violet to red in the reversed rainbow color scheme. As shown in the figure, a small value of γ (the violet lines) indicates that non-perturbative processes affect the heavy quark dynamics into very high momentum region, while a large value of γ (the red lines) indicates a quick conversion to the pQCD dominated region.

Therefore, the heavy quark transport coefficients are encoded by the parameters:

- α, β : the interception and slope of soft component $(D_s 2\pi T)^{\text{soft}}$;
- γ : the parameter which controls the contribution from $(D_s 2\pi T)^{\text{soft}}$ and $(D_s 2\pi T)^{\text{pQCD}}$.

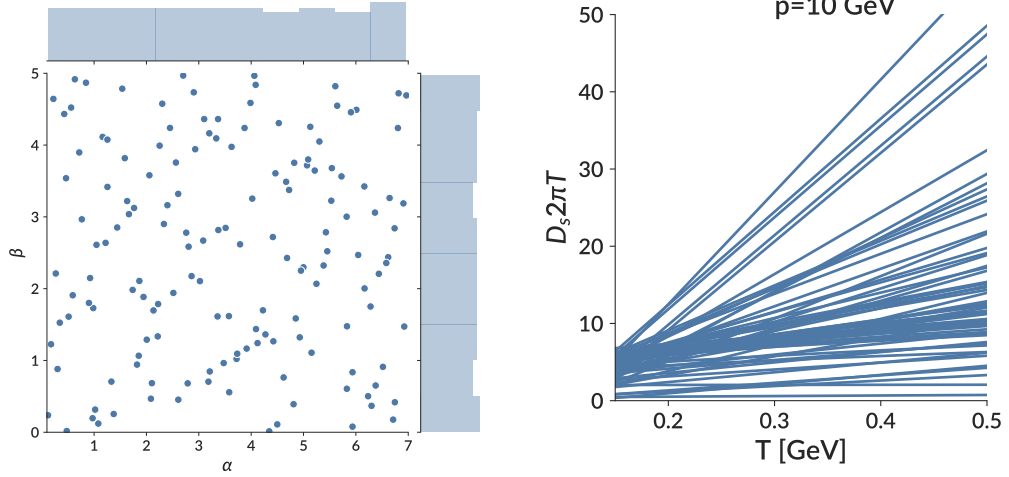


Figure 5.2: [LEFT]: Input parameters from the training dataset, which are sampled from the prior distribution. [RIGHT]: The prior range for the spatial diffusion coefficient with respect to temperature at fixed momentum $p = 10$ GeV.

5.2 Preparing the training dataset \mathcal{D}

Once we have constructed the parametrization of the heavy flavor transport coefficients, one can apply the Bayesian model-to-data comparison framework to calibrate the heavy flavor evolution model to experimental data, and obtain the posterior distribution of the parameters. However, in practice for a computationally expensive model, a surrogate model is often used to effectively predict the model's output at any arbitrary parameter point. Thus we choose Gaussian Process Emulators to function as the fast surrogate model to the heavy flavor evolution model.

5.2.1 Design points \tilde{X}

The training of Gaussian Process Emulator requires a construction of the training dataset: n sets of input parameters $\tilde{X} = \{\mathbf{x}_1, \mathbf{x}_2, \dots, \mathbf{x}_n\}$ are chosen, the heavy flavor observables \mathbf{y}_i are evaluated by the heavy quark transport model taking each input parameter \mathbf{x}_i . This is our training dataset $\mathcal{D} = \{x_i, y_i\}$. A poor choice of the input parameters could result in

Table 5.1: Prior range and description for the parameters that determines the diffusion coefficient

Parameter	Description	Range
α	$D_s 2\pi T$ at T_c	0.1 - 7
β	slope of $D_s 2\pi T^{\text{soft}}$ above T_c	0 - 5.0
γ	ratio between $D_s 2\pi T^{\text{soft}}$ and $D_s 2\pi T^{\text{pQCD}}$	0 - 0.6

significant bias to the Gaussian Process Emulator training, and increase the computational time. When one designs the input parameters, there are a few comments in practice:

- 1 First of all, one should specify a proper range for the parameter space since we have assumed that the probability of parameters taking the value outside of the parameter space is zero. This range should therefore be sufficiently large to cover all the possibilities but not too large as it will increase the computational time and random exploration difficulty.
- 2 Secondly, distributing the parameter points in the parameter space varies among different algorithms. For a grid uniform distribution in a p -dimensional space – that is evenly distributing k different values of parameters in every dimension – it requires $\mathcal{O}(k^p)$ total points, that’s too many parameter sets in a high-dimensional space. In this study, we use an advanced Latin hypercube algorithm, which semi-randomly generates the design points in the p -dimensional parameter space. The Latin hypercube algorithm aims at spreading the samples evenly across the parameter space by maximizing the distance among parameters, and therefore a small amount of samples $\mathcal{O}(10p)$ is sufficient enough to train the Gaussian Process Emulator to interpolate the p -dimensional parameter space effectively.

Table. 5.1 lists the parameter ranges for the corresponding parameters in the heavy flavor evolution model. A uniform distribution of the design points is sampled and displayed in the left panel of Fig. 5.2, which visualizes a joint distribution of 60 design points pro-

Table 5.2: D -meson variables to be compared between model calculation and experimental measurements

Experiment	variables	kinematic cut	centrality
AuAu@200 GeV	$R_{AA}(p_T)$	$2 \leq p_T \leq 8 \text{ GeV}/c, y < 1$	0-10
	$v_2(\text{EP})(p_T)$	$1 \leq p_T \leq 7 \text{ GeV}/c, y < 1$	0-80
	$v_2(\text{EP})(p_T)$	$1 \leq p_T \leq 7 \text{ GeV}/c, y < 1$	10-40
PbPb@2.76 TeV	$R_{AA}(n_{\text{part}})$	$5 \leq p_T \leq 8 \text{ GeV}/c, y < 0.5$	0-10, 10-20, ..., 50-80
	$R_{AA}(n_{\text{part}})$	$8 \leq p_T \leq 16 \text{ GeV}/c, y < 0.5$	0-10, 10-20, ..., 50-80
	$v_2(\text{EP})(p_T)$	$2 \leq p_T \leq 16 \text{ GeV}/c, y < 0.8$	30-50
PbPb@5.02 TeV	$R_{AA}(p_T)$	$3 \leq p_T \leq 36 \text{ GeV}/c, y < 0.5$	30-50
	$v_2\{2\}(p_T)$	$1 \leq p_T \leq 40 \text{ GeV}/c, y < 1$	10-30
	$v_2\{2\}(p_T)$	$8 \leq p_T \leq 40 \text{ GeV}/c, y < 1$	30-50

jected in the (α, β) plane. This represents the prior distributions of the parameters. The diffusion coefficient, taking the value of the design points, is plotted in the right figure of Fig. 5.2, as a function of temperature at fixed momentum $p = 10 \text{ GeV}$. The prior range for the diffusion coefficient is sufficiently large, spanning from a very strong interaction with $D_s 2\pi T$ close to zero to a weaker interaction with a large $D_s 2\pi T$. It is designed to cover the optimal value in order to describe the experimental measurements.

5.2.2 Model's output \tilde{Y}

At each of the design point \tilde{x}^1 , 5000 minimum bias hydro events are simulated and heavy quarks are oversampled in order to calculate the final observables $\tilde{\mathbf{y}} = (R_{AA}, v_2)$. Table. 5.2 summarizes the D -meson observables and corresponding kinetic cut for different collision systems.

In Fig. 5.3 I compare 60 sets of the model's calculation (the colored lines) with the experimental data (black dots with error-bars) for the heavy quark evolution in Au-Au collisions at 200 GeV, Pb-Pb collisions at 2.76 and 5.02 TeV. We can see that with the

¹Here the tilde simple \tilde{x}, \tilde{y} represents the training datasets, whose outputs are calculated from the heavy quark evolution model. It is used to distinguish the predicted dataset, which is later obtained from the GP Emulators and labeled with the star symbol x_*, y_* .

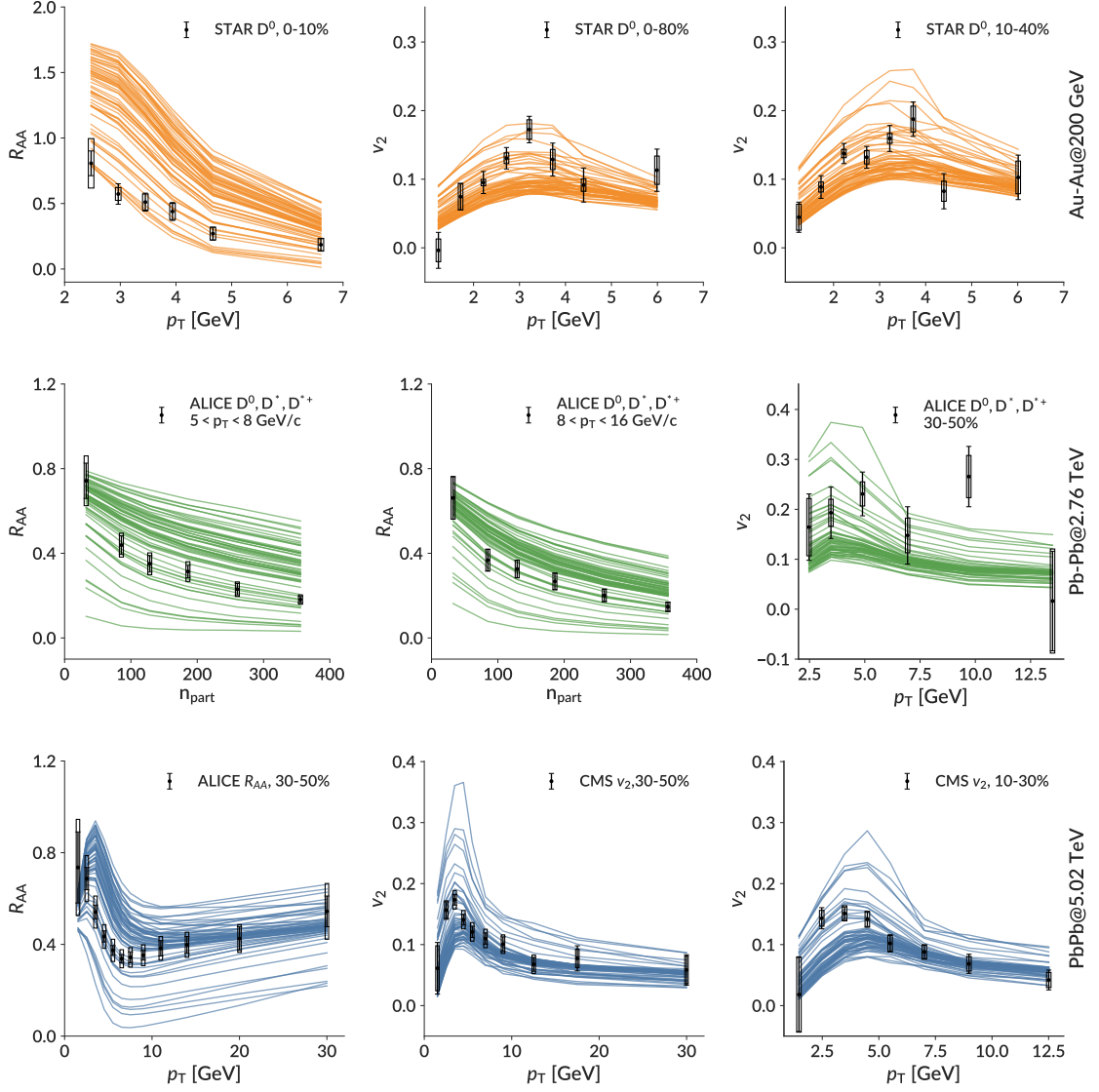


Figure 5.3: Improved Langevin model calculation of D -meson observables, compared to experimental data spanning over the full range of explored parameter space (i.e. the “prior”). Each frame contains 60 results from the calculations, corresponding to 60 design points of the analysis. From top to bottom: **[top]** Au-Au collisions at 200 GeV: D -meson p_T differential R_{AA} in 0-10% centrality, $v_2(p_T)$ in 0-80%, 10-40% centralities; **[middle]** Pb-Pb collisions at 2.76 TeV: D -meson R_{AA} as function of participant number n_{part} at high momentum range $5 \leq p_T \leq 8$ GeV and $8 \leq p_T \leq 16$ GeV, p_T differential $v_2(p_T)$ in 30-50% centrality; **[bottom]** Pb-Pb collisions at 5.02 TeV: D -meson R_{AA} in 30-50% centrality and $v_2(p_T)$ in 30-50% and 10-30% centralities. Experimental data are measured by STAR[69], ALICE[149, 18, 150, 19], and CMS[36, 127] collaborations.

unconstrained prior parameter sets, the model’s output spans a wide range in the physical observable space. The training dataset $\mathcal{D} = (\tilde{X}, \tilde{Y})$ is used to training the Gaussian Process Emulators. The details regarding the construction of the Gaussian Process kernel, the principal component analysis transformation can be found in Sec. 4.

Once the Gaussian Process Emulators are ready, one can perform the MCMC random walk to calibrate the heavy quark evolution model to the experimental measurements.

5.3 Results

5.3.1 A closure test: calibration to pseudo-experimental data

Before I apply the Bayesian model-to-data analysis framework to calibration the heavy quark evolution model to the experimental measurements y_{exp} , it is not a bad idea to conduct a closure test calibrate the heavy flavor evolution model to a pseudo-experiment result in order to verify its validity.

The pseudo-experiment result is proposed as follows: I generate one set of “pseudo parameters”: $\mathbf{x}_{\text{pseudo}} = (\alpha, \beta, \gamma) = (1.55, 2.59, 0.28)$, which are treated as the “true” values for the parameters in the heavy quark evolution model. Taking the “true” values, the improved Langevin model calculates the heavy flavor observables y_{pseudo} , which are plotted as the red dots in Fig. 5.4 for Pb-Pb collisions at 5.02 TeV. The central values are the model’s calculation of D -meson p_T differential R_{AA} at 30-50% centrality, v_2 at 10-30%, 30-50% centralities, and the errorbars are inherited from the ALICE measurements[150, 19] for corresponding p_T .

The goal for such an experiment is to apply the Bayesian framework to calibrate the heavy quark evolution model to the pseudo-experiment results, and compare the posterior distributions of the parameters. One would expect:

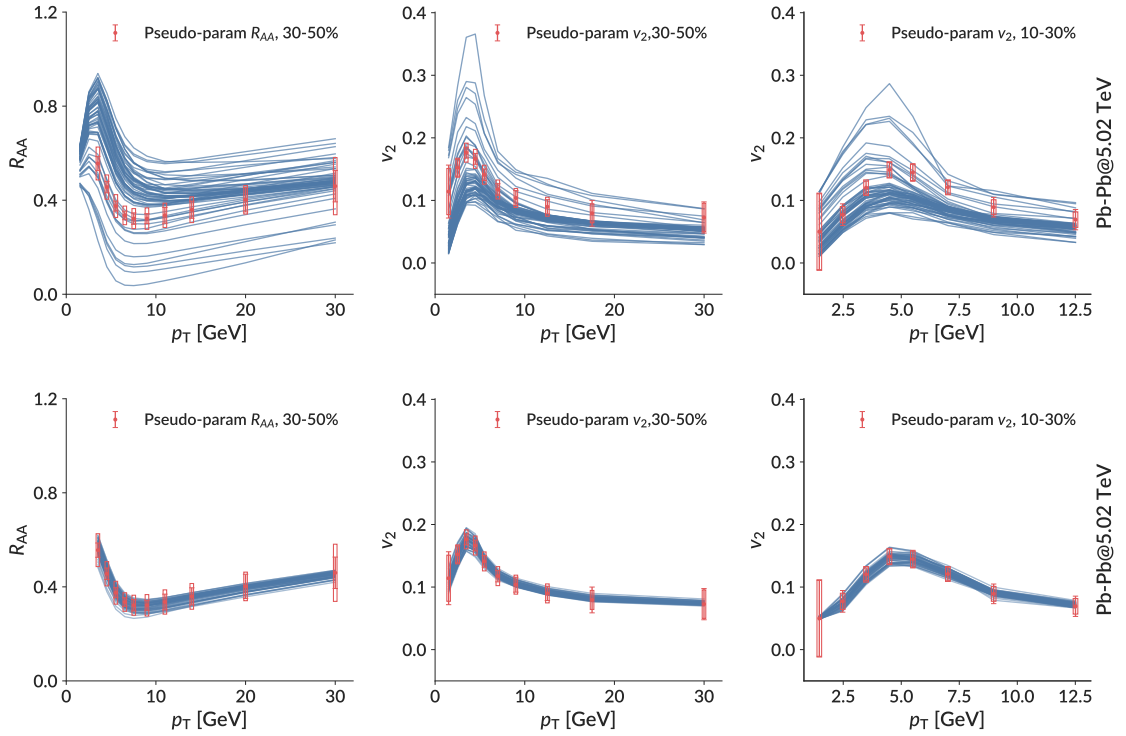


Figure 5.4: [Upper] Improved Langevin model calculation of D -meson observables in Pb-Pb collisions at 5.02 TeV taking the input parameters from the prior distribution; [Lower]: Calculation from Gaussian Process Emulators taking the parameters from the posterior distribution.

- After the calibration, the heavy quark evolution model is able to describe the results of the pseudo-experiment y_{pseudo} ;
- The posterior distributions of the parameters should be able to recover with the values of “pseudo parameters”.

The results of the calibration are shown in Fig. 5.4 and Fig. 5.5. From the lower panel of Fig. 5.4 one can see that with the calibration, the heavy quark evolution model indeed is able to describe the experimental data. In Fig. 5.5 I show the posterior distributions of the parameters (α, β, γ) , where the diagonal panels show the marginal distribution for a single parameter with all the other parameters integrated out, and the off-diagonal panels show the correlation between pairs of the parameters. The green colors correspond to the calibration to the “pseudo experiment” with the current experimental uncertainties, while the red colors correspond to the calibration to the “pseudo experiment” with the reduced experimental uncertainties (re-scaled by a factor of 0.2). The evaluated median value and the standard deviation are labeled as $\bar{x}_{\pm\sigma}$. One can see that with sufficient precise measurements, the Bayesian analysis is able to recover the “true” values of the parameters. The remaining deviation mainly comes from the uncertainty resulting from applying the Gaussian Process Emulator during the MCMC exploration. Our closure test has passed.

5.3.2 Calibration to experimental measurements

In this section, I will apply the Bayesian framework to real experimental measurements. In Fig. 5.3 I have already presented the calculation of the heavy quark evolution model taking the parameters from the prior distribution. The large spread visualizes the range of initial parameter values, which reflects the prior distribution of the parameters. After calibration to experimental data, the corresponding observables are visualized in Fig. 5.6, which are the Emulators’ prediction of 50 randomly selected parameters from the posterior

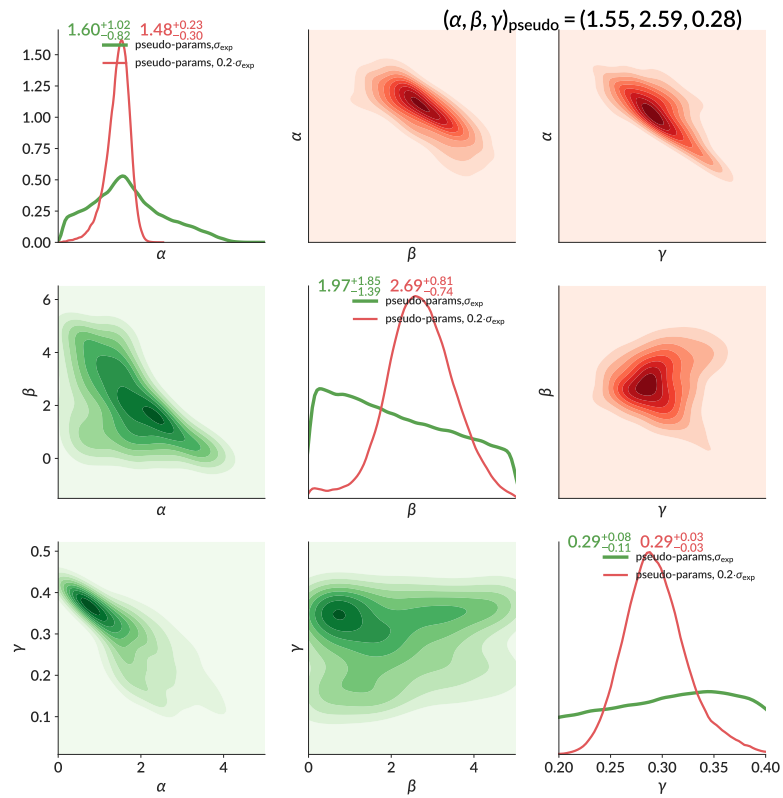


Figure 5.5: Posterior distribution of the diffusion coefficient parameters (α, β, γ) for calibrating on the “pseudo experimental” results. The green distribution corresponds to the calibration taking the current experimental uncertainties; while the red distribution corresponds to the calibration taking the scaled experimental uncertainties (scaled by 0.2).

distribution. They have been constrained with small variance. We find that after calibration, the improved Langevin approach is capable of describing the experimental data reasonably well. The biggest deviation is found for the R_{AA} points at very peripheral centrality and low p_T : peripheral collisions are not well described by our hydrodynamical background. Also the modeling of hadronization in the low p_T region is challenging due to significant non-perturbative effects.

posterior distribution $P(\mathbf{x}|\mathcal{D}, \mathbf{y}_{\text{exp}})$

The main results of the Bayesian analysis are the posterior probability distribution of the input parameters (α, β, γ) , which are displayed in Fig. 5.7. There are four different colors corresponding to four different Bayesian analyses calibrating on four different subsets of experimental measurements. For example, the orange color corresponds to the calibration to the experimental measurements for heavy quark observables in Au-Au collisions at 200 GeV, and the red one corresponds to the calibration to all the experimental observables regarding heavy flavors in three different collision systems: Au-Au collision at 200 GeV, Pb-Pb collision at 2.76 and 5.02 TeV. In principle, for a physical system that shares the universal properties, the more information and more precise measurements we have, the better constraints we will achieve for the posterior distribution estimation. Therefore for the estimation over different datasets, we would expect a distribution centering around similar values but spreading with different width. The width of the posterior distribution is affected by the uncertainties we have applied in the analysis. It explains that for the analysis (red distribution) using all the experimental observations we find the most narrow distribution.

Taking a closer look at the posterior distribution, each marginal distribution is annotated with the median value plus/minus 1 standard deviation $(\bar{x}_{\pm\sigma})$, which corresponding to the (16%, 50%, 84%) percentile values in the posterior distribution. We have observed that:

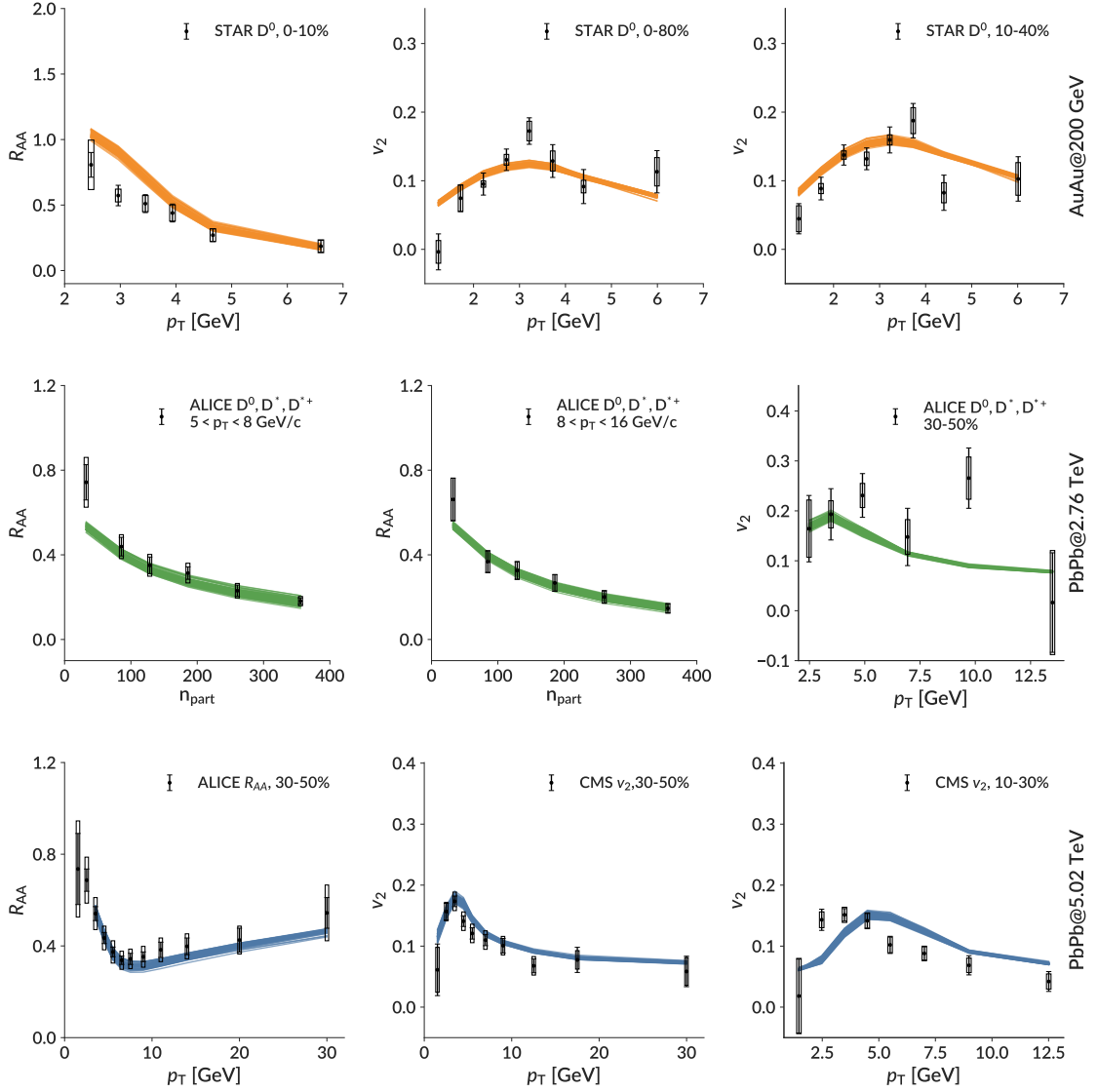


Figure 5.6: Gaussian Process Emulator prediction for 50 random parameter sets sampled from the posterior distribution. This figure is similar to Fig. 5.3 but with the input parameters chosen from the posterior distribution, and the outputs are predicted from the Gaussian Process Emulators.

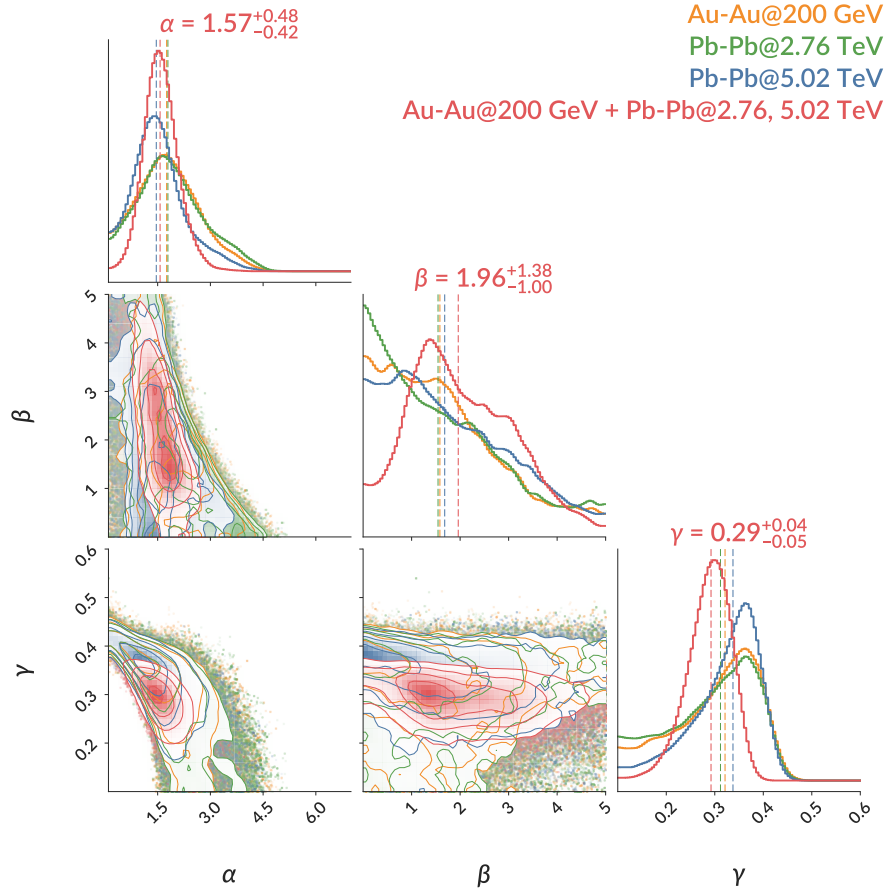


Figure 5.7: Posterior distribution of the transport coefficients parameters (α, β, γ) for individual collision systems as well as the global calibration. The diagonal plots are the histograms of the marginal distribution for each parameter with the others integrated out, while the off-diagonal plots display the joint distribution between pairs of parameters. The orange, green, blue and red distributions refers to the calibration on different sets of experimental measurements.

- The parameter α is well constrained with a peak value around (1.5 \sim 2.0) for all four analyses. This parameter determines the spatial diffusion coefficient $D_s 2\pi T$ at 0 momentum near T_c .
- The parameter γ controls the ratio between the soft component $(D_s 2\pi T)^{\text{soft}}$ and the pQCD component $(D_s 2\pi T)^{\text{pQCD}}$. It has a distribution which peaks around (0.25 \sim 0.35). It implies that the contribution from soft component is comparable with the one from $(D_s 2\pi T)^{\text{pQCD}}$ even at a sufficient large momentum range ($p_T \simeq 10$ GeV). As $\gamma^2 p = 1$ is the momentum region where the $(D_s 2\pi T)^{\text{soft}}$ and $(D_s 2\pi T)^{\text{pQCD}}$ contribute equally.
- Although the slope parameter β is poorly constraint, it shows a negative correlation with the parameter α .

heavy quark transport coefficients

Having established the posterior distribution of the parameters, one can now estimate the heavy quark transport coefficients according to Eqn.5.1. Figure. 5.8 displays the estimation of the posterior range for the charm quark diffusion coefficient. The gray area represents the prior range explored by the parametrization, and the red band is this posterior estimation with 90% credible region, with the solid red line being its median².

On the upper panel of Fig. 5.8, the diffusion coefficient is displayed with respect to temperature for fixed momentum: for the zero momentum limit ($p = 0$ GeV), the combined diffusion coefficient is solely determined by the soft component $(D_s 2\pi T)^{\text{soft}}$, with $D_s 2\pi T(p = 1) \sim 1 - 3$ around T_c . For our finite temperature region, its temperature dependence is not far from a simple linear relationship with a positive slope.

²Here the posterior distribution from the analysis over all the datasets are used, however, I should mention that the estimated posterior range for transport coefficients $D_s 2\pi T$ do not differ much between the analysis over different datasets.

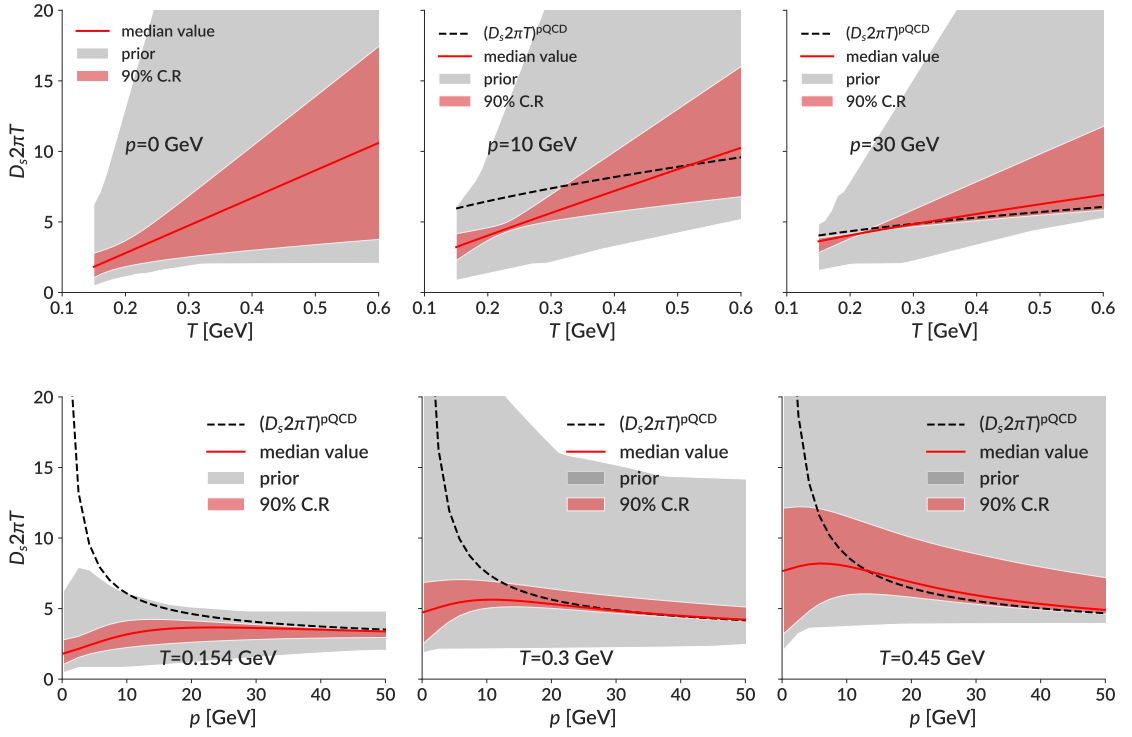


Figure 5.8: Posterior range of the spatial diffusion coefficient obtained from the the Bayesian analysis calibrated on the datasets of all three different collision systems. **[top]:** the spatial diffusion coefficient $D_s 2\pi T$ with respect to temperature at fixed momentum; **[bottom]** the spatial diffusion coefficient $D_s 2\pi T$ with respect to momentum at fixed temperature. The gray area refers to the prior range that the parametrization explores, and the red region refers to the posterior range after the calibration with 90% credible region. The red lines are the diffusion coefficient using the median value of the posterior distribution.

In addition, we observe that the 90% credible region suffers the least uncertainties in a temperature region around $T \sim 0.2 - 0.25$ GeV, which we argue it is the approximate average temperature that heavy quarks experience during their propagation through the medium. At higher temperature, the posterior range of the spatial diffusion coefficient broadens. A likely reason for this trend is – in addition to the larger deviation between the two $(D_s 2\pi T)^{\text{soft}}$ and $(D_s 2\pi T)^{\text{pQCD}}$ components – the short amount of time that the QGP medium retains this high temperature. As the system expands quickly, it rapidly cools down, leaving only a short period of time for the heavy quark to interact with the medium at such a high temperature, and therefore less information can be obtained.

On the lower panel of Fig. 5.8 we explore the momentum dependence of the charm quark diffusion coefficient at fixed temperatures. As the heavy quark momentum increases, the uncertainties of the posterior range decrease, and at sufficiently high momentum, the behavior of the combined transport coefficient converges to the pQCD-like: in our case, it is calculated by summing the leading order $2 \rightarrow 2$ scattering processes. The only freedom left in the parametrization is the pre-factor $(\gamma^2 p)^2 / (1 + (\gamma^2 p)^2)$, which varies merely for high momenta. In the low momentum region, the diffusion coefficient shows completely different behavior from the pQCD calculation, which can be only the result of non-negligible contributions from non-perturbative effects. Such a contribution is clearly needed in order to obtain a realistic description of heavy quark observables at low and intermediate momentum region.

5.4 A more flexible parametrization

So far we have discussed the heavy quark evolution model based on an improved Langevin model, which takes a parametrized diffusion coefficient as input. With an improved computational model, more parameters, and additional observables, the Bayesian analysis would

obtain more constraints on the properties of the QGP medium.

One significant change to the heavy quark evolution model is the addition of the pre-equilibrium stages for the soft medium, i.e., we now use a free-streaming evolution to simulate the dynamics of the collision system before the thermalization of the QGP medium, and correspondingly an energy loss stage for heavy quarks during the pre-equilibrium stage.

A second change is the relaxation of the fixed coupling constant for the $(D_s 2\pi T)^{p_{\text{QCD}}}$ component, now we allow the coupling constant to be tuned from a range of $\alpha_s \in (0.1, 0.6)$. This relaxation would not increase our constraint over the heavy flavor transport coefficients. On the contrary, it will significantly enlarge the parameter space, but leads to a more rigorous and complete exploration.

A third improvement is the consideration of the deviation between the theoretical model and true physics, which results in an additional uncertainty taken into account while one constructs the likelihood during the MCMC random walk exploration.

5.4.1 Pre-equilibrium dynamics

It is generally assumed that after the two nuclei collide with each other, the system takes a time of τ_0 fm/c to reach the local thermal equilibrium (rapidly), and the hydrodynamical model is valid to simulate the evolution of the QGP medium after that time. Computationally, pre-equilibrium dynamics is not required for our framework based on the relativistic viscous hydrodynamics model, as the key initial condition for the hydrodynamical model is the initial energy/entropy density, which can be generated by a parametric model (such as `TRENTO`) or other non-dynamical initial condition models. Since they map the nuclear thickness function to an energy/entropy deposition at any finite time τ , one can choose to initialize the system directly at the hydro start time τ_0 instead of 0^+ . In this way one does not need to consider the pre-equilibrium stage evolution. Such simplification of the

QGP evolution is commonly adopted in practice, and somehow does not prevent a good description of the experimental data in the soft section.

With a pure hydrodynamical approach, which ignores the details for how the system approaches equilibrium, the observed large momentum anisotropy can only be explained by the fact that the thermalization of the medium happens rapidly, within the first fm/c. Moreover, the static initialization of the QGP medium has to compensate in some way for the lack of initial flow, coming from the pre-equilibrium dynamics. A net effect is a decrease of the radial flow for the system, which eventually results in an underestimation of the mean p_T for identified particles [44].

Regarding the heavy quarks evolution, it has been argued that pre-equilibrium phase evolution could impact the heavy meson R_{AA} by about 20-25% if one applies a Boltzmann transport equation to the momentum evolution of the heavy quarks in heavy-ion collisions [151]³.

The most simple pre-equilibrium dynamics mode is free-streaming, where the system is treated as a massless parton gas which expands without interaction. Such a treatment can be considered as the extreme limit of a weakly interacting system. At a time τ_0 , the system undergoes an instantaneous thermalization and starts the hydrodynamical evolution. Freestreaming considered as an opposite limit of strongly interacting system⁴.

During the pre-equilibrium stage, the heavy quarks already start to interact with the medium and lose energy. However, since the system at this stage is still off-equilibrium, both kinetically and chemically, the local temperature is undefined. We, therefore, use the Landau matching to obtain the flow velocity $\vec{\beta}$ and energy density ϵ from the energy-

³Of course I should point out that one can, still, mimic the impact of the pre-equilibrium evolution using an early thermalized QGP medium.

⁴The sudden transition from a weakly interacting limit to a strongly interacting limit is a bit crucial. One would expect a much more smooth transition, which can be simulated by a dedicated weakly coupled effective kinetic model that gradually connects those two. For such kinetic modeling of the pre-equilibrium dynamics, please refer to [152, 153]. Other theoretical studies, including IP-Glasma model which describes the system evolution by solving the classical Yang-Mills equations, and strong coupling approaches.

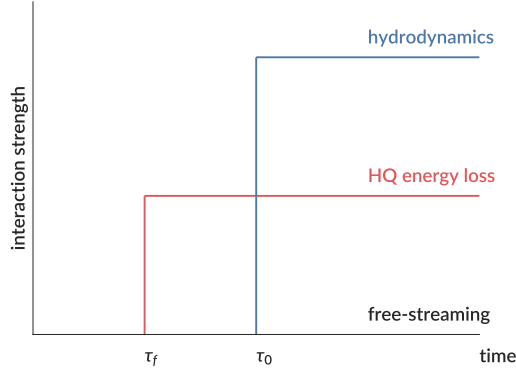


Figure 5.9: A septic to demonstrate the pre-equilibrium interaction

momentum tensor $T^{\mu\nu}$ in the pre-equilibrium stages, and convert it to an effective temperature using the QCD Equation of State (EoS) ⁵.

Heavy quarks are allowed to choose at which time they start to interact with the medium and lose energy by assigning a time parameter τ_f . For $\tau < \tau_f$, heavy quarks experience free-streaming with the medium partons; for $\tau_f < \tau < \tau_0$, heavy quarks start to lose energy while the medium continues to expand freely and take its path to equilibrium; for $\tau > \tau_0$, the system thermalizes and starts hydro evolution, meanwhile, the heavy quarks propagate through the thermal QGP medium. A smaller value of τ_f corresponds to a faster generation of color degrees of the freedom that can interact with the heavy quarks, and a larger value of τ_f corresponds to a turn-off of the pre-equilibrium energy loss for heavy quarks.

5.4.2 More inputs parameters

The value of the diffusion coefficient depends on the interaction strength between the heavy quarks and the medium, therefore by varying the value of the coupling constant, one would expect a different temperature and momentum dependence for the heavy quark transport coefficients. Figure. 5.10 present the $(D_s 2\pi T)^{p\text{QCD}}$ calculated in leading order pQCD with

⁵The energy momentum tensor $T^{\mu\nu}$ can be calculated by summing over all the particle components p^μ, p^ν .

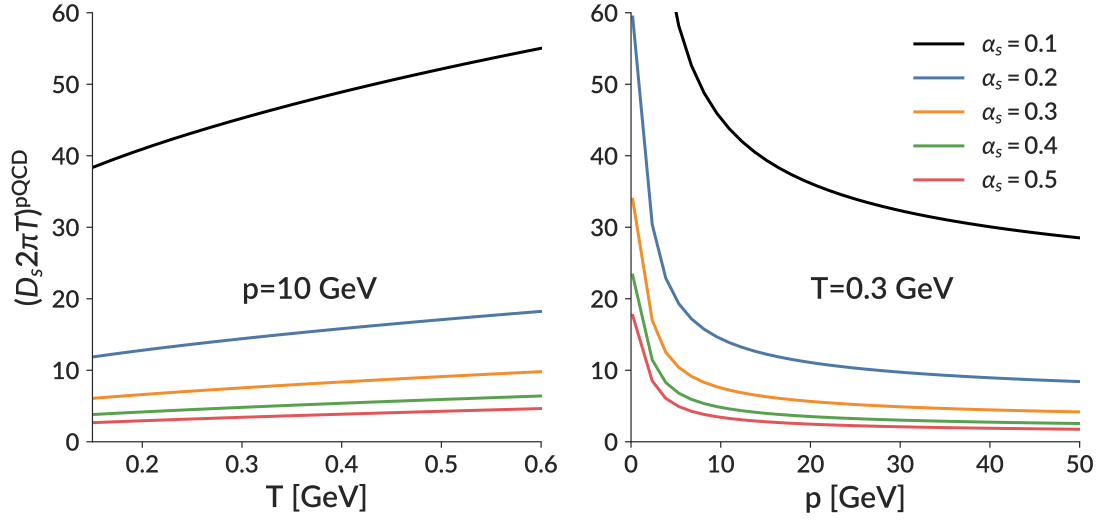


Figure 5.10: Heavy quark special diffusion coefficient as a function of temperature [**left**] and as a function of momentum [**right**] calculated via a leading order pQCD approach.

different values of α_s from $0.1 \sim 0.6$. With a small coupling constant, for example the black lines correspond to $\alpha_s = 0.1$, the interactions between heavy quarks and the medium are weak, results to a large value for the diffusion coefficient.

We can relax the value of the coupling constant α_s and treat it as another tunable parameter. The diffusion coefficient parametrization is then updated as:

$$D_s 2\pi T(\alpha_s, \alpha, \beta, \gamma; T, p) = \frac{1}{1 + (\gamma^2 p)^2} (D_s 2\pi T)^{\text{soft}} + \frac{(\gamma^2 p)^2}{1 + (\gamma^2 p)^2} (D_s 2\pi T)^{\text{pQCD}}(\alpha_s), \quad (5.3)$$

and the new prior range for the diffusion coefficient is plotted in Fig. 5.11 for different temperature/momentum values. Each black line represents one sample randomly drawn from the prior distribution and they are spanning over a much wider range – particularly in the low temperature and low momentum region, comparing to the previous prior range shown as the gray area in Fig. 5.8.

With the pre-equilibrium stage evolution, and the additional parameter as coupling con-

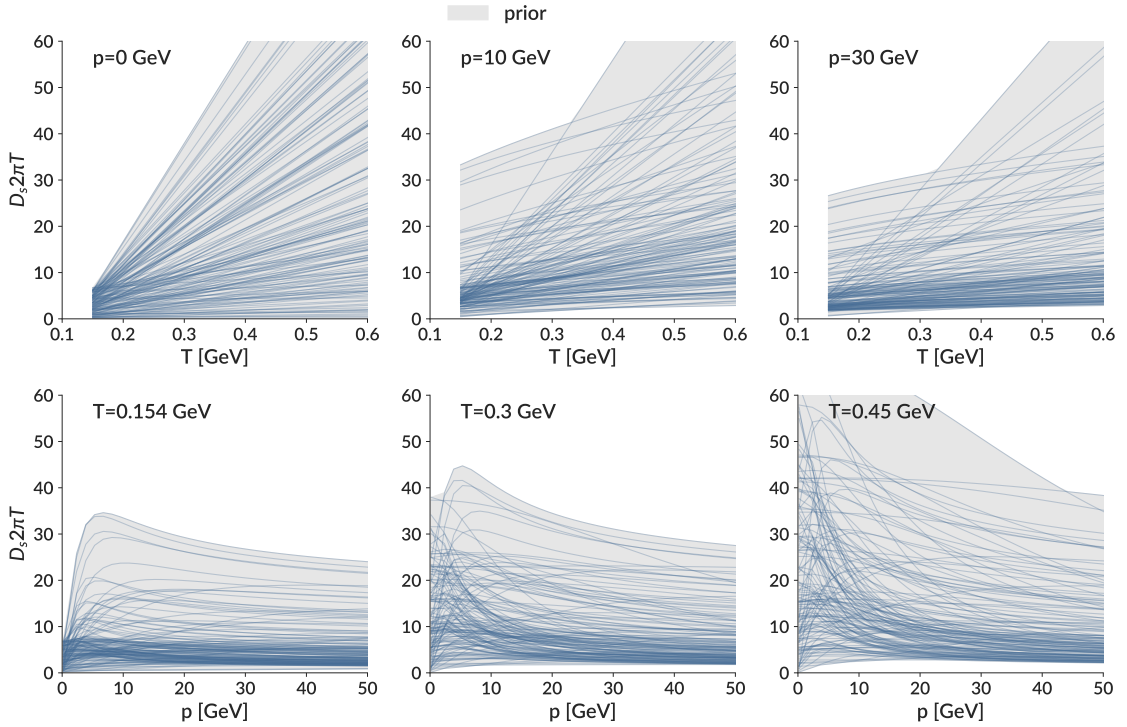


Figure 5.11: Prior range of the charm quark diffusion coefficient $D_s 2\pi T$ use the new parametrization of $(\alpha_s, \alpha, \beta, \gamma)$.

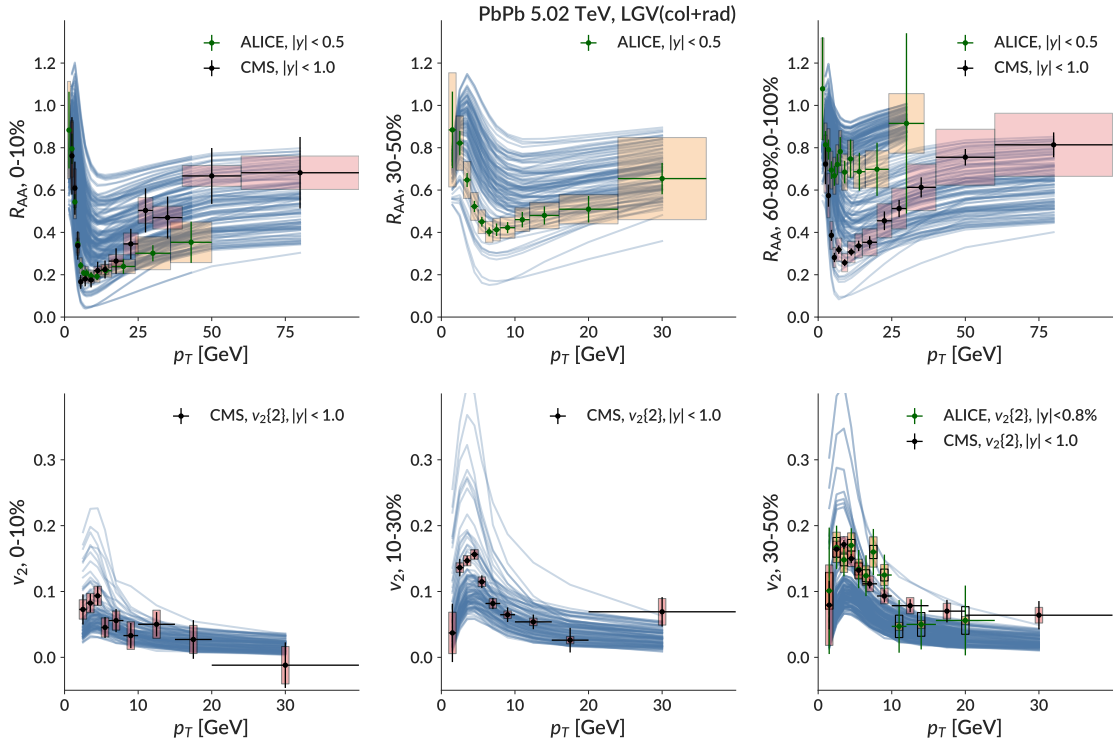


Figure 5.12: Improved Langevin model calculation of D -meson observables in Pb-Pb collisions at 5.02 TeV spanning over the full range of the parameter space and compared to experimental measurements (black errorbars). Each frame contains the calculation for evaluating 150 parameters sets.

Parameter	Description	Range
α_s	strong coupling constant	0.1 - 0.6
α	$D_s 2\pi T$ at T_c	0.1 - 7
β	slope of $D_s 2\pi T^{\text{soft}}$ above T_c	0 - 5.0
γ	ratio between $D_s 2\pi T^{\text{soft}}$ and $D_s 2\pi T^{\text{pQCD}}$	0 - 0.6
τ_f	free-streaming time	0.1 - 1

Table 5.3: Prior range and description for the parameters that determines the diffusion coefficient

stant α_s , now we have an updated list of parameters in the heavy quark evolution model listed in Tab. 5.3.

Additional parameters enlarge the parameter space, and require more design points, which increase the computational time. For this new calibration, I generate 150 sets of parameters $\tilde{\mathbf{X}} = \{\mathbf{x}_1, \dots, \mathbf{x}_n\}$, and at each parameter point, the heavy flavor observables $\tilde{\mathbf{Y}} = \{\mathbf{y}_1, \dots, \mathbf{y}_n\}$ — D -meson R_{AA} and v_2 at different centralities in Pb-Pb collisions at 5.02 TeV, plotted in Fig. 5.12 – are evaluated with the improved Langevin model. This is our training dataset $\mathcal{D} = \{\tilde{\mathbf{X}}, \tilde{\mathbf{Y}}\}$ for training the Gaussian Process Emulators. A MCMC random walk exploration of the parameter space will follow up and calculate the posterior distribution of the parameters as one calibrate the model to the experimental measurements.

5.4.3 Posterior results

The posterior distributions of the parameters with the new parametrization is plotted in Fig. 5.13, where again the diagonal frames display the marginal distribution of each individual parameters with all the others integrated out, and the off-diagonal frames visualize the joint distribution between each pair of parameters.

Comparing to the results from previous calibration shown in Fig. 5.8, one finds:

- The coupling constant has a fairly narrow distribution with a peak around $\alpha_s = 0.29$ and one standard deviation as ± 0.07 . It is a nice coincidence that the peak value is

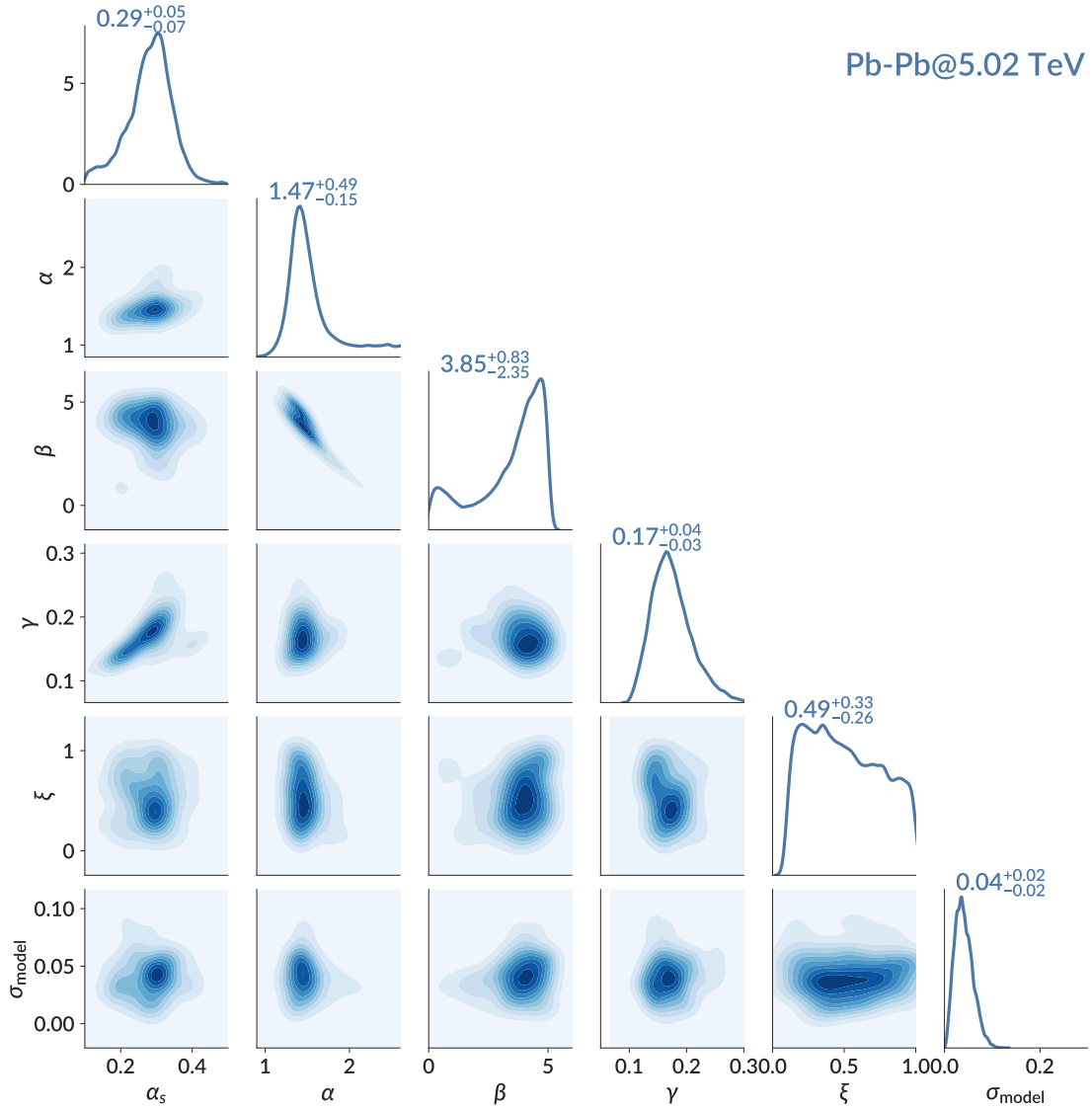


Figure 5.13: Posterior distribution of the heavy quark evolution model parameters ($\alpha_s, \alpha, \beta, \gamma, \xi$) for the calibration on the experimental measurements of D -meson R_{AA} and v_2 . In addition, the theoretical model's uncertainty are included.

not far away from the fixed coupling constant that we have been used in previous studies as $\alpha_s = 0.3$.

- The parameter α has a remarkable narrow distribution, with the estimated value around $\alpha = 1.47$. Recall that this value represents the charm quark diffusion coefficient at zero momentum limit near T_c , it indicates a strong interaction between heavy quarks and the medium in the low temperature region.
- The distribution of the slope parameter for the soft component β is quite broad, but has a trend to prefer a larger value. This implies a clear strong temperature-dependent soft component contribution. However, isolating the two parameters α and β separately leads to an incomplete picture of the soft component $(D_s 2\pi T)^{\text{soft}}$. The joint distribution between those two shows a clear negative correlation, similar to the previous analysis. Such a negative correlation implies a small value for α and a large value for β or vice versa, but both cannot be large or small at the same time. A better way to visualize the posterior distribution is shown in the most left upper panel of Fig. 5.14, where the soft component:

$$(D_s 2\pi T)^{\text{soft}} = \alpha \cdot (1 + \beta(T/T_c - 1)). \quad (5.4)$$

above the critical temperature T_c are plotted.

- The ratio parameter γ also shows a clear narrow distribution, with an estimated peak around $\gamma = 0.17_{-0.03}^{+0.04}$. The momentum region where the $(D_s 2\pi T)^{\text{pQCD}}$ and $(D_s 2\pi T)^{\text{soft}}$ contribute equally is around $p \sim 1/\gamma^2 = 30$ GeV. Comparing to the previous analysis based on the model without free-streaming stage evolution and fixed coupling constant, where we have the transition line around $p \sim 10 - 20$, this value has shifted to a larger p_T range. One reason could be the effects of the addi-

tional free-streaming stage evolution. However, I should note that, as displayed in the lower panel of Fig. 5.14, the charm quark diffusion coefficient turns out to have a mild momentum dependence, which means the change from $p_T \sim 20$ GeV does not cause much difference from $p_T = 30$ GeV. Therefore these two estimations are still consistent with each other.

- The free-streaming time parameter ξ , meanwhile, does not have a clear preference throughout the parameter range. It still excludes a very small value near zero, but there seems no effect on what time the heavy quark starts to interact with the medium.
- Finally, we have an additional parameter σ_{model} regarding the systematic uncertainty of the model's calculation. So far we have assumed that the model is able to describe the reality, given proper parameter design. And the uncertainty regarding the model's prediction comes from the fact we have used a surrogate model – Gaussian Process Emulator – to predict the model's output σ_{GP} .

However, it is possible that the theoretical model is able to describe the true physical process, but with some discrepancy:

$$\mathbf{y}_{\text{exp}} = \mathbf{y}_{\text{model}} + \sigma_{\text{exp}}^{\text{stat}} + \sigma_{\text{exp}}^{\text{sys}} + \sigma_{\text{GP}} + \boldsymbol{\delta}, \quad (5.5)$$

where $\sigma_{\text{exp}}^{\text{stat}}, \sigma_{\text{exp}}^{\text{sys}}$ are the experimental uncertainties, and $\boldsymbol{\delta}$ is the discrepancy term.

Since there is no information ever for what the discrepancy looks like, we use a simple gamma distribution for $\boldsymbol{\delta}$:

$$p(\boldsymbol{\delta}) \sim \delta^2 \exp^{-\delta/l}, \quad (5.6)$$

where we choose $l = 0.05$. The larger l , the more discrepancy we are allowed. This discrepancy will be marginalized with the posterior distribution of the model's

output.

In our analysis, the discrepancy has a preferred peak near $\delta = \sigma_{\text{model}} = 0.04_{-0.02}^{+0.02}$. It is defined as the relative uncertainty to the overall variance of the model, which indicates the model has a systematic uncertainty equal to 5% of its total variance. In addition, this posterior distribution of σ_{model} is highly correlated with the prior distribution. As the values of σ_{model} increases, the distributions of other parameters get wider. It means that with large systematic uncertainty, the constraining power of all the parameters becomes negligible, and the specific value for the parameters does not matter anymore.

posterior range for the transport coefficient $D_s 2\pi T$

With the posterior distribution for the parameters $(\alpha_s, \alpha, \beta, \gamma)$, one can construct the posterior range of the diffusion coefficient, which is plotted in Fig. 5.14 as a function of temperature in the upper panel and as a function of momentum dependence in the lower panel. The gray area is the prior range that the random walkers explored during the calibration. Instead of displaying the 90% credible region, here I show the result from the individual parameter set in order to better demonstrate the temperature and momentum dependence of the diffusion coefficient. Each blue line corresponds to one random sample drawn from the posterior distribution of the parameters (excluding the double side tails below 5% percentile).

First of all, the diffusion coefficient shows a clear strong positive dependence on temperature, as the higher the temperature, the larger the diffusion coefficient and the smaller interaction strength between heavy quarks and the medium. Such strong temperature dependence behavior is distinctly different from the behavior from the pQCD result – where the latter displays a mild temperature dependence as shown in Fig. 5.10. Such behavior can only come from the non-perturbative contribution.

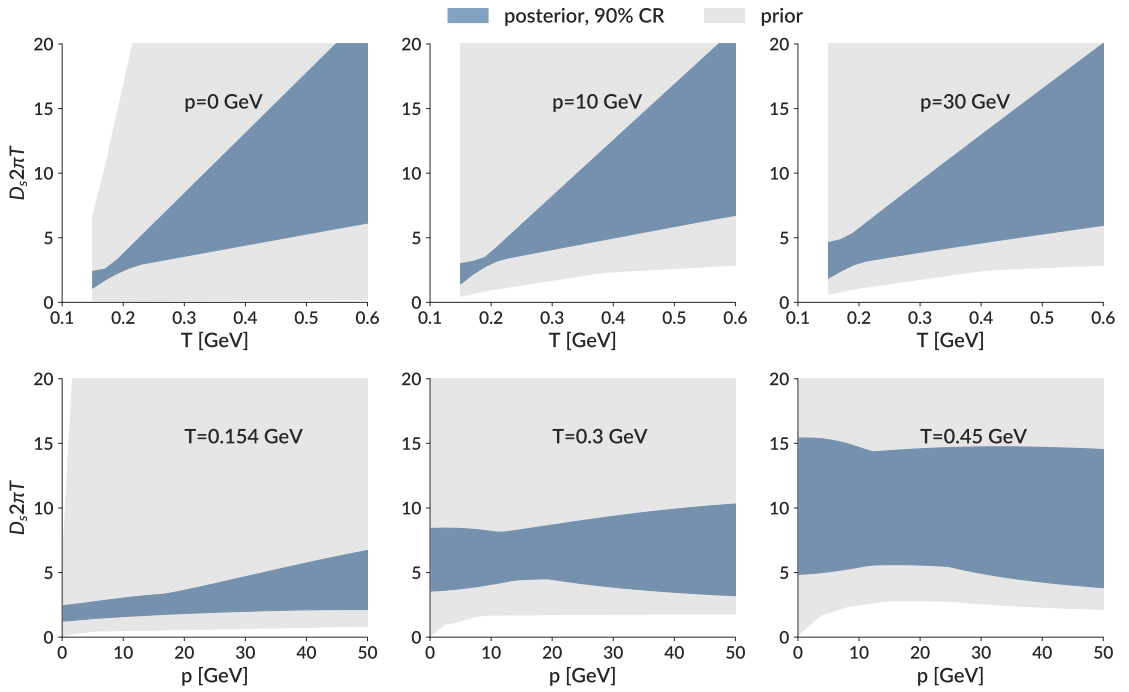


Figure 5.14: Posterior range of the spatial diffusion coefficient obtained from the the Bayesian analysis calibrated on D -meson observables in Pb-Pb collisions at 5.02 TeV. [**Upper**]: The spatial diffusion coefficient $D_s 2\pi T$ with respect to temperature at fixed momentum; [**Lower**] the spatial diffusion coefficient $D_s 2\pi T$ with respect to momentum at fixed temperature. The gray area refers to the prior range that the parametrization explores.

Secondly, the momentum dependence of the diffusion coefficient is not significant, even for the lower momentum region, whereas for the pQCD calculation, starting from the lower momentum region, there is a rapid decrease of the diffusion coefficient. It indicates that even for a heavy quark propagating in the QGP medium with slow momentum, the interaction between heavy quarks and the medium is still comparable with fast-moving heavy quarks, regarding of the collisional energy loss contribution.

Thirdly, recall that the total energy loss for heavy quark propagating in the medium includes both the collisional energy loss and the radiative energy loss.

$$\frac{dE}{dx} = \left. \frac{dE}{dx} \right|_{\text{col}} + \left. \frac{dE}{dx} \right|_{\text{rad}} \quad (5.7)$$

Therefore in order to faithfully evaluate the interaction between heavy quarks and the medium, we should also consider the radiative contribution. We investigate this schematically by propagating heavy quarks in a static medium for 1 fm/c, and dynamically evaluate the total (averaged) transport coefficients during their propagation. Due to the computational expense, I only select one set of parameters and the purpose of this dynamical calculation is just to illustrate the contribution from radiative energy loss. The comparison is shown in Fig 5.15, where for the particular set of diffusion coefficient, the green dash line represents the contribution from the collisional energy loss while the solid line with marker represents the total diffusion coefficient including both collisional and radiative energy loss. The difference between those two is the contribution from radiative energy loss. One can see that the radiative energy loss has a visible contribution for high temperature and high momentum region.

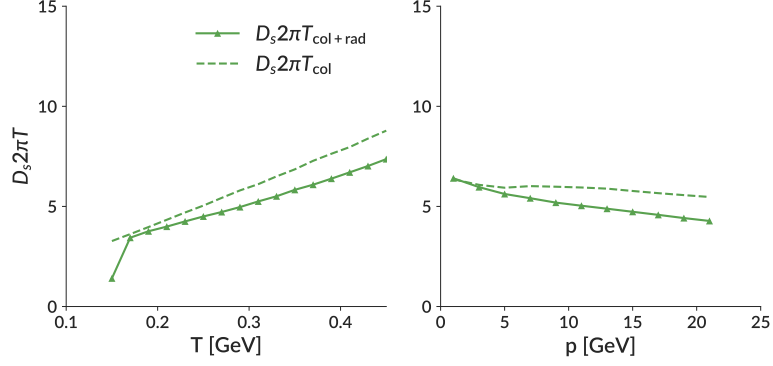


Figure 5.15: Charm quark diffusion coefficient evaluated dynamically. Comparison between collisional contribution (green dashed line) and collisional+radiative contribution (green solid line with marker).

maximum probability parameters

Final verification of the Bayesian calibration framework is to check the performance of the physical model by using parameters values that are drawn from the posterior distributions. Therefore I randomly selected 10 sets of parameters from the posterior distributions, at each of these parameter sets the heavy flavor observables are evaluated by the improved Langevin model and compared with the experimental measurements in Fig. 5.16. Although each parameter set imposes a different temperature/momentum dependence, the improved Langevin model is still able to reproduce the experimental measurements for all the posterior samples. There is quite a large uncertainty at the high momentum region $p_T > 50$ GeV due to the lack of measurements at that region. With future LHC upgrade plan, one hope that more observables with higher precision can help us to constrain the model's uncertainties.

Moreover, if the improved Langevin model does capture some of the reality, one would expect that it can also describe other observables that are not included in the training dataset. Therefore I computed several other observables, including the higher-order momentum anisotropy: the p_T differential triangle flow $v_3(p_T)$, which is defined as the third

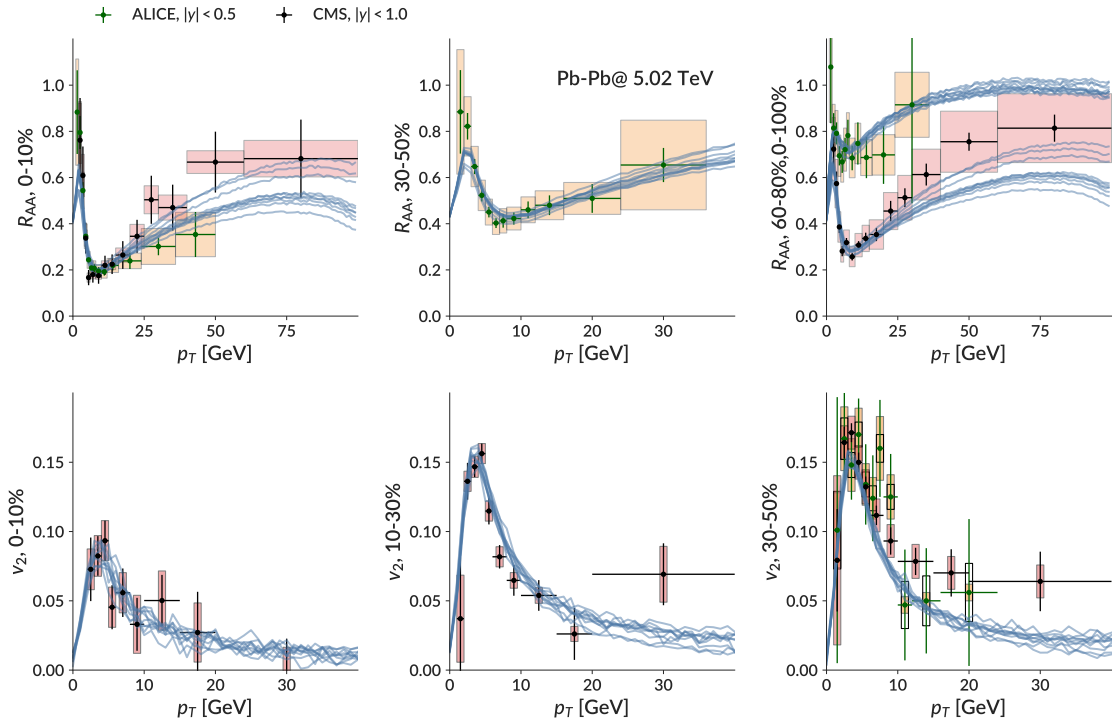


Figure 5.16: Improved Langevin calculation of the D -meson R_{AA} and v_2 in Pb-Pb collisions at 5.02 TeV, taking the parameters randomly drawn from the posterior distributions.

coefficient in the FOURIER decomposition of the final state particle azimuthal distribution:

$$\frac{d^2N}{d\phi dp_T} = \frac{dN}{2\pi dp_T} \left[1 + 2 \sum_{n=1}^{\infty} v_n(p_T) \cos n(\phi - \Phi_n) \right], \quad (5.8)$$

where Φ_n is the initial state spatial plane of the symmetry for the n-th hadronic. Here I use the two-particle cumulant method to calculate the triangle flow:

$$v_3\{2\} \equiv \frac{\langle \vec{u} \cdot \frac{\vec{Q}}{N} \rangle}{\sqrt{\frac{\vec{Q}_a}{N_a} \cdot \frac{\vec{Q}_b}{N_b}}}, \quad (5.9)$$

where the \vec{Q} -vector is defined as azimuthal distribution for the particle of reference (charged hadrons):

$$\vec{Q} = \sum_i \exp(3\phi_i), \quad (5.10)$$

that sums over all the charged particles i , ϕ_i is the azimuthal angle and N is the multiplicity of charged particles. \vec{Q}_a is a segment of charged particles with $0 < \eta < 0.8$ while \vec{Q}_b is the segment $-0.8 < \eta < 0$. \vec{u} is the cumulant for the particle of interest, in this case, the D -mesons with the specific kinetic and centrality cut. The results of the model's calculation of v_3 is compared with the experimental measurements in Fig. 5.17. Although due to the large experimental uncertainty, one can hardly make any conclusive statement, the model's calculation is comparable with experimental measurements.

Finally, I introduce a calculation using the Event Shape Engineering (ESE) technique [150], which is based on the observation of the large event-by-event v_n variance at fixed collision centrality and can be used to further investigate the dynamics of the heavy quarks in the medium. Instead of selecting D -mesons based on different centralities (which are binned according to the light hadron multiplicity), it measures the D -meson v_2 in classes of events in a given centrality interval but also with different magnitude of average event flow. The

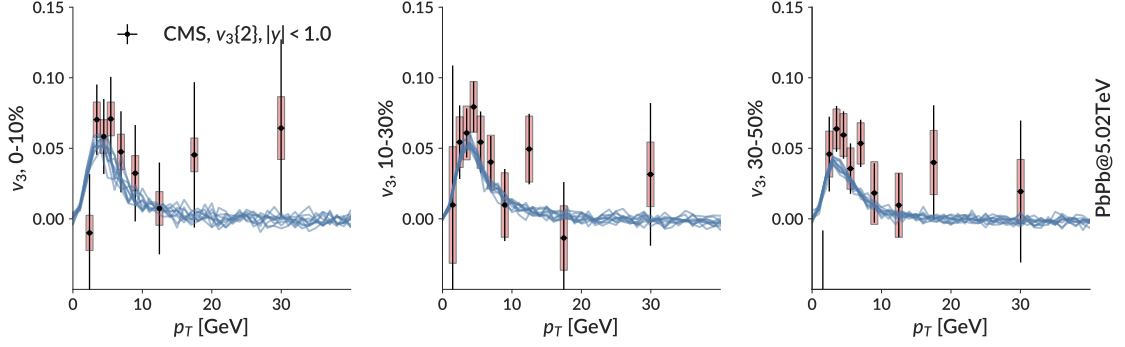


Figure 5.17: Improved Langevin calculation of the D -meson v_3 in Pb-Pb collisions at 5.02 TeV, taking the parameters randomly drawn from posterior distributions.

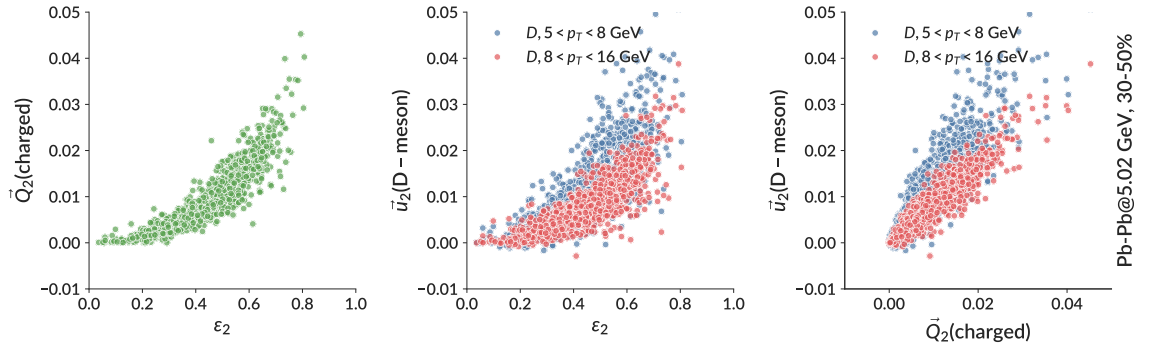


Figure 5.18: Event-by-event correlation among initial spatial eccentricity ϵ_2 , charged particles cumulants \vec{Q}_{charged} and D -meson cumulants \vec{u}_D for 30-50% centrality of Pb-Pb collisions at 5.02 TeV.

underlying reason for separating collision events based on the event flow is that the hydrodynamic calculation has shown a nearly linear correlation between the final state elliptic flow v_2 and corresponding spatial eccentricity ε_2 for the initial state energy density distribution (with a small value of η/s). Therefore in addition to the centrality cut, heavy-ion collision events can be selected with different initial geometrical shape via a selection of final state light hadrons. Therefore one can investigate the interplay between the anisotropic flow of D -meson and that of the soft matter. In addition, it provides more insights on how the initial geometry of the system affects the path-length-dependent energy loss that is experienced by the heavy quarks while they propagate in the QGP medium.

During the calculation, the minimum bias events are first binned into different centralities according to the light hadron multiplicity with $|\eta| < 0.8, 0.2 < p_T < 5$ – the same kinetic cut as the ALICE measurement. The events in each centrality bins are then further divided into different classes according to the magnitude of the second-order harmonic reduced flow vector q_2 , which is defined as:

$$q_2 = |\vec{Q}_2|/\sqrt{M}, \quad (5.11)$$

the \vec{Q}_2 is the second order flow cumulants that is defined as:

$$\vec{Q}_2 = \sum_i \exp(2\phi_2). \quad (5.12)$$

The D -meson flow is then calculated with the event-plane method as demonstrated in Sec.2.4.3 for different classes.

In Fig. 5.18 where I plot the event by event correlation among initial spatial eccentricity ε_2 , charged particles cumulants $\langle 2 \rangle_{\text{charged}}$ and D -meson cumulants $\langle 2 \rangle_D$ for 30-50% centrality of Pb-Pb collisions at 5.02 TeV. The left panel plots the correlation between the

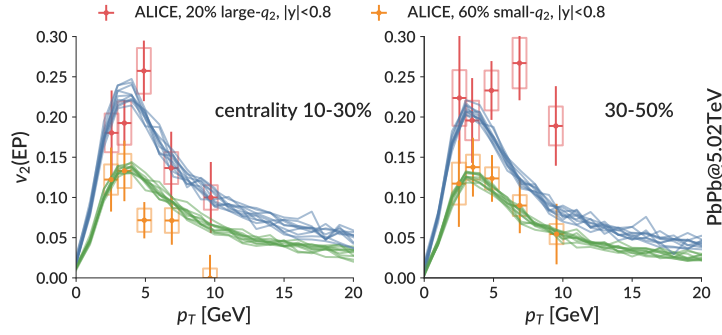


Figure 5.19: Improved Langevin calculation of the D -meson v_3 in Pb-Pb collisions at 5.02 TeV, taking the parameters randomly drawn from posterior distributions. Each point corresponds to the variable in a single heavy-ion collision event.

initial spatial eccentricity ε_2 and the charged hadron cumulant $\vec{Q}_2(\text{charged})$ for a fixed centrality 30-50%. Large variance is observed for the charged hadron cumulants, and it is the same case for D -meson cumulants. Regarding the correlation between charged hadrons and D -mesons, one finds different strength of the correlation for D -meson for different momentum ranges, as the slope of correlation is different from each other, which could imply different degrees of energy loss for heavy quarks propagating in the medium⁶.

The results of Event Shape Engineering D -meson flow is shown in Fig. 5.19, where the flow of D -meson in the 30-50% collision centrality are segmented into two classes: the one in which the charged hadron cumulants q_2 are the 20% largest, and the one in which q_2 are the 60% smallest. First of all, one can clearly see the separation due to the initial geometry, and the model's calculation is, although the experimental uncertainty is significantly large, consistent with experimental measurements. They both show a peak around $p_T = 5$ GeV.

⁶I should still note that, for the calculation in heavy quark flow observables, thousands of heavy quarks are oversampled with the same initial geometric condition. Therefore it is doubtful in a real heavy-ion collision event, where only a few dozens of heavy quarks are produced, that much correlation can be observed from the comparison between heavy quarks and charged hadrons.

5.5 Summary

In this chapter, I applied the Bayesian model-to-data analysis to a heavy quark evolution model in heavy-ion collisions. This analysis has proved its applicability in heavy flavor studies by simultaneously calibrating the theoretical model on experimental data in different collision systems, constraining and estimating the heavy flavor diffusion coefficient in the QGP medium, and predicting other observables that are not in the calibration dataset.

There are a few directions to further improve the framework:

- A more realistic description of the physical process will certainly decrease the systematic uncertainty from the computational model: for example one can use a kinetic model to describe the pre-equilibrium stage interaction among the collision system and the interaction between heavy quarks and the medium.
- More observables with higher precision will increase our constraining power of the transport coefficients: moving away from the mid-rapidity towards the forward and backward rapidity region, especially in an unsymmetrical system such as pA collisions, one could bias towards different temperature regions and explore the energy loss of heavy quarks in detail.
- Other transport models and data: one of the difficulties in the current comparison of the heavy quark transport coefficients among different theoretical model is that it is hard to quantify the performance of each model. The Bayesian framework is not specific to this model or data in this work and can be utilized to calibrate other models and conduct a systematic estimation of the transport coefficients, therefore we can make a fair comparison among different theoretical approaches.

Chapter 6

Comparison among different models

Heavy quarks, as one of the important probes of the QGP medium, provide us with an insight of both parton energy loss and development of collective flow in heavy-ion collisions. There exist a variety of different dynamical models – based on different assumptions of: the formation of the QGP matter, the nature of the medium degrees of freedom, the dynamical evolution within the medium and many other details – that have been developed. Each model also estimates the heavy quarks transport coefficients, with which the model is able to describe some of, if not all, the experimental measurements of the heavy flavor observables in heavy-ion collisions.

In Fig. 6.1 I compare our estimate of the diffusion coefficient between two sets of different calibration and among different theoretical approaches. The left panel shows the temperature dependence of the spatial diffusion coefficient at zero momentum for two different Bayesian calibrations: one with pre-equilibrium dynamics and one without. With additional pre-equilibrium dynamics, the estimation of $D_s 2\pi T(p = 0)$ does not differ much from the previous calibration. The right panel compares between different models. All the models' estimations are qualitatively consistent with each other: all of them shows a small value of $D_s 2\pi T$ near T_c – indicating a strong interaction with the medium, and positive temperature dependence, one can still find a factor of 4-5 difference among different models.

Some of the differences come from the different assumptions made regarding the heavy quark-medium interaction by each model, some, however, come from other components of the heavy-ion collisions. For example, the initial conditions, the description of the QGP medium, the hadronization models, whether or not the hadronic stage rescattering is in-

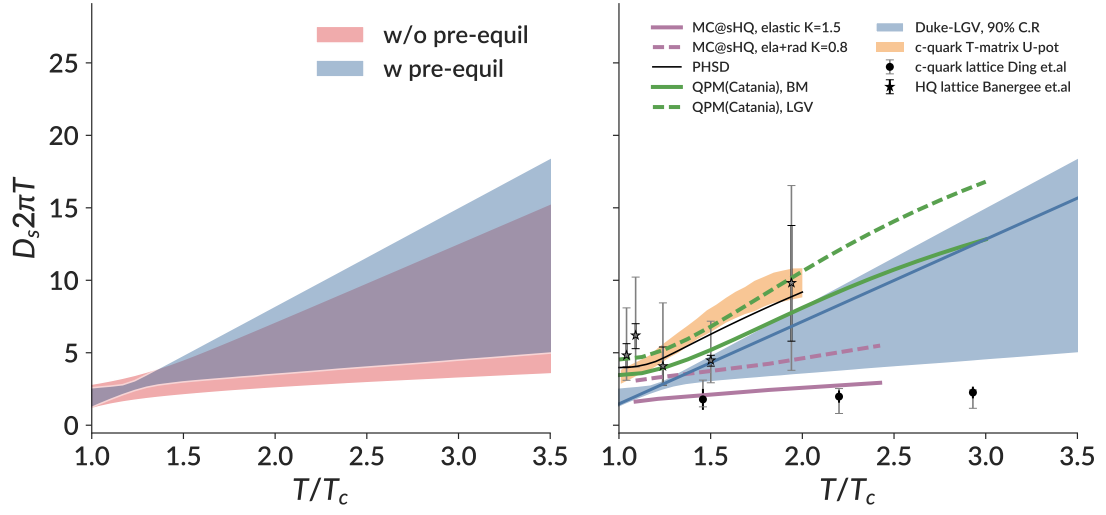


Figure 6.1: Heavy quark diffusion coefficient comparison between different theoretical model's estimation.

cluded. It is therefore important to understand how sensitive the heavy flavor observables are to those assumptions, to which degree it will affect the estimation of the heavy quark transport coefficients, and what kind of strategy one should pursue in order to ascertain the actual physical nature of the hot and dense QCD system.

In this chapter, I will try to investigate the differences between several of these components during the multi-stage heavy-ion collision evolution. Starting from a comparison between two descriptions of the QGP medium, I will demonstrate the importance of the pre-equilibrium flow in terms of calculating the momentum anisotropy of the medium. Later I will apply the control variable method to isolate different components and quantify the variance on the heavy quark observables caused by the different theoretical modeling assumption of each of the components.

6.1 QGP medium evolution

So far in this thesis, I have described the evolution of the QGP medium based on a relativistic viscous hydrodynamical framework, where the space-time evolution of the QGP medium is calculated by the hydrodynamical equations:

$$\partial_\mu T^{\mu\nu} = 0, \quad (6.1)$$

and the assumption of local equilibrium. To utilize the hydrodynamical framework to describe the evolution of the system, one would specify the medium with an initial condition model, and close the equations of motion using the QCD Equation of State (EoS). The initial condition model generates the outcome of the collision at the hydrodynamical thermalization time, (approximately of 1 fm/c), either through a dynamical evolution model or a static mapping function.

On the other hand, there are some dynamical models that relax the local equilibrium assumption, and describe the QGP medium evolution through a non-equilibrium transport approach. The non-equilibrium effects are considered to be the strongest during the early phase of the collision (pre-equilibrium stage) and may significantly impact the properties of QGP probes that are produced at early times. Moreover, the traces of the non-equilibrium effect could also be retained within some bulk observables, such as the correlation functions and the higher-order anisotropy coefficients[154–156]. One such non-equilibrium transport model is the Parton-Hadron-String-Dynamics (PHSD), which explores the microscopic interaction of the QGP medium based on the Kadanoff-Baym equations[157, 158] for Green's function representation in phase-space.

In this section, I would like to compare prominent models for the evolution of the QGP medium: a non-equilibrium transport approach – PHSD, and a (2+1)-dimensional viscous hydrodynamical model –VISHNU. In particular, I will focus on the interpretation of the

medium anisotropy during the QGP phase of the medium evolution, and show that despite large event-by-event fluctuations in PHSD, the ensemble average is close to that the in hydrodynamical limit.

6.1.1 Description of the models

PHSD transport approach

The PHSD transport approach is a microscopic covariant dynamical model that describes the full evolution of a heavy-ion collision from the initial hard scatterings and string formation, through the dynamical deconfinement phase transition to the strongly-interacting QGP towards the hadronization and the subsequent interactions in the expanding hadronic phase. The interaction between the quarks and gluons in PHSD is based on the Dynamical Quasi-Particle Model (DQPM) where the parton interactions are constructed to reproduce the lattice QCD result for the QGP EoS in the thermodynamical equilibrium[159]. The effective parton propagators incorporate finite masses for the gluon and quarks, as well as a finite width $\Gamma_i(T, \mu_q)$ that describes the medium dependent interaction rate. However, PHSD differs from the conventional Boltzmann approach in:

- The PHSD model incorporates dynamical quasi-particles with finite width of the spectral functions (imaginary part of the propagators); it is based on a realistic Equation of State from lattice QCD and thus describes the speed of sound $c_s(T)$ reliably;
- It involves scalar mean-fields that substantially drive the collective flow in the partonic phase. The effective partonic cross sections are not given by pQCD but are self-consistently determined within the DQPM and probed by the transport coefficients (correlators) in thermodynamic equilibrium;
- The hadronization is described by the fusion of off-shell partons to off-shell hadronic

states (resonances or strings) and does not violate the second law of thermodynamics; all conservation laws (energy-momentum, flavor currents) are fulfilled in the hadronization contrary to coalescence models.

2D+1 viscous hydrodynamics

In chapter 2, I have briefly introduced the hydrodynamical framework, which calculates the space-time evolution of the QGP medium via the conservation equations:

$$\partial_\mu T^{\mu\nu} = 0 \quad (6.2)$$

for the energy-momentum tensor

$$T^{\mu\nu} = e u^\mu u^\nu - \Delta^{\mu\nu} (P + \Pi) + \pi^{\mu\Xi}. \quad (6.3)$$

In order to start the hydrodynamical calculation, one needs to specify an initial condition. We initialize the hydrodynamical calculation with an initial condition extracted from the PHSD evolution, so that we have a common starting configuration for both models.

non-equilibrium initial conditions

The PHSD model starts its calculation of a heavy-ion collision events ab initio with two colliding nuclei and makes no equilibrium assumptions regarding the nature of the hot and dense system during its evolution from initial nuclear overlap to final hadronic freeze-out. In order to generate an initial condition for the hydrodynamical evolution – initial energy density e_0 , initial flow $\vec{\beta}_0$ – we select the earliest possible time during the PHSD evolution where the system is in a state in which a hydrodynamical evolution is feasible (i.e. the viscous corrections are already small enough). At time τ_0 , the energy-momentum tensor

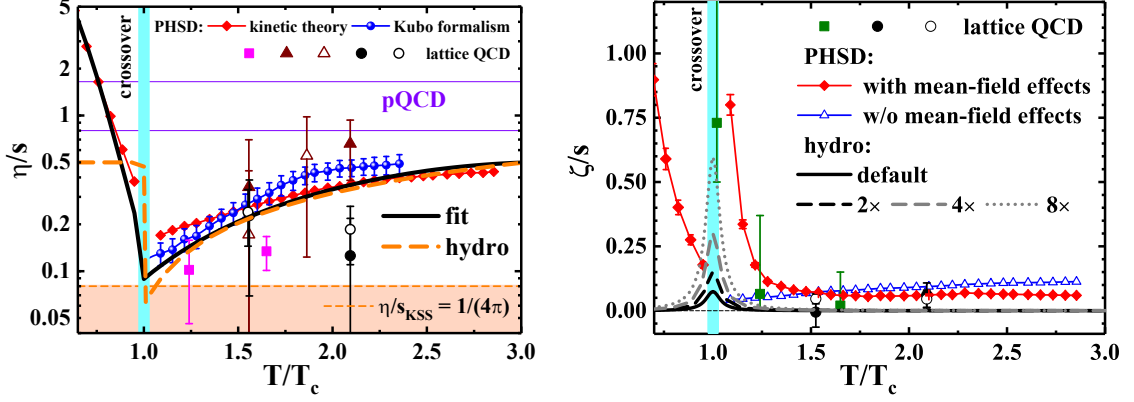


Figure 6.2: Shear and bulk viscosity $\eta/s, \zeta/s$ versus scaled temperature T/T_c . **[Left]:** the symbols indicate the PHSD results of η/s from Ref. [160], calculated using different methods: the relaxation-time approximation (red line + diamonds) and the Kubo formalism (blue line + dots); the black line corresponds to the parametrization of the PHSD results for η/s . The orange short dashed line demonstrates the Kovtun-Son-Starinets bound [161, 162] – $(\eta/s)_{\text{KSS}} = 1/(4\pi)$. For comparison, the results from the virial expansion approach (green line) [163] are shown as a function of temperature too. The orange dashed line is the η/s of VISHNU hydrodynamical model that has been recently determined by the Bayesian analysis; **[Right]:** ζ/s from PHSD simulation from Ref. [160] and the ζ/s that is adapted in our hydrodynamical simulations.

$T^{\mu\nu}(\vec{x})$ can be calculated by summing all the particles in the corresponding coarse grid $V_{\vec{x}}$ in the computational frame:

$$T^{\mu\nu}(\vec{x}) = \sum_i \int_0^\infty \frac{d^3 p_i}{(2\pi)^3} f_i(E_i) \frac{p_i^\mu p_i^\nu}{E_i}. \quad (6.4)$$

The local energy density e is identified as the eigenvalue of $T^{\mu\nu}$ (Laudau matching) and the corresponding time-like eigenvector is defined as the 4-velocity u_ν :

$$T^{\mu\nu} u_\nu = e u^\mu = (e g^{\mu\nu}) u_\nu. \quad (6.5)$$

In addition the parallel ensemble algorithm is used for the test particle method, which has an impact on the fluctuating initial conditions. For a large number of parallel ensembles (NUM), the energy density profile is smoother since it is calculated on the mean-field level

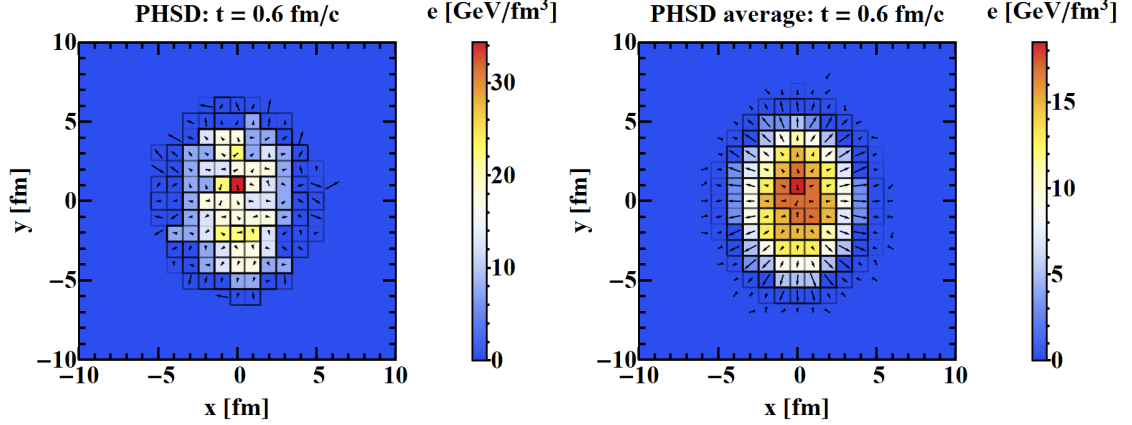


Figure 6.3: Initial condition for hydrodynamics: the energy density profile from a single PHSD event [**left**] and averaged over 100 PHSD events [**right**], taken at $t = 0.6$ fm/c for a peripheral ($b = 6$ fm) Au-Au collision at $\sqrt{s_{\text{NN}}} = 200$ GeV.

by averaging over all ensembles. Figure 6.3 show the initial condition at time $t = 0.6$ fm/c which is extracted from a single PHSD event averaged over ($\text{NUM} = 30$) parallel events on the left panel and averaged on ($\text{NUM} = 100$) on the right panel. In our comparison $\text{NUM} = 30$ is chosen to provides the same level of the smoothing of the initial energy density as in a typical PHSD simulation. And even though the initial profiles are averaged over $\text{NUM} = 30$ parallel events, the energy density distribution still captures the feature of event-by-event initial state fluctuations.

6.1.2 Space-time evolution of the QGP medium: PHSD vs. hydrodynamics

Starting with the same initial condition, the evolution of the QGP medium is now simulated by the two different models: the non-equilibrium dynamics model — PHSD, and the hydrodynamics – (2+1)-dimensional VISHNU. The upper panel of Fig. 6.4 shows the time evolution of the local energy density $e(x, y, z = 0)$ in the transverse plane from a single PHSD event ($\text{NUM} = 30$) at different proper time for a Au-Au collision at $\sqrt{s_{\text{NN}}} = 200$ GeV, while the lower panel shows the same evolution from a hydrodynamical simulation starting from the same initial conditions as the PHSD event above. In both simulations, the

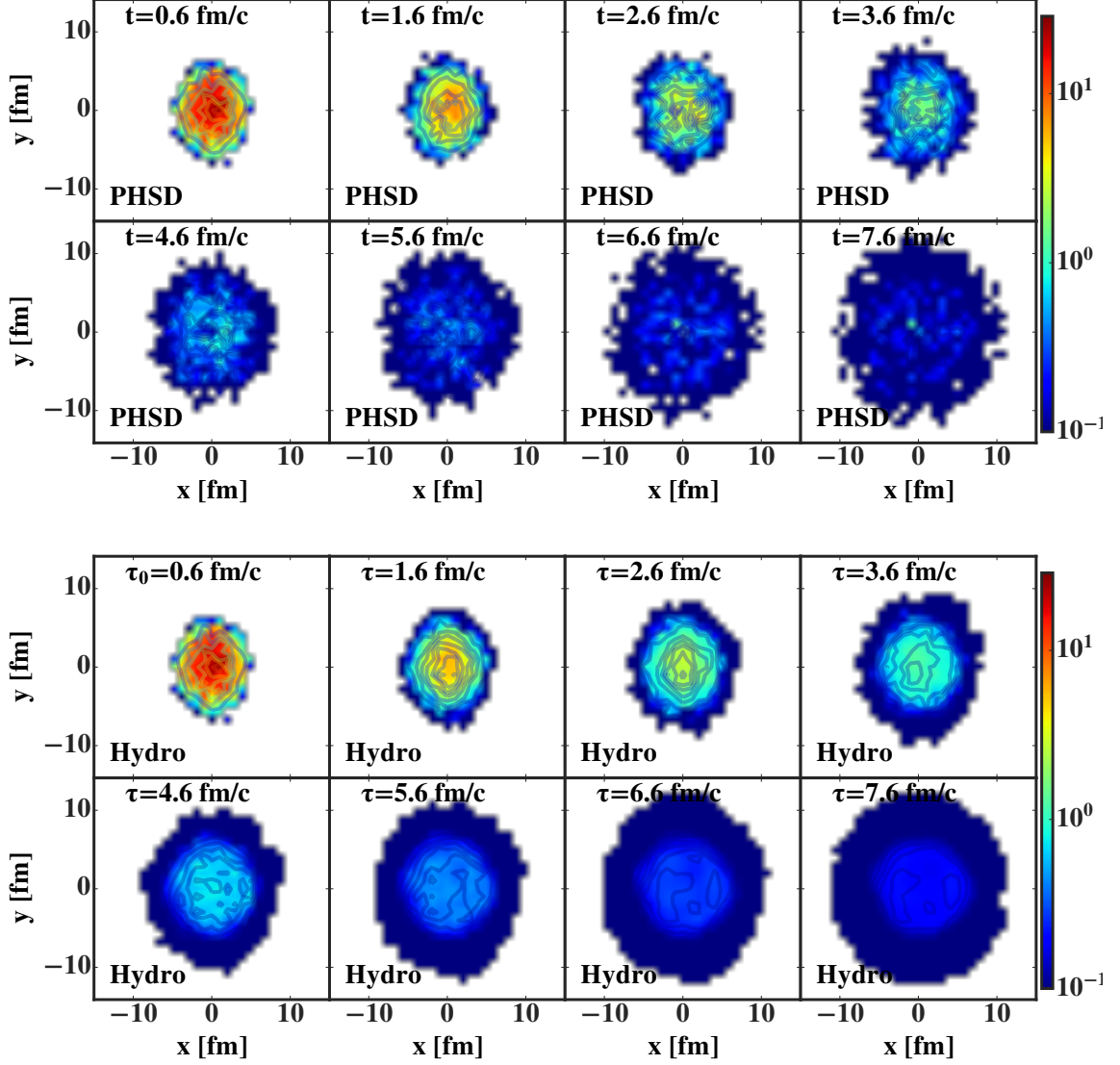


Figure 6.4: [Upper]: Contour plots of the local energy density e in the transverse plane from the PHSD simulation of one event, for a peripheral Au-Au collision ($b = 6$ fm) at $\sqrt{s_{\text{NN}}} = 200$ GeV. [Lower]: same as upper panels but for the single event from the hydrodynamical simulation.

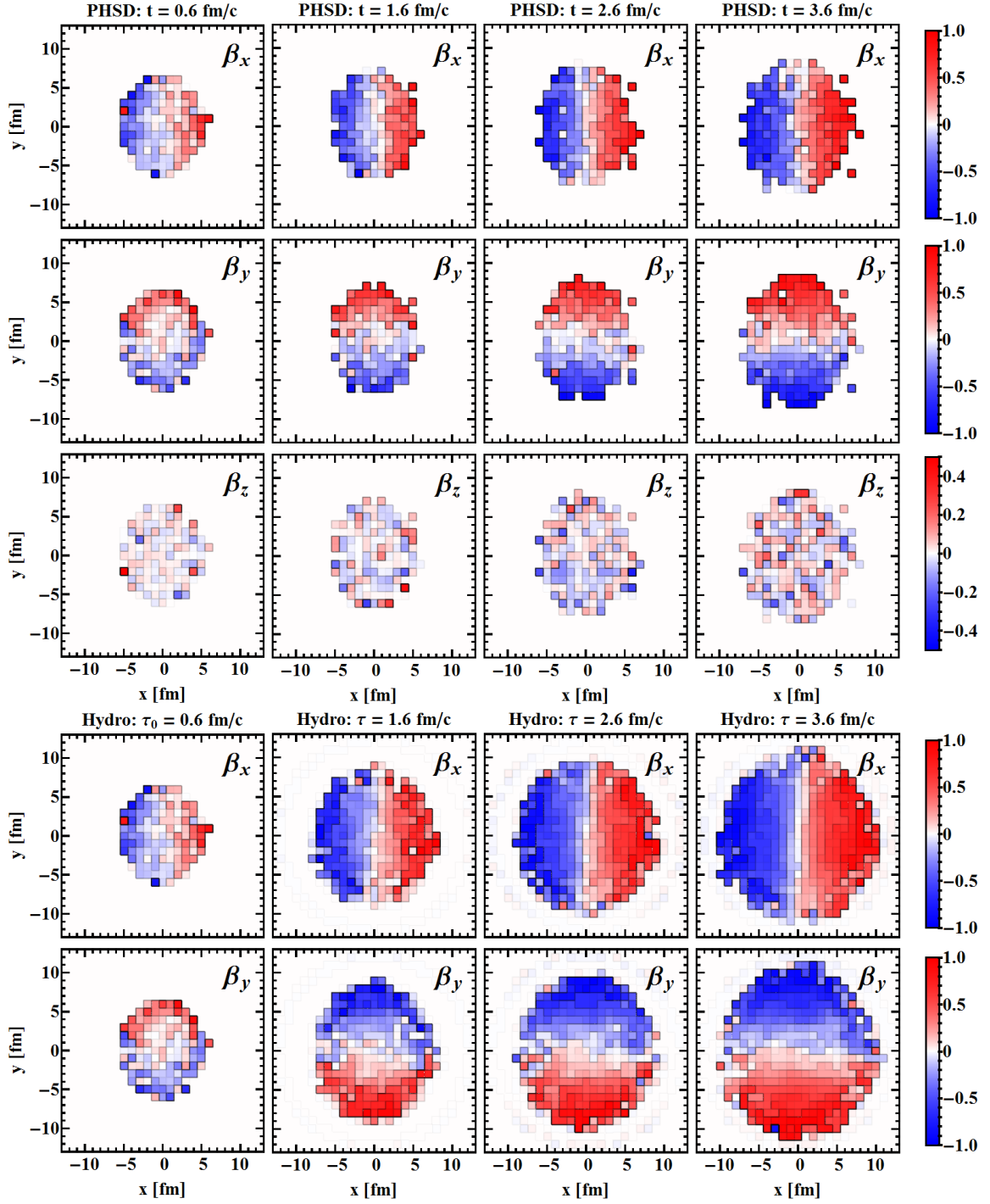


Figure 6.5: [Upper]: components of the 3-velocity ($\beta_x, \beta_y, \beta_z$) in the transverse plane for a single PHSD event (NUM=30) at different proper time for a peripheral Au-Au collision at $\sqrt{s_{NN}}$. β_z is scaled differently from β_x, β_y for better visualization. [Lower]: similar to upper panels but for a single hydrodynamical event (taking the same initial condition as the PHSD event above).

energy density decreases rapidly as the medium expands in the transverse and longitudinal directions. On the other hand, distinct differences are already seen in the energy density evolution: in the PHSD description, the energy density retains many small hot spots during its evolution due to its spatial non-uniformity. In hydrodynamics, the initial hot spots of energy density quickly dissolve and the medium becomes much smoother with increasing time. Moreover, due to the initial spatial anisotropy, the pressure gradient in the x -direction is larger than that in y -direction, leading to a slightly faster expansion in the x -direction. We attribute these differences directly to the non-equilibrium nature of the PHSD evolution.

In Fig. 6.5 I show the time evolution of the flow velocity $\vec{\beta} = (\beta_x, \beta_y, \beta_z)$ in the transverse plane for the same PHSD initial condition evolved through PHSD and hydrodynamics correspondingly. The longitudinal velocity β_z shown in PHSD remains approximately 0 on average, and much smaller than the transverse flow since we only consider a narrow interval in z -direction. At $\tau_0 = 0.6$ fm/c, the transverse flow has already developed and can reach values of 0.5 at the edge of the profile. Even though the velocity increases with time in both PHSD and hydrodynamical evolution, it is clearly seen that the development of flow in a hydrodynamical event is much faster than in a PHSD event. In addition, local fluctuations in a single event are more visible in the PHSD event. The velocity in x -direction is slightly larger than the one in the y -direction in both events, while the initial spatial anisotropy is converted into momentum anisotropy.

In order to quantify the in-homogeneity of the medium, we transform the energy density via a FOURIER transform:

$$\tilde{e}(k_x, k_y) = \frac{1}{m} \frac{1}{n} \sum_{x=0}^{m-1} \sum_{y=0}^{n-1} e(x, y) \exp^{2\pi i \left(\frac{xk_x}{m} + \frac{yk_y}{n} \right)}. \quad (6.6)$$

The zero mode $\tilde{e}_{k_x=0, k_y=0}$ is the total sum of the energy density, while higher order coefficients contain information about the correlations of the local energy density on different

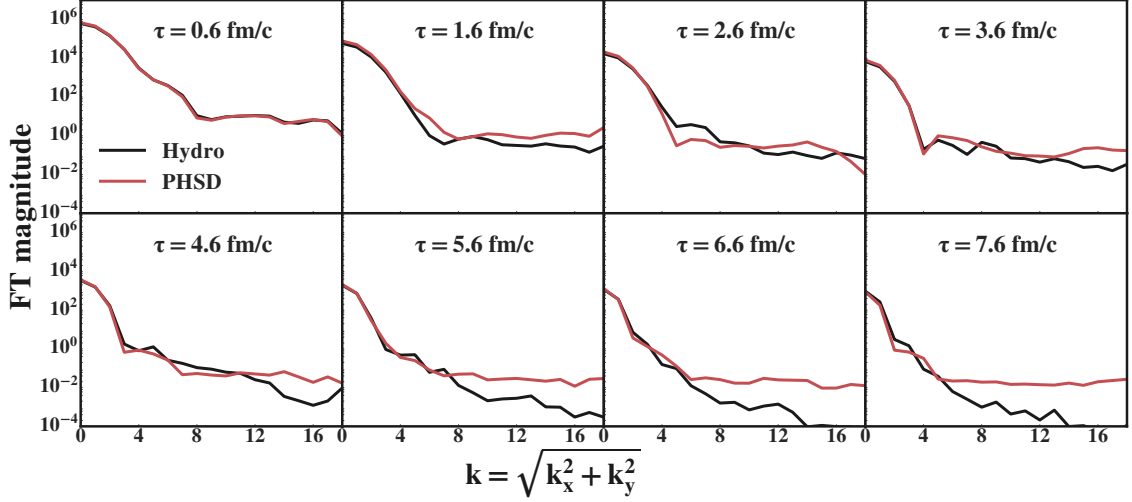


Figure 6.6: Radial distribution of the Fourier modes of the energy density for different proper time in both PHSD and hydrodynamical events. The red line corresponds to the PHSD simulation and the black line corresponds to VISHNU simulation.

length scales. For a medium with long-wavelength structures, the higher order coefficients should be suppressed and the typical global shape of the event should become dominant.

The differences of the FOURIER modes in the two models can be seen in Fig. 6.6, where I plot the distribution of the FOURIER coefficients $\langle \tilde{\epsilon}_{\sqrt{k_x^2 + k_y^2}} \rangle$. For the lower order Fourier modes, which carries the information of the global event scale, the microscopically evolving medium and the hydrodynamical medium are identical. However, for the higher-order coefficients, which corresponds to the shorter wavelength modes of the medium evolution, they decrease rapidly at the beginning of the hydrodynamical evolution while still retains a finite value for the PHSD evolution.

spatial and momentum anisotropy

During the medium evolution, the initial spatial gradient is transformed into momentum anisotropies by the medium pressure. While experimentally only the final state particle spectra are measured, one can compare the evolution of the spatial and momentum

anisotropy between theoretical models which simulate the full space-time evolution of the QGP medium.

For our comparison in this section, since we want to compare the evolution of the medium during the QGP phase without involving the specific hadronization mechanisms — which will add another variance in our comparison – we will compare the spatial ellipticity and the momentum ellipticity in both media: The spatial ellipticity quantifies the spatial anisotropy and is defined as:

$$\varepsilon_2 \exp(i2\Phi_n) = -\frac{\int r dr d\phi r^2 \exp(in\phi) e(r, \phi)}{\int r dr d\phi r^2 e(r, \phi)}, \quad (6.7)$$

where $e(r, \phi)$ is the local energy density in the transverse plane. It is the origin of the elliptic flow v_2 . The momentum ellipticity quantifies the momentum anisotropy. It is directly related to the integrated elliptic flow v_2 and is determined from the energy-momentum tensor as:

$$\varepsilon_p = \frac{\int dx dy (T^{xx} - T^{yy})}{\int dx dy (T^{xx} + T^{yy})}. \quad (6.8)$$

Figure. 6.7 shows the time evolution of the ellipticity $\langle \varepsilon_2 \rangle$ for both PHSD and hydrodynamical medium. For the PHSD simulation, we observe large oscillations at the beginning of the evolution due to the initial geometry and different collision times between nucleons. After sufficient overlap of the colliding nuclei at initial time τ_0 , the average $\langle \varepsilon_2 \rangle$ is stabilized in PHSD.

In contrast, in a single hydrodynamical event ε_2 deviates from the average, but remains a smooth function of time. Due to the faster expansion in x -direction, the spatial anisotropy decreases during the evolution for both medium descriptions, although the spatial anisotropy decreases faster when the initial pre-equilibrium flow β_i (extracted from the early PHSD evolution) is included in the hydrodynamical evolution. In this case, the time evolution of the event-by-event averaged spatial anisotropy is very similar in PHSD and in

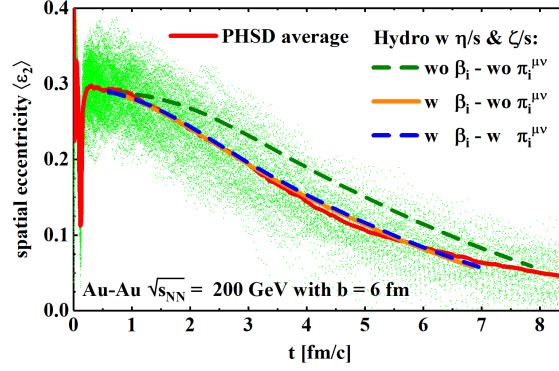


Figure 6.7: Event-by-event averaged spatial eccentricity ε_2 of 100 PHSD events and 100 VISHNU events with respect to proper time, for a peripheral Au-Au collision ($b = 6$ fm) at $\sqrt{s_{NN}} = 200$ GeV. The green dots show the distribution of each of the 100 PHSD events used in this analysis. The solid red line is the average over the green dots. The blue, yellow and black lines correspond to hydrodynamical evolution taking different initial condition scenario.

hydrodynamics. Initializing with the shear-stress tensor $\pi_i^{\mu\nu}$ may also have slight effects on the spatial eccentricity but not large enough to be visible.

Similar features are also seen in the evolution of momentum ellipticity. The left panel of Fig. 6.8 shows the time evolution of the event-by-event averaged $\langle \varepsilon(p) \rangle$ for the hydrodynamical medium description with and without pre-equilibrium flow for initializing the medium. One can see that including the initial flow leads to a finite momentum anisotropy at τ_0 , which subsequently increases as the pressure transforms the spatial anisotropy in collective flow. Consequently, the ε_p is larger than that of the scenario without initial flow throughout the entire evolution. Given the unresolved question of the bulk viscosity in heavy-ion collisions, we investigate the effect of tuning the bulk viscosity ζ_{hydro} in the hydrodynamical model from the standard value to four times that value, which comes closer to the bulk viscosity ζ_{quasi} found in different quasi-particle calculations [164, 165]. We see that with an enhanced bulk viscosity around T_c , the momentum anisotropy develops a bump at later times, which is more pronounced for larger bulk viscosity.

In the right panel, the hydrodynamical simulation is compared to the results from PHSD,

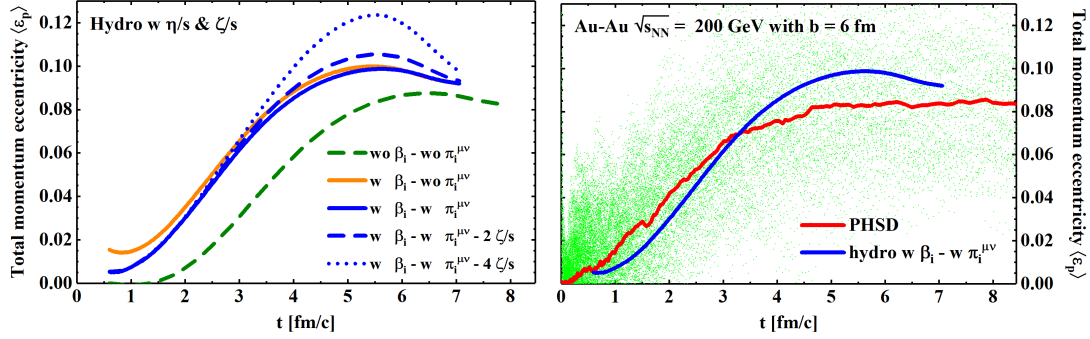


Figure 6.8: Event-by-event averaged total momentum anisotropy of 100 PHSD events and 100 VISHNU events with respect to proper time for a peripheral Au-Au collision at $\sqrt{s_{AA}} = 200$ GeV with impact parameter $b = 6$ fm. **[Left]:** the total momentum eccentricity of hydrodynamical evolution for different initial scenarios as well as different bulk viscosity adapted in the hydrodynamical simulation. **[Right]:** comparison of the total momentum eccentricity from PHSD events compared with the standard hydrodynamical events. The green dots show the distribution of each of the 100 PHSD events used in this analysis. The solid red line is an average over the green dots. The blue line corresponds to the standard hydrodynamical evolution taking the 100 initial conditions which are generated from PHSD events.

where the event-by-event averaged quantities and the event-by-event fluctuations are indicated by the spread of the cloud. It can be observed that before τ_0 the averaged momentum anisotropy in PHSD develops continuously during the initial stage, before it reaches the value which is provided in the initial condition for hydrodynamics. Despite the seemingly large bulk viscosity that's encoded in the quasi-particle evolution picture, the momentum anisotropy in PHSD does not show any hint of a bump like in the hydrodynamical calculation. The response to intrinsic bulk viscosity in a microscopic transport model does not seem to be as strong as in hydrodynamics.

6.2 Heavy quark evolution in the QGP medium

Ideally, one would derive the heavy quark transport coefficients through a first principle calculation and confront them directly with experimental data. However, most of the mi-

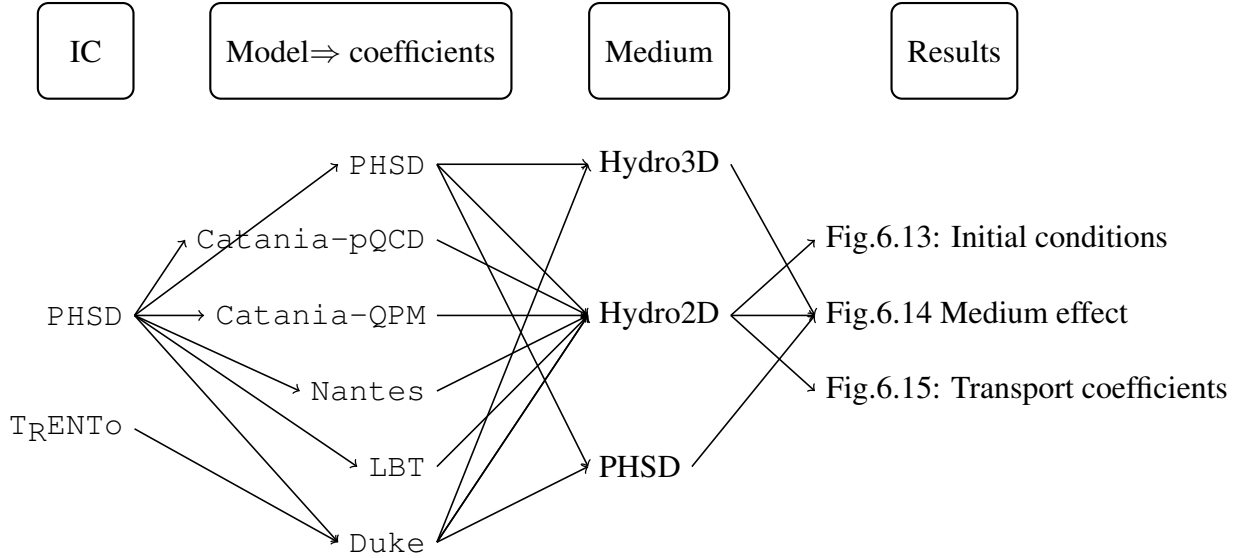


Figure 6.9: A skeleton showing each ingredients during the implementation of heavy quark evolution could affect the estimation of the transport coefficients in the QGP phase.

crossopic transport models that are utilized to estimate the heavy quark transport coefficients have approached the problem more or less in a data-driven way: by introducing and tuning some parameters that are related to the properties of system, the model reproduces the experimental data and thus in return, probes the medium properties.

In Fig. 6.1 where we compare the estimation of the heavy flavor diffusion coefficient reported by different models using the criterion that each model is able to describe the D -meson R_{AA} and v_2 in Au-Au collisions and/or Pb-Pb collisions at RHIC and LHC, we have observed a persistent deviation between the models. Those are often referred to as the theoretical uncertainties in the estimation of the heavy quark transport coefficients.

Clearly, part of the difference stems from the different intrinsic interaction mechanism that is considered when the model is implemented, such as Langevin dynamics and Boltzmann dynamics. Yet part of the discrepancy also comes from different choices of other components, such as the initial conditions, the hadronization process, the medium evolution and so on, as shown in Fig. 6.9. All of those can have non-negligible effects on the final output, and thus, in turn, affect the estimation of the transport coefficients in the QGP

phase.

It is, therefore, necessary to isolate those components and investigate the origin of the deviation by controlling variables. During the past, much theoretical effort has been made to compare among different calculations, such as a systematic comparison of different charm quark transport coefficients in a static medium contributed by the JET-HQ collaboration [166], and a broad investigation on the heavy quark evolution modeling components conducted by the EMMI framework [167]. In this chapter, I continue the investigation by quantifying how different model assumptions other than heavy quark medium interaction contribute to the observed variability in the extracted heavy quark transport coefficients. I will evaluate the response of the charm quark evolution inside a realistic QGP medium using different sets of transport coefficients – which are estimated by different microscopic transport models – in a standard Langevin evolution framework. The six sets of transport coefficients to be compared are estimated from the following microscopic transport models: PHSD, Catania-QPM, Catania-pQCD, Nantes, CCNU-LBT, Duke-Langevin, whose key components and assumptions are briefly summarized at the beginning of chapter 3.

6.2.1 Transport coefficients

Figure. 6.10 compares the total drag and momentum transport coefficients from different models. For models consider only the collisional energy loss, i.e. PHSD, Catania-QPM, Catania-pQCD, Nantes¹, they are calculated from the collisional energy loss process. However, for models incorporating both collisional and radiative energy loss, i.e. Duke, CCNU-LBT, the inelastic process contribution may be significant and the drag and momentum transport coefficients consider both contributions. The drag and momentum

¹I should mention that the Nantes model can have both collisional only and collisional + radiative energy loss evolution. Here in this comparison, we choose the collisional energy loss only version.

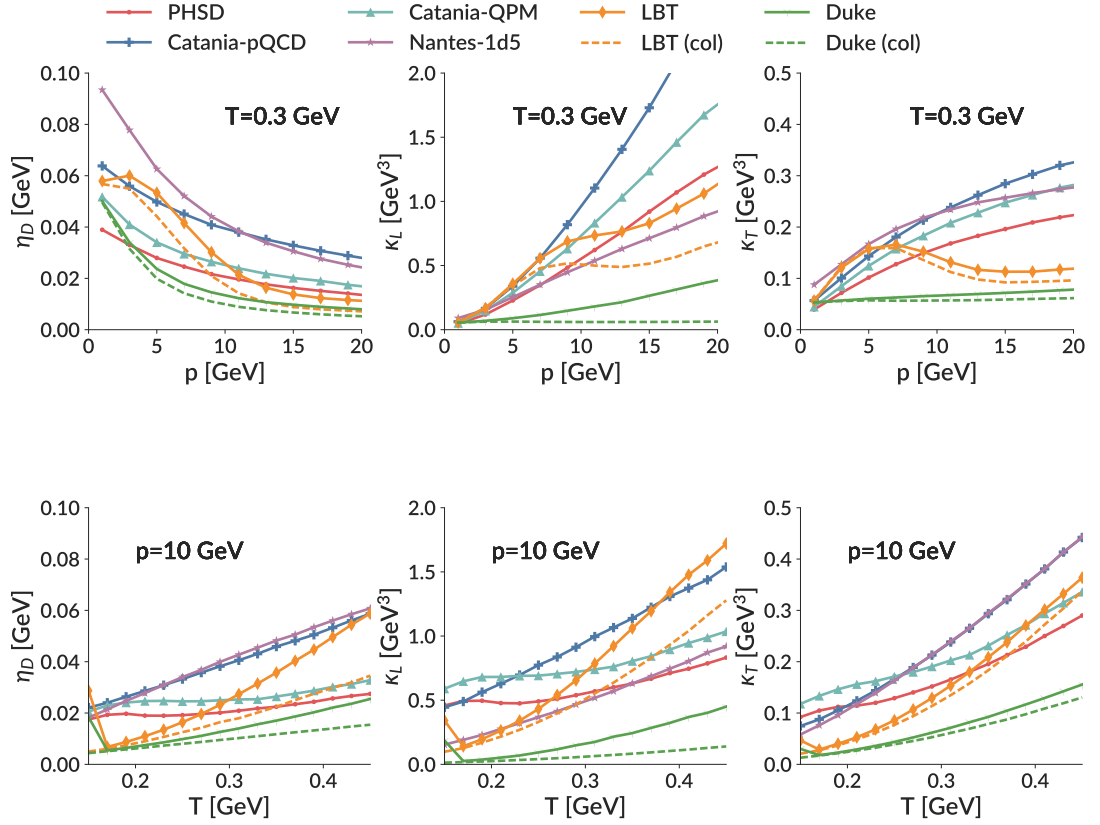


Figure 6.10: Total charm quark transport coefficients with radiative process considered if necessary. The values are estimated by propagating charm quarks inside a static medium for 1 fm/c. The solid lines represent the total transport coefficients, while the dashed lines represent the contribution from collisional only process. The difference between those two is the contribution from higher order radiative process.

transport coefficients are separated into two groups, where the PHSD, Catania-QPM, Catania-pQCD and Nantes (collisional) models employ only the collisional energy loss, and the Duke, CCNU-LBT models employ both collisional and radiative energy loss for heavy quarks.

For the drag coefficient η_D , all the models show a monotonously rising temperature dependence and a decrease for increasing momentum. The Nantes coefficients have the largest gradient in the high temperature and low momentum region, which is due to a momentum dependent coupling constant.

Both the momentum transport coefficients κ_L, κ_T show a strong positive momentum dependence and a mild temperature dependence, except for the Duke-Langevin coefficients, which feature an isotropy assumption unlike the others and have the smallest absolute value. The PHSD coefficients are consistently smaller but still compatible with the Catania-QPM coefficients, while some interplay appears in the low momentum region when one compares between Nantes and Catania-pQCD coefficients. The non-trivial peak for the CCNU-LBT coefficients in the low momentum region is due to the non-constant K -factor introduced in the model, which is included in order to provide a satisfactory description of experimental data, and its parametrization reads as $K = 1 + K_p \exp(-p^2/2\sigma_p^2)$.

Finally, comparing between the overall coefficients (solid lines) and the contribution from elastic processes (dashed lines for those models who has radiative contribution), the difference between these two is the additional contributions from inelastic processes. We can already see that for the Duke and CCNU-LBT models the gluon radiation contributes effectively at higher momenta and at temperatures which we observe at the beginning of the QGP expansion. The existence of the radiative processes can partially explain why the transport coefficients estimated by Duke and CCNU-LBT models are comparatively smaller than those in models containing solely the elastic interactions, when one only in-

cludes the elastic components in the analysis.

Here in this section, I will implement the charm quark propagation inside a QGP medium using the Langevin dynamics coupled to a realistic description of the QGP medium in Au-Au collisions at $\sqrt{s_{NN}} = 200$ GeV. I will test the impact of several model components – initial condition, QGP medium evolution, heavy quark transport – and compare the charm quark energy loss at the end of the QGP phase. The two observables evaluated are, again, the nuclear modification factor R_{AA} , here defined as the ratio between the final state spectra and the initial state spectra $R_{AA} = \frac{dN_{\text{final}}/dp_T dy}{dN_{\text{initial}}/dp_T dy}$, and the elliptic flow $v_2 = \left\langle \frac{p_y^2 - p_x^2}{p_y^2 + p_x^2} \right\rangle^2$.

initial conditions

Th two different initial condition to be compared are the PHSD and `trento`. Although the initial event-by-event fluctuations are generally regarded as an important feature in modeling the collision and have been shown to have a considerable impact on flow observables, here for the sake of simplicity, I will use the averaged `trento` initial conditions which are obtained using 50 single `trento` events.

Figure 6.11 shows a PHSD initial condition, a single `trento` event and an averaged `trento` initial condition for Au-Au collisions at 200 GeV with a impact parameter $b = 6$ fm at the hydro starting time $\tau_0 = 0.6$ fm/c. The upper panels are the initial energy density for the soft medium, while the lower panels are the histograms of initial heavy quark positions for the same corresponding events. The (averaged) `trento` initial condition is constructed by averaging over 50 independent `trento` events, which are selected to have a similar spatial ellipticity ε_2 as the PHSD initial condition. Those initial conditions are then used as input for the (2+1)-dimensional hydrodynamical model, starting from τ_0 .

²I shall emphasis again that I do not intend to compare the different hadronization mechanisms, which are among the least understood processes yet have investigated in [167].

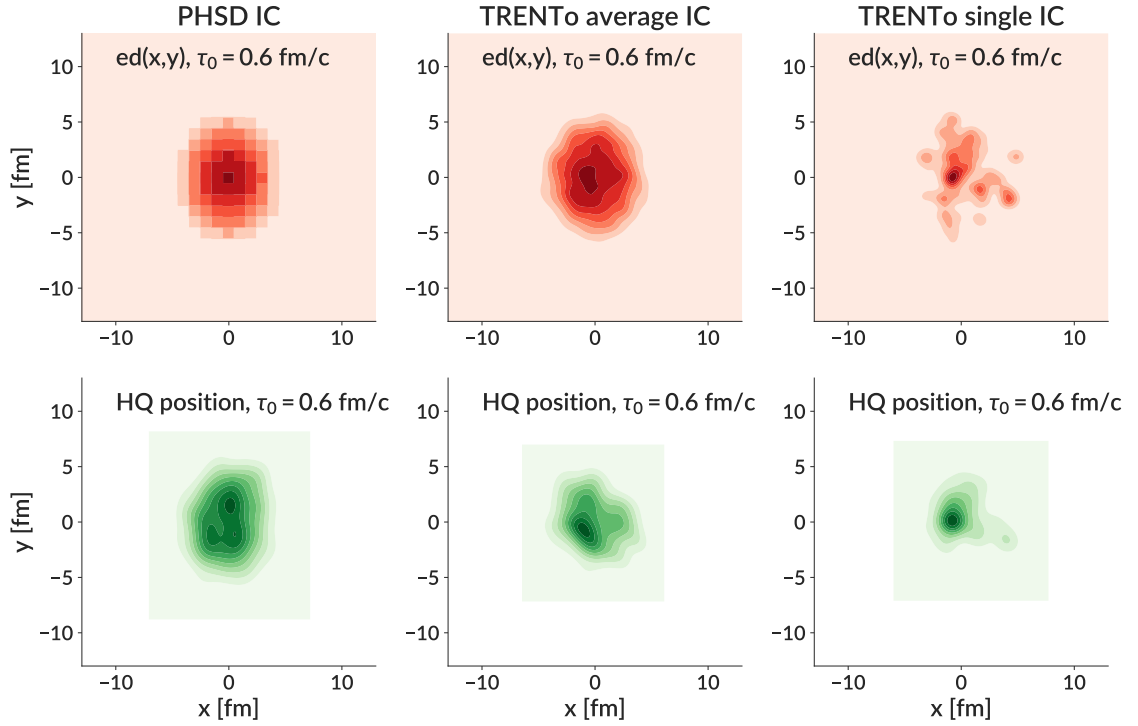


Figure 6.11: Initial conditions at $\tau_0 = 0.6$ fm/c for Au-Au collisions at 200 GeV with impact parameter $b = 6$ fm. The initial conditions are generated from **[left]**: PHSD initial conditions; **[middle]**: `trento` average initial condition, which is averaged by 50 `trento` events who share the similar spatial eccentricity as in PHSD initial condition ; **[right]**: one example of a single `trento` event.

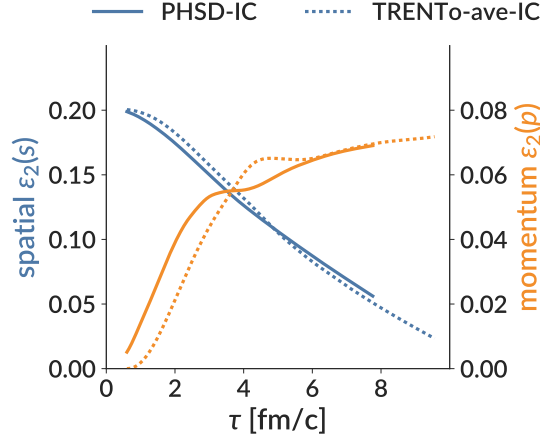


Figure 6.12: Time evolution of the spatial and momentum anisotropy of the QGP medium that is simulated by a (2+1)-D hydrodynamical model – `VISHNU`. The medium starts from two different initial conditions: PHSD initial condition, and averaged `trento` initial condition.

Figure. 6.12 shows the time evolution of the spatial and momentum ellipticity of the medium, which displays the well-known behavior of decreasing ε_2 and increasing $\varepsilon_2(p)$ as the system expands. The momentum ellipticity can be interpreted as the response of the system to the initial spatial eccentricity. The hydrodynamic medium evolution with the PHSD initial condition shows a more rapidly increasing momentum anisotropy at earlier times of the evolution (due to the initial flow $\vec{\beta}$ introduced in the system) and slowing down after the first few fm/c. The final momentum anisotropy however, is comparable to the one with an averaged `trento` initial condition.

With these initial conditions and the sequential medium evolution, we then propagate charm quarks in the QGP medium till the end of the QGP phase (where the local temperature as $T_c = 0.154$ GeV) using the `Duke-Langevin` transport coefficients. The left panel of Fig. 6.13 shows the time evolution of the elliptic flow of charm quarks. A significant fraction of the elliptic flow is generated at the later times during the heavy quark evolution, when the medium itself has a larger momentum anisotropy. A consistent difference of the charm quark v_2 generated by those two different initial conditions is observed. This implies

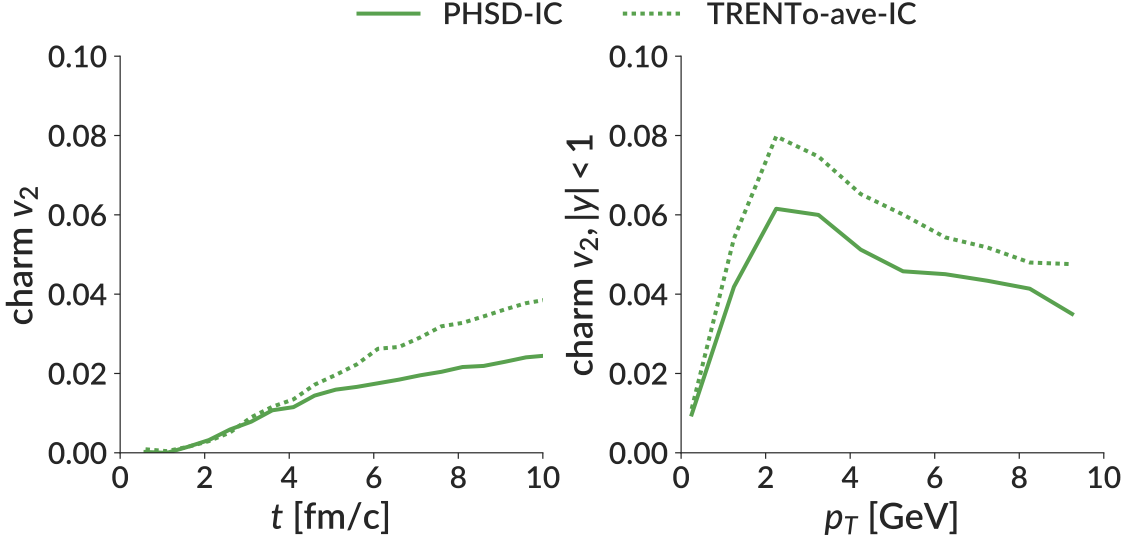


Figure 6.13: [Left]: development of charm quark elliptic flow inside a (2+1)-D hydrodynamical medium during the QGP phase. [Right]: charm quarks $v_2(p_T)$ evaluated at the end of the QGP phase. The charm quarks interact with the medium following an improved Langevin dynamics with the `Duke` coefficients applied.

that the charm quarks can actually not only retain information about the initial condition, but also keep a record of the QGP medium expanding history, particularly, the later stages of the evolution. At the end of the QGP phase, charm quarks starting from an averaged `trento` initial condition have picked up a larger v_2 than the ones from the PHSD initial conditions, as shown on the right panel of Fig. 6.13.

QGP medium evolution

The interaction between heavy quarks and the medium depends on the local temperature and flow velocity of the medium. Moreover, it also depends on the medium degrees of freedom. The comparison between a hydrodynamical model and an expanding fireball model already reveals some significant differences regarding the charm quark v_2 at the end of the QGP phase due to the different development of radial and elliptic flow in those two models [168, 169]. In this section, I will compare the charm quark propagation through the

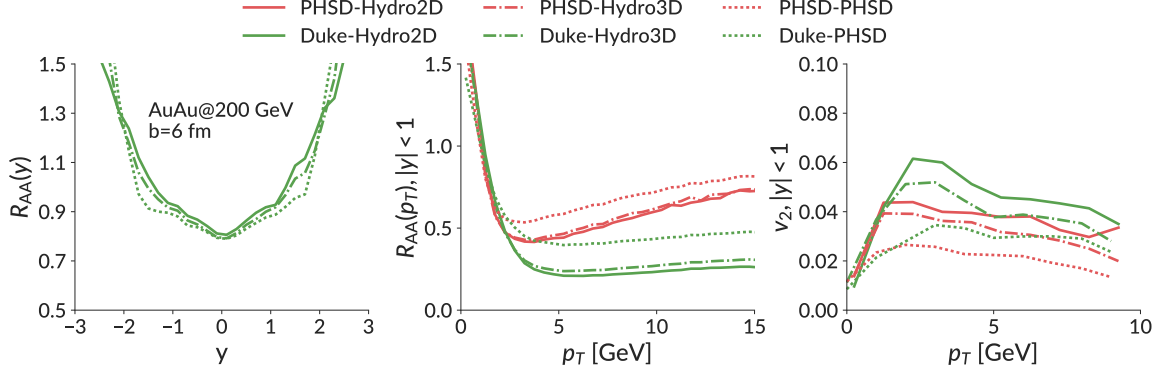


Figure 6.14: Charm quark R_{AA} as a function of rapidity y [left] and p_T [middle], elliptic flow v_2 as a function of p_T [right] at the end of the QGP phase. The charm quarks are following a Langevin dynamics with two sets of transport coefficients applied: PHSD(red) and Duke-Langevin(green).

medium described by the hydrodynamical model – the (2+1)-dimensional hydrodynamical v_{HLLLE} medium and (3+1)-dimensional hydrodynamical $VISHNU$ medium – and the non-equilibrium microscopic PHSD model. Starting from the same initial conditions that are generated by the PHSD model, the QGP media are simulated with different assumptions. The charm quarks then propagate through the three media using our standard Langevin dynamics, where two sets of the transport coefficients are chosen as examples: the collisional only PHSD coefficients, and the collisional + radiative Duke-Langevin coefficients.

In Fig. 6.14 I evaluate the charm quark $R_{AA}(y)$, $R_{AA}(p_T)$ and v_2 at the end of the QGP phase. The evolution of the charm quarks inside hydrodynamical models — (2+1)-D $VISHNU$ and (3+1)-D v_{HLLLE} — are quite similar to each other. For the R_{AA} with respect to rapidity y , discrepancies among the three media appear at large rapidity, and the low p_T charm quarks are most suppressed in a PHSD medium around $|y| \simeq 2$. High p_T charm quarks propagating inside a hydrodynamical medium (solid and solid dots lines) show a larger suppression than in the PHSD medium (dots lines), and develop a larger elliptic flow v_2 . While $R_{AA}(y)$ and $R_{AA}(p_T)$ are almost identical for (2+1)-D and (3+1)-D hydrodynamical calculations, the values of v_2 differ by about 15%. This is understandable

as the medium anisotropy is weaker in a (3+1)-dimensional simulation but also reveals the limitation of the predictive power of (2+1)-D hydrodynamical calculations. The difference between charm quark propagating in a hydrodynamical medium and a PHSD medium, however, is more significant. A factor of 2 difference in the momentum differential flow v_2 is observed in the high momentum region.

It has already been shown that although the shear(bulk) implemented in the hydrodynamical medium are compatible(much smaller) than what is embedded in the PHSD model, the latter has a weaker response to the bulk pressure, resulting in a slightly smaller momentum eccentricity for the bulk section at later times of the evolution in the PHSD model. Note that charm quarks develop a significant part of their flow at later evolution times. The substantial discrepancy between the charm quark evolution inside the two different media, shows that charm quarks are more susceptible to the different bulk pressures of the media, compared to the bulk matter itself. One of the caveats is that different combinations of the transport coefficients and the medium expansions can lead to very similar results in one observable – for example, the charm quark v_2 results of the PHSD(coefficients)-Hydro3D(medium) combination and the Duke-Langevin(coefficients)-PHSD(medium), the results are rather different. This reveals that multiple additional observables are necessary to uniquely determine the transport coefficients and the medium expansion even if all the other ingredients, like the initial conditions, are known.

heavy quark transport coefficients

The interaction strength between the heavy quarks and the medium are encoded into transport coefficients, which have a non-trivial temperature and momentum dependence.

In the following, I will implement different sets of charm quark transport coefficients into the Langevin dynamics coupled to the same (2+1)-D hydrodynamical medium, evolved from the same PHSD initial condition. This setup will not only provide us with a direct

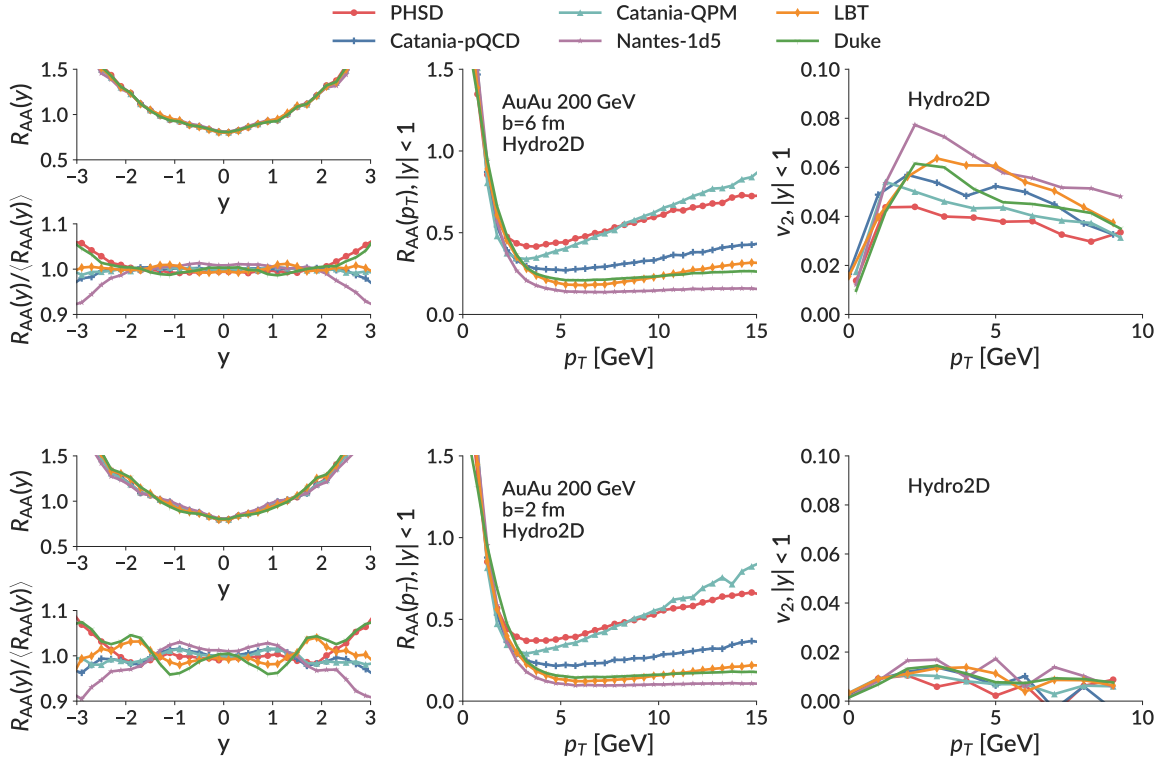


Figure 6.15: Charm quark R_{AA} as a function of rapidity y [left], and p_T [middle], elliptic flow v_2 as a function of p_T [right] at the end of the QGP phase. The charm quarks are propagating in a hydrodynamical medium simulation for Au-Au collisions at 200 GeV with impact parameter $b = 6$ fm [upper] and $b = 2$ fm [lower].

comparison between the response of the charm quark observables (R_{AA} and v_2) to the transport coefficients, but also give us some insight into the difference of the interaction mechanism employed by each model, in particular, a Langevin dynamics versus other microscopic transport dynamics.

The result of charm quark R_{AA} and v_2 at the end of the QGP phase are plotted in Fig. 6.15. At intermediate and higher p_T ($> 5\text{GeV}$), notable differences appear among different sets of coefficients. The PHSD and Catania-QPM models have very similar transport coefficients, and therefore their R_{AA} and v_2 are comparable to each other. Both generate the least suppression and smallest momentum anisotropy. The R_{AA} also levels up at higher p_T due to the lack of radiative energy loss.

The Duke and CCNU-LBT coefficients result in moderate suppression and flow among the six, although the Duke coefficients are the smallest of all. This is the consequence of including the radiative energy loss in the improved Langevin equation, which significantly strengthens the interaction between heavy quarks and the medium. The Nantes coefficients result in the strongest suppression and the largest flow, even though the Nantes (κ_L, κ_T) are not the largest. In fact, when one examines the Nantes and the Catania-pQCD coefficients, these two are comparable with each other yet the R_{AA} and v_2 are substantially different. This could be the consequence of the stronger momentum dependence of the drag coefficient η_D , which could result in a greater energy loss in a dynamical medium.

The R_{AA} with respect to rapidity, which is dominantly driven by the low p_T charm quarks, has less differentiating power in terms of different transport coefficients. However, the rapidity dependence of heavy charm observables may still be useful for distinguishing features in the medium evolution, as shown in Fig. 6.14.

6.3 Summary

In this chapter, I have investigated a number of components in the modeling of the heavy quark evolution in heavy-ion collisions in order to evaluate their possible contribution to the determination of the heavy quark transport coefficients in the QGP medium. A few key observations are found:

- Heavy quarks are sensitive to the history of the QGP medium evolution. Due to their incomplete thermalization, heavy quarks preserve information on the entire evolution from the initial condition till the late stage of the collision;
- Different initial conditions could cause up to 20% of the discrepancy for the final observable v_2 ;
- The results of the v_2 observable depend on the medium which heavy quarks propagate. If the expanding medium fulfills local equilibrium we obtain higher values for v_2 compared the non-equilibrium PHSD approach, given the same initial conditions. In addition, a 15% of the difference in v_2 has been observed for heavy quark propagating in a 2+1-dimensional hydrodynamical medium compared with a 3+1-dimensional hydrodynamical medium;
- The inclusion of radiative energy loss has a large effect on the estimation the leading order transport coefficients, particularly for the determination of \hat{q} , which omits higher order radiative processes. In order to make a fair comparison, one should include all contributions.

Chapter 7

Conclusions

Ultra-relativistic heavy-ion collisions produce one of the most extraordinary forms of matter — the Quark-Gluon Plasma (QGP), which is a system of quarks and gluons describable by Quantum Chromodynamics (QCD). The QGP behaves like a nearly perfect fluid whose evolution can be modeled by the relativistic viscous hydrodynamical model. Investigating this strongly coupled system provides us insights into the fundamental laws of QCD, as well as into the evolution of our early Universe after the Big Bang. Heavy quarks experience the full evolution history of heavy-ion collisions from the initial hard scattering to the end of the hadronic interaction. During their propagation in the QGP medium, heavy quarks interact with the medium, lose energy and participate in the buildup of the collective flow. Studying the interactions between heavy quarks and the medium provides us unique opportunities to understand the parton energy loss mechanisms and the underlying properties of the QGP medium.

Due to its short lifetime (approximately ~ 20 fm/c), the QGP medium cannot be directly measured. Instead, we infer its properties by matching the calculation of a theoretical model to the corresponding experimental observations. In this thesis, I incorporate the evolution of heavy quarks into a viscous hydrodynamical framework in order to describe the evolution of the heavy quarks in heavy-ion collisions: a) With a parametric initial condition model, one generates a consistent picture of an event-by-event initial energy density profile for the soft medium and an initial position distribution for heavy quarks in position space. The initial momentum distribution is calculated using a pQCD calculation of the fixed-order plus next-to-leading log formula (FONLL). In addition, cold nuclear matter effects such as nuclear shadowing are considered. b) The heavy quark in-medium propaga-

tion is described by a heavy quark transport model — an improved Langevin model — that incorporates both collisional and radiative energy loss of heavy quarks and is compared to linearized Boltzmann dynamics. c) After hadronization into heavy hadrons, the hadron-hadron interactions in the hadronic resonance gas state are described by a microscopic transport model — $UrQMD$ based on the Boltzmann equation. By encoding the related physical properties – specifically the heavy quark transport coefficients – as the inputs of the model and tuning the parameters, we can therefore describe the experimental data and estimate the fundamental properties of the QGP medium.

Such model-to-data comparisons have been utilized in heavy-ion collisions before but with limited execution. Previous studies focus only on one or two model parameter(s) and a subset of the experimental observables, and the evaluation of the model’s ability to describe the experimental data done by “eye-ball fitting” or “ χ -squared fitting” which lacks meaningful treatment of uncertainties. In this thesis, I adopted a state-of-the-art Bayesian model-to-data comparison framework — which has been successfully applied in the soft sector of the heavy-ion collisions — to calibrate a dynamical evolution model of heavy quarks to simultaneously describe various experimental data and estimate the relevant transport properties with quantitative uncertainties: a) The heavy quark spatial diffusion coefficient is parametrized as a general formula which explores a wide range of possibilities; 2) By performing Markov chain Monte Carlo random walk through the parameter space, the likelihood of different parameters to describe the experimental data are evaluated and the posterior distributions of the parameters are estimated; 3) After calibration, the heavy quark transport model is not only able to describe the calibrated experimental data, but also to predict additional observables. Moreover, using the posterior distribution of the parameters for the diffusion coefficient parametrization, we have estimated a posterior 90% credibility region for the diffusion coefficient. The width of the uncertainties is sensitive to the performance of the theoretical model and the precision of the experimental measure-

ments. The estimation of the heavy quark diffusion coefficient shows a minimum value $D_s 2\pi T \sim 1.8_{-0.76}^{+0.98}$ around $T_c = 154$ MeV, and a strong positive temperature dependence above T_c .

Furthermore, I have compared the different heavy flavor transport coefficients estimated by various heavy flavor theoretical models. A number of different modeling components — such as the initial condition generators, the soft medium descriptions — have been investigated in order to evaluate their possible contributions to the determination of the heavy quark transport coefficients. One finds that the different sources of uncertainties, produce a variability on the same order of magnitude as the variability resulting from the different sets of transport coefficients. To ensure a fair comparison among different estimation in the future, one has to reduce the uncertainties laid out in our studies either through theoretical improvements or by adding new observables into the comparison.

Finally, the launch of new detectors at RHIC (sPHENIX) and the more measurements scheduled at the LHC (run 3) will certainly bring the heavy-ion physics into a new era of high precision. Heavy quarks, being one of the valuable probes of the QGP medium, have been studied extensively and our understanding of their interaction and evolution inside the QGP medium has been improved greatly. Now it is believed that heavy quarks experience both significant collisional and radiative energy loss of the QGP medium, participate in the collective flow with the soft sector, and hadronize into hadrons through both fragmentation and recombination. A future study regarding the heavy quarks should focus on but not limit to: the heavy flavor dynamics in the intermediate transverse momentum region where the different interaction terms compete with each other; the heavy flavor partonic interaction in the pre-equilibrium stages before the thermal medium formation; a sophisticated model to describe the heavy flavor hadronization processes into different heavy flavor hadrons; application of the Bayesian framework to different heavy flavor evolution models and a meaningful evaluation of their performance.

Appendix A

Appendix

A.0.1 Relativistic kinematics

In relativistic nucleus-nucleus collisions, it is convenient to present particles in terms of rapidity and pseudo-rapidity variables y, η , as they take the simple form under Lorentz transformation.

A particle is presented by its 4-momentum: $p_\mu = (E, \mathbf{p})$, which is related to the rest mass m as:

$$E^2 = |\mathbf{p}|^2 + m^2 = p_x^2 + p_y^2 + p_z^2 + m^2. \quad (\text{A.1})$$

The rapidity of a particle is defined as:

$$y = \frac{1}{2} \ln \left(\frac{E + p_z}{E - p_z} \right). \quad (\text{A.2})$$

whose difference is invariant with respect to Lorentz boosts along the z -axis:

$$y'_1 - y'_2 = y_1 - y_2. \quad (\text{A.3})$$

Pseudo-rapidity η , which describes the angle of a particle relative to the beam axis, is defined as:

$$\eta \equiv \frac{1}{2} \ln \left(\frac{|p| + p_z}{|p| - p_z} \right) = -\ln \tan \frac{\theta}{2}. \quad (\text{A.4})$$

where θ is the angle made by the particle trajectory with the beam pipe $p_z/p = \cos \theta$. For high relativistic particles — $p \gg m$ — $y \simeq \eta$. The pseudo-rapidity is more accessible since it only depends on the polar angle of the momentum vector.

A.0.2 Mandelstam variables

The Mandelstam variables are useful to express the matrix element since they are invariant in different frame of reference.

For a $2 \rightarrow 2$ process, they are defined as:

$$\begin{aligned} s &= (p_1 + p_2)^2 = (p_3 + p_4)^2, \\ t &= (p_1 - p_3)^2 = (p_2 + p_4)^2, \\ u &= (p_1 - p_4)^2 = (p_2 - p_3)^2, \end{aligned} \tag{A.5}$$

where p_1, p_2 are the incoming and p_3, p_4 are the outgoing momenta. s is also referred as the squared center-of-mass energy.

They are related to the masses of the particles via:

$$s + t + u = \sum_{i=1}^4 m_i^2. \tag{A.6}$$

A.0.3 Hydrodynamics equations

Relativistic hydrodynamical models calculate the space-time evolution of the QGP medium via the conservation equations:

$$\partial_\mu T^{\mu\nu} = 0. \tag{A.7}$$

for the energy-momentum tensor

$$T^{\mu\nu} = e u^\mu u^\nu - \Delta^{\mu\nu} (P + \Pi) + \pi^{\mu\nu}. \tag{A.8}$$

The particular implementation of viscous hydrodynamics calculates the time evolution of the viscous corrections through the second-order Israel-Stewart equations in the 14-

momentum approximation, which yields a set of relaxation-type equations:

$$\tau_{\Pi}\dot{\Pi} + \Pi = -\xi\theta - \delta_{\Pi\Pi}\theta + \phi_1\Pi^2 + \lambda_{\Pi\pi}\pi^{\mu\nu}\sigma_{\mu\nu} + \phi_3\pi^{\mu\nu}\pi_{\mu\nu}, \quad (\text{A.9})$$

$$\begin{aligned} \tau_{\pi}\dot{\pi}^{<\mu\nu>} + \pi^{\mu\nu} = & 2\eta\sigma^{\mu\nu} + 2\pi_{\alpha}^{<\mu}w^{\nu>\alpha} - \delta_{\pi\pi}\pi^{\mu\nu}\theta \\ & + \phi_7\pi_{\alpha}^{<\mu}\pi^{\nu>\alpha} - \tau_{\pi\pi}\pi_{\alpha}^{<\mu}\sigma^{\nu>\alpha} \\ & + \lambda_{\pi\Pi}\Pi\sigma^{\mu\nu} + \phi_6\Pi\pi^{\mu\nu}. \end{aligned} \quad (\text{A.10})$$

Here η and ξ are the shear and bulk viscosities. For the remaining transport coefficients, we use analytic results derived for a gas of classical particles in the limit of small but finite masses.

A.0.4 Derive Fokker Planck equation from Langevin equation

One way to show the equivalence between Fokker-Planck and Langevin equation is to convert the Langevin equation to a path interval expression and to recognize the Fokker-Planck equation is a Euclidean Schrodinger equation which also has the path interval representation [170]. Another way to derive the Fokker-Planck equation is first derive the equation of motion for the probability distribution $\rho(\mathbf{x}, \mathbf{p}, t)$ to find the Brownian particles in the interval $(x, x + dx), (p, p + dp)$ at time t for one realization of the random kicks $\xi(t)$. Then average $\rho(\mathbf{x}, \mathbf{p}, t)$ over many realization of the random force. The phase space distribution $f(t, \mathbf{x}, \mathbf{p})$ is the macroscopic probability

$$f(t, \mathbf{x}, \mathbf{p}) = \langle \rho(\mathbf{x}, \mathbf{p}, t) \rangle_{\xi}. \quad (\text{A.11})$$

Probability density $\rho(\mathbf{x}, \mathbf{p}, t)$

The probability density $\rho(\mathbf{x}, \mathbf{p}, t)d\mathbf{x}d\mathbf{p}$ describes the probability that the Brownian particle is located in the infinitesimal area $d\mathbf{x}d\mathbf{p}$. $\dot{\mathbf{x}}\rho$ is the current density. In the phase space, we

have:

$$\int_{-\infty}^{\infty} d\mathbf{x} \int_{-\infty}^{\infty} d\mathbf{p} \rho(\mathbf{x}, \mathbf{p}, t) = 1. \quad (\text{A.12})$$

And the continuity equation in the phase space states:

$$\frac{\partial}{\partial t} \rho(\mathbf{x}, \mathbf{p}, t) = -\nabla \cdot (\dot{\mathbf{x}} \rho(\mathbf{x}, \mathbf{p}, t)) = -\frac{\partial}{\partial x_i} (\dot{x}_i \rho(\mathbf{x}, \mathbf{p}, t)) - \frac{\partial}{\partial p_i} (\dot{p}_i \rho(\mathbf{x}, \mathbf{p}, t)) \quad (\text{A.13})$$

Brownian particles

For a particle moving in the medium follows the Langevin equation, insert Eqn. 3.40 into Eqn. A.13 gives:

$$\begin{aligned} \frac{\partial}{\partial t} \rho(\mathbf{x}, \mathbf{p}, t) &= -\frac{\partial}{\partial x_i} (\dot{x}_i \cdot \rho(\mathbf{x}, \mathbf{p}, t)) - \frac{\partial}{\partial p_i} (\dot{p}_i \rho(\mathbf{x}, \mathbf{p}, t)) \\ &= -\frac{\partial}{\partial x_i} \left(\frac{p_i}{E} \cdot \rho(\mathbf{x}, \mathbf{p}, t) \right) - \frac{\partial}{\partial p_i} ((-\eta_D p_i + \xi_i) \cdot \rho(\mathbf{x}, \mathbf{p}, t)) \\ &= \left(-\frac{p_i}{E} \frac{\partial}{\partial x_i} + p_i \frac{\partial}{\partial p_i} \eta_D p_i \right) \rho(\mathbf{x}, \mathbf{p}, t) - \xi_i(t) \frac{\partial}{\partial p_i} \rho(\mathbf{x}, \mathbf{p}, t) \\ &= -L_0 \rho(\mathbf{x}, \mathbf{p}, t) - L_1(t) \rho(\mathbf{x}, \mathbf{p}, t). \end{aligned} \quad (\text{A.14})$$

The differential operation L_0 and $L_1(t)$ are defined as:

$$\begin{aligned} L_0 &= \frac{p_i}{E} \frac{\partial}{\partial x_i} - \frac{\partial}{\partial p_i} \eta_D p_i, \\ L_1 &= \xi_i(t) \frac{\partial}{\partial p_i}. \end{aligned} \quad (\text{A.15})$$

$$\begin{aligned} L_0 &= \frac{p_i}{E} \frac{\partial}{\partial x_i} - \eta_D - p_i \frac{\partial}{\partial p_i} \eta_D, \\ L_1 &= \xi_i(t) \frac{\partial}{\partial p_i}. \end{aligned} \quad (\text{A.16})$$

Let $\rho(\mathbf{x}, \mathbf{p}, t) = e^{-L_0 t} \sigma(\mathbf{x}, \mathbf{p}, t)$, Eqn. A.14 is then simplified as:

$$\frac{\partial}{\partial t} \sigma(\mathbf{x}, \mathbf{p}, t) = -e^{L_0 t} L_1(t) e^{-L_0 t} \sigma(\mathbf{x}, \mathbf{p}, t) = -V(t) \sigma(\mathbf{x}, \mathbf{p}, t), \quad (\text{A.17})$$

and has the solution:

$$\sigma(t) = \exp \left[- \int_0^t dt' V(t') \right] \sigma(0) \quad (\text{A.18})$$

Taking the average $\langle \dots \rangle_\xi$ over the Gaussian noise $\xi(t)$, $\langle \sigma(t) \rangle_\xi$ is the characteristic function of the Gaussian random variable $X(t) = i \int_0^t dt_1 V(t_1)$, which also satisfies:

$$\langle X(t) \rangle_\xi = 0, \quad \langle (X(t))^2 \rangle = \frac{1}{2} \int_0^t dt_1 \int_0^t dt_2 \langle V(t_1) V(t_2) \rangle. \quad (\text{A.19})$$

We find:

$$\langle \sigma(t) \rangle_\xi = \exp \left[\frac{1}{2} \int_0^t dt_1 \int_0^t dt_2 \langle V(t_1) V(t_2) \rangle_\xi \right] \sigma(0). \quad (\text{A.20})$$

And the integral in Eqn. A.20 can be calculated as:

$$\begin{aligned} \frac{1}{2} \int_0^t dt_1 \int_0^t dt_2 \langle V(t_1) V(t_2) \rangle_\xi &= \frac{1}{2} \int_0^t dt_1 \int_0^t dt_2 \left\langle e^{L_0 t_1} L_1(t_1) e^{-L_0 t_1} e^{L_0 t_2} L_1(t_2) e^{-L_0 t_2} \right\rangle \\ &= \frac{1}{2} \int_0^t dt_1 \int_0^t dt_2 \left\langle e^{L_0 t_1} \xi_i(t_1) \frac{\partial}{\partial p_i} e^{-L_0 t_1} e^{L_0 t_2} \xi_j(t_2) \frac{\partial}{\partial p_j} e^{-L_0 t_2} \right\rangle \\ &= \frac{1}{2} \int_0^t dt_1 \int_0^t dt_2 \left\langle e^{L_0 t_1} \frac{\partial}{\partial p_i} e^{-L_0(t_1-t_2)} \xi_i(t_1) \xi_j(t_2) \frac{\partial}{\partial p_j} e^{-L_0 t_2} \right\rangle \\ &= \frac{1}{2} \int_0^t dt_1 e^{L_0 t_1} \frac{\partial}{\partial p_i} \kappa^{ij} \frac{\partial}{\partial p_j} e^{-L_0 t_1}. \end{aligned}$$

Then:

$$\frac{\partial}{\partial t} \langle \sigma(t) \rangle_\xi = \frac{1}{2} e^{L_0 t} \frac{\partial}{\partial p_i} \kappa^{ij} \frac{\partial}{\partial p_j} \langle \sigma(t) \rangle_\xi, \quad (\text{A.21})$$

Substitute $\sigma(t) = e^{L_0 t} \rho(t)$, one gets the equation for averaged probability $\langle \rho(t) \rangle_\xi$:

$$\frac{\partial}{\partial t} \langle \rho(\mathbf{x}, \mathbf{p}, t) \rangle_\xi = -L_0 \langle \rho(\mathbf{x}, \mathbf{p}, t) \rangle_\xi + \frac{1}{2} \frac{\partial}{\partial p_i} \kappa^{ij} \frac{\partial}{\partial p_j} \langle \rho(\mathbf{x}, \mathbf{p}, t) \rangle_\xi, \quad (\text{A.22})$$

and the equation for the probability distribution in the phase space as:

$$\begin{aligned} \frac{\partial}{\partial t} P(\mathbf{x}, \mathbf{p}, t) &= -L_0 P(\mathbf{x}, \mathbf{p}, t) + \frac{1}{2} \frac{\partial}{\partial p_i} \kappa^{ij} \frac{\partial}{\partial p_j} P(\mathbf{x}, \mathbf{p}, t) \\ &= -\frac{p_i}{E} \frac{\partial}{\partial x_i} P(\mathbf{x}, \mathbf{p}, t) - \frac{\partial}{\partial p_i} (\eta_D p_i P(\mathbf{x}, \mathbf{p}, t)) + \frac{1}{2} \frac{\partial}{\partial p_i} \kappa^{ij} \frac{\partial}{\partial p_j} P(\mathbf{x}, \mathbf{p}, t), \end{aligned} \quad (\text{A.23})$$

which is the Fokker-Planck equation for the full phase distribution $P(\mathbf{x}, \mathbf{p}, t)$. Integrate over position phase space, and compare with Eqn. 3.37, one can find the corresponding relationship between the drag term $A_i(\mathbf{p})$ and the momentum transport terms:

$$\begin{aligned} A_i(\mathbf{p}) &= -\eta_D p_i, \\ B_{ij}(\mathbf{p}) &= \kappa_{ij} = \kappa_L \frac{p_i p_j}{p^2} + \kappa_L \left(\delta_{ij} - \frac{p_i p_j}{p^2} \right). \end{aligned} \quad (\text{A.24})$$

Bibliography

- [1] D. H. Rischke, *The Quark gluon plasma in equilibrium*, *Prog. Part. Nucl. Phys.* **52** (2004) 197 [nucl-th/0305030].
- [2] PARTICLE DATA GROUP collaboration, *Review of Particle Physics*, *Phys. Rev.* **D98** (2018) 030001.
- [3] D. J. Gross and F. Wilczek, *Ultraviolet Behavior of Nonabelian Gauge Theories*, *Phys. Rev. Lett.* **30** (1973) 1343.
- [4] H. D. Politzer, *Reliable Perturbative Results for Strong Interactions?*, *Phys. Rev. Lett.* **30** (1973) 1346.
- [5] E. V. Shuryak, *Quantum Chromodynamics and the Theory of Superdense Matter*, *Phys. Rept.* **61** (1980) 71.
- [6] Y. Akiba et al., *The Hot QCD White Paper: Exploring the Phases of QCD at RHIC and the LHC*, 1502.02730.
- [7] HOTQCD collaboration, *Equation of state in (2+1)-flavor QCD*, *Phys. Rev.* **D90** (2014) 094503 [1407.6387].
- [8] P. Braun-Munzinger and J. Wambach, *The Phase Diagram of Strongly-Interacting Matter*, *Rev. Mod. Phys.* **81** (2009) 1031 [0801.4256].
- [9] K. Rajagopal and F. Wilczek, *The Condensed matter physics of QCD*, in *At the frontier of particle physics. Handbook of QCD. Vol. 1-3*, M. Shifman and B. Ioffe, eds., pp. 2061–2151, (2000), hep-ph/0011333, DOI.
- [10] M. A. Stephanov, *QCD phase diagram: An Overview*, *PoS LAT2006* (2006) 024 [hep-lat/0701002].
- [11] O. Philipsen, *Lattice QCD at non-zero temperature and baryon density*, in *Modern perspectives in lattice QCD: Quantum field theory and high performance computing. Proceedings, International School, 93rd Session, Les Houches, France, August 3-28, 2009*, pp. 273–330, 2010, 1009.4089.
- [12] R. Pasechnik and M. Šumbera, *Phenomenological Review on Quark–Gluon Plasma: Concepts vs. Observations*, *Universe* **3** (2017) 7 [1611.01533].
- [13] R. Rapp and E. V. Shuryak, *Resolving the anti-baryon production puzzle in high-energy heavy ion collisions*, *Phys. Rev. Lett.* **86** (2001) 2980 [hep-ph/0008326].
- [14] P. Braun-Munzinger, J. Stachel and C. Wetterich, *Chemical freezeout and the QCD*

- phase transition temperature, Phys. Lett. B596* (2004) 61 [nucl-th/0311005].
- [15] R. Stock, *The Parton to hadron phase transition observed in Pb + Pb collisions at 158-GeV per nucleon, Phys. Lett. B456* (1999) 277 [hep-ph/9905247].
- [16] J. Noronha-Hostler, M. Luzum and J.-Y. Ollitrault, *Hydrodynamic predictions for 5.02 TeV Pb-Pb collisions, Phys. Rev. C93* (2016) 034912 [1511.06289].
- [17] H. Niemi, K. J. Eskola, R. Paatelainen and K. Tuominen, *Predictions for 5.023 TeV Pb + Pb collisions at the CERN Large Hadron Collider, Phys. Rev. C93* (2016) 014912 [1511.04296].
- [18] ALICE collaboration, *Higher harmonic anisotropic flow measurements of charged particles in Pb-Pb collisions at $\sqrt{s_{NN}}=2.76$ TeV, Phys. Rev. Lett. 107* (2011) 032301 [1105.3865].
- [19] ALICE collaboration, *Anisotropic flow of charged particles in Pb-Pb collisions at $\sqrt{s_{NN}} = 5.02$ TeV, Phys. Rev. Lett. 116* (2016) 132302 [1602.01119].
- [20] M. L. Miller, K. Reygers, S. J. Sanders and P. Steinberg, *Glauber modeling in high energy nuclear collisions, Ann. Rev. Nucl. Part. Sci. 57* (2007) 205 [nucl-ex/0701025].
- [21] PHENIX collaboration, *Formation of dense partonic matter in relativistic nucleus-nucleus collisions at RHIC: Experimental evaluation by the PHENIX collaboration, Nucl. Phys. A757* (2005) 184 [nucl-ex/0410003].
- [22] P. Romatschke and U. Romatschke, *Viscosity Information from Relativistic Nuclear Collisions: How Perfect is the Fluid Observed at RHIC?, Phys. Rev. Lett. 99* (2007) 172301 [0706.1522].
- [23] CMS collaboration, *Study of high-pT charged particle suppression in PbPb compared to pp collisions at $\sqrt{s_{NN}} = 2.76$ TeV, Eur. Phys. J. C72* (2012) 1945 [1202.2554].
- [24] Wikipedia contributors, *Jet (particle physics)*, 2004.
- [25] PHENIX collaboration, *Centrality dependence of direct photon production in $s(NN)^{1/2} = 200$ -GeV Au + Au collisions, Phys. Rev. Lett. 94* (2005) 232301 [nucl-ex/0503003].
- [26] CMS collaboration, *W, Z and photon production in CMS, Nucl. Phys. A910-911* (2013) 139 [1208.4927].
- [27] L. L. Frankfurt and M. I. Strikman, *Hard Nuclear Processes and Microscopic Nuclear Structure, Phys. Rept. 160* (1988) 235.

- [28] K. J. Eskola, H. Paukkunen and C. A. Salgado, *EPS09: A New Generation of NLO and LO Nuclear Parton Distribution Functions*, *JHEP* **04** (2009) 065 [0902.4154].
- [29] STAR collaboration, *Energy dependence of π^+ , p and anti- p transverse momentum spectra for Au+Au collisions at $\sqrt{s_{NN}} = 62.4$ and 200-GeV*, *Phys. Lett.* **B655** (2007) 104 [nucl-ex/0703040].
- [30] PHENIX collaboration, *Common suppression pattern of eta and π^0 mesons at high transverse momentum in Au+Au collisions at $\sqrt{s_{NN}} = 200$ -GeV*, *Phys. Rev. Lett.* **96** (2006) 202301 [nucl-ex/0601037].
- [31] PHENIX collaboration, *Single electrons from heavy flavor decays in $p+p$ collisions at $\sqrt{s} = 200$ -GeV*, *Phys. Rev. Lett.* **96** (2006) 032001 [hep-ex/0508034].
- [32] PHENIX collaboration, *Nuclear modification of electron spectra and implications for heavy quark energy loss in Au+Au collisions at $\sqrt{s_{NN}} = 200$ -GeV*, *Phys. Rev. Lett.* **96** (2006) 032301 [nucl-ex/0510047].
- [33] R. Nouicer, *Formation of Dense Partonic Matter in High Energy Heavy-Ion Collisions: Highlights of RHIC Results*, in *Advanced Studies Institute on Symmetries and Spin (SPIN-Praha-2008) Prague, Czech Republic, July 20-26, 2008, 2009*, 0901.0910.
- [34] CMS collaboration, *Charged-particle nuclear modification factors in PbPb and pPb collisions at $\sqrt{s_{NN}} = 5.02$ TeV*, *JHEP* **04** (2017) 039 [1611.01664].
- [35] CMS collaboration, *Measurement of the B^\pm Meson Nuclear Modification Factor in Pb-Pb Collisions at $\sqrt{s_{NN}} = 5.02$ TeV*, *Phys. Rev. Lett.* **119** (2017) 152301 [1705.04727].
- [36] CMS collaboration, *Nuclear modification factor of D^0 mesons in PbPb collisions at $\sqrt{s_{NN}} = 5.02$ TeV*, *Phys. Lett.* **B782** (2018) 474 [1708.04962].
- [37] C. F. Perdrisat, V. Punjabi and M. Vanderhaeghen, *Nucleon Electromagnetic Form Factors*, *Prog. Part. Nucl. Phys.* **59** (2007) 694 [hep-ph/0612014].
- [38] D. Kharzeev, E. Levin and M. Nardi, *The Onset of classical QCD dynamics in relativistic heavy ion collisions*, *Phys. Rev.* **C71** (2005) 054903 [hep-ph/0111315].
- [39] H.-J. Drescher, A. Dumitru, A. Hayashigaki and Y. Nara, *The Eccentricity in heavy-ion collisions from color glass condensate initial conditions*, *Phys. Rev.* **C74** (2006) 044905 [nucl-th/0605012].
- [40] B. Schenke, P. Tribedy and R. Venugopalan, *Fluctuating Glasma initial conditions*

- and flow in heavy ion collisions, Phys. Rev. Lett.* **108** (2012) 252301 [1202.6646].
- [41] B. Schenke, P. Tribedy and R. Venugopalan, *Event-by-event gluon multiplicity, energy density, and eccentricities in ultrarelativistic heavy-ion collisions, Phys. Rev. C* **86** (2012) 034908 [1206.6805].
- [42] J. S. Moreland, J. E. Bernhard and S. A. Bass, *Alternative ansatz to wounded nucleon and binary collision scaling in high-energy nuclear collisions, Phys. Rev. C* **92** (2015) 011901 [1412.4708].
- [43] H. Song and U. W. Heinz, *Causal viscous hydrodynamics in 2+1 dimensions for relativistic heavy-ion collisions, Phys. Rev. C* **77** (2008) 064901 [0712.3715].
- [44] J. E. Bernhard, J. S. Moreland, S. A. Bass, J. Liu and U. Heinz, *Applying Bayesian parameter estimation to relativistic heavy-ion collisions: simultaneous characterization of the initial state and quark-gluon plasma medium, Phys. Rev. C* **94** (2016) 024907 [1605.03954].
- [45] S. A. Bass et al., *Microscopic models for ultrarelativistic heavy ion collisions, Prog. Part. Nucl. Phys.* **41** (1998) 255 [nucl-th/9803035].
- [46] M. Bleicher et al., *Relativistic hadron hadron collisions in the ultrarelativistic quantum molecular dynamics model, J. Phys. G* **25** (1999) 1859 [hep-ph/9909407].
- [47] M. Cacciari, M. Greco and P. Nason, *The $P(T)$ spectrum in heavy flavor hadroproduction, JHEP* **05** (1998) 007 [hep-ph/9803400].
- [48] M. Cacciari, S. Frixione and P. Nason, *The $p(T)$ spectrum in heavy flavor photoproduction, JHEP* **03** (2001) 006 [hep-ph/0102134].
- [49] K. J. Eskola, H. Paukkunen and C. A. Salgado, *Nuclear PDFs at NLO - status report and review of the EPS09 results, Nucl. Phys. A* **855** (2011) 150 [1011.6534].
- [50] T. Sjostrand, S. Mrenna and P. Z. Skands, *A Brief Introduction to PYTHIA 8.1, Comput. Phys. Commun.* **178** (2008) 852 [0710.3820].
- [51] Z. Xu and C. Greiner, *Thermalization of gluons in ultrarelativistic heavy ion collisions by including three-body interactions in a parton cascade, Phys. Rev. C* **71** (2005) 064901 [hep-ph/0406278].
- [52] Z. Xu and C. Greiner, *Transport rates and momentum isotropization of gluon matter in ultrarelativistic heavy-ion collisions, Phys. Rev. C* **76** (2007) 024911 [hep-ph/0703233].

- [53] W. Cassing and E. L. Bratkovskaya, *Parton transport and hadronization from the dynamical quasiparticle point of view*, *Phys. Rev.* **C78** (2008) 034919 [0808.0022].
- [54] W. Cassing and E. L. Bratkovskaya, *Parton-Hadron-String Dynamics: an off-shell transport approach for relativistic energies*, *Nucl. Phys.* **A831** (2009) 215 [0907.5331].
- [55] J. S. Moreland, J. E. Bernhard and S. A. Bass, *Estimating initial state and quark-gluon plasma medium properties using a hybrid model with nucleon substructure calibrated to p-Pb and Pb-Pb collisions at $\sqrt{s_{NN}} = 5.02$ TeV*, 1808.02106.
- [56] J. S. Moreland and R. A. Soltz, *Hydrodynamic simulations of relativistic heavy-ion collisions with different lattice quantum chromodynamics calculations of the equation of state*, *Phys. Rev.* **C93** (2016) 044913 [1512.02189].
- [57] J. E. Bernhard, *Bayesian parameter estimation for relativistic heavy-ion collisions*, Ph.D. thesis, Duke U., 2018-04-19. 1804.06469.
- [58] C. Shen, Z. Qiu, H. Song, J. Bernhard, S. Bass and U. Heinz, *The iEBE-VISHNU code package for relativistic heavy-ion collisions*, *Comput. Phys. Commun.* **199** (2016) 61 [1409.8164].
- [59] W. Israel and J. M. Stewart, *Transient relativistic thermodynamics and kinetic theory*, *Annals Phys.* **118** (1979) 341.
- [60] C. Peterson, D. Schlatter, I. Schmitt and P. M. Zerwas, *Scaling Violations in Inclusive $e^+ e^-$ Annihilation Spectra*, *Phys. Rev.* **D27** (1983) 105.
- [61] Z.-w. Lin, T. G. Di and C. M. Ko, *Charm meson scattering cross-sections by pion and rho meson*, *Nucl. Phys.* **A689** (2001) 965 [nucl-th/0006086].
- [62] ALICE collaboration, *Centrality dependence of the charged-particle multiplicity density at midrapidity in Pb-Pb collisions at $\sqrt{s_{NN}} = 5.02$ TeV*, *Phys. Rev. Lett.* **116** (2016) 222302 [1512.06104].
- [63] J. Stachel, A. Andronic, P. Braun-Munzinger and K. Redlich, *Confronting LHC data with the statistical hadronization model*, *J. Phys. Conf. Ser.* **509** (2014) 012019 [1311.4662].
- [64] ALICE collaboration, *Production of identified charged hadrons in Pb-Pb collisions at $\sqrt{s_{NN}} = 5.02$ TeV*, *Nucl. Phys.* **A967** (2017) 421 [1704.06030].
- [65] N. Borghini, P. M. Dinh and J.-Y. Ollitrault, *A New method for measuring azimuthal distributions in nucleus-nucleus collisions*, *Phys. Rev.* **C63** (2001)

054906 [nucl-th/0007063].

- [66] N. Borghini, P. M. Dinh and J.-Y. Ollitrault, *Flow analysis from multiparticle azimuthal correlations*, *Phys. Rev.* **C64** (2001) 054901 [nucl-th/0105040].
- [67] A. Bilandzic, R. Snellings and S. Voloshin, *Flow analysis with cumulants: Direct calculations*, *Phys. Rev.* **C83** (2011) 044913 [1010.0233].
- [68] CMS collaboration, *Multiplicity and Transverse Momentum Dependence of Two- and Four-Particle Correlations in pPb and PbPb Collisions*, *Phys. Lett.* **B724** (2013) 213 [1305.0609].
- [69] STAR collaboration, *Observation of D^0 Meson Nuclear Modifications in Au+Au Collisions at $\sqrt{s_{NN}} = 200$ GeV*, *Phys. Rev. Lett.* **113** (2014) 142301 [1404.6185].
- [70] ALICE collaboration, *Open heavy-flavour and quarkonium production in Pb-Pb and p-Pb collisions measured by the ALICE detector at the LHC*, in *Proceedings, 51st Rencontres de Moriond on QCD and High Energy Interactions: La Thuile, Italy, March 19-26, 2016*, pp. 273–276, 2016, 1606.03970.
- [71] A. Andronic et al., *Heavy-flavour and quarkonium production in the LHC era: from proton–proton to heavy-ion collisions*, *Eur. Phys. J.* **C76** (2016) 107 [1506.03981].
- [72] S. Cao, G.-Y. Qin and S. A. Bass, *Heavy-quark dynamics and hadronization in ultrarelativistic heavy-ion collisions: Collisional versus radiative energy loss*, *Phys. Rev.* **C88** (2013) 044907 [1308.0617].
- [73] Y. Xu, M. Nahrgang, J. E. Bernhard, S. Cao and S. A. Bass, *A data-driven analysis of the heavy quark transport coefficient*, *Nucl. Phys.* **A967** (2017) 668 [1704.07800].
- [74] W. Ke, Y. Xu and S. A. Bass, *Linearized Boltzmann-Langevin model for heavy quark transport in hot and dense QCD matter*, *Phys. Rev.* **C98** (2018) 064901 [1806.08848].
- [75] H. Song and U. W. Heinz, *Suppression of elliptic flow in a minimally viscous quark-gluon plasma*, *Phys. Lett.* **B658** (2008) 279 [0709.0742].
- [76] T. Song, H. Berrehrhah, D. Cabrera, J. M. Torres-Rincon, L. Tolos, W. Cassing et al., *Tomography of the Quark-Gluon-Plasma by Charm Quarks*, *Phys. Rev.* **C92** (2015) 014910 [1503.03039].
- [77] Z.-W. Lin, C. M. Ko, B.-A. Li, B. Zhang and S. Pal, *A Multi-phase transport model for relativistic heavy ion collisions*, *Phys. Rev.* **C72** (2005) 064901

[nucl-th/0411110].

- [78] X.-N. Wang, *Role of multiple mini - jets in high-energy hadronic reactions*, *Phys. Rev.* **D43** (1991) 104.
- [79] P. B. Gossiaux and J. Aichelin, *Towards an understanding of the RHIC single electron data*, *Phys. Rev.* **C78** (2008) 014904 [0802.2525].
- [80] P. B. Gossiaux, R. Bierkandt and J. Aichelin, *Tomography of a quark gluon plasma at RHIC and LHC energies*, *Phys. Rev.* **C79** (2009) 044906 [0901.0946].
- [81] M. Nahrgang, J. Aichelin, P. B. Gossiaux and K. Werner, *Azimuthal correlations of heavy quarks in Pb + Pb collisions at $\sqrt{s} = 2.76$ TeV at the CERN Large Hadron Collider*, *Phys. Rev.* **C90** (2014) 024907 [1305.3823].
- [82] W. A. Horowitz and M. Gyulassy, *Heavy quark jet tomography of Pb + Pb at LHC: AdS/CFT drag or pQCD energy loss?*, *Phys. Lett.* **B666** (2008) 320 [0706.2336].
- [83] W. A. Horowitz, *Testing pQCD and AdS/CFT Energy Loss at RHIC and LHC*, *AIP Conf. Proc.* **1441** (2012) 889 [1108.5876].
- [84] S. Plumari, W. M. Alberico, V. Greco and C. Ratti, *Recent thermodynamic results from lattice QCD analyzed within a quasi-particle model*, *Phys. Rev.* **D84** (2011) 094004 [1103.5611].
- [85] F. Scardina, S. K. Das, V. Minissale, S. Plumari and V. Greco, *Estimating the charm quark diffusion coefficient and thermalization time from D meson spectra at energies available at the BNL Relativistic Heavy Ion Collider and the CERN Large Hadron Collider*, *Phys. Rev.* **C96** (2017) 044905 [1707.05452].
- [86] J. Uphoff, O. Fochler, Z. Xu and C. Greiner, *Heavy quark production at RHIC and LHC within a partonic transport model*, *Phys. Rev.* **C82** (2010) 044906 [1003.4200].
- [87] J. Uphoff, O. Fochler, Z. Xu and C. Greiner, *Elliptic Flow and Energy Loss of Heavy Quarks in Ultra-Relativistic heavy Ion Collisions*, *Phys. Rev.* **C84** (2011) 024908 [1104.2295].
- [88] J. Uphoff, F. Senzel, Z. Xu and C. Greiner, *Momentum imbalance of D mesons in ultra-relativistic heavy-ion collisions at LHC*, *Phys. Rev.* **C89** (2014) 064906 [1310.1340].
- [89] J. Uphoff, O. Fochler, Z. Xu and C. Greiner, *Elastic and radiative heavy quark interactions in ultra-relativistic heavy-ion collisions*, *J. Phys.* **G42** (2015) 115106 [1408.2964].
- [90] S. Wicks, W. Horowitz, M. Djordjevic and M. Gyulassy, *Elastic, inelastic, and path*

- length fluctuations in jet tomography*, *Nucl. Phys.* **A784** (2007) 426 [nucl-th/0512076].
- [91] S. Wicks, W. Horowitz, M. Djordjevic and M. Gyulassy, *Heavy quark jet quenching with collisional plus radiative energy loss and path length fluctuations*, *Nucl. Phys.* **A783** (2007) 493 [nucl-th/0701063].
- [92] M. He, R. J. Fries and R. Rapp, *D_s-Meson as Quantitative Probe of Diffusion and Hadronization in Nuclear Collisions*, *Phys. Rev. Lett.* **110** (2013) 112301 [1204.4442].
- [93] M. He, R. J. Fries and R. Rapp, *Thermal Relaxation of Charm in Hadronic Matter*, *Phys. Lett.* **B701** (2011) 445 [1103.6279].
- [94] M. He, R. J. Fries and R. Rapp, *Heavy Flavor at the Large Hadron Collider in a Strong Coupling Approach*, *Phys. Lett.* **B735** (2014) 445 [1401.3817].
- [95] S. K. Das, F. Scardina, S. Plumari and V. Greco, *Heavy-flavor in-medium momentum evolution: Langevin versus Boltzmann approach*, *Phys. Rev.* **C90** (2014) 044901 [1312.6857].
- [96] S. et al., *Hot and Dense QCD matter, Unraveling the Mysteries of the Strongly Interacting Quark-Gluon-Plasma, White Paper (Brookhaven National Lab)* (2012) .
- [97] J. Ghiglieri, G. D. Moore and D. Teaney, *Jet-Medium Interactions at NLO in a Weakly-Coupled Quark-Gluon Plasma*, *JHEP* **03** (2016) 095 [1509.07773].
- [98] E. Braaten and R. D. Pisarski, *Simple effective Lagrangian for hard thermal loops*, *Phys. Rev.* **D45** (1992) R1827.
- [99] S. Caron-Huot, *O(g) plasma effects in jet quenching*, *Phys. Rev.* **D79** (2009) 065039 [0811.1603].
- [100] G. D. Moore and D. Teaney, *How much do heavy quarks thermalize in a heavy ion collision?*, *Phys. Rev.* **C71** (2005) 064904 [hep-ph/0412346].
- [101] J. F. Gunion and G. Bertsch, *HADRONIZATION BY COLOR BREMSSTRAHLUNG*, *Phys. Rev.* **D25** (1982) 746.
- [102] M. G. Mustafa, D. Pal, D. K. Srivastava and M. Thoma, *Radiative energy loss of heavy quarks in a quark gluon plasma*, *Phys. Lett.* **B428** (1998) 234 [nucl-th/9711059].
- [103] Y. L. Dokshitzer and D. E. Kharzeev, *Heavy quark colorimetry of QCD matter*, *Phys. Lett.* **B519** (2001) 199 [hep-ph/0106202].
- [104] R. Abir, C. Greiner, M. Martinez, M. G. Mustafa and J. Uphoff, *Soft gluon emission*

- off a heavy quark revisited*, *Phys. Rev.* **D85** (2012) 054012 [1109.5539].
- [105] Y. L. Dokshitzer and D. E. Kharzeev, *Heavy quark colorimetry of QCD matter*, *Phys. Lett.* **B519** (2001) 199 [hep-ph/0106202].
- [106] A. Majumder, *The In-medium scale evolution in jet modification*, 0901.4516.
- [107] A. Majumder, R. J. Fries and B. Muller, *Photon bremsstrahlung and diffusive broadening of a hard jet*, *Phys. Rev.* **C77** (2008) 065209 [0711.2475].
- [108] A. Majumder and B. Muller, *Higher twist jet broadening and classical propagation*, *Phys. Rev.* **C77** (2008) 054903 [0705.1147].
- [109] X.-f. Guo and X.-N. Wang, *Multiple scattering, parton energy loss and modified fragmentation functions in deeply inelastic $e A$ scattering*, *Phys. Rev. Lett.* **85** (2000) 3591 [hep-ph/0005044].
- [110] A. Majumder, *Hard collinear gluon radiation and multiple scattering in a medium*, *Phys. Rev.* **D85** (2012) 014023 [0912.2987].
- [111] R. Baier, Y. L. Dokshitzer, A. H. Mueller, S. Peigne and D. Schiff, *The Landau-Pomeranchuk-Migdal effect in QED*, *Nucl. Phys.* **B478** (1996) 577 [hep-ph/9604327].
- [112] R. Baier, Y. L. Dokshitzer, A. H. Mueller, S. Peigne and D. Schiff, *Radiative energy loss of high-energy quarks and gluons in a finite volume quark - gluon plasma*, *Nucl. Phys.* **B483** (1997) 291 [hep-ph/9607355].
- [113] R. Baier, Y. L. Dokshitzer, A. H. Mueller, S. Peigne and D. Schiff, *Radiative energy loss and $p(T)$ broadening of high-energy partons in nuclei*, *Nucl. Phys.* **B484** (1997) 265 [hep-ph/9608322].
- [114] R. Baier, Y. L. Dokshitzer, A. H. Mueller and D. Schiff, *Radiative energy loss of high-energy partons traversing an expanding QCD plasma*, *Phys. Rev.* **C58** (1998) 1706 [hep-ph/9803473].
- [115] M. Gyulassy, P. Levai and I. Vitev, *Jet quenching in thin quark gluon plasmas. 1. Formalism*, *Nucl. Phys.* **B571** (2000) 197 [hep-ph/9907461].
- [116] M. Gyulassy, P. Levai and I. Vitev, *Jet quenching in thin plasmas*, *Nucl. Phys.* **A661** (1999) 637 [hep-ph/9907343].
- [117] M. Gyulassy, P. Levai and I. Vitev, *Reaction operator approach to nonAbelian energy loss*, *Nucl. Phys.* **B594** (2001) 371 [nucl-th/0006010].
- [118] M. Gyulassy, P. Levai and I. Vitev, *NonAbelian energy loss at finite opacity*, *Phys. Rev. Lett.* **85** (2000) 5535 [nucl-th/0005032].

- [119] M. Gyulassy, P. Levai and I. Vitev, *Jet tomography of Au+Au reactions including multigluon fluctuations*, *Phys. Lett.* **B538** (2002) 282 [nucl-th/0112071].
- [120] P. B. Arnold, G. D. Moore and L. G. Yaffe, *Photon emission from ultrarelativistic plasmas*, *JHEP* **11** (2001) 057 [hep-ph/0109064].
- [121] P. B. Arnold, G. D. Moore and L. G. Yaffe, *Photon emission from quark gluon plasma: Complete leading order results*, *JHEP* **12** (2001) 009 [hep-ph/0111107].
- [122] P. B. Arnold, G. D. Moore and L. G. Yaffe, *Photon and gluon emission in relativistic plasmas*, *JHEP* **06** (2002) 030 [hep-ph/0204343].
- [123] P. B. Arnold, G. D. Moore and L. G. Yaffe, *Effective kinetic theory for high temperature gauge theories*, *JHEP* **01** (2003) 030 [hep-ph/0209353].
- [124] N. Armesto et al., *Comparison of Jet Quenching Formalisms for a Quark-Gluon Plasma 'Brick'*, *Phys. Rev.* **C86** (2012) 064904 [1106.1106].
- [125] S. A. Bass, C. Gale, A. Majumder, C. Nonaka, G.-Y. Qin, T. Renk et al., *Systematic Comparison of Jet Energy-Loss Schemes in a realistic hydrodynamic medium*, *Phys. Rev.* **C79** (2009) 024901 [0808.0908].
- [126] ALICE collaboration, *Measurement of the D-meson Nuclear Modification Factor and Elliptic Flow in Pb–Pb Collisions at $\sqrt{s_{NN}} = 5.02$ TeV with ALICE at the LHC*, *Int. J. Mod. Phys. Conf. Ser.* **46** (2018) 1860018 [1802.09245].
- [127] CMS collaboration, *D^0 meson v_n harmonics in PbPb collisions at 5.02 TeV*, .
- [128] R. Sharma, I. Vitev and B.-W. Zhang, *Light-cone wave function approach to open heavy flavor dynamics in QCD matter*, *Phys. Rev.* **C80** (2009) 054902 [0904.0032].
- [129] T. Song, H. Berrehrah, D. Cabrera, W. Cassing and E. Bratkovskaya, *Charm production in Pb + Pb collisions at energies available at the CERN Large Hadron Collider*, *Phys. Rev.* **C93** (2016) 034906 [1512.00891].
- [130] H. van Hees, M. Mannarelli, V. Greco and R. Rapp, *Nonperturbative heavy-quark diffusion in the quark-gluon plasma*, *Phys. Rev. Lett.* **100** (2008) 192301 [0709.2884].
- [131] S. Caron-Huot and G. D. Moore, *Heavy quark diffusion in QCD and N=4 SYM at next-to-leading order*, *JHEP* **02** (2008) 081 [0801.2173].
- [132] F. Riek and R. Rapp, *Quarkonia and Heavy-Quark Relaxation Times in the Quark-Gluon Plasma*, *Phys. Rev.* **C82** (2010) 035201 [1005.0769].

- [133] S. Cao, T. Luo, G.-Y. Qin and X.-N. Wang, *Linearized Boltzmann transport model for jet propagation in the quark-gluon plasma: Heavy quark evolution*, *Phys. Rev.* **C94** (2016) 014909 [1605.06447].
- [134] H. T. Ding, A. Francis, O. Kaczmarek, F. Karsch, H. Satz and W. Soeldner, *Charmonium properties in hot quenched lattice QCD*, *Phys. Rev.* **D86** (2012) 014509 [1204.4945].
- [135] J. Novak, K. Novak, S. Pratt, J. Vredevoogd, C. Coleman-Smith and R. Wolpert, *Determining Fundamental Properties of Matter Created in Ultrarelativistic Heavy-Ion Collisions*, *Phys. Rev.* **C89** (2014) 034917 [1303.5769].
- [136] S. Pratt, E. Sangaline, P. Sorensen and H. Wang, *Constraining the Eq. of State of Super-Hadronic Matter from Heavy-Ion Collisions*, *Phys. Rev. Lett.* **114** (2015) 202301 [1501.04042].
- [137] J. Auvinen, J. E. Bernhard, S. A. Bass and I. Karpenko, *Investigating the collision energy dependence of η/s in the beam energy scan at the BNL Relativistic Heavy Ion Collider using Bayesian statistics*, *Phys. Rev.* **C97** (2018) 044905 [1706.03666].
- [138] N. Benitez, *Bayesian photometric redshift estimation*, *Astrophys. J.* **536** (2000) 571 [astro-ph/9811189].
- [139] A. Hocker, H. Lacker, S. Laplace and F. Le Diberder, *A New approach to a global fit of the CKM matrix*, *Eur. Phys. J.* **C21** (2001) 225 [hep-ph/0104062].
- [140] LIGO SCIENTIFIC, VIRGO collaboration, *Properties of the Binary Black Hole Merger GW150914*, *Phys. Rev. Lett.* **116** (2016) 241102 [1602.03840].
- [141] D. Higdon, J. D. McDonnell, N. Schunck, J. Sarich and S. M. Wild, *A Bayesian Approach for Parameter Estimation and Prediction using a Computationally Intensive Model*, *J.Phys.* **G42** (2015) 034009 [1407.3017].
- [142] A. O'Hagan, *Bayesian analysis of computer code outputs: a tutorial*, *Rel.Engin.Sys.Safety* **91** (2006) 1290.
- [143] C. E. Rasmussen and C. K. I. Williams, *Gaussian Processes for Machine Learning*. MIT Press, Cambridge, MA, 2006.
- [144] Wikipedia contributors, *Plagiarism — Wikipedia, the free encyclopedia*, 2004.
- [145] G. L. J. Steve Brooks, Andrew Gelman and X.-L. Meng, *Handbook of Markov Chain Monte Carlo*. Chapman and Hall/CRC., Cambridge, MA, 2006.
- [146] D. Foreman-Mackey, D. W. Hogg, D. Lang and J. Goodman, *emcee: The mcmc hammer*, *PASP* **125** (2013) 306 [1202.3665].

- [147] J. Goodman and J. Weare, *Ensemble samplers with affine invariance*, *Comm.App.Math.Comp.Sc.* **5** (2010) 65.
- [148] S. Caron-Huot and G. D. Moore, *Heavy quark diffusion in perturbative QCD at next-to-leading order*, *Phys. Rev. Lett.* **100** (2008) 052301 [0708.4232].
- [149] ALICE collaboration, *Azimuthal anisotropy of D meson production in Pb-Pb collisions at $\sqrt{s_{NN}} = 2.76$ TeV*, *Phys. Rev.* **C90** (2014) 034904 [1405.2001].
- [150] ALICE collaboration, *Event-shape engineering for the D-meson elliptic flow in mid-central Pb-Pb collisions at $\sqrt{s_{NN}} = 5.02$ TeV*, *JHEP* **02** (2019) 150 [1809.09371].
- [151] S. K. Das, M. Ruggieri, F. Scardina, S. Plumari and V. Greco, *Effect of pre-equilibrium phase on R_{AA} and v_2 of heavy quarks in heavy ion collisions*, *J. Phys.* **G44** (2017) 095102 [1701.05123].
- [152] L. Keegan, A. Kurkela, A. Mazeliauskas and D. Teaney, *Initial conditions for hydrodynamics from weakly coupled pre-equilibrium evolution*, *JHEP* **08** (2016) 171 [1605.04287].
- [153] W. van der Schee, P. Romatschke and S. Pratt, *Fully Dynamical Simulation of Central Nuclear Collisions*, *Phys. Rev. Lett.* **111** (2013) 222302 [1307.2539].
- [154] R. Derradi de Souza, T. Koide and T. Kodama, *Hydrodynamic Approaches in Relativistic Heavy Ion Reactions*, *Prog. Part. Nucl. Phys.* **86** (2016) 35 [1506.03863].
- [155] R. Derradi de Souza, J. Takahashi, T. Kodama and P. Sorensen, *Effects of initial state fluctuations in the final state elliptic flow measurements using the NeXSPheRIO model*, *Phys. Rev.* **C85** (2012) 054909 [1110.5698].
- [156] H. Niemi, G. S. Denicol, H. Holopainen and P. Huovinen, *Event-by-event distributions of azimuthal asymmetries in ultrarelativistic heavy-ion collisions*, *Phys. Rev.* **C87** (2013) 054901 [1212.1008].
- [157] S. Juchem, W. Cassing and C. Greiner, *Quantum dynamics and thermalization for out-of-equilibrium ϕ^4 theory*, *Phys. Rev.* **D69** (2004) 025006 [hep-ph/0307353].
- [158] S. Juchem, W. Cassing and C. Greiner, *Nonequilibrium quantum field dynamics and off-shell transport for ϕ^4 theory in (2+1)-dimensions*, *Nucl. Phys.* **A743** (2004) 92 [nucl-th/0401046].
- [159] H. Berrehrah, E. Bratkovskaya, T. Steinert and W. Cassing, *A dynamical quasiparticle approach for the QGP bulk and transport properties*, *Int. J. Mod.*

- Phys. E* **25** (2016) 1642003 [1605.02371].
- [160] V. Ozvenchuk, O. Linnyk, M. I. Gorenstein, E. L. Bratkovskaya and W. Cassing, *Shear and bulk viscosities of strongly interacting “infinite” parton-hadron matter within the parton-hadron-string dynamics transport approach*, *Phys. Rev.* **C87** (2013) 064903 [1212.5393].
- [161] G. Policastro, D. T. Son and A. O. Starinets, *The Shear viscosity of strongly coupled $N=4$ supersymmetric Yang-Mills plasma*, *Phys. Rev. Lett.* **87** (2001) 081601 [hep-th/0104066].
- [162] P. Kovtun, D. T. Son and A. O. Starinets, *Viscosity in strongly interacting quantum field theories from black hole physics*, *Phys. Rev. Lett.* **94** (2005) 111601 [hep-th/0405231].
- [163] S. Mattiello and W. Cassing, *Shear viscosity of the Quark-Gluon Plasma from a virial expansion*, *Eur. Phys. J.* **C70** (2010) 243 [0911.4647].
- [164] C. Sasaki and K. Redlich, *Bulk viscosity in quasi particle models*, *Phys. Rev.* **C79** (2009) 055207 [0806.4745].
- [165] M. Bluhm, B. Kampfer and K. Redlich, *Bulk and shear viscosities of the gluon plasma in a quasiparticle description*, *Phys. Rev.* **C84** (2011) 025201 [1011.5634].
- [166] S. Cao et al., *Towards the extraction of heavy-quark transport coefficients in quark-gluon plasma*, 1809.07894.
- [167] A. Beraudo et al., *Extraction of Heavy-Flavor Transport Coefficients in QCD Matter*, *Nucl. Phys.* **A979** (2018) 21 [1803.03824].
- [168] P. B. Gossiaux, S. Vogel, H. van Hees, J. Aichelin, R. Rapp, M. He et al., *The Influence of bulk evolution models on heavy-quark phenomenology*, *Submitted to: Phys. rev. C* (2011) [1102.1114].
- [169] W. M. Alberico, A. Beraudo, A. De Pace, A. Molinari, M. Monteno, M. Nardi et al., *Heavy-flavour spectra in high energy nucleus-nucleus collisions*, *Eur. Phys. J.* **C71** (2011) 1666 [1101.6008].
- [170] P. B. Arnold, *Symmetric path integrals for stochastic equations with multiplicative noise*, *Phys. Rev.* **E61** (2000) 6099 [hep-ph/9912209].
- [171] VENUS collaboration, *Measurement of the running of effective QED coupling at large momentum transfer in the space - like region*, *Phys. Rev. Lett.* **81** (1998) 2428.
- [172] PHENIX collaboration, *Centrality dependence of π^0 and eta production at large transverse momentum in $s(NN)^{1/2} = 200$ -GeV $d+Au$ collisions*, *Phys. Rev. Lett.*

- 98 (2007) 172302 [nucl-ex/0610036].
- [173] N. Armesto, C. A. Salgado and U. A. Wiedemann, *Medium induced gluon radiation off massive quarks fills the dead cone*, *Phys. Rev.* **D69** (2004) 114003 [hep-ph/0312106].
- [174] M. G. Mustafa, *Energy loss of charm quarks in the quark-gluon plasma: Collisional versus radiative*, *Phys. Rev.* **C72** (2005) 014905 [hep-ph/0412402].
- [175] Z. Qiu and U. W. Heinz, *Event-by-event shape and flow fluctuations of relativistic heavy-ion collision fireballs*, *Phys. Rev.* **C84** (2011) 024911 [1104.0650].
- [176] M. He, R. J. Fries and R. Rapp, *Heavy-Quark Diffusion and Hadronization in Quark-Gluon Plasma*, *Phys. Rev.* **C86** (2012) 014903 [1106.6006].
- [177] A. Beraudo, A. De Pace, M. Monteno, M. Nardi and F. Prino, *Heavy flavors in heavy-ion collisions: quenching, flow and correlations*, *Eur. Phys. J.* **C75** (2015) 121 [1410.6082].
- [178] A. Beraudo, A. De Pace, M. Monteno, M. Nardi and F. Prino, *Heavy-flavour production in high-energy d-Au and p-Pb collisions*, *JHEP* **03** (2016) 123 [1512.05186].
- [179] T. Lang, H. van Hees, J. Steinheimer and M. Bleicher, *Elliptic flow and nuclear modification factors of D-mesons at FAIR in a Hybrid-Langevin approach*, 1305.1797.
- [180] J.-Y. Ollitrault, *Anisotropy as a signature of transverse collective flow*, *Phys. Rev.* **D46** (1992) 229.
- [181] STAR collaboration, *Elliptic flow in Au + Au collisions at $(S(NN))^{1/2} = 130$ GeV*, *Phys. Rev. Lett.* **86** (2001) 402 [nucl-ex/0009011].
- [182] T. Epelbaum and F. Gelis, *Pressure isotropization in high energy heavy ion collisions*, *Phys. Rev. Lett.* **111** (2013) 232301 [1307.2214].
- [183] F. Gelis, E. Iancu, J. Jalilian-Marian and R. Venugopalan, *The Color Glass Condensate*, *Ann. Rev. Nucl. Part. Sci.* **60** (2010) 463 [1002.0333].
- [184] H. Niemi, K. J. Eskola and R. Paatelainen, *Event-by-event fluctuations in a perturbative QCD + saturation + hydrodynamics model: Determining QCD matter shear viscosity in ultrarelativistic heavy-ion collisions*, *Phys. Rev.* **C93** (2016) 024907 [1505.02677].
- [185] M. Alvioli, H. J. Drescher and M. Strikman, *A Monte Carlo generator of nucleon configurations in complex nuclei including Nucleon-Nucleon correlations*, *Phys. Lett.* **B680** (2009) 225 [0905.2670].

- [186] P. Huovinen and H. Petersen, *Particlization in hybrid models*, *Eur. Phys. J.* **A48** (2012) 171 [1206.3371].
- [187] R. J. Fries, B. Muller, C. Nonaka and S. A. Bass, *Hadronization in heavy ion collisions: Recombination and fragmentation of partons*, *Phys. Rev. Lett.* **90** (2003) 202303 [nucl-th/0301087].
- [188] B. L. Combridge, *Associated Production of Heavy Flavor States in $p p$ and anti- $p p$ Interactions: Some QCD Estimates*, *Nucl. Phys.* **B151** (1979) 429.
- [189] R. Rapp and H. van Hees, *Heavy Quark Diffusion as a Probe of the Quark-Gluon Plasma*, 0803.0901.
- [190] D. K. Srivastava, R. Chatterjee and S. A. Bass, *Transport dynamics of parton interactions in pp collisions at energies available at the CERN Large Hadron Collider*, *Phys. Rev.* **C97** (2018) 064910 [1801.07482].
- [191] D. K. Srivastava, R. Chatterjee and S. A. Bass, *Landau-Pomeranchuk-Midgal effect and charm production in pp collisions at energies available at the CERN Large Hadron Collider using the parton cascade model*, *Phys. Rev.* **C98** (2018) 054910 [1806.10311].
- [192] J. Liu, C. Shen and U. Heinz, *Pre-equilibrium evolution effects on heavy-ion collision observables*, *Phys. Rev.* **C91** (2015) 064906 [1504.02160].
- [193] C. A. G. Prado, J. Noronha-Hostler, R. Katz, A. A. P. Suaide, J. Noronha, M. G. Munhoz et al., *Event-by-event correlations between soft hadrons and D^0 mesons in 5.02 TeV PbPb collisions at the CERN Large Hadron Collider*, *Phys. Rev.* **C96** (2017) 064903 [1611.02965].
- [194] P. Nason, S. Dawson and R. K. Ellis, *The Total Cross-Section for the Production of Heavy Quarks in Hadronic Collisions*, *Nucl. Phys.* **B303** (1988) 607.
- [195] G. S. Denicol, S. Jeon and C. Gale, *Transport Coefficients of Bulk Viscous Pressure in the 14-moment approximation*, *Phys. Rev.* **C90** (2014) 024912 [1403.0962].
- [196] W. Ke, Y. Xu and S. A. Bass, *Towards an extraction of \hat{q} with an uncertainty-controlled energy loss Monte-Carlo*, *PoS HardProbes2018* (2018) 155.
- [197] W. Ke, Y. Xu and S. A. Bass, *Towards an extraction of \hat{q} with an uncertainty controlled energy loss Monte-Carlo*, 2018, 1812.06149.
- [198] X. Yao, W. Ke, Y. Xu, S. Bass and B. Müller, *Quarkonium production in heavy ion collisions: coupled Boltzmann transport equations*, *PoS HardProbes2018* (2018) 157 [1812.02238].
- [199] W. Ke, Y. Xu and S. A. Bass, *A modified-Boltzmann approach for modeling the hot*

QCD medium-induced splitting vertices in the deep LPM region, 1810.08177.

- [200] Y. Xu et al., *Resolving discrepancies in the estimation of heavy quark transport coefficients in relativistic heavy-ion collisions*, *Phys. Rev.* **C99** (2019) 014902 [1809.10734].
- [201] X. Yao, W. Ke, Y. Xu, S. Bass and B. Müller, *Quarkonium production in heavy ion collisions: coupled Boltzmann transport equations*, *Nucl. Phys.* **A982** (2019) 755 [1807.06199].
- [202] P. Moreau, Y. Xu, T. Song, M. Nahrgang, S. Bass and E. Bratkovskaya, *Traces of non-equilibrium dynamics in relativistic heavy-ion collisions*, *PoS CPOD2017* (2018) 042 [1711.10223].
- [203] Y. Xu, J. E. Bernhard, S. A. Bass, M. Nahrgang and S. Cao, *Data-driven analysis for the temperature and momentum dependence of the heavy-quark diffusion coefficient in relativistic heavy-ion collisions*, *Phys. Rev.* **C97** (2018) 014907 [1710.00807].
- [204] Y. Xu, S. Cao, M. Nahrgang, J. E. Bernhard and S. A. Bass, *Data-driven analysis of the temperature dependence of the heavy-quark transport coefficient*, *Nucl. Part. Phys. Proc.* **289-290** (2017) 257.
- [205] Y. Xu, P. Moreau, T. Song, M. Nahrgang, S. A. Bass and E. Bratkovskaya, *Traces of nonequilibrium dynamics in relativistic heavy-ion collisions*, *Phys. Rev.* **C96** (2017) 024902 [1703.09178].
- [206] Y. Xu, S. Cao, G.-Y. Qin, W. Ke, M. Nahrgang, J. Auvinen et al., *Heavy-flavor dynamics in relativistic p-Pb collisions at $\sqrt{S_{NN}} = 5.02$ TeV*, *Nucl. Part. Phys. Proc.* **276-278** (2016) 225 [1510.07520].

Biography

After completing her schoolwork at Rudong High School in Nantong in 2009, Yingru entered Nanjing University in September 2009. She received her Bachelor of Science degree (physics major) from Nanjing University in June 2013. In August of the same year, she was admitted to the Graduate School of Duke University. She joined in the QCD Theory Group in the Department of Physics and worked with Professor Steffen A. Bass ever since. She passed the preliminary exam and became a doctoral candidate in December 2015, and is expected to receive the Doctor Degree of Philosophy in Summer 2019. During her Ph.D studies, she has published articles as the first author including:

- Y. Xu, S. A. Bass, P. Moreau, T. Song, M. Nahrgang, E. Bratkovskaya, P. Gossiaux, J. Aichelin, S. Cao, V. Greco, G. Coci, and K. Werner, *Resolving discrepancies in the estimation of heavy quark transport coefficients in relativistic heavy-ion collisions*, *Phys. Rev. C* 99 (2019) 014902 [1809.10734].
- Y. Xu, J. E. Bernhard, S. A. Bass, M. Nahrgang, and S. Cao, *Data-driven analysis for the temperature and momentum dependence of the heavy-quark diffusion coefficient in relativistic heavy-ion collisions*, *Phys. Rev. C* 97 (2018) 014907 [1710.00807].
- Y. Xu, P. Moreau, T. Song, M. Nahrgang, S. A. Bass, and E. Bratkovskaya, *Traces of nonequilibrium dynamics in relativistic heavy-ion collisions*, *Phys. Rev. C* 96 (2018) 024902 [1703.09178].
- Y. Xu, S. Cao, M. Nahrgang, J. E. Bernhard, S. A. Bass, *Data-driven analysis of the temperature dependence of the heavy-quark transport coefficient*, *Nucl.Part.Phys.Proc.* 289-290 (2017).
- Y. Xu, M. Nahrgang, J. E. Bernhard, S. Cao, S. A. Bass, *A data-driven analysis of the heavy quark transport coefficient*, *Nucl.Phys.* A967 (2017) [1704.07800].
- Y. Xu, S. Cao, M. Nahrgang, W. Ke, G. Qin, J. Auvinen, S. A. Bass, *Heavy-flavor dynamics in relativistic p-Pb collisions at 5.02 TeV*, *Nucl.Part.Phys.Proc.* 276-278 (2016) [1510.07520].

The whole list of publications is [73, 74, 166, 196–206].